

AFOSR FINAL REPORT
Grant No: FA9550-041-1-0042

WAYNE STATE UNIVERSITY
Department of Mechanical Engineering
Detroit, MI 48202

PIs: Raouf A. Ibrahim* and Ronald F. Gibson
*** Tel. (313) 577-3885**

Graduate Students Supported:

1. Dumitru M. Beliou
2. Stefan C. Castravete
3. Srinivasa D. Thoppul

Project Title:

**Nonlinear Stochastic Flutter of a Cantilever Wing with Joint Relaxation
and Random Loading**

Date: February 21, 2008

20080331083

REPORT DOCUMENTATION PAGE			Form Approved OMB No. 0704-0188	
<small>Public reporting burden for this collection of information is estimated to average 1 hour per response, including the time for reviewing instructions, searching existing data sources, gathering and maintaining the data needed, and completing and reviewing this collection of information. Send comments regarding this burden estimate or any other aspect of this collection of information, including suggestions for reducing this burden to Department of Defense, Washington Headquarters Services, Directorate for Information Operations and Reports (0704-0188), 1215 Jefferson Davis Highway, Suite 1204, Arlington, VA 22202-4302. Respondents should be aware that notwithstanding any other provision of law, no person shall be subject to any penalty for failing to comply with a collection of information if it does not display a currently valid OMB control number. PLEASE DO NOT RETURN YOUR FORM TO THE ABOVE ADDRESS.</small>				
1. REPORT DATE (09-02-2008)	2. REPORT TYPE: Final		3. DATES COVERED (From 02-01-04 - To 06-30-07)	
4. TITLE AND SUBTITLE Nonlinear Stochastic Flutter of a Cantilever Wing with Joint Relaxation and Random Loading			5a. CONTRACT NUMBER	
			5b. GRANT NUMBER FA9550-04-1-0042	
			5c. PROGRAM ELEMENT NUMBER	
6. AUTHOR(S) Raouf A. Ibrahim, and Ronald F. Gibson Ronald G. Gibson			5d. PROJECT NUMBER	
			5e. TASK NUMBER	
			5f. WORK UNIT NUMBER	
7. PERFORMING ORGANIZATION NAME(S) AND ADDRESS(ES) Wayne State University, Department of Mechanical Engineering, Detroit, MI 48202			8. PERFORMING ORGANIZATION REPORT NUMBER	
9. SPONSORING / MONITORING AGENCY NAME(S) AND ADDRESS(ES) U.S. Air Force (AFOSR) 875 N Randolph St Arlington VA 22203 Dr Victor Giurgintu/NA			10. SPONSOR/MONITOR'S ACRONYM(S)	
			11. SPONSOR/MONITOR'S REPORT	
12. DISTRIBUTION / AVAILABILITY STATEMENT: Unlimited				
13. SUPPLEMENTARY NOTES See the attached technical Report				
14. ABSTRACT The research project has generated a number of problems addressing the uncertainties and relaxation problems in aeroelastic structures. Specifically, three main problems that are of important concern to the aerospace industry and the Air Force technology have been addressed. These are: <ol style="list-style-type: none"> 1. The influence of structure uncertainties of the flutter of an aircraft wing. 2. Influence of joint relaxation on the flutter of aeroelastic structures (experimental and analytical investigations). 3. Stabilization of wing flutter via parametric excitation. These problems are addressed in more details in the attached technical report.				
15. SUBJECT TERMS				
16. SECURITY CLASSIFICATION OF: Unclassified			17. LIMITATION OF ABSTRACT	18. NUMBER OF PAGES
a. REPORT	b. ABSTRACT	c. THIS PAGE	19a. NAME OF RESPONSIBLE PERSON	
			19b. TELEPHONE NUMBER (include area code)	

Table of Contents

REPORT DOCUMENTATION PAGE

AFOSR FINAL REPORT

ABSTRACT	1
CHAPTER 1: EFFECT OF STIFFNESS UNCERTAINTIES ON THE FLUTTER OF A CANTILEVER WING	2
CHAPTER 2: THE INFLUENCE OF JOINT RELAXATION ON THE FLUTTER OF AEROELASTIC STRUCTURES	25
Part 1: Experimental Investigation	25
Part 2: Analytical Investigation	53
CHAPTER 3: FLUTTER SUPPRESSION OF A PLATE-LIKE WING VIA PARAMETRIC EXCITATION	94
Appendix: List of Publications Generated from the Grant	148
List of Ph.D. Theses Generated	149

ABSTRACT

The research project has generated a number of problems addressing the uncertainties and relaxation problems in aeroelastic structures. Specifically, three main problems that are of important concern to the aerospace industry and the Air Force technology have been addressed. These are:

1. The influence of structure uncertainties of the flutter of an aircraft wing.
2. Stabilization of wing flutter via parametric excitation.
3. Influence of joint relaxation on the flutter of aeroelastic structures.

These problems are addressed in the next three chapters.

CHAPTER 1.

EFFECT OF STIFFNESS UNCERTAINTIES ON THE FLUTTER OF A CANTILEVER WING

Summary of Results

This research project deals with the influence of structural uncertainties and joint relaxation on the flutter probability and safety of nonlinear cantilever wings. The tasks of the research have been accomplished using analytical, numerical, and experimental techniques. The influence of span-wise distribution of bending and torsion stiffness uncertainties on the flutter behavior of an aeroelastic wing using a stochastic finite element approach was studied using a numerical algorithm to simulate unsteady, nonlinear, incompressible flow (based on the unsteady vortex lattice method) interacting with linear aeroelastic structure in the absence of uncertainties. The air flow and wing structure were treated as elements of a single dynamical system. Parameter uncertainties were represented by a truncated Karhunen-Love expansion. Both perturbation technique and Monte Carlo simulation were used to establish the boundary of stiffness uncertainty level at which the wing exhibits flutter in the form of limit-cycle oscillations (LCO) and above which the wing experiences dynamic instability. The results of the perturbation approach were compared with those predicted by Monte Carlo simulation and the comparison revealed good correlation for low values of stiffness uncertainty levels. The major findings are:

- As uncertainty level increases, the perturbation method loses the accuracy.
- For the prediction of LCO, the perturbation method is very accurate for all levels of bending stiffness uncertainty examined, but the method loses its accuracy at upper levels of torsion stiffness uncertainty.
- The stability boundary in the flow speed versus stiffness uncertainty reveals the appearance of LCOs just below the flutter speed boundary. Further increase of uncertainty level produces instability.
- The uncertainties in torsion stiffness induce a greater disturbance in the system. A smaller level of torsion stiffness uncertainty induces instability in the system.

State-of-the-Art

The presence of parameter uncertainties in aeroelastic structures adds a new dimension to an already complicated problem. Parameter uncertainties owe their origin to a number of sources, which include:

- (i) randomness in material properties due to variations in material composition;
- (ii) randomness in structural dimensions due to manufacturing variations and thermal effects;
- (iii) randomness in boundary conditions due to preload and relaxation variations in mechanical joints; and,
- (iv) randomness of external excitations.

Generally, uncertainty is described as either parametric or non-parametric. Parametric uncertainty is due to variability in the value of input parameters, while non-parametric

uncertainty includes all other sources, such as modeling errors, coarse finite element mesh fidelity, or un-modeled nonlinear effects.

Parameter uncertainties may cause sensitivity and variability of the response and eigenvalues of structural stochasticity¹⁻³. The early developments relied on Monte Carlo simulation and later on first- and second-order perturbation methods to compute second-order moments of structure response. Furthermore, the general sources of uncertainty affecting the design and testing of aeroelastic structures were discussed. In particular, Pettit³ addressed a number of applications of uncertainty quantification to various aeroelastic problems such as flutter flight testing, prediction of limit-cycle oscillations (LCO), and design optimization with aeroelastic constraints. Different computational methodologies have been employed^{4,5} to quantify the uncertain response of aeroelastic structures with parametric variability. These methodologies include finite element and perturbation methods.

One of the major problems of incorporating the random field into finite element analyses is to deal with abstract spaces which have limited physical support^{6,7}. The difficulty involves the treatment of random variables defined on these abstract spaces. Usually the problem is solved through Monte Carlo simulation or stochastic finite element methods. Due to the large number of samples, which require high computational time, the Monte Carlo simulation is used mainly to verify other approaches. The perturbation⁸⁻¹¹ and Neumann expansion^{10,12} methods proved acceptable results for small random variation in the material properties. It was found that these methods are comparable in accuracy, but the most efficient solution procedure is the perturbation finite element method, which requires a single simulation. However, perturbation method requires the system uncertainty to be small enough to guarantee convergence and accurate results.

The perturbation stochastic finite element method (SFEM) has been adopted by several researchers using the Karhunen-Loeve (K-L) expansion to discretize the random fields due to structure mechanical properties¹³⁻¹⁵. Jensen¹⁶ considered an extension of the deterministic finite element method to the space of random function. A Neumann dynamic SFEM of vibration for structures with stochastic parameters under random excitation was treated by Lei and Qiu¹⁷. The equation of motion was transformed into quasi-static equilibrium equation for the solution of displacement in time domain. The Neumann expansion method was applied to the equation for deriving the statistical solution of the dynamic response within the framework of Monte Carlo simulation. The K-L expansion has proven to be a powerful tool in modeling parameter uncertainties in the structural dynamics community. However, it has not been utilized in the randomness and variability of parameters in aeroelastic structures. The present work is an attempt to employ the K-L expansion to discretize the span-wise distribution of bending and torsion stiffness uncertainties of an aircraft wing.

Structural and material uncertainties have a direct impact on the flutter characteristics of aeroelastic structures and they have begun to attract some attention in the literature. They were considered in studying the flutter of panels and shells¹⁸⁻²². Liaw and Yang^{18,19} quantified the effect of parameter uncertainties on the reduction of the structural reliability and stability boundaries of initially compressed laminated plates and shells. For buckling analysis, the uncertainties were included in the modulus of elasticity, thickness, and fiber orientation of individual lamina, as well as geometric imperfections. For flutter analysis, further uncertainties such as mass density, air density, and in-plane load were also considered. Kuttentkeuler and

Ringertz²⁰ performed an optimization study of the onset of flutter, with respect to material and structural uncertainties using finite element analysis and the doublet-lattice method. Lindsley et al.^{21,22} considered uncertainties in the modulus of elasticity and boundary conditions for a nonlinear panel in supersonic flow. The probabilistic response distributions were obtained using Monte Carlo simulation. It was reported that uncertainties have the greatest nonlinear influence on LCO amplitude near the deterministic point of LCO. Poirion^{23,24} employed a first-order perturbation method to solve for the probability of flutter given uncertainty in the structural mass and stiffness operators.

Recently, the influence of parameter uncertainties on the response of a typical airfoil section was considered by few researchers²⁵⁻²⁸. The sensitivity of uncertainty of aeroelastic phenomena was evaluated using Monte Carlo simulation. The effect of parametric uncertainty on the response of a nonlinear aeroelastic system was studied by Attar and Dowell²⁸ using a response surface method to map the random input parameters to the root-mean square wing tip response.

Civil engineers have been involved in studying the influence of uncertainties of structural properties, in particular damping, on the reliability analysis of flutter of a bridge girder and a flat plate was determined in few studies²⁹⁻³¹. The prediction of the flutter wind speed was found to be associated with a number of uncertainties such that the critical wind speed can be treated as a stochastic variable. The probability of the bridge failure due to flutter was defined as the probability of the flutter speed exceeding the extreme wind speed at the bridge site for a given period of time. The probabilistic dynamic response of a wind-excited structure has been studied in terms of uncertain parameters such as wind velocity, lift and drag coefficients by Kareem³². The influence of uncertainty in these parameters was found to propagate in accordance with the functional relationships that relate them to the structural response. Note that while in aerospace structures, one is interested in estimating the onset flutter due to parameter uncertainty, civil engineers, on the other hand, focus on probabilistic reliability analysis to determine a probability of the bridge or a structure failure due to flutter for a given return period rather than stating a single critical wind speed.

A ground vibration test was used by Potter and Lind³³ to obtain uncertainty models, such as natural frequencies and their associated variations, which can update analytical models for the purpose of predicting robust flutter speeds. Different norm approaches were used to formulate uncertainty models that cover the entire range of observed variations. Lind and Brenner³⁴ introduced a tool referred to as the "flutterometer" for predicting the onset of flutter during a flight test. The flutterometer computes the onset of flutter for an analytical model with respect to an uncertainty description. Brenner³⁵ considered a technique that identifies model parameters and their associated variances from flight data. Later, Prazenica, et al.³⁶ introduced a technique for estimating uncertainty descriptions based on a wavelet approach, but relies on Volterra kernels.

The present work deals with the influence of stiffness uncertainties on the flutter behavior of an aeroelastic wing. A numerical algorithm originally developed by Predikman and Mook³⁷ to simulate unsteady, nonlinear, incompressible flow interacting with linear aeroelastic wing in the absence of uncertainties is adopted. In order to implement this algorithm in the presence of uncertainties we introduce a random field that represents bending or torsion stiffness parameters or both as a truncated Karhunen-Love (K-L) expansion⁶. The air flow and wing structure are treated as elements of a single dynamic system. Both perturbation technique and Monte Carlo simulation are used to establish the boundary of stiffness uncertainty level at which the wing

exhibits LCO and above which the wing experiences dynamic instability. In this paper the term limit cycle oscillation is used to denote the flutter boundary, where for a linear system, effective damping is zero. The analysis also includes the limitation of perturbation solution for relatively large level of stiffness uncertainty. The analytical modeling of aerodynamic loading based on the unsteady vortex lattice method, structural forces interacting with the aerodynamic loading, and stiffness uncertainties based on The K-L expansion are briefly described in sections II through IV, respectively. Section V establishes the entire system modeling by combining the three models (aerodynamic, structure, and uncertainty) in the wing governing equations of motion in the finite element discretized form. Sections VI and VII present the perturbation analysis solution and Monte Carlo simulation results, respectively, together with a comparison of the corresponding results.

II. AERODYNAMIC MODELING

Aerodynamic modeling requires the estimation of aerodynamic forces and at the same time accounts for a wing elastic deformation. This is achieved by using the unsteady vortex lattice method (VLM). The VLM accounts for aerodynamic nonlinearities associated with the angle of attack, static deformation, vorticity-dominated flow, and unsteady behavior. It is also not limited to small periodic motion. The general unsteady vortex-lattice model imitates the boundary layers and the wakes as vortex sheets³⁷. The vortex sheets are of two types, bound-vortex sheet, and free vortex sheet. The bound-vortex sheets create the boundary layer on the surface of the wing while free-vortex sheets represent the wakes.

The lifting surface is approximated by a set of lattices of short segments of constant circulation each. Each segment occupies a portion of the wing surface and is enclosed by a loop of vortex segments. Figure 1(a) shows the discretization of the lifting surface, where N-frame is the ground fixed coordinate system and B-frame is the coordinate system on the wing body and is moving with the wing. The leading segment of the vortex loop is located at a distance equivalent to quarter of the panel length. The velocities are calculated at a finite number of points called control or collocation points located at the lattice center. Figure 1(b) represents the position of an arbitrary control point P on the lattice as a result of the wing structure displacement.

The point P^0 represents the point P before the wing is deformed. In the N-frame, the positions of P^0 and P are given by the vectors, \mathbf{R}_0 , and \mathbf{R} , respectively. The corresponding vectors in the B-frame are \mathbf{r}_0 and \mathbf{r} . The displacement of the aerodynamic point P due to deformation of the wing is, $\Delta \mathbf{r}_{Ap}$. The vectors \mathbf{R} and \mathbf{r} can be represented as functions of the wing displacement, $\Delta \mathbf{r}_{Ap}$, i.e., $\mathbf{R} = \mathbf{R}_0 + \Delta \mathbf{r}_{Ap}$, and $\mathbf{r} = \mathbf{r}_0 + \Delta \mathbf{r}_{Ap}$. The pressure $p(t)$ at point P was estimated using Bernoulli's equation for unsteady flow from which the non-dimensional aerodynamic load at point P is³⁸

$$\bar{\mathbf{F}}_{A,P}(\tau) = 2 \left\{ \Delta \bar{\mathbf{V}}_p \cdot [\bar{\mathbf{V}}_{mp} - {}^N \bar{\mathbf{V}}^B - {}^B \bar{\mathbf{r}}^P - \bar{\boldsymbol{\omega}}^B \times {}^B \bar{\mathbf{r}}^P] + \frac{D}{D\tau} [\bar{G}_p] \right\} \bar{A}_p \mathbf{n} \quad (1)$$

where \mathbf{n} is the unit normal vector at the control point, $\bar{A}_p = A_p / L_c^2$ is the non-dimensional area of the element P , A_p is the area of the element, L_c represents the chord-wise length of one element on the bound lattice, $\tau = t / T_c$, $\bar{\mathbf{R}} = \mathbf{R} / L_c = \bar{\mathbf{R}}_0 + \Delta \bar{\mathbf{r}}_{Ap}$, $\bar{\mathbf{R}}_0 = \mathbf{R}_0 / L_c$, $\Delta \bar{\mathbf{r}}_{Ap} = \Delta \mathbf{r}_{Ap} / L_c$, $T_c = L_c / V_\infty$ is a

characteristic time, $\bar{V}_F = V_F / V_\infty$, V_F is the absolute velocity of the air flow, V_∞ is the free stream velocity. $\Delta \bar{V}_p = \Delta V_p / V_\infty$ is the non-dimensional tangential velocity difference across the vortex lattice and $\bar{V}_{m,p}$ is the “mean” velocity which does not recognize the presence of the local vorticity. $\bar{V}_{m,p}$ can be considered as the flow velocity at the midpoint of the vortex sheet thickness. \bar{G}_p is the circulation loop in non-dimensional form of the vortex lattice element which encloses the control point P , ${}^N \bar{v}^B(\tau)$ is the absolute velocity of O_B , ${}^B \bar{r}^P$ and ${}^B \bar{v}^P$ are the position and velocity of P relative to the B-frame, respectively, and ${}^N \bar{\omega}^B(\tau)$ is the angular velocity of the B-frame. The expression for the aerodynamic load at point P in dimensional form is:

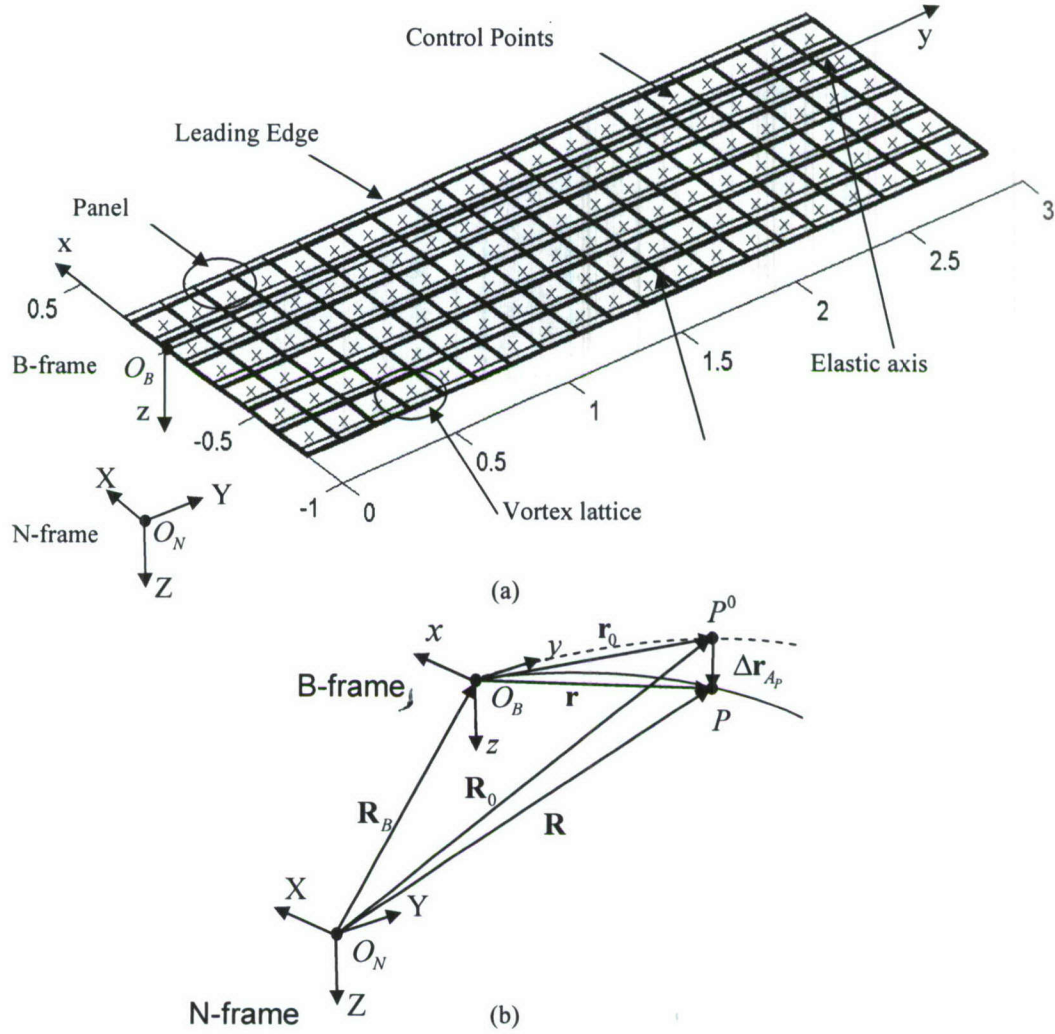


Figure 1. (a) Lifting Surface Discretization, (b) The position of an arbitrary point P on the lifting surface caused by the wing structure deformation

$$\mathbf{F}_{A,P}(t) = \left[(\rho_\infty V_\infty^2 / 2) L_C^2 \right] \bar{\mathbf{F}}_{A,P}(\tau) \quad (2)$$

where ρ is the density of the fluid. This aerodynamic force is acting at the center of each lattice and interacts with the elastic and inertia forces of the wing structure and their modeling is given in the next section.

III. STRUCTURAL MODELING

Figure 2(a) shows a cantilever wing with a straight elastic axis at distance δ_3 from the inertia axis. The wing is structurally modeled as an Euler-Bernoulli beam. The coordinate system coincides with the B-frame coordinate system from the aerodynamic modeling. The wing is divided into elements as shown in Figure 2(b), where a single element with two nodes is shown in Figure 2(c).

The displacements of each element, $\tilde{u}(y,t)$, $\tilde{v}(y,t)$, and $\tilde{w}(y,t)$, are expressed in terms of the nodal displacements u_i , v_i , w_i in x , y , and z directions, respectively, and nodal rotations β_i , α_i , γ_i about x , y , and z axes, respectively. The relationships between the element and nodal displacements are

$$\tilde{u}(y,t) = \mathbf{Y}_u^T(y) \mathbf{u}_e(t), \quad \tilde{v}(y,t) = \mathbf{Y}_v^T(y) \mathbf{v}_e(t) \quad (3)$$

$$\tilde{w}(y,t) = \mathbf{Y}_w^T(y) \mathbf{w}_e(t), \quad \tilde{\alpha}(y,t) = \mathbf{Y}_\alpha^T(y) \mathbf{a}_e(t)$$

$$\text{where } \mathbf{Y}_u^T(y) = \mathbf{Y}_w^T(y) = \{Y_3 \ Y_5 \ Y_4 \ Y_6\}, \quad \mathbf{Y}_v^T(y) = \mathbf{Y}_\alpha^T(y) = \{Y_1 \ Y_2\},$$

$$\mathbf{u}_e = \begin{Bmatrix} u_i \\ \gamma_i \\ u_{i+1} \\ \gamma_{i+1} \end{Bmatrix}, \quad \mathbf{v}_e = \begin{Bmatrix} v_i \\ v_{i+1} \end{Bmatrix}, \quad \mathbf{w}_e(t) = \begin{Bmatrix} w_i \\ \beta_i \\ w_{i+1} \\ \beta_{i+1} \end{Bmatrix}, \quad \mathbf{a}_e(t) = \begin{Bmatrix} \alpha_i \\ \alpha_{i+1} \end{Bmatrix}$$

Y_j , $j = 1, 2, \dots, 6$ the shape functions given by Preidikman³⁹. Applying Lagrange's equation to each coordinate gives the following set of equations of motion:

$$m \left(\int_{y_i}^{y_{i+1}} \mathbf{Y}_u(y) \mathbf{Y}_u(y)^T dy \right) \ddot{\mathbf{u}}_e(t) + \left(\int_{y_i}^{y_{i+1}} EI_z \mathbf{Y}_u(y)'' (\mathbf{Y}_u(y)'')^T dy \right) \mathbf{u}_e(t) = \left(\int_{y_i}^{y_{i+1}} F_u \mathbf{Y}_u(y) dy \right) \quad (4a)$$

$$m \left(\int_{y_i}^{y_{i+1}} \mathbf{Y}_v(y) \mathbf{Y}_v(y)^T dy \right) \ddot{\mathbf{v}}_e(t) + \left(\int_{y_i}^{y_{i+1}} AE \mathbf{Y}_v(y)' (\mathbf{Y}_v(y)')^T dy \right) \mathbf{v}_e(t) = \left(\int_{y_i}^{y_{i+1}} F_v \mathbf{Y}_v(y) dy \right) \quad (4b)$$

$$m \left(\int_{y_i}^{y_{i+1}} \mathbf{Y}_w(y) \mathbf{Y}_w(y)^T dy \right) \ddot{\mathbf{w}}_e(t) + m \delta_3 \left(\int_{y_i}^{y_{i+1}} \mathbf{Y}_w(y) \mathbf{Y}_\alpha(y)^T dy \right) \ddot{\mathbf{a}}_e(t) + \left(\int_{y_i}^{y_{i+1}} EI_x \mathbf{Y}_w(y)'' (\mathbf{Y}_w(y)'')^T dy \right) \mathbf{w}_e(t) = \left(\int_{y_i}^{y_{i+1}} F_w \mathbf{Y}_w(y) dy \right) \quad (4c)$$

$$\left(\int_{y_i}^{y_{i+1}} I_\alpha \mathbf{Y}_\alpha(y) \mathbf{Y}_\alpha(y)^T dy \right) \ddot{\mathbf{a}}_e(t) + m \delta_3 \left(\int_{y_i}^{y_{i+1}} \mathbf{Y}_\alpha(y) \mathbf{Y}_w(y)^T dy \right) \ddot{\mathbf{w}}_e(t) + \left(\int_{y_i}^{y_{i+1}} cG \mathbf{Y}_\alpha(y)' (\mathbf{Y}_\alpha(y)')^T dy \right) \mathbf{a}_e(t) = \left(\int_{y_i}^{y_{i+1}} M_\alpha \mathbf{Y}_\alpha(y) dy \right) \quad (4d)$$

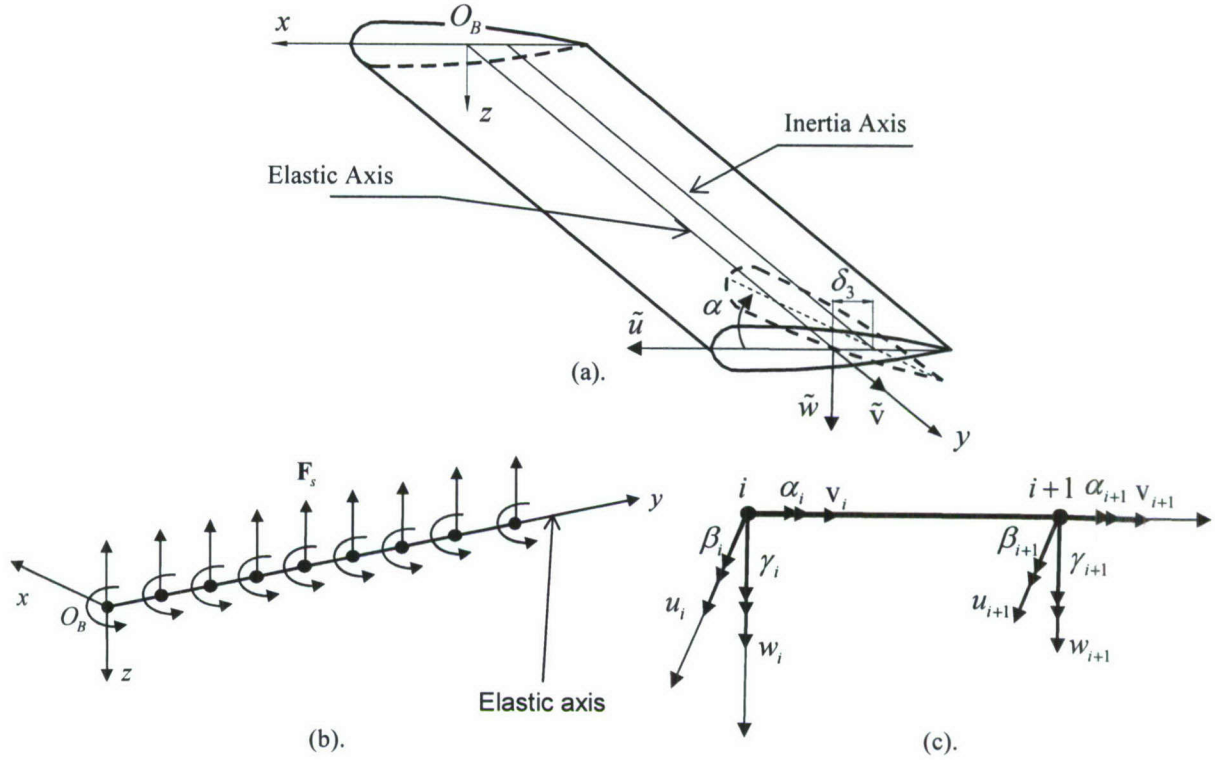


Figure 2. (a) Schematic diagram of a cantilever wing model, (b) Finite elements discretization, (c) A finite element representation

where a prime denotes a derivative with respect to spatial variable y . m is mass per unit length, I_0 is mass moment of inertia (about inertia axis) per unit length, and L is the wing length. A is the wing cross-sectional area, E is Young's modulus, I_x is the area moment of inertia of the wing cross-section about x axis, I_z is the area moment of inertia of the wing cross-section about z axis, J is the polar moment of inertia of the wing cross-section about z -axis, G is the modulus of rigidity, and c is a factor accounting for the non-circular geometry of the wing cross-section. The value of c depends on the cross-section geometry and is documented in the literature⁴⁰. F_u , F_v , and F_w are the external forces acting along x -, y -, and z -axes, respectively, and M_α is the external moment about the inertia axis. Equations (4) may be written in the matrix form:

$$\mathbf{M}^e \ddot{\mathbf{U}}^e + \mathbf{K}^e \mathbf{U}^e = \mathbf{F}^e \quad (5)$$

where $\mathbf{U}^e = \{u_i \ v_i \ w_i \ \beta_i \ \alpha_i \ \gamma_i \ u_{i+1} \ v_{i+1} \ w_{i+1} \ \beta_{i+1} \ \alpha_{i+1} \ \gamma_{i+1}\}^T$.

Equation (5) constitutes the governing equations of motion for a single element without uncertainties. The inclusion of material uncertainties will be considered in the next section.

IV. MODELING OF MATERIAL UNCERTAINTIES

Material uncertainty is considered for bending and torsion stiffness parameters. Let the bending and torsion stiffness parameters be represented in the form,

$$EI_x(y) = \overline{EI}_x + \widetilde{EI}_x(y), \quad GJ(y) = \overline{GJ} + \widetilde{GJ}(y) \quad (6a)$$

The mean values $\overline{EI}_x \gg 0$, and $\overline{GJ} \gg 0$ are assumed to be much larger than the root-mean-square of the random field variability represented by $\widetilde{EI}_x(y)$ and $\widetilde{GJ}(y)$. Both $\widetilde{EI}_x(y)$ and $\widetilde{GJ}(y)$ are assumed to be Gaussian distributed with zero mean and their standard deviations σ_{EI_x} , and σ_{GJ} are much smaller than the corresponding mean value, i.e., $\sigma_{EI_x}/\overline{EI}_x \ll 1$, and $\sigma_{GJ}/\overline{GJ} \ll 1$. This implies that the stiffness parameters $EI_x(y)$ and $GJ(y)$ form positive-valued random fields. Let the stiffness parameters be represented by the random function $\chi(y, \theta)$, where θ is a parameter that belongs to the space of random events and $y \in [-L/2, L/2]$. The random field $\chi(y, \theta)$ can be expressed by the truncated K-L expansion⁶:

$$\chi(y, \theta) = \bar{\chi}(y) + \sum_{n=1}^N \xi_n(\theta) \sqrt{\lambda_n} f_n(y) \quad (6b)$$

where $\bar{\chi}(y)$ is the mean value of $\chi(y, \theta)$, λ_n are the eigenvalues of the random field as defined in equation (7) and (9b) below, $f_n(y)$ is a set of eigen-functions, and $\xi_n(\theta)$ is a set of random variables with zero mean and $E[\xi_n(\theta)\xi_m(\theta)] = \delta_{nm}$, δ_{nm} is the Kronecker delta. Where λ_n are the eigenvalues of the covariance operators in equations (7) and (8), and $f_n(y)$ are the corresponding eigenfunctions by the solution of the integral equation

$$\int_{-L/2}^{L/2} C(y, y_1) f_n(y_1) dy_1 = \lambda_n f_n(y) \quad (7)$$

where $C(y, y_1)$ is the covariance kernel of the random field $\chi(y, \theta)$.

Expansion (6b) is mathematically well founded and is guaranteed to converge. The convergence and accuracy of the K-L expansion were proven by Huang et al.⁴¹ by comparing the second-order statistics of the simulated random process with that of the target process. It was shown that the factors affecting convergence are mainly the ratio of the length of the process over correlation parameter and the form of the covariance function. The K-L expansion has an advantage over the spectral analysis for highly correlated processes. For long stationary processes, the spectral method is generally more efficient as the K-L expansion method requires substantial computational effort to solve the integral equation. In addition, it is optimum in the sense that it minimizes the mean square error resulting from truncating the series at a finite number of terms. The bending and torsion stiffness parameters will be modeled by one-dimensional Gaussian random field models with bounded mean squares. Ghanem and Spanos⁶ and Loeve⁴² showed that for a Gaussian process the K-L expansion converges. The covariance kernel of the random field $\chi(y, \theta)$ may be assumed in the form:

$$C(y, y_1) = \sigma_\chi^2 e^{-|y-y_1|/l_{cor}} \quad (8)$$

where σ_χ^2 is the variance of the random field χ , such that $\sigma_\chi \ll \bar{\chi}(y)$ implying that $\chi(y, \theta)$ will always be positive, l_{cor} is correlation length such that $l_{cor} \rightarrow L$. For one-dimensional case, the eigenvalue problem (7) possesses the closed form analytical solution⁶

$$f_n(y) = \frac{\cos(\omega_n y)}{\sqrt{\frac{L}{2} + \frac{\sin(2\omega_n L/2)}{2\omega_n}}}, \quad \lambda_n = \frac{2\sigma_\chi^2 / l_{cor}}{\omega_n^2 + 1/l_{cor}^2} \quad (9a,b)$$

where ω_n are the roots of the characteristic equation:

$$\left[\frac{1}{l_{cor}} - \omega \tan\left(\omega \frac{L}{2}\right) \right] \left[\omega + \frac{1}{l_{cor}} \tan\left(\omega \frac{L}{2}\right) \right] = 0 \quad (10)$$

Introducing the expressions (9) into (6) the random field takes the form:

$$\chi(y, \theta) = \bar{\chi}(y) + \sum_{n=1}^N 2\xi_n(\theta) \sigma_\chi \sqrt{\frac{\omega_n / l_{cor}}{(\omega_n^2 + 1/l_{cor}^2)[L\omega_n + \sin(2\omega_n L/2)]}} \cos(\omega_n y) \quad (11)$$

For bending stiffness, the random field χ is denoted by $El_x(y)$ with mean value \overline{El}_x and variance $\sigma_{El_x}^2$; and for torsion stiffness the random field χ is denoted by $GJ(y)$ with mean value \overline{GJ} and variance σ_{GJ}^2 . For simplicity, it is assumed that both parameters are uncorrelated. The elemental stiffness expression \mathbf{K}^e is

$$\mathbf{K}^e(\theta) = \mathbf{K}_0^e + \sum_{n=1}^N \mathbf{K}_{b,n}^e \xi_n(\theta) + \sum_{n=1}^N \mathbf{K}_{t,n}^e \xi_n(\theta) \quad (12)$$

where

$$\mathbf{K}_0^e = El_z \int_{y_i}^{y_{i+1}} \mathbf{Y}_u'' (\mathbf{Y}_u'')^T dy + AE \int_{y_i}^{y_{i+1}} \mathbf{Y}_v' (\mathbf{Y}_v')^T dy + \overline{El}_x \int_{y_i}^{y_{i+1}} \mathbf{Y}_w'' (\mathbf{Y}_w'')^T dy + c\overline{GJ} \int_{y_i}^{y_{i+1}} \mathbf{Y}_a' (\mathbf{Y}_a')^T dy \quad (13a)$$

$$\mathbf{K}_{b,n}^e = \int_{y_i}^{y_{i+1}} 2\xi_n(\theta) \sigma_{El_x} \sqrt{\frac{\omega_n / l_{cor}}{(\omega_n^2 + 1/l_{cor}^2)[L\omega_n + \sin(2\omega_n L/2)]}} \cos(\omega_n y) \mathbf{Y}_w'' (\mathbf{Y}_w'')^T dy \quad (13b)$$

$$\mathbf{K}_{t,n}^e = \int_{y_i}^{y_{i+1}} 2\xi_n(\theta) \sigma_{GJ} \sqrt{\frac{\omega_n / l_{cor}}{(\omega_n^2 + 1/l_{cor}^2)[L\omega_n + \sin(2\omega_n L/2)]}} \cos(\omega_n y) \mathbf{Y}_a' (\mathbf{Y}_a')^T dy \quad (13c)$$

Assembling the elemental matrices we obtain

$$\mathbf{M}\ddot{\mathbf{U}}(\theta) + \left[\mathbf{K}_0 + \left(\sum_{n=1}^N \mathbf{K}_{b,n} \xi_n(\theta) \right) + \left(\sum_{n=1}^N \mathbf{K}_{t,n} \xi_n(\theta) \right) \right] \mathbf{U}(\theta) = \mathbf{F}_s(\mathbf{U}) \quad (14)$$

where \mathbf{M} is a $(6n_s \times 6n_s)$ mass matrix represents the assembled elemental mass matrix \mathbf{M}^e , n_s is the number of points in the structural grid, \mathbf{K}_0 is a $(6n_s \times 6n_s)$ matrix representing the assembled elemental mean value of the stiffness matrix \mathbf{K}_0^e . $\mathbf{K}_{b,n}$ and $\mathbf{K}_{t,n}$ are $(6n_s \times 6n_s)$ matrices representing the assembled elemental bending $\mathbf{K}_{b,n}^e$ and torsion $\mathbf{K}_{t,n}^e$ random stiffness matrices, respectively. $\mathbf{F}_s(\mathbf{U}, t, \theta)$ is a $(6n_s \times 1)$ vector representing the assembled elemental force vector \mathbf{F}_s^e , and $\mathbf{U}(t, \theta)$ is a $(6n_s \times 1)$ vector of the displacements of the points in the structural grid and represents the assembled elemental displacement vector \mathbf{U}^e .

Note that the left-hand side of equation (14) constitutes a set of stochastic second-order differential equations with random variable coefficients with Gaussian distribution. In the absence of aerodynamic forces, these equations are always stable, since the stiffness matrices are real positive definite. This is guaranteed by the fact that the uncertain components of the stiffness parameters are very small compared with their mean values as stated in the beginning of this section. In the next section the aerodynamic nodes will be connected to the structural finite element mesh and the aerodynamic forces will be transferred to the structural grid.

V. SYSTEM MODELING

Figure 3(a) shows the structural grid superimposed to the aerodynamic grid.

The relationship between the displacements of the aerodynamic grid points and displacements of the structural grid points is:

$$\Delta \underline{\mathbf{r}}_A = \begin{Bmatrix} \Delta \mathbf{r}_1 \\ \Delta \mathbf{r}_2 \\ \vdots \\ \Delta \mathbf{r}_{n_A} \end{Bmatrix} = \mathbf{G}_{AS} \mathbf{U} \quad (15)$$

where $\Delta \underline{\mathbf{r}}_A$ is a $(3n_A \times 1)$ vector representing the displacements of the control points in the aerodynamic grid, n_A is the number of control points in the aerodynamic grid, \mathbf{G}_{AS} is an $3n_A \times 6n_s$ interpolation matrix that connects the displacements of the nodal points in the aerodynamic grid to the displacements of the nodal points in the structural grid³⁷.

Figure 3(b) shows how an aerodynamic point is connected to an internal structural grid point, where an aerodynamic point P_A is connected to a point P_S on the elastic axis between two successive structural nodes. For the present study, the structural nodes are labeled by the index i , where $i = 1, 2, \dots, 8 (= n_s)$ while the aerodynamic points are labeled by the index j , where $j = 1, 2, \dots, 18 (= n_A)$. The points P_S and P_A are in the same plane, which is perpendicular to the elastic axis. The relative position between P_A and P_S is given by the vector $\mathbf{r}_j^{AS} = (x_j, y_j, z_j)$. The displacement of the point P_A is given by $\Delta \mathbf{r}_j^A = \{\Delta r_1^A, \Delta r_2^A, \Delta r_3^A\}^T$ and the displacement of the point

P_S is given by $U_i = \{u_i^s, v_i^s, w_i^s, \beta_i^s, \alpha_i^s, \gamma_i^s\}^T$. The relationship between the points P_A and P_S is given by³⁸:

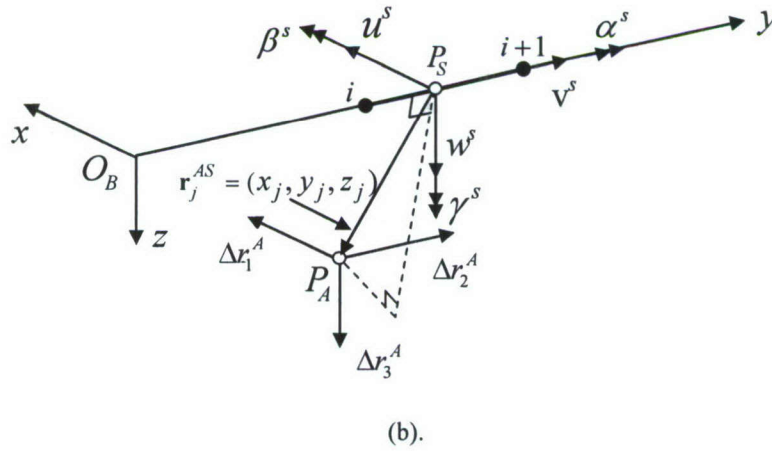
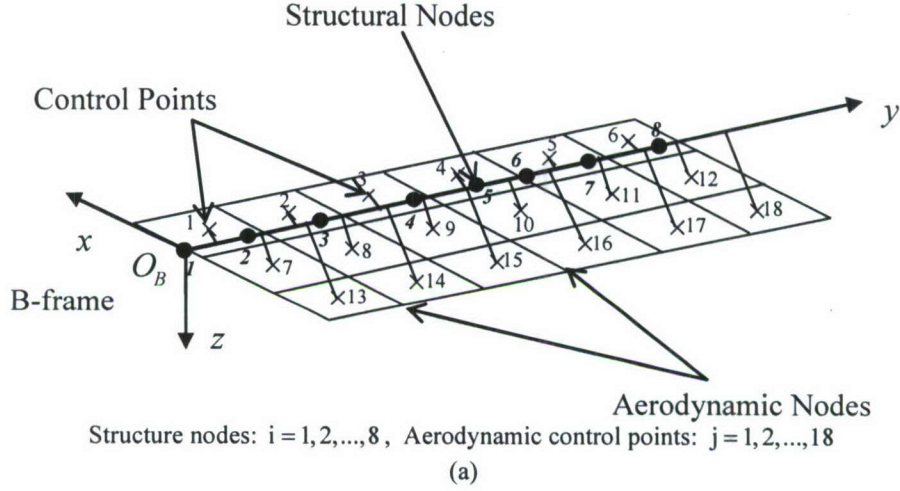


Figure 3. (a) Structural grid superimposed to the aerodynamic grid, (b) Connection of an aerodynamic grid point to an internal point of the structural grid point

$$\Delta \mathbf{r}_{jA} = \tilde{\mathbf{G}}_{ji} \mathbf{U}_{iS}, \quad \tilde{\mathbf{G}}_{ji} = \begin{bmatrix} 1 & 0 & 0 & 0 & z_j & 0 \\ 0 & 1 & 0 & -z_j & 0 & x_j \\ 0 & 0 & 1 & 0 & -x_j & 0 \end{bmatrix} \quad (16)$$

The displacement vector \mathbf{U}_{P_S} is obtained by finite element interpolation as a function of displacements on nodes i and $i+1$ as follows³⁷:

$$\mathbf{U}_{P_S} = \begin{bmatrix} \mathbf{Y}_{11} & \mathbf{Y}_{12} & \mathbf{Y}_{13} & \mathbf{Y}_{14} \\ \mathbf{Y}_{21} & \mathbf{Y}_{22} & \mathbf{Y}_{23} & \mathbf{Y}_{24} \end{bmatrix} \mathbf{U}_{i,i+1} = \tilde{\mathbf{Y}} \mathbf{U}_{i,i+1} \quad (17)$$

Where $\mathbf{U}_{i,i+1} = \{u_i \ v_i \ w_i \ \beta_i \ \alpha_i \ \gamma_i \ u_{i+1} \ v_{i+1} \ w_{i+1} \ \beta_{i+1} \ \alpha_{i+1} \ \gamma_{i+1}\}^T$, and the detailed structures of \mathbf{Y}_{ij} are given in the Appendix. Introducing equation (17) into equation (16) gives:

$$\Delta \mathbf{r}_{jA} = [\tilde{\mathbf{G}}_{ji} \tilde{\mathbf{Y}}] \begin{Bmatrix} \mathbf{U}_i \\ \mathbf{U}_{i+1} \end{Bmatrix} = [\mathbf{G}_{j,i} \ \mathbf{G}_{j,i+1}] \begin{Bmatrix} \mathbf{U}_i \\ \mathbf{U}_{i+1} \end{Bmatrix} \quad (18)$$

Next, the matrix $\mathbf{G}_{j,i}$ will be assembled into the global matrix, \mathbf{G}_{AS} , which is introduced into equation (15). In order to obtain the relationship between the aerodynamic forces \mathbf{F}_A and structural forces \mathbf{F}_S , the two force systems must have the same work for any virtual displacement, i.e.,

$$\delta(\Delta \mathbf{r}_A)^T \mathbf{F}_A = \delta \mathbf{U}_{St}^T \left\{ (\mathbf{G}_{AS})^T \mathbf{F}_A \right\} = \delta \mathbf{U}_{St}^T \mathbf{F}_S \quad (19)$$

where $\delta(\Delta \mathbf{r}_A)$ and $\delta \mathbf{U}_{St}^T$ are virtual displacements of control points of the aerodynamic grid and of structural nodes, respectively. \mathbf{G}_{AS} is the global matrix which connects the control points of the aerodynamic grid to the structural grid points, \mathbf{F}_A is the matrix of aerodynamic force, which is located at the aerodynamic control point, and \mathbf{F}_S is the matrix of the structural load, which is located at the structural grid points. Equation (19) yields the relationship between structural forces and the aerodynamic forces,

$$\mathbf{F}_S = (\mathbf{G}_{AS})^T \mathbf{F}_A = \mathbf{G}_{SA} \mathbf{F}_A \quad (20)$$

where $(\mathbf{G}_{AS})^T = \mathbf{G}_{SA}$. Introducing equation (20) into the equation (14), the equations of motion of the system is:

$$\mathbf{M} \ddot{\mathbf{U}}(\theta) + \left[\mathbf{K}_0 + \left(\sum_{n=1}^N \mathbf{K}_{b,n} \xi_n(\theta) \right) + \left(\sum_{n=1}^N \mathbf{K}_{t,n} \xi_n(\theta) \right) \right] \mathbf{U}(\theta) = \mathbf{G}_{SA} \mathbf{F}_A(\theta) \quad (21)$$

Equation (21) constitutes the equations of motion of a wing involving stiffness uncertainties. A modal analysis of equation (21) is performed and gives:

$$\mathbf{K}_0 \tilde{\Psi} = \mathbf{M} \tilde{\Psi} \tilde{\Lambda} \quad (22)$$

where $\tilde{\Psi}$ is an $N \times N$ eigenvector matrix where N is the number of degrees of freedom of the finite element model, and $\tilde{\Lambda}$ is a $N \times N$ diagonal matrix of eigenvalues. Equation (21) will be solved using perturbation analysis in the next section.

VI. PERTURBATION ANALYSIS

In order to develop the perturbation analysis, it is convenient to introduce the following coordinate transformation, which approximates the deformation of the beam:

$$\mathbf{U}(t, \theta) \cong \sum_{k=1}^{\tilde{N}} \Psi_k q_k = \Psi \mathbf{q}; \quad (23a)$$

where Ψ is a truncated form of $\tilde{\Psi}$. For the present application, the method requires displacement vector be expanded into the truncated Taylor series:

$$\mathbf{U}(t, \theta) = \Psi \left[\mathbf{q}_0(t) + \sum_{n=1}^N \frac{\partial \mathbf{q}}{\partial \xi_n} \Big|_{\xi=0} \xi_n(\theta) + \frac{1}{2} \sum_{n=1}^N \sum_{m=1}^N \frac{\partial^2 \mathbf{q}}{\partial \xi_n \partial \xi_m} \Big|_{\xi=0} \xi_n(\theta) \xi_m(\theta) + \dots \right] \quad (23b)$$

Note that Ψ is an $\tilde{N} \times \tilde{N}$ matrix that includes first \tilde{N} mode shape vector, \mathbf{q} is an $\tilde{N} \times 1$ generalized coordinates vector, and \mathbf{q}_0 is the mean value of \mathbf{q} . Substituting equation (23b) into equation (21), pre-multiplying both sides by $\mathbf{M}^{-1} \Psi^T$ and collecting terms of the same power of ξ yields a set of perturbational equations of zero-order, first-order, second-order, and so on. For simplification sake we restrict the analysis up to the first-order and the following perturbational equations are obtained:

- Zero-order equation (coefficients of ξ_n^0):

$$\ddot{\mathbf{q}}_0 + [\Psi^T \mathbf{K}_0 \Psi] \mathbf{q}_0 = [\mathbf{M}^{-1} \Psi^T \mathbf{G}_{SA}] \mathbf{F}_{A,0} \quad (24a)$$

- First-order equation (coefficients of ξ_n^1):

$$\ddot{\mathbf{q}}_{1,n} + [\Psi^T \mathbf{K}_0 \Psi] \mathbf{q}_{1,n} = -[\Psi^T \mathbf{K}_{b,n} \Psi + \Psi^T \mathbf{K}_{t,n} \Psi] \mathbf{q}_0 + [\mathbf{M}^{-1} \Psi^T \mathbf{G}_{SA}] \frac{\partial \mathbf{F}_A}{\partial \xi_n} \quad (24b)$$

where $n=1 \dots N$, $\mathbf{q}_{1,n} = \frac{\partial \mathbf{q}}{\partial \xi_n}$, and $[\Psi^T \mathbf{K}_0 \Psi]$ is an $\tilde{N} \times \tilde{N}$ diagonal matrix of first \tilde{N} eigenvectors. The aerodynamic loading \mathbf{F}_A as defined by equation (1) depends on the wing displacement $\Delta \mathbf{r}_{Ap}$ which is time dependent. Note that $\frac{\partial \mathbf{F}_A}{\partial \xi_n}$ is obtained by taking the derivative of equation (1) with respect to ξ_n after substituting for $\Delta \mathbf{r}_{Ap}$ which is expressed in equation (16) and equation (23b) which is a function of ξ_n .

Equations (24) are numerically integrated once using an adapted Hamming's fourth order predictor-corrector method. The numerical solutions are performed using the following values of the wing⁴³: $\overline{EI}_x = 10^6 \text{ Nm}^2$; $\overline{EI}_z = 50 \times 10^6 \text{ Nm}^2$; $\overline{GJ} = 1.5 \times 10^6 \text{ Nm}^2$; $EA = 20 \times 10^6 \text{ N}$; $m = 10 \text{ kg/m}$; $I_0 = 15 \text{ kg m}$; $\delta_3 = 0.15 \text{ m}$; wing length $L = 3 \text{ m}$; wing chord $C = 1 \text{ m}$; angle of attack $\alpha_a = 5^\circ$; $L_C = 0.16667 \text{ m}$; and $l_{cor} = L = 3 \text{ m}$. In order to obtain realistic results, the wing will be discretized using 9 elements for the wing structure and 6×10 elements for the lattice. The response will be obtained from perturbation method at various flow speeds and various bending and torsion stiffness uncertainty levels, i.e.,

$$q_{ben}(\tau, \theta) = q_{0,ben}(\tau) + \sum_{n=1}^N q_{1,ben}(\tau) \xi_n(\theta), \quad q_{tor}(\tau, \theta) = q_{0,tor}(\tau) + \sum_{n=1}^N q_{1,tor}(\tau) \xi_n(\theta) \quad (25a,b)$$

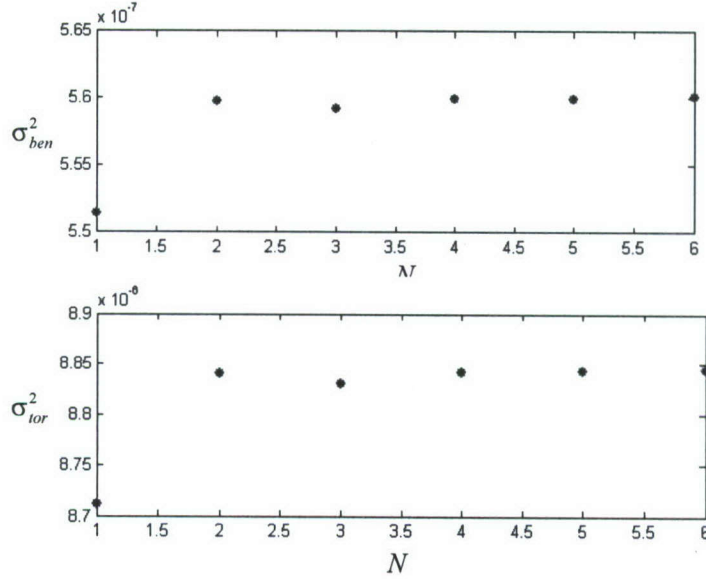


Figure 4. Dependence of wing response variances on the number of terms N in the Karhunen-Loeve expansion showing the convergence is achieved for $N \geq 2$.

where $q_{0,ben}$ and $q_{0,tor}$ are obtained from the equation (24a), $q_{1,ben}$ and $q_{1,tor}$ from the equation (24b). The analysis is carried out for $N=2$ since for $N>2$ the results converge as shown in Figure 4. The temporal component of the response variance along the ensemble is given by:

$$s_{ben}^2(t, \theta) = (q_{ben}(t, \theta) - E[q_{ben}(t, \theta)])^2, \quad s_{tor}^2(t, \theta) = (q_{tor}(t, \theta) - E[q_{tor}(t, \theta)])^2 \quad (26a,b)$$

The wing bending and torsion time history records are numerically estimated using equations (25) together with the corresponding variances (as computed from equations (26)) for airflow speed 120 m/s and angle of attack $\alpha = 5^\circ$, in the absence of uncertainty. The solutions are obtained for initial conditions $q_{ben}(0) = -0.05$, $\dot{q}_{ben}(0) = 0.0$, $q_{tor}(0) = 0.01$, and $\dot{q}_{tor}(0) = 0.0$. It is found that the wing is stable under this airflow speed. In the presence of small level of bending stiffness uncertainty up to $\sigma_{EI_x} / \overline{EI_x} = 0.09$ and zero torsion uncertainty, $\sigma_{GJ} / \overline{GJ} = 0.0$, and under the same airflow speed the wing remains stable and both time history records and their variances decay with time. When the bending stiffness uncertainty reaches the critical value $\sigma_{EI_x} / \overline{EI_x} = 0.1$ the wing experiences instability, loses its zero equilibrium state and reaches the flutter boundary in the form of LCOs due to aerodynamic nonlinearity. Above that level of bending stiffness uncertainty the wing oscillations grow without limit. As the air flow speed increases, the flutter boundary takes place for lower values of bending stiffness uncertainty defined by the bound $\sigma_{EI_x} / \overline{EI_x} < 0.1$. An extensive number of numerical solutions have been carried out for the purpose of establishing the flutter boundary on air flow speed, V_∞ , versus the variance of bending stiffness uncertainty, $\sigma_{EI_x} / \overline{EI_x}$. Figure 5(a) shows the stability bifurcation diagram $V_\infty - \sigma_{EI_x} / \overline{EI_x}$, where the region occupied by small empty circles, “o”, designates stable wing response, and the

region covered by small empty triangles, “ Δ ”, belongs to an unstable wing. The line separating the two regions signals the occurrence of flutter, designated by empty squares “ \square ”.

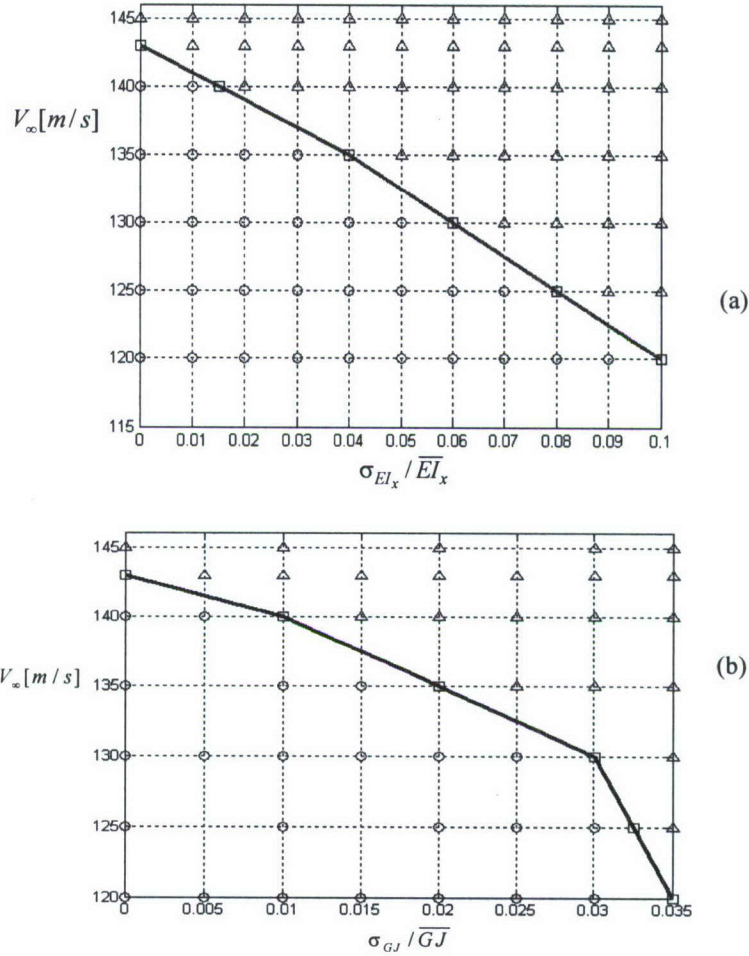


Figure 5. (a) Stability bifurcation diagram V_∞ vs. $\sigma_{EI_x} / \overline{EI_x}$, (b) Stability bifurcation diagram V_∞ vs. $\sigma_{GJ} / \overline{GJ}$

○ Stable, □ LCO, △ Unstable

In the absence of bending stiffness uncertainty, and over a small range of torsion stiffness uncertainty, the wing remains stable until $\sigma_{GJ} / \overline{GJ} = 0.035$, at which the wing experiences flutter for airflow speed 120 m/s, above that level the wing is unstable. Figure 5(b) shows the stability bifurcation diagram $V_\infty - \sigma_{GJ} / \overline{GJ}$. It is seen that the stable region in the presence of torsion stiffness uncertainty is smaller than the stable region in the presence of bending stiffness uncertainty. This demonstrates the significant influence of torsion stiffness uncertainty on the stability of the wing.

Figure 6 shows the influence of both bending and torsion uncertainties on the stability of the wing. Figure 6 reveals the stability boundaries for the bending-torsion combination uncertainties ($\sigma_{EI_x} / \overline{EI_x} - \sigma_{GJ} / \overline{GJ}$) at different flow speeds.

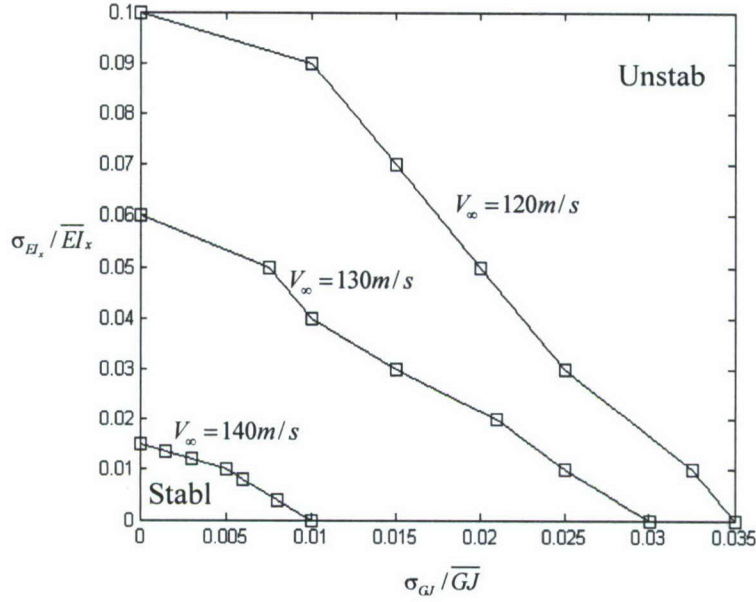


Figure 6. Stability boundaries $\sigma_{EI_x} / \overline{EI_x}$ vs. $\sigma_{GJ} / \overline{GJ}$ at different flow speeds.

VII. MONTE CARLO SIMULATION

In order to define the limitation of the perturbation method, the Monte Carlo simulation will be performed. First consider the deterministic equations of motion for one element as given by equation (5). Uncertainties will be introduced in bending stiffness, which is described by equation (6a). Assembling the elemental matrices given in the equation (5) and introducing the aerodynamic loads given by expression (20), gives the system equations of motion:

$$\mathbf{M}\ddot{\mathbf{U}} + \mathbf{K}\mathbf{U} = \mathbf{G}_{SA}\mathbf{F}_A \quad (27)$$

Using the coordinate transformation given by equation (23), equation (27) takes the form

$$\ddot{\mathbf{q}} + [\Psi^T \mathbf{K}_0 \Psi] \mathbf{q} = [\mathbf{M}^{-1} \Psi^T \mathbf{G}_{SA}] \mathbf{F}_A \quad (28)$$

Equation (28) will be integrated numerically once, based on the assumption that the response is ergodic. The Monte Carlo simulation confirms the perturbation results in predicting the flutter boundary for low values of bending stiffness variance. Figure 7(a) shows a comparison of perturbation (shown by solid curves) and Monte Carlo simulation (shown by dashed curves) results for bending and torsion variances for flow speed 120 m/s, and stiffness uncertainty parameters $\sigma_{EI_x} / \overline{EI_x} = 0.1$, $\sigma_{GJ} / \overline{GJ} = 0.0$. Figures 7(b) show another set for airflow speed of 140 m/s and bending uncertainty level $\sigma_{EI_x} / \overline{EI_x} = 0.015$ and zero torsion uncertainty. Figure 7(b) reveals good agreement between perturbation and Monte Carlo simulation results.

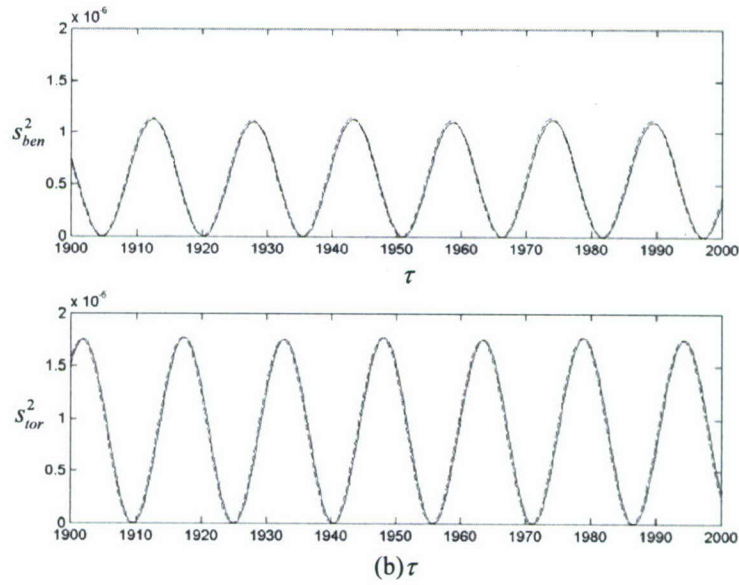
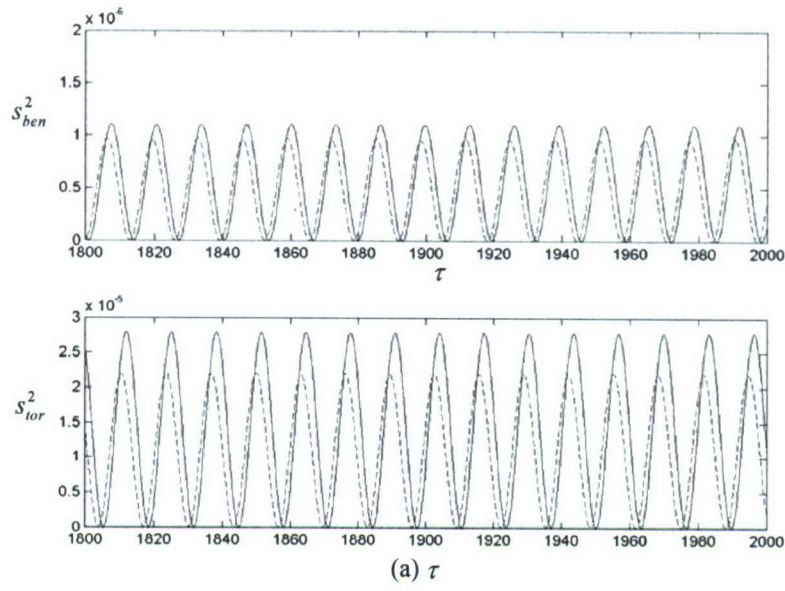


Figure 7. Time history records of bending and torsion response variance as estimated from perturbation method,

—— and Monte Carlo Simulation, -----, for $\alpha_a = 5^\circ$, $\sigma_{GJ} / \overline{GJ} = 0$, $q_{ben}(0) = -0.05$, $\dot{q}_{ben}(0) = 0$,

$$q_{tor}(0) = 0.01, \dot{q}_{tor}(0) = 0$$

(a) $V_\infty = 120 \text{ m/s}$, $\sigma_{EI_x} / \overline{EI_x} = 0.1$. (b) $V_\infty = 140 \text{ m/s}$, $\sigma_{EI_x} / \overline{EI_x} = 0.015$.

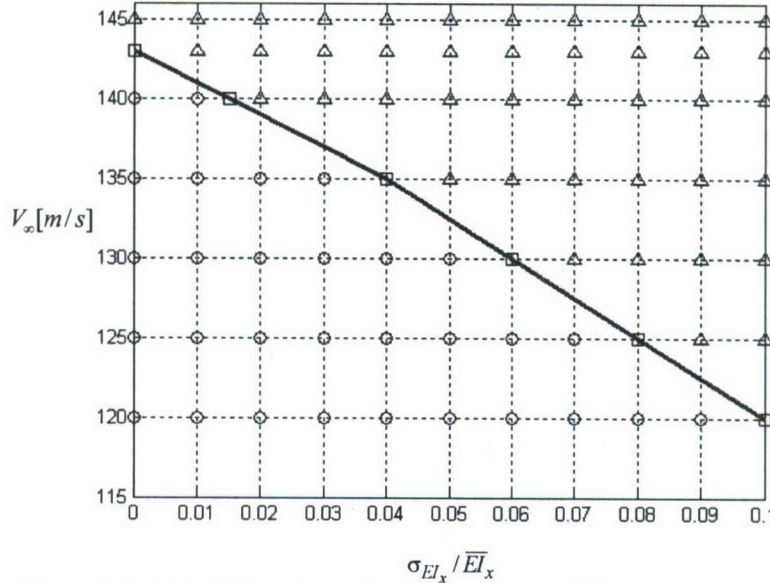


Figure 8. Stability bifurcation diagram V_∞ vs. $\sigma_{EI_x} / \overline{EI}_x$ for Monte Carlo Simulation

○ Stable, □ LCO, △ Unstable

The bifurcation diagram shown in Figure 8, obtained from Monte Carlo simulation, is identical with the one shown in Figure 5 estimated by perturbation method. This demonstrates that the perturbation method is very accurate in the prediction of the flutter boundary and the establishment of stability boundaries in the presence of bending uncertainties and absence of torsion uncertainties. The dependence of bending and torsion variances on bending uncertainties is shown in Figure 9 for different values of airflow speed.

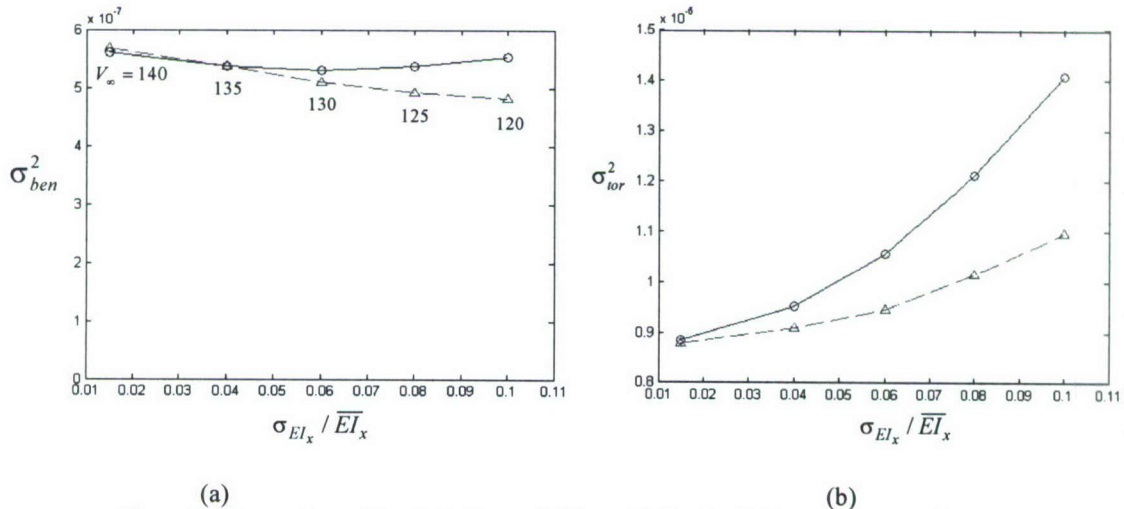


Figure 9. Comparison of perturbation and Monte Carlo simulation response variances: (a) bending, and (b) torsion

—○— Perturbation Method; ---△--- Monte Carlo Simulation

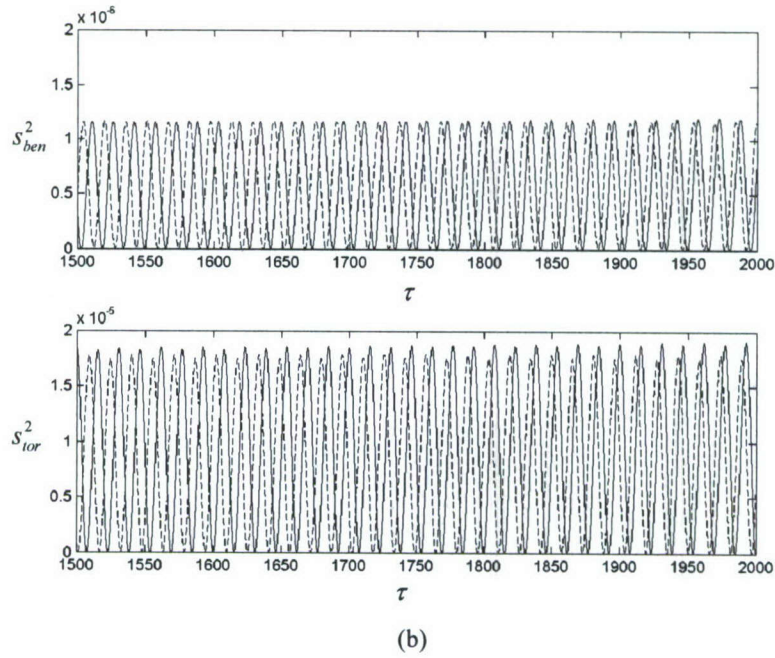
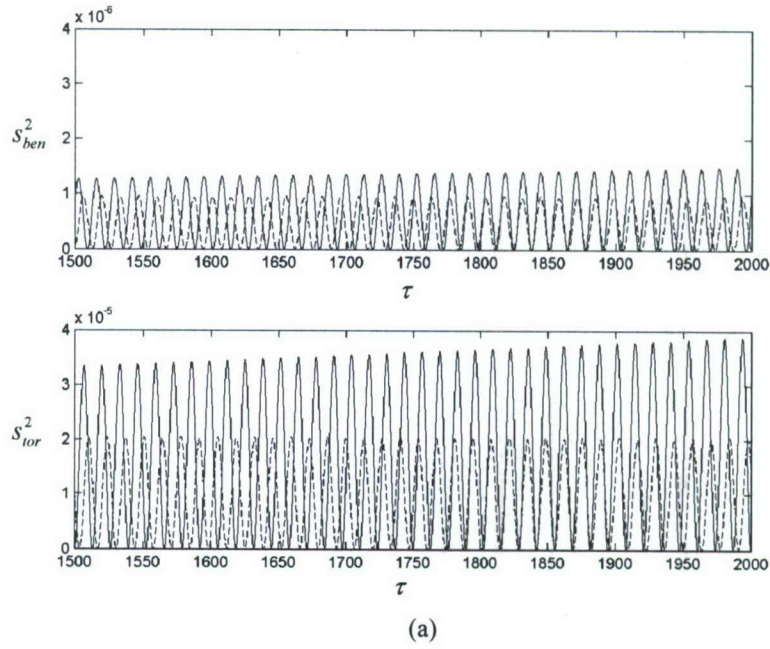


Figure 10. Time history records of bending and torsion response variances as estimated from perturbation method, —, Monte Carlo Simulation, -----, for $\alpha_a = 5^\circ$, $\sigma_{EI_x} / \overline{EI_x} = 0$, $q_{ben}(0) = -0.05$, $\dot{q}_{ben}(0) = 0$, $q_{tor}(0) = 0.01$, $\dot{q}_{tor}(0) = 0$. (a) $V_\infty = 120 \text{ m/s}$, $\sigma_{GJ} / \overline{GJ} = 0.05$, (b) $V_\infty = 140 \text{ m/s}$, $\sigma_{GJ} / \overline{GJ} = 0.01$.

Figures 10(a) and 10(b) show the Monte Carlo simulation time history response variances for two values of airflow speed, 120m/s and 140m/s, and two different levels of torsion stiffness

uncertainty, $\sigma_{GJ}/\overline{GJ} = 0.05$ and 0.01 , respectively. The comparison shown in Figure 10(a) reveals a poor approximation of the perturbation method as compared to Monte Carlo simulation for flow speed 120 m/s and $\sigma_{EI_x}/\overline{EI_x} = 0$, $\sigma_{GJ}/\overline{GJ} = 0.05$.

Note that the Monte Carlo simulation yields LCOs while the perturbation method gives unstable response. Better correlation between the two methods is obtained at higher speeds but lower uncertainty levels as demonstrated in Figure 10(b) for flow speed 140 m/s, $\sigma_{EI_x}/\overline{EI_x} = 0$, $\sigma_{GJ}/\overline{GJ} = 0.01$.

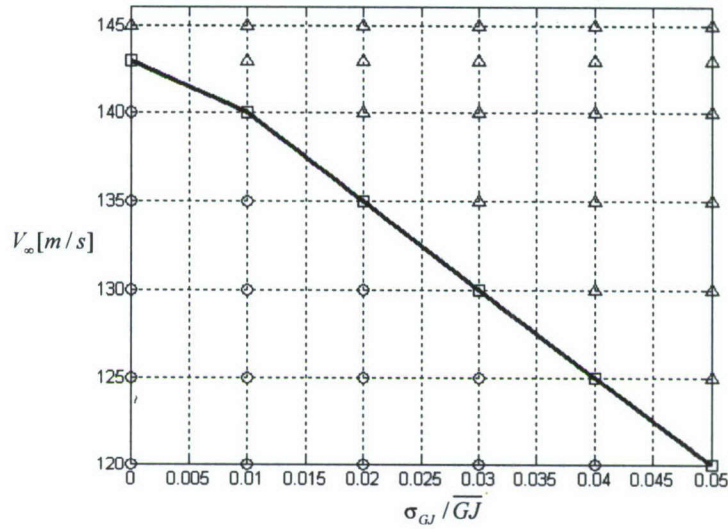


Figure 11. Stability bifurcation diagram V_∞ vs. $\sigma_{GJ}/\overline{GJ}$ for Monte Carlo Simulation

○ Stable, □ LCO, △ Unstable

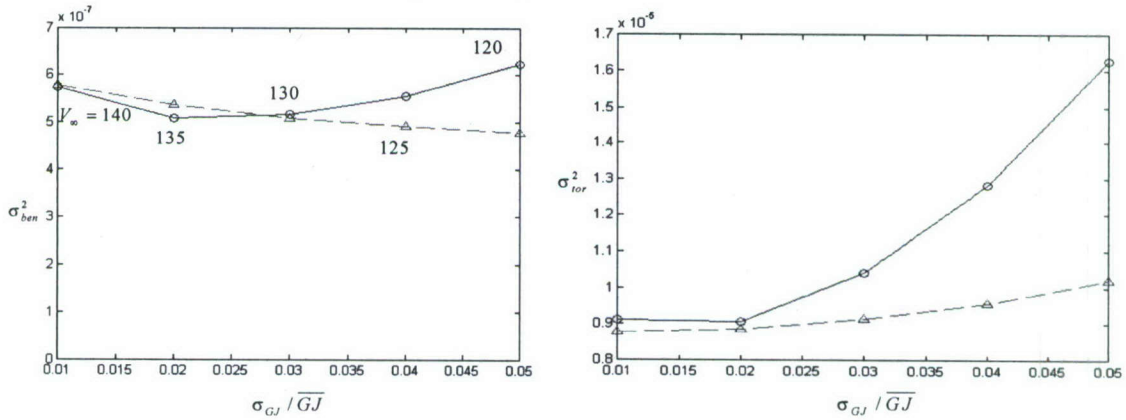


Figure 12. Perturbation method convergence

—○— Perturbation Method; ---△--- Monte Carlo Simulation

The stability bifurcation diagram $V_\infty - \sigma_{GJ}/\overline{GJ}$ obtained from Monte Carlo simulation is shown in Figure 11. Comparing the bifurcation diagrams from Figures 5(b) and 11, one observes a good

correlation in the prediction of flutter boundary up to flow speed 130 m/s and $\sigma_{GJ}/\overline{GJ} = 0.03$. As the flow speed decreases and torsion stiffness uncertainty level increases, the perturbation method loses the ability to predict the flutter boundary. For example, at flow speed 120 m/s, the flutter onset is obtained from Monte Carlo simulation at $\sigma_{GJ}/\overline{GJ} = 0.05$, while from perturbation method at $\sigma_{GJ}/\overline{GJ} = 0.035$. Figure 12(a) and 12(b) shows the dependence of bending and torsion variances on the torsion stiffness uncertainty level for different values of airflow speed indicated on each curve. Both diagrams reveal the validity of the perturbation method for a low level of stiffness uncertainty.

VIII. CONCLUSIONS

The influence of uncertainties of bending and torsion stiffness parameters on the flutter behavior of an aeroelastic wing is examined. The uncertainties are modeled using a modified first order stochastic perturbation method together with a truncated Karhunen-Loeve expansion instead of Taylor series. However, the Taylor series is used for displacement vector expansion. The results of the perturbation approach are compared with those predicted by Monte Carlo simulation and the comparison revealed good correlation for low values of stiffness uncertainty levels. As uncertainty level increases, the perturbation method loses the accuracy. For the prediction of LCO, the perturbation method is very accurate for all levels of bending stiffness uncertainty examined, but the method loses its accuracy at upper levels of torsion stiffness uncertainty. The stability boundary in the flow speed versus stiffness uncertainty reveals the appearance of LCOs just below the flutter speed boundary. Further increase of uncertainty level produces instability. The uncertainties in torsion stiffness induce a greater disturbance in the system. A smaller level of torsion stiffness uncertainty induces instability in the system.

REFERENCES

- 1 Ibrahim, R. A., "Structural Dynamics with Parameter Uncertainties," *ASME Applied Mechanics Reviews*, Vol. 40, No. 3, 1987, pp. 309-328.
- 2 Manohar, C. S. and Ibrahim, R. A., "Progress in Structural Dynamics with Stochastic Parameter Variations: 1987-1998," *ASME Applied Mechanics Reviews*, Vol. 52, No. 5, 1999, pp. 177-196.
- 3 Pettit, C. L., "Uncertainty Quantification in Aeroelasticity: Recent Results and Research Challenges," *Journal of Aircraft*, Vol. 41, No. 5, 2004, pp. 1217-1229.
- 4 Bae, H. R., Grandhi, R. V., Canfield, R. A., "An Approximation Approach for Uncertainty Quantification Using Evidence Theory," *Reliability Engineering and System Safety*, Vol. 86, 2004, pp. 215-235.
- 5 Beran, P. S., Pettit, C. L., and Millman, D. R., "Uncertainty Quantification of Limit-Cycle Oscillations," *Journal of Computational Physics*, Vol. 217, No. 1, 2006, pp. 217-247.
- 6 Ghanem, G. G. and Spanos, P.D., *Stochastic Finite Elements: A Spectral Approach*, Springer-Verlag New York, 1991.
- 7 Kleiber, M., Tran, D.H. and Hien, T. D., *The Stochastic Finite Element Method*, Chichester, John Wiley, 1992.
- 8 Cambou, B., "Application of First-Order Uncertainty Analysis in the Finite Element Method in Linear Elasticity," Proceedings of the 2nd International Conference on *Application of Statistics and Probability in Soil and Structural Engineering*, Aachen, Germany, Deutsche Gesellschaft für Grd-und Grundbau ev, Essen, FRG, pp. 67-87, 1975.
- 9 Nakagiri, S. and Hisada, T., "Stochastic Finite Element Method Applied to Structural Analysis with Uncertain Parameters," Proceedings of the International Conference on *Finite Element Method*, pp. 206-211, 1982.

- 10 Shinozuka, M. and Yamazaki, F., "Stochastic Finite Element Analysis: An introduction," *Stochastic Structural Dynamics: Progress in Theory and Applications*, S. T. Ariaratnam, G. I. Schueller, and I. Elishakoff, I. (Editors), Elsevier Applied Science, London, Chapter 14, pp. 241-291, 1988.
- 11 Liu, W. K., Belytschko, T. and Mani, A., "Probabilistic Finite Elements for Nonlinear Structural Dynamics," *Computer Methods in Applied Mechanics and Engineering*, 1986, 56(1), pp. 61-81.
- 12 Yamazaki, F., Shinozuka, M. and Dasgupta, G., "Neumann Expansion for Stochastic Finite Element Analysis," *Journal of Engineering Mechanics*, Vol. 114, No. 8, 1988, pp. 1335-1354.
- 13 Nieuwenhof, B. V. d. and Coyette, J.-P., "A Perturbation Stochastic Finite Element Method for the Time-Harmonic Analysis of Structures with Random Mechanical Properties," *Proceedings of the 5th World Congress on Computational Mechanics*, 2002.
- 14 Muscolino, G., Ricciardi, G., and Impollonia, N., "Improved Dynamic Analysis of Structures with Mechanical Uncertainties under Deterministic Input," *Probabilistic Engineering Mechanics*, Vol. 15, No. 2, 2000, pp. 199-212.
- 15 Cacciola, P. and Muscolino, G., "Dynamic Response of a Rectangular Beam with a Known Non-Propagating Crack of Certain and Uncertain Depth," *Computers and Structures*, Vol. 80, Nos. 27-30, 2002, pp. 2387-2396.
- 16 Jensen, H. A., *Dynamic Response of Structures with Uncertain Parameters*, Ph.D. Dissertation, California Institute of Technology, Pasadena, California, 1990.
- 17 Lei, Z. and Qiu, C., "Neumann Dynamic Stochastic Finite Element Method of Vibration for Structures with Stochastic Parameters to Random Excitation," *Computers and Structures*, Vol. 77, No. 6, 2000, pp. 651-657.
- 18 Liaw, D. G. and Yang, H. T. Y., "Reliability of Uncertain Laminated Shells Due to Buckling and Supersonic Flutter," *AIAA Journal*, Vol. 29, No. 10, 1991, pp. 1698-1708.
- 19 Liaw, D. G. and Yang, H. T. Y., "Reliability of Initially Compressed Uncertain Laminated Plates in Supersonic Flow," *AIAA Journal*, Vol. 29, No. 6, 1991, pp. 952-960.
- 20 Kutteneuler, J. and Ringertz, U., "Aeroelastic Tailoring Considering Uncertainties in Material Properties," *Structural Optimization*, Vol. 15, Nos. 3/4, 1998, pp. 157-162.
- 21 Lindsley, N. J., Beran, P. S. and Pettit, C.L., "Effects of Uncertainty on the Aerothermoelastic Flutter Boundary of a Nonlinear Plate," *AIAA Paper 2002-5136*, 2002.
- 22 Lindsley, N. J., Beran, P. S. and Pettit, C. L., "Effects of Uncertainty on Nonlinear Plate Aeroelastic Response," *AIAA Paper 2002-1271*, 2002.
- 23 Poirion, F., "Impact of Random Uncertainty on Aircraft Aeroelastic Stability," *Proceedings of the 3rd International Conference on Stochastic Structural Dynamics*, San Juan, PR, 1995.
- 24 Poirion, F., "On Some Stochastic Methods Applied to Aeroservoelasticity," *Aerospace Science and Technology*, Vol. 4, No. 3, 2000, pp. 201-214.
- 25 Pettit, C. L. and Beran, P. S., "Effects of Parametric Uncertainty on Airfoil Limit-Cycle Oscillation," *Journal of Aircraft*, Vol. 40, No. 5, 2003, pp. 1004-1006.
- 26 Pettit, C. L. and Beran, P. S., "Polynomial Chaos Expansion Applied to Airfoil Limit-Cycle Oscillations," *Collection of Technical Papers - AIAA/ASME/ASCE/AHS/ASC Structures, Structural Dynamics and Materials Conference*, Palm Springs, CA, 1975-1985, 2004.
- 27 Ueda, T., "Aeroelastic Analysis Considering Structural Uncertainty," *Aviation*, Vol. 9, No. 1, 2005, pp. 3-7.
- 28 Attar, P. J. and Dowell, E. H., "A Stochastic Analysis of the Limit-Cycle Behavior of a Nonlinear Aeroelastic Model Using the Response Surface Method," *Proceedings of the 46th AIAA/ASME/ASCE/AHS/ASC Structures, Structural Dynamics and Materials Conference*, Austin, Texas, pp. 2318-2338, 2005.
- 29 Ostenfeld-Rosenthal, P., Madsen, H. O. and Larsen, A., "Probabilistic Flutter Criteria for Long Span Bridges," *Journal of Wind Engineering and Industrial Aerodynamics*, Vol. 42, Nos. 1-3, 1992, pp. 1265-1276.
- 30 Ge, Y. J., Xiang, H. F. and Tanaka, H., "Application of the Reliability Analysis Model to Bridge Flutter under Extreme Winds," *Journal of Wind Engineering and Industrial Aerodynamics*, Vol. 86, No. 2, 2000, pp. 155-167.

- 31 Jakobsen, J. B. and Tanaka, H., "Modeling Uncertainties in Prediction of Aeroelastic Bridge Behavior," *Journal of Wind Engineering and Industrial Aerodynamics*, Vol. 91, Nos. 12-15, 2003, pp. 1485-1498.
- 32 Kareem, A., "Aerodynamic Response of Structures with Parameter Uncertainties," *Structural Safety*, Vol. 5, No. 3, 1988, pp. 205-225.
- 33 Potter, S. and Lind, R. *Developing Uncertainty Models for Robust Flutter Analysis Using Ground Vibration Test Data*, NASA/TM-2001-210392, 2001.
- 34 Lind, R. and Brenner, M., "Flutterometer: An On-Line Tool to Predict Robust Flutter Margins," *Journal of Aircraft*, Vol. 37, No. 6, 2000, pp. 1105-1112.
- 35 Brenner, M. J., "Aeroelastoc Uncertainty Model Identification from Flight Data," *Journal of Guidance, Control, and Dynamics*, Vol. 25, No. 4, 2002, pp. 748-754.
- 36 Prazenica, R. J., Lind, R. and Kurdila, A. J., "Uncertainty Estimation from Volterra Kernels for Robust Flutter Analysis," *Journal of Guidance, Control, and Dynamics*, Vol. 26, No. 2, 2003, pp. 331-339.
- 37 Preidikman, S. and Mook, D., "Time-Domain Simulations of Linear and Nonlinear Aeroelastic Behavior," *Journal of Vibration and Control*, Vol. 6, 2000, pp. 1135-1175.
- 38 Preidikman, S., *Numerical Simulations of Interactions among Aerodynamics, Structural Dynamics, and Control Systems*, Ph.D. Dissertation, Virginia Polytechnic Institute and State University, Blacksburg, Virginia, 1998.
- 39 Chandrupatla, T. R. and Belegundu, A. D., *Introduction to Finite Elements in Engineering*, Prentice Hall, Upper Saddle River, N.J, 2002.
- 40 Cris, H. D., *Fundamentals of Aircraft Structural Analysis*, McGraw-Hill, New York, 1997.
- 41 Huang, S. P., Quek, S. T., and Phoon, K. K., "Convergence study of the Truncated Karhunen-Loeve Expansion for Simulation of Stochastic Processes," *International Journal of Numerical Methods in Engineering*, Vol. 52, 2001, pp. 1029-1043.
- 42 Loeve, M., *Probability Theory*, Springer-Verlag, Berlin, 1977.
- 43 Hall, B. D., *Numerical Simulations of the Aeroelastic Response of an Actively Controlled Flexible Wing*, M.S. Thesis in Engineering Mechanics from Virginia Polytechnic Institute and State University, Blacksburg, Virginia, 1999.

Appendix

The detailed structures of Y_{ij} of equation (17)

$$\begin{aligned}
 Y_{11} &= \begin{bmatrix} Y_3 & 0 & 0 \\ 0 & Y_1 & 0 \\ 0 & 0 & Y_3 \end{bmatrix}, & Y_{12} &= \begin{bmatrix} 0 & 0 & -Y_5 \\ 0 & 0 & 0 \\ Y_5 & 0 & 0 \end{bmatrix}, & Y_{13} &= \begin{bmatrix} Y_4 & 0 & 0 \\ 0 & Y_2 & 0 \\ 0 & 0 & Y_4 \end{bmatrix}, & Y_{14} &= \begin{bmatrix} 0 & 0 & -Y_6 \\ 0 & 0 & 0 \\ Y_6 & 0 & 0 \end{bmatrix}, \\
 Y_{21} &= \begin{bmatrix} 0 & 0 & -Y_3' \\ 0 & 0 & 0 \\ Y_3' & 0 & 0 \end{bmatrix}, & Y_{22} &= \begin{bmatrix} Y_5' & 0 & 0 \\ 0 & Y_1 & 0 \\ 0 & 0 & Y_5' \end{bmatrix}, & Y_{23} &= \begin{bmatrix} 0 & 0 & -Y_4' \\ 0 & 0 & 0 \\ Y_4' & 0 & 0 \end{bmatrix}, & Y_{24} &= \begin{bmatrix} Y_6' & 0 & 0 \\ 0 & Y_2 & 0 \\ 0 & 0 & Y_6' \end{bmatrix}
 \end{aligned}$$

where a prime denotes a derivative with respect to y and Y_i are the finite element shape functions given by

$$\begin{aligned}
 Y_1 &= \frac{y_{i+1} - y}{y_{i+1} - y_i}, \quad Y_2 = \frac{y - y_i}{y_{i+1} - y_i}, \quad Y_3 = 1 - 3 \left(\frac{y - y_i}{y_{i+1} - y_i} \right)^2 + 2 \left(\frac{y - y_i}{y_{i+1} - y_i} \right)^3, \quad Y_4 = 3 \left(\frac{y - y_i}{y_{i+1} - y_i} \right)^2 - 2 \left(\frac{y - y_i}{y_{i+1} - y_i} \right)^3, \\
 Y_5 &= (y - y_i) - \frac{2}{y_{i+1} - y_i} (y - y_i)^2 + \frac{1}{(y_{i+1} - y_i)^2} (y - y_i)^3, \quad Y_6 = -\frac{1}{y_{i+1} - y_i} (y - y_i)^2 + \frac{1}{(y_{i+1} - y_i)^2} (y - y_i)^3, \\
 & \quad y_i \leq y \leq y_{i+1}.
 \end{aligned}$$

CHAPTER 2:

**THE INFLUENCE OF JOINT RELAXATION
ON THE FLUTTER OF AEROELASTIC STRUCTURES:**

Part 1: Experimental Investigation

ABSTRACT

The influence of boundary conditions relaxation on two-dimensional panel flutter is studied in the presence of in-plane loading. The boundary value problem of the panel involves time-dependent boundary conditions that are converted into autonomous form using a special coordinate transformation. Galerkin's method is used to discretize the panel partial differential equation of motion into six nonlinear ordinary differential equations. The influence of boundary conditions relaxation on the panel modal frequencies and LCO amplitudes in the time and frequency domains is examined using the windowed short time Fourier transform and wavelet transform. The results revealed:

- The relaxation and system nonlinearity are found to have opposite effects on the time evolution of the panel frequency.
- Depending on the system damping and dynamic pressure, the panel frequency can increase or decrease with time as the boundary conditions approach the state of simple supports.

The effects of various bolt preloads, viscoelasticity and external applied static and dynamic loads on bolt load relaxation in a carbon/epoxy composite bolted joint have been studied. Both phenomenological modeling and finite element analysis (FEA) of bolt-connected three-point bending specimens were employed in the studies. The experimental measurements showed that:

- Relaxation of 1.25% - 4.25% over a period of 30 hours was observed depending on the initial preload and applied external loads.
- It was observed that for any magnitude of external load the bolt load relaxation decreases with increasing initial preload. These findings emphasize the importance of the magnitude of the preload.
- Only about 1/3 of the relaxation in composite specimens is due to viscoelastic behavior of the polymer matrix in the composite, and the remaining 2/3 of the relaxation is due to other mechanisms such as bolt thread slip, plasticity and/or external excitation.

State-of-the Art

The purpose of the present investigation is to conduct experiments and develop phenomenological models of relaxation in composite joints under external static and dynamic loads. An attempt was also made to indirectly estimate the effect of viscoelasticity on relaxation by comparing experimental relaxation curves for a composite bolted joint with those of a steel joint, which does not exhibit viscoelastic behavior at room temperature. Phenomenological models were derived from the experimental results based on regression analysis. Three-dimensional FEA models for the composite bolted joints including the time-dependent material properties under 3 point bending were developed and a quasi-elastic approach was used to estimate the bolt load relaxation for static and dynamic loads and for various values of preloads.

The relevant previous work reported in the literature addresses the design, analysis and relaxation of bolted joints, and is reviewed in the next two subsections.

Design, Analysis and Characterization of Joints

The design of structural systems involves elements that are connected through adhesive bonds, bolts, rivets, pins, and various combinations of these connections. Joints and fasteners are used to transfer loads from one structural element to another. In composite structures, three types of joints are commonly used, namely, mechanically fastened joints, adhesively bonded joints, and hybrid mechanically fastened/adhesively bonded joints. General aspects of design, analysis and characterization of composite joints have been discussed by Camanho and Mathews [1], Erki [2], Jones [3], Wang, et al. [4], Rastogi, et al. [5,6,7], and Hart-Smith [8-9]. Adhesive joints depend on the size of the parts to be joined and the amount of overlap required to carry the load. Adhesive joints are often acceptable for secondary structures, but are generally avoided in primary structures on account of strength, temperature and moisture effects, and reliability. Bolted joints or hybrid bolted/bonded joints are still the dominant fastening mechanisms used in joining of primary structural parts for advanced composites.

The complex behavior of connecting elements plays an important role in the overall dynamic characteristics such as natural frequencies, mode shapes, and response characteristics to external excitations. The joint represents a discontinuity in the structure and results in high stresses that often initiate joint failure. Ibrahim and Pettit [10] presented an overview of the problems pertaining to structural dynamics with bolted joints. The contact forces are not ideally plane due to manufacturing tolerances. Furthermore, the initial forces will be redistributed non-uniformly in the presence of lateral loads. Under environmental dynamic loading, the preload in joints experiences some relaxation that results in time variation of the structure's dynamic properties. Most of the reported studies have focused on the energy dissipation of bolted joints, linear and nonlinear identification of the dynamic properties of the joints, parameter uncertainties and relaxation, and active control of the joint preload.

Although utilized quite extensively, bolted joints in laminated composites are not well understood. Packman, et al. [11], Schulz, et al. [12] and Lin and Jen [13] presented experimental and statistically-based investigations of ultimate strengths of bolted joints for laminated composites. Stress concentrations at hole-edges in advanced composites can be very high (Jones, [3]) and joint efficiencies are often as low as 50% (Hart-Smith, [14]). The design of composite fasteners subjected to transverse loads was considered by Running, et al. [15]. Rosner and Rizkalla [16,17] experimentally and analytically examined the behavior of bolted connections in composite materials used for civil engineering applications. A design procedure was introduced to account for material orthotropy, pseudo-yielding capability, and other factors that influence bolted-connection behavior.

Andreasson, et al. [18], Menendez and Guemes [19], and Li, et al. [20] analytically and experimentally studied the tensile response and failure of bolted or riveted joints made from carbon fiber-reinforced plastic (CFRP). They observed that the dynamic behavior of composite joints is much more complicated than its behavior for the quasi-static condition due to strain rate and inertia effects. The effect of clamping on the tensile strength of composite plates with a bolt-filled hole was studied by Horn [21], Hung [22], Hung, et al. [23,24], and Yan, et al. [25]. Early work by Van Siclen [26] on composite bolted joints made of graphite/epoxy involved the development of joint allowables and alternating reinforcing concepts for increasing joint

strength. Semi-empirical procedures combined with experimental data were used to predict the joint strength as a function of basic laminate properties and joint geometrical parameters. Studies reported in the literature address the importance of joint allowables [27, 28], selection of optimum ply stacking sequence [8], washer size, effects of clamping force or bolt preload on joint strength and failure modes [9,29,30]. Yet, some of these questions remain unanswered. For example, how much bolt preload should be applied to composite joints to minimize relaxation and what other factors have the most influence on relaxation in such joints?

Some designers use the existing design code MSFC-STD-486B from the NASA Marshall Space Flight Center [31], which was developed originally for metallic joints. This code recommends that, for typical preloaded structural assemblies in tension, the bolt preload should be less than 65 percent of the tensile yield strength of the fastener, while the corresponding bolt preload for lap-shear joints should be less than 60 percent of the fastener yield strength. However, the above preload values are directly related to the tension in the fastener but not the structural members to be connected. In the case of composite joints, only half of the bolt preload value recommended for steel joints has been suggested for any given bolt size [32]. Thomas and Zhao [33] tested composite joints made of graphite/epoxy with different thicknesses and bolt diameters and found that preload limits as specified by MSFC-STD-486B are acceptable, but recommended that a torque-tension test be performed while simultaneously monitoring the energy levels using acoustic emissions to prevent damage to the joint. The reason for this is that mechanical fasteners such as bolts and rivets typically generate clamping forces in the through-the-thickness (TTT) direction of composite structures, perpendicular to the direction of fiber reinforcement. Such structures are known to have poor properties in the TTT direction and are susceptible to damage and failure. This is particularly important for viscoelastic behavior, because the time-dependent viscoelastic behavior of polymer matrix composites is typically most evident in the matrix-dominated TTT direction.

Cooper and Turvey [34] investigated the effects of bolt tightening torque on failure loads, critical joint geometry and joint stiffness in single bolt double lap tension joints in pultruded glass reinforced plastics (GRP) sheet material. It was observed that as the bolt tightening torque was increased from 3 N-m (lightly torqued) to 30 N-m (heavily torqued) the bearing failure load increased by about 50% and the critical end distance, determined by the E/D ratio (where E is the edge distance, and D is the bolt diameter) which ensures bearing failure, was also found to increase, but the stiffness of the joint remained unaffected. It was also shown by Lim, et al. [35] that for a glass/epoxy bolted composite joint with a stacking sequence of $[\pm\theta/0_8]_s$, static shear strengths increased by about 30% when clamping pressure was varied from 0 to 60 MPa. In addition, the specimens with lower preloads failed at 80,000 cycles whereas specimens with higher preloads lasted up to 3 million cycles. In all of the above studies the clamp-up forces were selected randomly, the effects of external loads on relaxation were not considered and in some cases the relaxation in the bolted joint was not monitored.

Bolt Preload Relaxation Under External Excitation

There are several factors affecting relaxation in bolted metallic joints, which are well documented by Bickford [36]. A fastener subjected to vibration will not lose all pre-loads immediately. First there will be a slow loss of pre-load caused by some of the relaxation mechanisms. Vibration will increase relaxation because wear and hammering will take place during vibration. After sufficient pre-load is lost, friction forces drop below a critical level and the nut actually starts to back off and shake loose. In this case, the joints will not resemble the

ideal boundary conditions but will involve uncertainties. With higher initial pre-load, longer or more severe vibration is required to reduce pre-load to the critical point at which back-off occurs. In fact, in some circumstances, if pre-load is high enough to start with; nut back off will never take place. It is not known if these observations apply to composite bolted joints. Jiang et al. [37] conducted experimental investigations and finite element analysis (FEA) on relaxation in steel joints under cyclic loading. Depending on the loading conditions and preload, the loss of clamping force ranged from a few percent to 40% after 200 cycles. Three-dimensional FEA with an advanced cyclic-plasticity model was implemented to predict the clamping force reduction.

Schmitt and Horn [38], and Horn and Schmitt [39] studied the relaxation process in bolted thermoplastic composite joints. From single lap-shear tests of bolted thermoplastic composite lap joints involving viscoelastic effects, Horn and Schmitt [39] observed that by increasing clamp-up force the joint bearing failure load increased by as much as 28%. Clamp-up force relaxation was also monitored and 6% - 16% relaxation from the initial clamp-up force was observed for short duration (1400 hours) and long duration (100,000 hours), respectively. The rate of relaxation was predicted to be as high as 37% at an elevated temperature of 250° F for the duration of 100,000 hours. Zhao and Gibson [40] showed that compressive clamping stress relaxed by 18% and 15% in E-glass/epoxy beams with and without polymeric interleaves, respectively, for a period of 50 hours, whereas the corresponding relaxation in an aluminum beam was negligible.

Using finite element analysis (FEA), Shivakumar and Crews [41] predicted bolt force relaxation of up to 31% at room temperature for a 20 year duration in a double lap joint made of graphite/epoxy. It was also observed that the rate of relaxation increases with increasing temperature and moisture levels. But these findings were for a randomly selected clamp-up force and neither the effect of different clamp-up forces nor the effects of external loads on relaxation were considered.

EXPERIMENTAL INVESTIGATION

Experimental Setup

Figure 1 shows the configuration of the specimen in 3-point bending. The design of the specimen support was selected in such a way to maintain combined bending and shear loading. The joints were made from unidirectional carbon/epoxy prepreg tapes (Prepreg type: P2254-20-305 T800 carbon/epoxy) from Toray Composites America, Inc. A total of 48 layers of prepreg were laid on top of each other in the mold along with bleeder cloth and release fabric. The mold assembly was cured in the molding chamber of a TMP autoclave-style vacuum press, and the cured thickness of the sample plate was found to be 7.75 mm. Two rectangular beams were cut from the plate and machined to the required dimensions as shown in Figure 1. Joint clamping force was generated by an instrumented hexagonal head steel bolt with built-in strain-gages (Strainsert® Model SXS-FB, 9.525 mm or 3/8 inch in diameter). The driving force for stress relaxation is the imposed strain, as governed by the initial strained length of the bolt. This is a relaxation problem, not a creep problem. The creep strain under applied stress depends on the stress level, but the stress relaxation depends on the imposed strain, which should be independent of washer size. Therefore, only one washer size (19 mm diameter) was used to clamp the composite specimen from either side.

Two separate data acquisition systems were used, one for the instrumented bolt and another to control the Enduratec servo-pneumatic testing machine. The beam load and displacement values

were monitored by transducers which were built in to the Enduratec machine. The bolt preload selection was based on the maximum tensile load recommended by the manufacturer (Strainert[®]). Bolt preloads selected for this study were 4200 N, 5050 N, 6700 N and 7850 N, which correspond to 12.5%, 15%, 20% and 23.5%, respectively, of the maximum manufacturer-recommended tensile load in the instrumented bolt. The corresponding through-the-thickness compressive stresses generated in the composite specimen were approximately 25%, 29%, 38% and 45%, respectively, of the estimated transverse compressive strength of the composite. After applying an initial preload to the composite bolted joint, the bolt load was monitored for a period of 30 hours for the following cases: 1) bolt preload in the absence of external beam load, 2) bolt preload plus a static applied load of 250 N at beam midspan (combination of ramp and dwell), and 3) bolt preload plus a dynamic load of 250 N amplitude and frequencies of 1 Hz and 5 Hz at beam midspan as shown in Figure 2(a). Only one composite joint specimen was manufactured and tested. However, some of the relaxation tests were repeated with the same specimen under different loading conditions (for example: 5050 N bolt preload at 5 Hz and 7850 N preload only condition). It was found that the relaxation was reproducible and the differences in the relaxation from one test to another were less than 0.5%. A stability check on the data acquisition system was carried out by monitoring the signal from the instrumented bolt for a period of 30 hours without the application of load to the bolts. The drift in the signal for the above period was less than 1%. Also, the drift in the signal was taken into account when the percentage relaxation was calculated.

Static and dynamic load experiments were carried out on a 3-point bend fixture mounted on the Enduratec servo-pneumatic testing machine as shown in Figure 2(b). For the first case, experiments were also conducted on a steel joint having the same dimensions as those of the composite joint. Since the relaxation in the steel joint was expected to be mainly due to thread slip and/or other mechanisms rather than viscoelastic material behavior, these tests were done in order to better interpret the results of the composite joint tests. The bolt load was monitored for a period of 30 hours using the same 3-point bend set-up and the instrumented bolt for preloads mentioned above. All the above experiments were conducted without any thread seal. In an attempt to gain some insight into the importance of slip in the bolt threads as one of the possible relaxation mechanisms, another set of experiments was conducted in the absence of any external applied load with Teflon tape thread seal wrapped around the threads. The Teflon thread seal (Polytetrafluoroethylene, or PTFE) meets standard MIL T-27730A. The bolt load was monitored for the duration of 30 hours.

EXPERIMENTAL RESULTS AND PHENOMENOLOGICAL MODELING

Effect of preload on relaxation in composite and steel joints

Experimental measurements of bolt load relaxation for composite and steel bolted joints with initial preloads of 4200 N, 5050 N, 6700 N and 7850 N and no applied beam load are shown in Figure 3. This figure represents the time evolution of the preload (represented by the normalized load parameter, $P = P(t)/P_0$, where P_0 is the initial bolt preload and $P(t)$ is the relaxed preload at time t). It is observed that for the composite bolted joint, the magnitude of the relaxation decreases with increasing bolt preload. For steel joints, the magnitude of the relaxation is approximately the same for the preloads selected and the relaxation for a period of 27 hours is less than that of the composite joint. Relaxation of approximately 4% in the bolt preload (4200 N) for the composite joint was observed for a period of 30 hours, but the relaxation decreased to approximately 3 % for higher preloads (7850 N). Figure 4 reveals that the preload relaxation

magnitude in composite joints increases when bolted with a thread seal, indicating that a significant portion of the relaxation observed is due to slip in the threads and/or viscoelastic relaxation in the Teflon thread seal. However, it is again observed that the bolt load relaxation decreases with increasing initial bolt preload.

Effect of applied static loading

Figure 5 shows the effect of static beam load on bolt load relaxation in the composite bolted joint under the 3 point bend setup. It is seen that the magnitude of the relaxation again decreases with increasing bolt preload. However, when compared with the preload only condition, the trend of decreasing bolt load relaxation with increasing bolt preload only becomes clear for higher preloads (6700 N and 7850 N) and the result for the lowest preload (4200 N) seems inconsistent with that trend.

Effect of applied dynamic loading

Figures 6 and 7 show the preload relaxation plots under dynamic applied loading on the beam $F(t) = F_0 + \Delta F \sin 2\pi ft$, where F_0 is the static component, $\Delta F = 250 \text{ N}$ is the amplitude of the sinusoidal component, and f is the frequency taken as 1 Hz or 5 Hz. It is seen that under the excitation frequency of 1 Hz, the magnitude of preload relaxation decreases with increasing bolt preload and is nearly the same for higher preloads (6700 N and 7850 N). However, as the frequency of the external beam load is increased to 5 Hz, the magnitude of the relaxation tends to increase as shown in Figure 7. For lower preloads (5050 N) the magnitude of relaxation in the bolt preload exceeds that of the higher preload cases during the initial time interval of the experiment, however, this trend reverses for longer times. The increase in the magnitude of relaxation at higher frequencies of excitation and longer times may be due to the increase in the number of cycles as reported in Bickford [36]. This is associated with a corresponding increase in frictional heating. The temperature at the interface of the lap joint was measured before and immediately after the experiment with a general purpose type K (Chromel / Alumel) thermocouple and was found to increase by 3°C , and 1°C , respectively, when the composite bolted joint was preloaded to 6700 N and excited with 5 Hz and 1 Hz frequency, respectively, for the duration of 30 hours. When the relaxation in bolt load due to applied dynamic load at 5 Hz is compared with those due to applied static loads, it is found that for lower preloads (5050 N) the applied static load increases the bolt preload relaxation whereas for higher bolt preloads (6700 N and 7800 N) the bolt load relaxation decreases.

PHENOMENOLOGICAL MODELING

The experimental bolt force relaxation data in Figures 3-7 can be adequately described by an inverse power law of the type suggested by Shivakumar and Crews [41]. In normalized dimensionless form, this equation can be written as

$$\frac{P(t)}{P_0} = \frac{1}{1 + Kt^N} \quad (1)$$

where

P_0 = initial bolt preload

$P(t)$ = relaxed bolt preload at time t

K = constant in (hours)^{-N}

N = dimensionless exponent

t = time in hours

For the data in Figures 3-7, the constants K and N in Equation (1) were evaluated using the least-squares regression analysis in MATLAB [42] at the 99% confidence level and are tabulated in Tables (1a – 1f) for the different preloads and beam loads. For each case the coefficient of multiple determination, R^2 , is also given. This coefficient is a statistical measure of the goodness of the fit of the equation to the data, where $R^2 = 1.0$ corresponds to a perfect fit. It should be noted that the constants K and N listed in Table (1a - 1f) are valid only up to 30 hours, which is the maximum test duration. It is seen that there are no consistent trends in the variations of K and N with increasing preload, but the combined effect of the variations in these two quantities is such that increasing preload reduces the relaxation.

VISCOELASTIC ANALYSIS AND MATERIAL CHARACTERIZATION

The three-dimensional (3-D) elastic lamina properties needed for the finite element analysis were calculated from composite micromechanics equations [43] (for example: the rule of mixtures to calculate the longitudinal modulus and Tsai-Hahn equations to calculate the transverse modulus and shear modulus) using the fiber and matrix properties together with the following assumptions:

1. The fibers are linear elastic.
2. The matrix is linear viscoelastic, with its creep compliance described by a power law
3. The composite is specially orthotropic and transversely isotropic
4. The viscoelastic response depends only on the time elapsed since application of the load (i.e. the material is assumed to be non aging).

The analysis consisted of three parts. First, since the viscoelastic creep and relaxation data for the epoxy resin used in the prepreg is not available, Beckwith's [44] measured linear viscoelastic properties for Shell 58-68 epoxy at 75° F were assumed. Next, these properties were used in the FEA to predict the bolt load relaxation for an epoxy beam under different loading conditions using the quasi-elastic approach. Since ABAQUS viscoelastic modeling capability is limited to isotropic materials, it was necessary to validate the quasi-elastic approach (explained in the next section). Beckwith's [44] creep test results were extrapolated out to 50 hrs from the available data, by using the empirical power law equation for creep compliance:

$$D(t) = D_0 + D_1 t^n \quad (2)$$

Where, from [44],

$D(t)$ = time dependent isotropic creep compliance of matrix

D_0 = initial elastic compliance of matrix = $2.726 \times 10^{-4} \text{ (MPa)}^{-1}$

D_1 = creep coefficient of matrix = $1.0 \times 10^{-3} \text{ (MPa)}^{-1} \text{ (min)}^{-n}$

t = time in minutes

n = dimensionless creep exponent = 0.19

The time-dependent viscoelastic properties of the composite joint were assumed to depend only on the time-dependent properties of the epoxy matrix material. Based on the linear viscoelastic assumption, a time-dependent matrix modulus, $E_m(t)$, was estimated from the following equation:

$$E_m(t) \approx \frac{1}{D(t)}$$

(3)

It was assumed that the power law constants; D_0 , D_1 and n at room temperature are the same as those measured by Beckwith for Shell 58-68 epoxy [44]. By using these constants and the power law, the time-dependent creep compliance, $D(t)$, for the epoxy material was calculated. The time-dependent Young's modulus of the matrix material, $E_m(t)$, (see Table 2) was found from Equation (3). The tensile modulus data for T800 carbon fibers was obtained from the fiber manufacturer, Toray Composites America, Inc. as $E_f = 294$ GPa and was assumed to be independent of time. Viscoelastic properties of the lamina (i.e., longitudinal modulus $E_1(t)$, transverse moduli $E_2(t)$ and $E_3(t)$, Poisson's ratios $\nu_{12}(t)$, $\nu_{13}(t)$ and $\nu_{23}(t)$, longitudinal shear modulus $G_{12}(t)$, and transverse shear moduli $G_{13}(t)$ and $G_{23}(t)$ were estimated using elastic fiber properties and time-dependent viscoelastic resin properties through an application of the Elastic-Viscoelastic Correspondence Principle to the micromechanics equations [43] with a fiber volume fraction, $v_f = 0.45$ (see Table 2). Fiber volume fraction for the composite laminate was indirectly estimated using the combined experimental/numerical technique. Measured load-displacement response from static 3 point bend tests was compared with the predicted response (FE models) initially assuming the fiber volume fraction to be 0.6. The difference between the predicted and measured response was then minimized using fiber volume fraction as curve fitting parameter. These properties were then used in the FEA to calculate the bolt load relaxation.

Due to the limitations of ABAQUS [45], the quasi-elastic approach [43] was used to predict the bolt load relaxation for the orthotropic composite beams. In this approach, the viscoelastic solutions were approximated by a series of elastic solutions corresponding to different elastic properties at different times, while the stresses were assumed to be constant within each time increment.

FINITE ELEMENT ANALYSIS

Numerical Modeling

The purpose of the FEA is to develop predictive numerical models, and to promote a more meaningful interpretation of the experimental results. Hypermesh[®] 5.0 [46] was used for model development and post-processing, and ABAQUS[®] V 6.3 Standard 3-D [45] was used predict the bolt load relaxation using the quasi-elastic analysis. In order to benchmark the quasi-elastic prediction against the theoretically "exact" viscoelastic solution in ABAQUS (which is only applicable to isotropic materials), comparisons were made between ABAQUS viscoelastic solution and the quasi-elastic relaxation predictions for an un-reinforced isotropic epoxy beam [47]. The only reason for this part of the study was to compare the relaxation predictions made from viscoelastic (exact) analysis with those from the quasi-elastic analysis. In these studies, the bolt preload relaxation was predicted for different static and dynamic loads using both viscoelastic and quasi-elastic approaches. Relaxation of about 4.75% in the bolt preload was predicted for a period of 50 hours, and the difference between viscoelastic and quasi-elastic predictions was shown to be less than 2% [47].

With the confidence gained from the benchmarking study, a FEA model (Figure 8) for the composite bolted joint was developed using the quasi-elastic approach only. A global-local submodeling technique was used to model the bolted composite joint, where the displacements around the bolted joint section in the global model (a one-piece beam with no bolt) are used to

drive the refined local model (Figure 8). This technique has the advantage that more detailed results in the vicinity of the bolted joint can be obtained with fewer elements than with the full model. All models were developed using type C3D8 and C3D6 3-D solid elements. Since the model is symmetric about the vertical midplane of the beam, only a half model was used, and symmetric boundary conditions were applied. A mesh sensitivity study was performed for both global and local model to ensure that the finite element meshes were fine enough to give satisfactory results. For example, the bolt preload predicted by the local model with 4664 elements was compared with the local model with a coarser mesh having only 2857 elements, and the difference was found to be 5%. By increasing the number of elements in the local model to 5632 elements the model was found to be converging and the difference in the predicted bolt load was found to be less than 1%. Therefore, all of the analyses were carried out using the local model with 4664 elements.

The threads in the bolt were neglected in the FEA models, and the bolt was assumed to be a solid cylinder. Thus, possible bolt load relaxation due to plastic deformation and/or thread slip in the threads was not included in the models. The solid bolt simulation requires that contact surfaces be defined between all the surfaces that are in contact, and these surfaces were modeled using the contact pair approach in ABAQUS. The contact pairs are defined from free element faces. Since the sliding between the surfaces was expected to be small, the 'small sliding' option was used in all analyses. Friction coefficients were set to 0.2 for all contact surfaces, as used by Ireman [48]. The coefficient of friction (COF) is very difficult to control and measure or predict as it depends on the surface conditions of the joining parts. Several authors [49-52] have measured COFs (both static and kinetic) of polymer materials without any reinforcements, polymeric based composite materials in contact with composites as well as when in contact with metals. COFs reported in the literature range from as low as 0.096 to as high as 0.74. The COF has been shown to be independent of the applied normal load [49, 50]. Herrington, et al. [49] found the static friction coefficient to be in the range of 0.096 - 0.128 for a simple double shear arrangement (without bolts) with steel plates on the outer surface of the composite specimen. Schon [50, 51] observed that the friction coefficient initially for composite-composite is about 0.65 but only 0.23 when the composite is in contact with aluminum [51]. Xiao et al. [52] have measured the COF to be in the range of 0.125 - 0.3, when a steel pin is sliding against the edge of a unidirectional carbon fiber/epoxy (T800H/3631) laminate. It should also be noted that several studies found in the literature consider frictionless pins or bolted models for their analysis. Since "small sliding" contact is assumed for the current study, the use of COF equal to 0.2 seems reasonable.

The beam load was applied as a concentrated nodal force at midspan. Pretension in the bolt was applied in a separate loading step by defining a pre-tension section in the bolts. Assembly loads were transmitted across the pre-tension section by means of a pre-tension node. Pre-load was applied by giving an initial displacement (in the direction parallel to the bolt axis) to this node. Bolt preload was maintained by using the fixed option under boundary conditions, and was monitored by checking the total force output on that node. The model geometry and boundary conditions were the same as for the experiments, as shown in Figure 1. For the composite beams, both experiments and FEA (using the global-local model and quasi-elastic approach) were conducted, but only experiments were conducted for steel joints.

Bolt load relaxation was predicted for a period of 30 hours in composite bolted joints using a quasi-elastic analysis and the material properties listed in Table 2 for a preload of 4200 N under

the following types of loading: 1) bolt preloading in the absence of external beam loading, 2) bolt preloading in the presence of a static beam load of 250 N, and 3) bolt preloading in the presence of dynamic loading of amplitude 250 N at a frequency of 1 Hz. The dynamic beam load was applied using the periodic loading option in ABAQUS for 5 cycles under each quasi-elastic step and mean bolt load data was recorded in each case

Numerical Results

Figure 9 shows the predicted bolt load relaxation for composite beams under static and dynamic beam loads using the quasi-elastic approach with the material properties listed in Table 2. It is observed that the predicted bolt loads are shifted slightly with the application of the static and dynamic beam loads, but otherwise the relaxation curves are not significantly affected by the beam loads. Again, the mean bolt load is plotted for the dynamic analysis.

Even though the FEA results captured the bolt load relaxation in composite joints with and without external loads, Figure 10 reveals that, in the absence of external loading, there is no change in the predicted magnitude of bolt load relaxation with increasing bolt preloads. This contradicts the experimental observation that relaxation decreases with increasing bolt preload. There are several possible reasons for this disagreement.

First, the material model does not capture the viscoelastic effects in the polymer matrix material at the micromechanical level. The micromechanical analysis referred to in the discussion following Equation 3 was based on "mechanics of materials" type models which do not take into account the details of the in-situ stress and strain distributions in the viscoelastic polymer matrix. A 3-D finite element micromechanics model which takes into account the micromechanical geometry is needed to accurately simulate the effects of such parameters as boundary conditions at the bolt-composite interface on the viscoelastic relaxation of the composite. In the absence of such a detailed 3-D micromechanics analysis, an analysis of the effects of preload on the macromechanical volume-averaged von Mises stress was conducted. One measure of the principal stress differences and corresponding shear stresses is the von Mises stress given by

$$\sigma_v = \sqrt{\frac{1}{2}[(\sigma_1 - \sigma_2)^2 + (\sigma_2 - \sigma_3)^2 + (\sigma_1 - \sigma_3)^2]} \quad (4)$$

Where, σ_1 , σ_2 and σ_3 are principal stresses in 1, 2 and 3 directions, respectively. Figure 11 shows a comparison of macromechanical volume-averaged (or "effective") von Mises stresses, $\bar{\sigma}_v$, in the immediate vicinity of the bolt hole in the composite material for different preloads. One can conclude that the contribution of the preload to the total effective von Mises stresses (i.e. for preload + applied static load) clearly increases with increasing bolt preloads. One would normally expect that the increase in the von Mises stress would be associated with a corresponding increase in the tendency to exhibit viscoelastic behavior. However, the experimental observation indicates reduced relaxation with increased bolt preload. The results in Figure 11 are based on a macromechanical analysis, and a micromechanical analysis of the viscoelastic behavior of the polymer matrix material may lead to a different conclusion. Another possible reason for the FEA model's inability to predict the effect of increasing bolt preload on the relaxation response is that the initial radial gap between the outside diameter of the bolt and the inside diameter of the bolt hole in the composite may be closed as the increasing bolt preload squeezes the composite and causes the hole size to shrink. This, in turn, could lead to time-dependent boundary conditions at the inner surface of the hole as the relaxation proceeds. As the

composite presses against the bolt, the effect would be to increase the constraint on the composite and reduce its relaxation response. Further work in this area is clearly needed.

COMPARISONS AND VALIDATION WITH EXPERIMENTAL RESULTS

FEA results obtained for composite bolted joints with 4200 N preload under preload only, with static preload of 250 N and dynamic beam load at 1 Hz frequency are compared with the experimental bolt load relaxation in Figures 3, 5 and 6. FEA results agree very well with the experimental observations for a fixed preload of 4200 N. The model not only captures the reduction in the bolt load during the first few hours, but also the general tendency of decay in bolt load with increasing loading cycles. However, as pointed out in the discussion of Figure 10, the model does not predict the experimentally observed decrease in relaxation response with increased bolt preload. It should be noted that the measured relaxation is the total of all relaxation mechanisms, whereas the predicted value is only due to the viscoelastic relaxation in the composite matrix material. Relaxation in the average tensile normal stresses, σ_z , across the pre-tension section in the bolt was also observed as shown in Figure 12 but the corresponding relaxation of average shear stresses was negligible for a 20 hour duration. The shift in the average tensile normal stresses is due to the application of static beam load.

The percentage of bolt load relaxation ($p = (P_0 - P(t))/P_0 * 100$) in composite joints at the end of 30 hour duration is shown in Figure 13 for various preloads with different loading conditions. It is observed that for any external loading condition, the bolt load relaxation decreases with increasing initial bolt preload. These findings emphasize the importance of preload selection. For higher preloads (6700 and 7850 N) the bolt load relaxation increases with increasing frequency of excitation, with lowest relaxation occurring at 1 Hz frequency. But for lower preloads (5050 N) the relaxation decreases with increased frequency of excitation.

Comparing the percentage bolt load relaxation in steel and composite joints for the duration of 30 hours (Figure 14), it is observed that only about 1/3 of the total relaxation is due to viscoelastic behavior of the polymer matrix in the composite, while the remaining 2/3 is apparently due to the other relaxation mechanisms such as plasticity and/or slip in the bolt threads, which also occur in steel joints. Table 3 shows some comparisons of bolt load relaxation in steel joints found in the literature with the current predictions for composite joints extrapolated using MATLAB® [42]. It appears that the data in Table 3 from references [36] and [37] are for steel lap joints loaded in dynamic shear, but this is the only relaxation data for dynamic loading that was readily available in the literature. For the case of low cycle loading (i.e. 200 and 1000 cycles), the current relaxation rates are far smaller than those of in references [16, 17], and the current extrapolated relaxation rates only become significant for millions of cycles of loading. It can be concluded that the viscoelastic behavior in the through-thickness direction of composite bolted joints may lead to significant reductions in the bolt preload over the service period of the joint depending upon the design life and there is a need for long-term experiments on relaxation in bolted joints.

CONCLUSIONS

- Experiments have been employed to study the effects of various bolt preloads, along with the effects of static and dynamic external loads on bolt load relaxation in composite bolted joints, and phenomenological models have been developed from these results.
- Finite element models for bolt load relaxation in bolted composite joints based on a global/local quasi-elastic approach show reasonably good agreement with experiments except that the experimentally observed decrease in relaxation with increased bolt preload is not predicted by the models.
- Experiments show that for any external loading condition the bolt load relaxation decreases with increasing initial bolt preload, and these findings emphasize the importance of bolt preload selection.
- If the bolt preloads are small enough (as a percentage of bolt failure load), applied static and dynamic beam loads at 1 Hz frequency increase the magnitude of bolt load relaxation. However, for higher bolt preloads the bolt load relaxation decreases for both static and dynamic loads.
- It is observed that increasing the frequency of the external dynamic load from 1 Hz to 5 Hz increases the rate of relaxation, and that the friction-induced heating is at least partially responsible for this effect.
- It is observed from the FEA model that the average normal stress across the pre-tension section in the bolt relaxes with time for the duration 20 hours, whereas the relaxation in shear stresses is negligible.
- The FEA predictions of bolt load relaxation agree well with the experimental observations when subjected to external static and dynamic loads, however, more detailed modeling of the polymer matrix behavior at the micromechanical level and possible time-dependent boundary conditions at the bolt-composite interface are needed to understand the experimentally observed relationship between bolt preload and bolt force relaxation.
- Results of relaxation experiments with bolted steel joints and with bolted composite joints with Teflon tape thread seal on the bolt threads strongly suggest that slip and/or other relaxation mechanisms in the bolt threads may be as important as or even more important than the through-the-thickness viscoelastic relaxation in the composite material being fastened.

References

1. Camanho, P. P., and Mathews, F. L., (1997). Stress analysis and strength prediction of mechanically fastened joints in FRP: A review. *Composites Part A: Applied Science and Manufacturing* 28(6): 529-547.
2. Erki, M. A., Rosner, C. N., and Dutta, A. (1993). Design of glass-fibre-reinforced plastic bolted connections, *Microcomputers in Civil Engineering*, 8(5): 367-376.
3. Jones, R. M. (1999). *Mechanics of Composite Materials, Second Edition*, Taylor and Francis, London.
4. Wang, J. T., Banbury, A., and Kelly, D. W. (1998). Evaluation of approaches for determining design allowables for bolted joints in laminated composites, *Compos. Struct.*, 41(2): 167-176.
5. Rastogi, N., Deepak, B. P., and Soni, S. R. (1997a). Stress analysis codes for bonded joints in composite structures, *AIAA/ASME/ASCE/AHS/ASCE Struct. Struct. Dyn. Mater. Conf.*, 4: 2772-2782.
6. Rastogi, N., Xie, M., and Soni, S. R.. (1997b). Strength prediction codes for bolted joints in composite structures, *Proc. AIAA/ASME/ASCE/AHS/ASCE Struct. Struct. Dyn. Mater. Conf.*, 2: 1088-1098.
7. Rastogi, N., Soni, S. R., and Nagar, A. (1998). A combined analytical and experimental study of design parameters in composite bonded joints, *Proc. 39th AIAA/ASME/ASCE/AHS/ASCE Struct. Struct. Dyn. Mater. Conf.*, Part 2: 1567-1577.

8. Hart-Smith L.J. (1994). The key to designing efficient bolted composite joints, *Composites*, **25**(8): 835-837.
9. Hart-Smith, L.J. (1977). Bolted joints in graphite/epoxy composites, *National Aeronautics and Space Administration*, NASA Cr144899, January, Washington, DC
10. Ibrahim, R. A. and Petit, C. L. (2005). Uncertainties and dynamic problems of bolted joints and other fasteners, *J. Sound and Vibration*, **279**: 857-936.
11. Packman, P. F., Hietala, H. J., and Schulz, K. C. (1993). Experimental and statistical analysis of some fastener anomalies on the bolted joint strength of graphite/epoxy laminates, *Proc. SAMPE Symp. Exhib.*, **38**(1): 66-80.
12. Schulz, K. C., Hietala, H. J., and Packman, P. F. (1996). A statistical approach to the analysis of ultimate strengths of bolted joints in laminated composites, *Compos. Sci. Tech.*, **56**: 505-517.
13. Lin, W. H., and Jen, M. H. R. (1999). Strength of bolted and bonded single-lapped composite joints in tension, *J. Compos. Mater.*, **33**(7): 640-666.
14. Hart-Smith, L. J. (1978). Mechanically fastened joints for advanced composites- Phenomenological Considerations and Simple Analysis, *McDonnell Douglas Corp*, DO6748A.
15. Running, D. M., Ligon, J. B., and Miskioglu, I. (1999). Fastener design for transversely loaded composite plates, *J. Compos. Mater.*, **33**(10): 928-940.
16. Rosner, C. N., and Rizkalla, S. H.. (1995a). Bolted connections for fiber-reinforced composite structural members: Experimental program, *ASCE J. Mater. Civil Eng.*, **7**(4): 223-231.
17. Rosner, C. N., and Rizkalla, S. H.. (1995b). Bolted connections for fiber-reinforced composite structural members- Analytical model and design recommendations, *ASCE J. Mater. Civil Eng.*, **7**(4): 232-238.
18. Andreasson, N., Mackinlay, C. P., and Soutis, C. (1998). Experimental and numerical failure analysis of bolted joints in CFRP woven laminates, *Aeronaut. J.*, **102**(1018): 445-450.
19. Menendez, J. M., and Guemes, J. A. (1999). Strain measurements inside thick CFRP laminates at the vicinity of bolted joints, *Proc. SPIE – Int. Soc. Optical Eng.*, **3670**: 184-194.
20. Li, Q. M., Mines, R. A. W., and Birch, R. S. (2001). Static and dynamic behavior of composite riveted joints in tension, *Int. J. Mech. Sci.*, **43**: 1591-1610.
21. Horn, W. J. (1994). Influence of clamp-up force on the strength of bolted composite joints, *AIAA J.*, **32**(3): 665-667.
22. Hung, C. L., Yan, Y., and Chang, F. K. (1994). Strength envelope of bolted composite joints under multi-axial bypass loads, *AIAA/ASME/ASCE/AHS/ASCE Struct. Struct. Dyn. Mater. Conf.*, 2298-2307.
23. Hung, C. L., and Chang, F. K. (1996a). Bearing failure of bolted composite joints. Part II: model and verification, *J. Compos. Mater.*, **30**(12): 1359-1400.
24. Hung, C. L., and Chang, F. K. (1996b). Strength envelope of bolted composite joints under bypass loads", *J. Compos. Mater.*, **30**(13): 1402-1435.
25. Yan, Y., Wen, W. D., Chang, F. K., and Shyprykevich, P. (1999). Experimental study on clamping effects on the tensile strength of composite plates with a bolt-filled hole, *Compos. - Part A: Appl. Sci. Manufact.*, **30**(10): 1215-1229.
26. Van Siclen, R. C. (1974). Evaluation of bolted joints in graphite/epoxy, *Proceedings of the Army Symposium on Solid Mechanics*, Massachusetts, 120-138.
27. Hart-Smith, L.J. (2004). Bolted joint analyses for composite structures - Current Empirical Methods and Future Scientific Prospects, *Joining and Repair of Composite Structures*, STP 1455: 127-160.
28. Sawicki, A. (1991). Development of design and analysis methodology for composite bolted joints, *AHS National Technical Specialists Meeting on Rotorcraft Structures*, Williamsburg, VA, Proceedings A93-27951 10-05.
29. Sun, H.T., Qing, X., and Chang, F-K. (2002). The response of composite joints with bolt-clamping loads, part I: model development, *J. of Composite Materials*, **36**(1): 47-67.
30. Sun, H.T., Qing, X., and Chang, F-K. (2002). The response of composite joints with bolt-clamping loads, part II: model verification, *J. of Composite Materials*, **36**(1): 69-91.
31. MSFC-STD-486B. (1992). Torque limits for standard, Threaded Fasteners, Nov.
32. Zhao, Y., Ford, D., and Richardson, S. (2001). Torque limit for fasteners in composites, Technical Report, NASA/MSFC/ED23, Aug.
33. Thomas, F. P., and Zhao, Y. (2005). Torque limits for composites joined with mechanical fasteners, *46th AIAA/ASME/AHS/ASCE/ASC Struc. Struc. Dyn. and Mat. Conf.*, AIAA 2005-2351.
34. Cooper, C. and Turvey, G.J. (1995), Effects of joint geometry and bolt torque on the structural performance of single bolt tension joints in pultruded GRP sheet material, *Composite Structures*, **32**: 217-226.
35. Lim, T.S, Kim, B.C. and Lee D.C. (2006). Fatigue characteristics of the bolted joints for unidirectional composite laminates, *Composite Structures*, **72**(1): 58-68.

36. Bickford, J. H. (1995). *An introduction to the design and behavior of bolted joints*, **Third Edition**, CRC Press, Taylor and Francis Group, Boca Raton, Florida.
37. Jiang, Y., Zhang, M., and Lee, C. (2003). A study of early stage self-loosening of bolted joints, *J. of Mechanical Design*, **125**: 518-526.
38. Schmitt, R. R., Horn, W. J. (1990). Viscoelastic relaxation in bolted thermoplastic composite joints, *Proc. SAMPE Symp. Exhib.*, **35**(2): 1336-1347.
39. Horn, W. J. and Schmitt R. R. (1993). Relaxation in bolted thermoplastic composite joints, *AIAA Journal*, **32**(3): 485-494.
40. Zhao, H., and Gibson, R. F. (1995). Influence of clamping force relaxation on vibration damping measurements for polymer composite cantilever beams, *Proc. SEM Spring Conf.*, Grand Rapids, MI, 735-738.
41. Shivakumar, K.N. and Crews J.H. (1983). Bolt clampup relaxation in a Graphite/Epoxy Laminate, *ASTM STP 813*, Philadelphia, 5-22.
42. *MATLAB® V 6.1, User's manual*, The MathWorks, Inc.
43. Gibson, R. F. (2007). *Principles of composite material mechanics*, **Second Edition**, CRC Press, Taylor and Francis Group, Boca Raton, Florida.
44. Beckwith, S. W. (1984). Viscoelastic creep behavior of filament-wound case materials, *J. of Spacecraft and Rockets*, **21**(6): 546-552.
45. *ABAQUS® V 6.3, User's Manual and Theory Manual*, Hibbit, Karlson and Sorensen, Inc
46. *Hypermesh® V 5.0, User's Manual*, Altair Engineering, Inc.
47. Thoppul, S.D, Gibson, R.F. and Ibrahim, R.A. (2006). Analytical and experimental characterization of the effects of vibration on relaxation in composite bolted joints, *Proc. American Society for Composites 21st Technical Conference*, Dearborn, MI, Paper No. 192.
48. Ireman, T. (1998). Three-dimensional stress analysis of bolted single-lap composite joints, *Comp. Structures*, **43**: 195-216.
49. Herrington, P.G. and Sabbaghian, M. (1991). Factors affecting the friction coefficients between metallic washers and composite surfaces, *Composites*, **22**(6): 418-424
50. Schon, J. (2004). Coefficient of friction and wear of a carbon fiber epoxy matrix composite, *Wear*, **257**(3-4):395-407
51. Schon, J. (2004). Coefficient of friction for aluminum in contact with a carbon fiber epoxy composite. *Tribology International*, **37**:395-404
52. Xiao, Y., Matsubara, T., Wang, W. X., Takao, Y. (1998). Effect of carbon fiber direction of unidirectionally reinforced epoxy composites on frictional behavior. *Journal of the Society of Materials Science Japan*, **47**(6):618-624. In Japanese.

Table 1. Constants K and N in Equation (1) evaluated using least-squares regression analysis

(a) Composite joint – Preload only with no beam load (see Figure 3)

Preload	K	N	R^2
4200 N	0.01592	0.3405	0.9886
5050 N	0.02038	0.1604	0.9442
6700 N	0.01433	0.2472	0.9847
7850 N	0.01698	0.1605	0.9893

(f) Composite joint - Preload + 250 N dynamic beam load @ 5 Hz (see Figure 7)

Preload	K	N	R^2
5050 N	0.0184	0.1293	0.9363
6700 N	0.01339	0.3027	0.9989
7850 N	0.01475	0.2271	0.9986

(b) Steel joint – Preload only with no beam load (see Figure 3)

Preload	K	N	R^2
5050 N	0.01167	0.2317	0.9885
6700 N	0.007192	0.3371	0.996
7850 N	0.008088	0.2813	0.998

(c) Composite joint - Preload only with thread seal (see Figure 4)

Preload	K	N	R^2
5050 N	0.03324	0.182	0.9667
6700 N	0.03397	0.09815	0.9019
7850 N	0.02452	0.1698	0.9771

(d) Composite joint - Preload + 250 N static beam load (see Figure 5)

Preload	K	N	R^2
4200 N	0.01338	0.4062	0.9952
5050 N	0.02313	0.1603	0.9714
6700 N	0.01594	0.1621	0.9595
7850 N	0.009239	0.2557	0.9918

(e) Composite joint - Preload + 250 N dynamic beam load @ 1 Hz (see Figure 6)

Preload	K	N	R^2
4200 N	0.02151	0.1858	0.9891
5050 N	0.02101	0.1024	0.9892
6700 N	0.01086	0.218	0.9564
7850 N	0.009212	0.2415	0.9345

Table 2. Micromechanics estimate of time-dependent material properties for unidirectional carbon/epoxy*

Time (Hrs)	$E_m(t)$ (GPa)	$E_1(t)$ (GPa)	$E_2(t) = E_3(t)$ (GPa)	$G_{12}(t) = G_{13}(t)$ (GPa)	$v_{12}(t) = v_{13(t)}(t) = v_{23}(t)$	$G_{23}(t)$ (GPa)
0	3.662	134.5	12.07	3.612	0.30004	2.535
1	3.607	134.4	11.66	3.469	0.30711	2.446
2	3.515	134.4	11.55	3.449	0.30806	2.434
4	3.495	134.4	11.51	3.428	0.30914	2.421
6	3.482	134.4	11.48	3.414	0.30983	2.412
8	3.473	134.4	11.45	3.403	0.31035	2.405
10	3.465	134.4	11.40	3.395	0.31078	2.400
15	3.450	134.4	11.37	3.379	0.31159	2.390
20	3.439	134.4	11.34	3.366	0.31220	2.382
25	3.430	134.4	11.32	3.356	0.31269	2.376
30	3.422	134.4	11.55	3.348	0.31311	2.371

* Toray Composites America T800 carbon fibers with assumed viscoelastic compliance for Shell 58-68 epoxy matrix material [44]

Table 3. Comparison of rate of bolt load relaxation due to dynamic loads from previous and current predictions

Number of Cycles	Plastic deformation of Threads (Expt. on steel joints) (Jiang, et al, [37])	Current Viscoelasticity Measurements (composite joints) preload 4200 N	General Expt. observation (Steel joints) (Bickford, [36])
200	41 %	0.92%	30 %
1000	NA	1.5%	70 %
108000	NA	3.98 %	NA
3690000	NA	10 % ^a	NA
36000000	NA	50% ^a	NA

a - Extrapolated by exponential curve fit using MATLAB[®] [42]- current model
NA – no data available

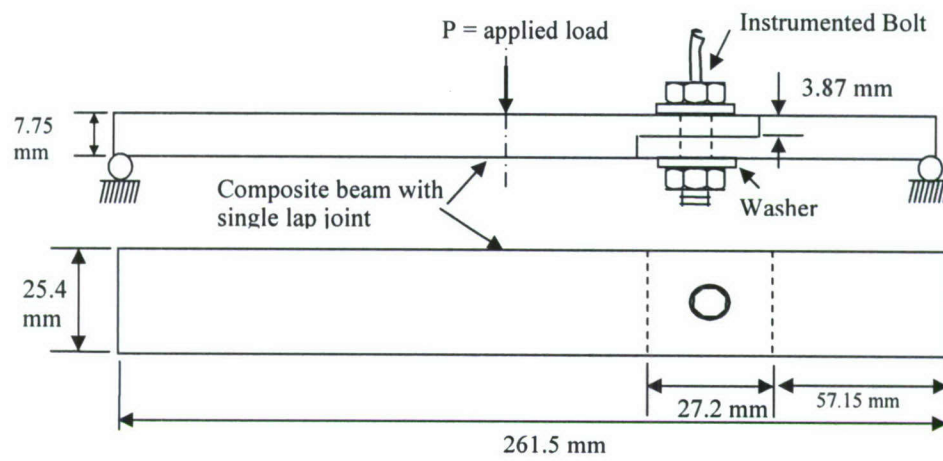


Figure 1. Specimen Configuration

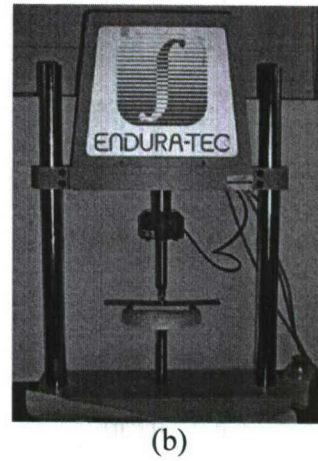
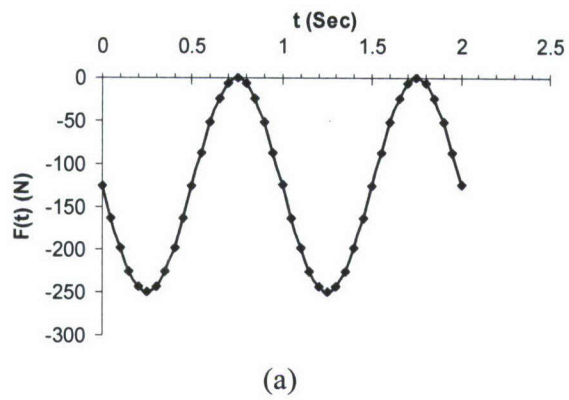


Figure 2. (a) Sinusoidal load of 250 N amplitude at frequency of 1 Hz (b) Enduratec servo-pneumatic testing machine with 3 point bend set-up

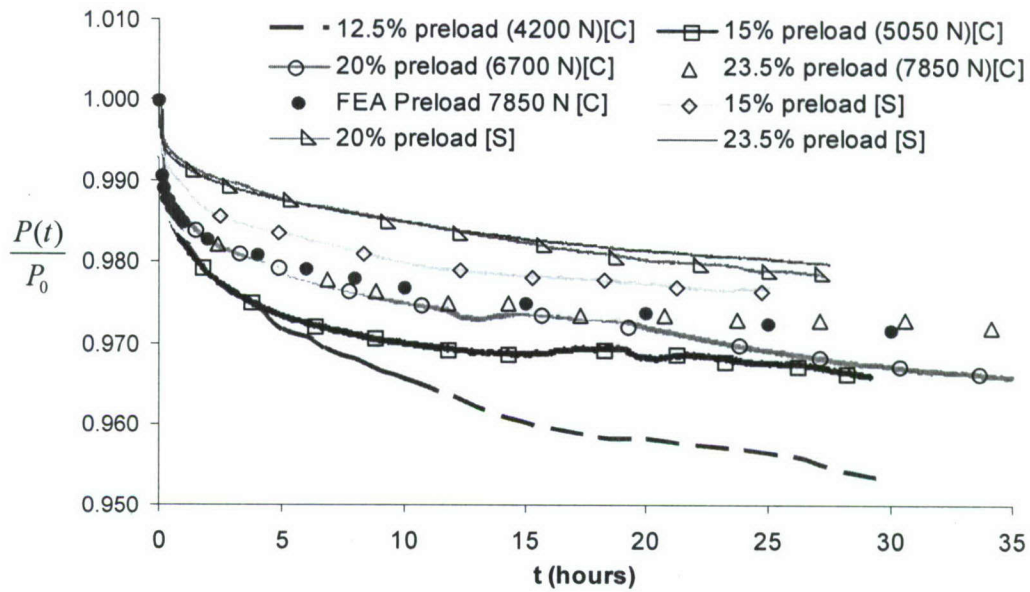


Figure 3. Measured bolt load relaxation in composite and steel bolted joints normalized to the initial preload for several preloads, along with predicted (FEA) bolt load relaxation in composite joint for preload of 7850 N (Note: S = Steel and C = Composite)

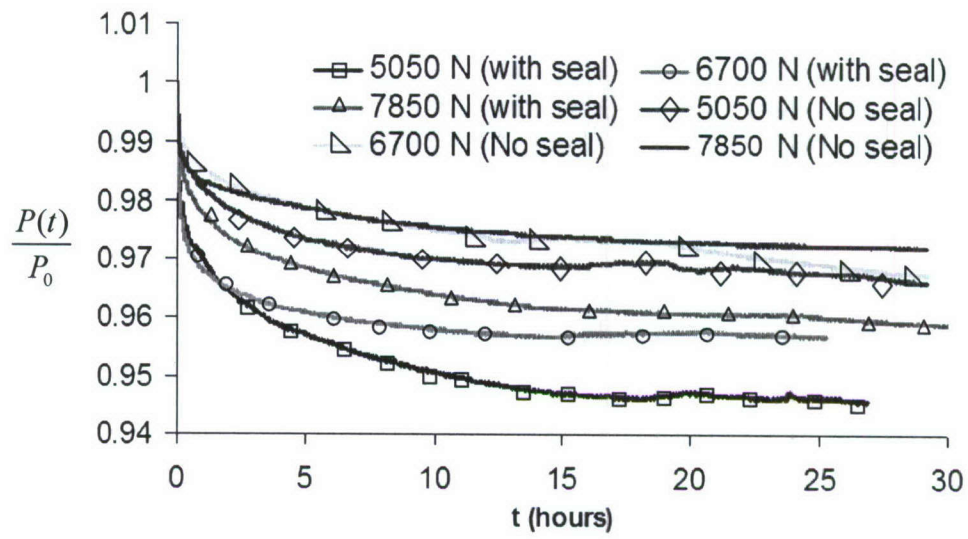


Figure 4. Measured bolt load relaxation in composite with and without thread seal

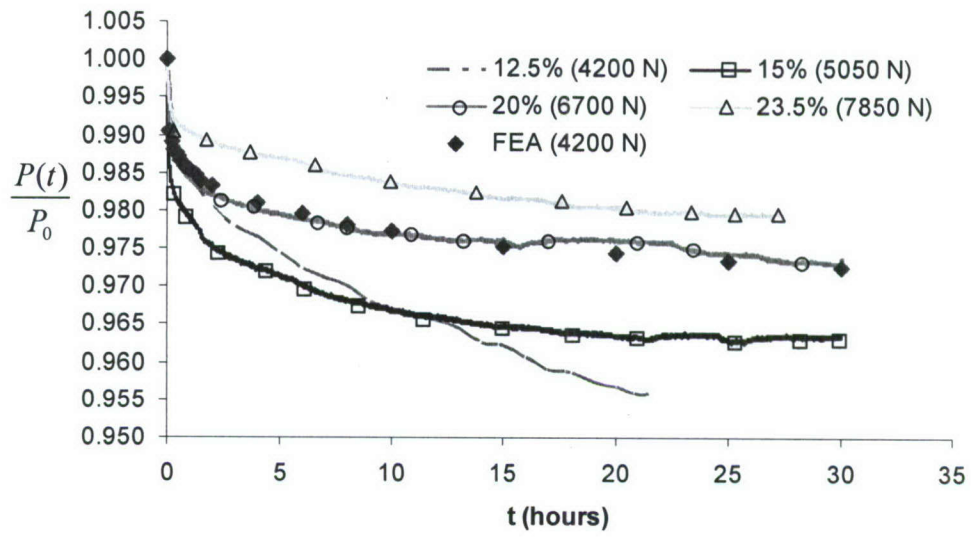


Figure 5. Bolt load relaxation for composite bolted joint with various preloads and static 250 N beam load ($F_o=250$ N).

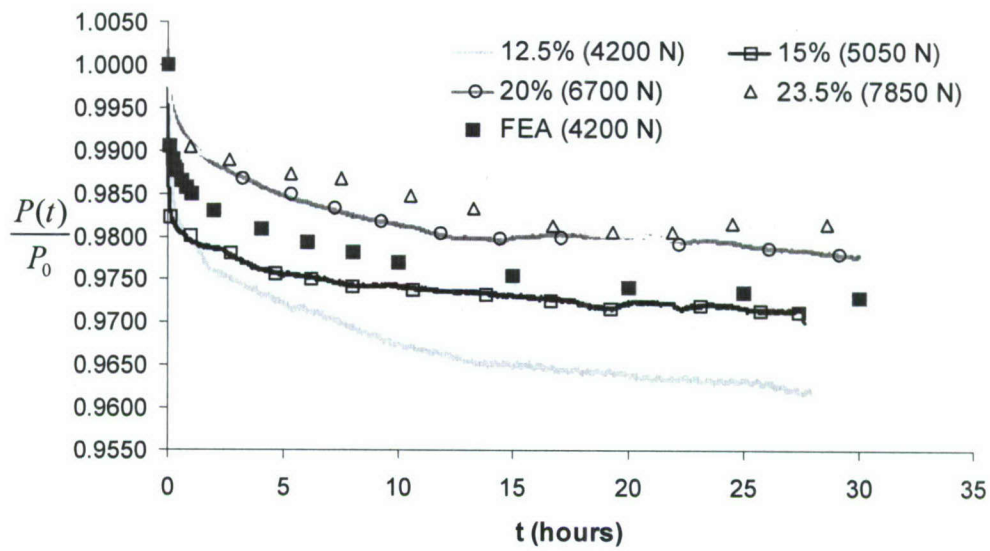


Figure 6. Bolt load relaxation for composite bolted joint with various preloads and a 250 N amplitude dynamic beam load at 1 Hz frequency ($F(t)=250 \sin 2\pi(1)t$ N))

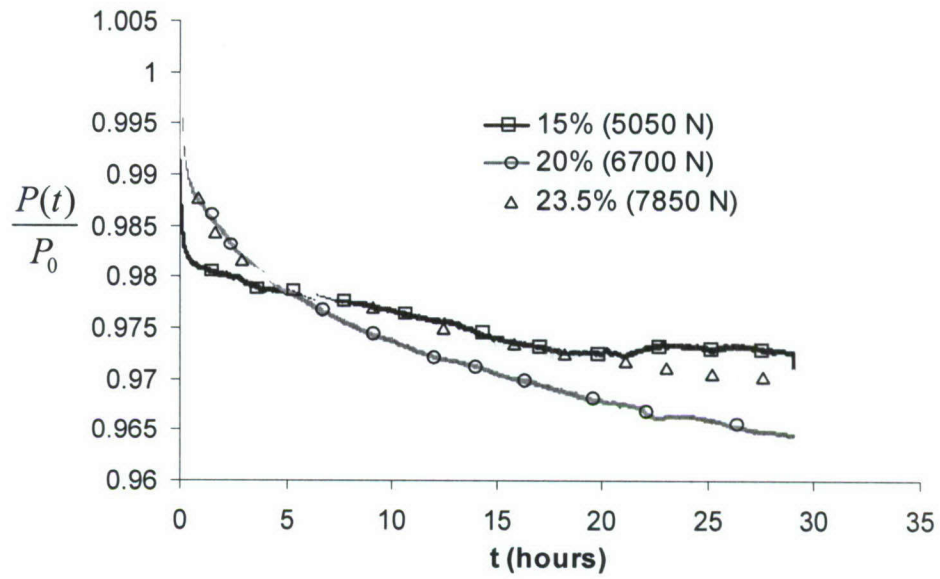


Figure 7. Bolt load relaxation for composite bolted joint with various preloads and a 250 N amplitude dynamic beam load at 5 Hz frequency ($F(t)=250 \sin 2\pi(5)t$ N)

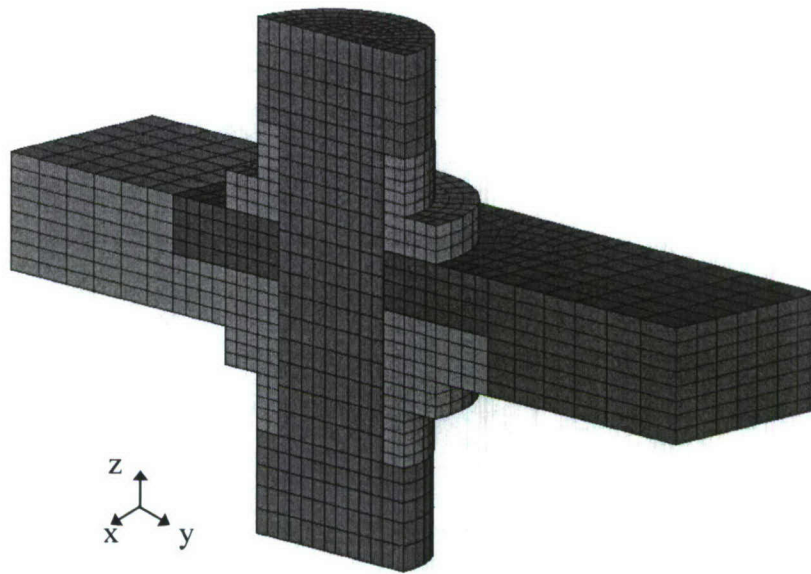


Figure 8. Bolt FEA model (Local)

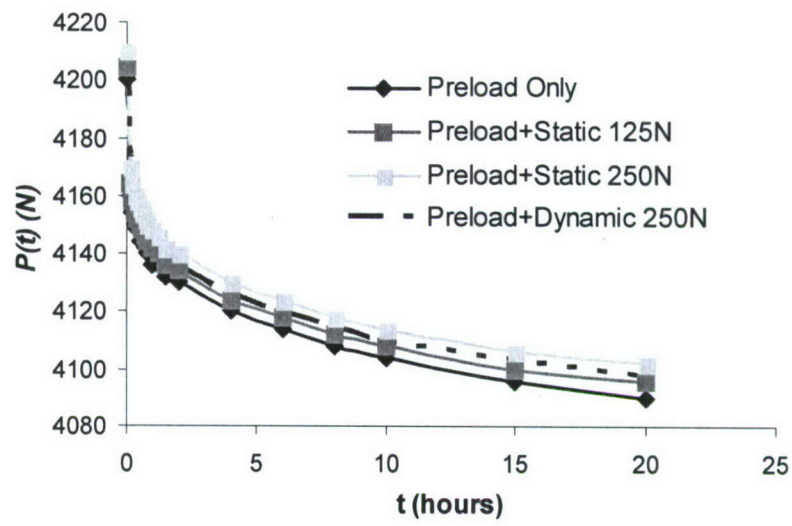


Figure 9. Predicted bolt load relaxation for composite bolted joints with preload 4200 N

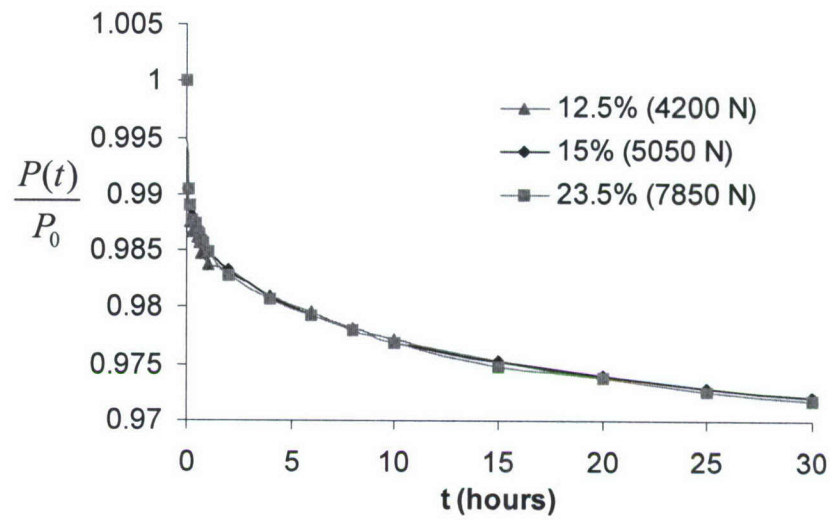


Figure 10. Predicted bolt load relaxation for composite bolted joints with various preloads

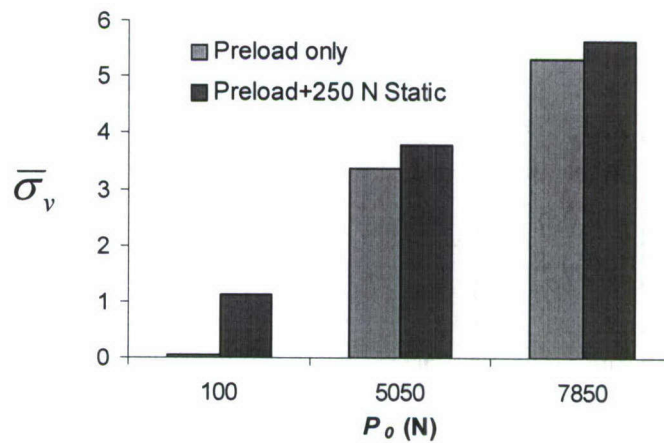


Figure 11. Volume averaged macromechanical (or "effective") von Mises stresses in the immediate vicinity of the bolt in composite material

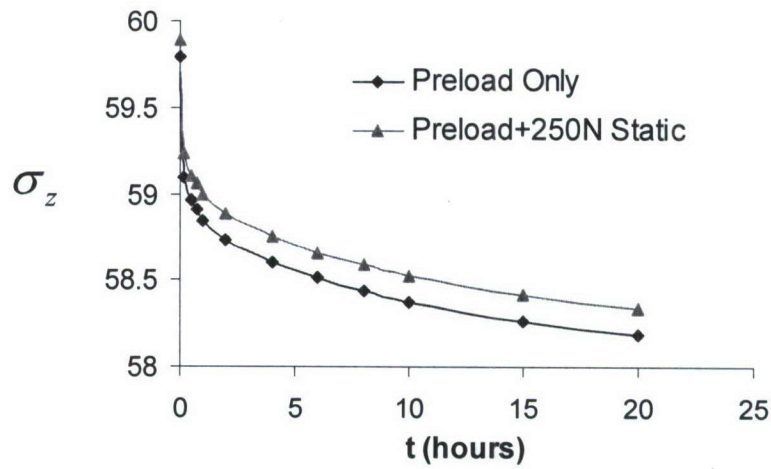


Figure 12. Average normal stress relaxation in the pretension section of bolt when composite joint is preloaded to 4200 N

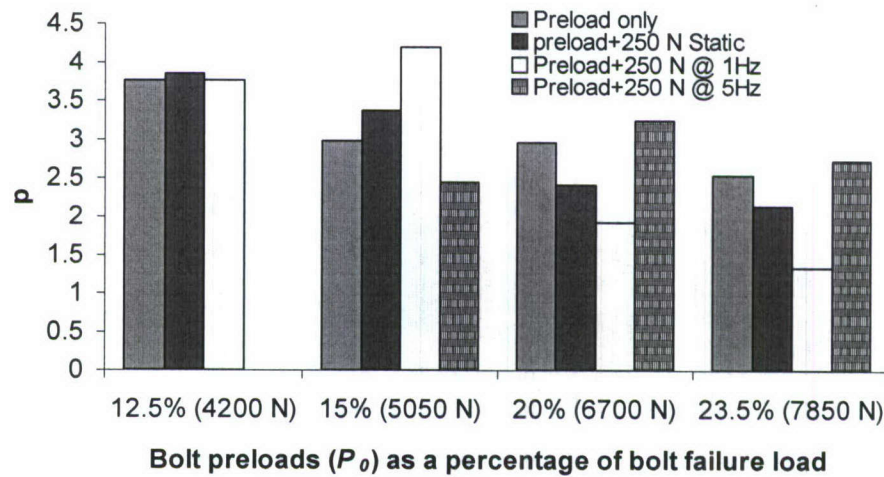


Figure 13. Measured bolt load relaxation in composite bolted joint at 30 hour duration

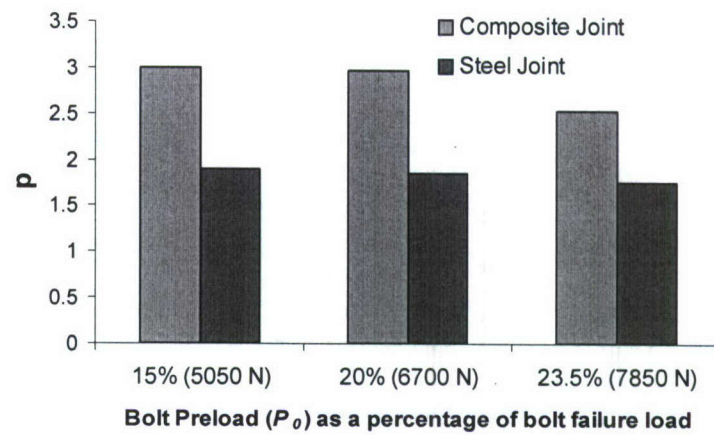


Figure 14. Bolt load relaxation comparison in steel and composite bolt joint for various preloads under preload only condition

Part 2: Analytical Investigation

INFLUENCE OF BOUNDARY CONDITIONS RELAXATION ON PANEL FLUTTER WITH COMPRESSIVE IN-PLANE LOADS

Summary of Results

The influence of boundary conditions relaxation on two-dimensional panel flutter is studied in the presence of in-plane loading. The boundary value problem of the panel involves time-dependent boundary conditions that are converted into autonomous form using a special coordinate transformation. Galerkin's method is used to discretize the panel partial differential equation of motion into six nonlinear ordinary differential equations. The influence of boundary conditions relaxation on the panel modal frequencies and LCO amplitudes in the time and frequency domains is examined using the windowed short time Fourier transform and wavelet transform. The results of this task revealed:

- The relaxation and system nonlinearity are found to have opposite effects on the time evolution of the panel frequency.
- Depending on the system damping and dynamic pressure, the panel frequency can increase or decrease with time as the boundary conditions approach the state of simple supports.
- The largest Lypunov exponent is also determined. They reveal complex dynamic characteristics of the panel, including regions of periodic, quasi-periodic, and chaotic motions.

State-of-the-Art

It has been observed that apparently identical aircraft can exhibit different dynamic characteristics under the same flight conditions. This difference owes its origin to the stochastic nature of structural properties and the environment. That is, the sensitivity of the dynamic system behavior is directly linked to variations in its physical properties. The physical properties of aeroelastic structures are affected by boundary conditions relaxation and joint uncertainties. Generally, the main sources of uncertainties of aerospace structures include:

- (v) Randomness in material properties due to variations in material composition.
- (vi) Randomness in structural dimensions due to manufacturing variations and thermal effects.
- (vii) Randomness in boundary conditions due to preload and relaxation variations in mechanical joints.
- (viii) Randomness of external excitations.

The present work deals with the third source and its mechanisms. There are many factors that affect mechanical joints and fasteners, such as friction, hardness, finish, and dimensions of all parts, and gasket creep (Bickford, 1990). Each factor will vary from fastener to fastener and joint to joint because of manufacturing or usage tolerances. Moreover, a fastener subjected to vibration will not lose its pre-load immediately. First there is a slow loss of pre-load caused by various relaxation mechanisms. Vibration increases relaxation through consequent wear and

hammering. After sufficient pre-load is lost, friction forces drop below a critical level and, if the joint is bolted, the nut actually starts to back off and shake loose. As relaxation occurs, the joint fails to mimic ideal boundary conditions; instead, the joint's properties become time dependent and uncertain.

The present work is motivated by some recent results on the sensitivity and variability of the response of structural stochasticity (see, for example, Ibrahim, 1987, and Manohar and Ibrahim, 1999) and by the recent assessment of joint uncertainties by Ibrahim and Pettit (2004). These problems are complex in nature because every joint involves different sources of uncertainty and non-smooth nonlinear characteristics. For example, the contact forces are not ideally plane because of manufacturing tolerances. Furthermore, the initial forces will be redistributed non-uniformly in the presence of lateral loads. This is in addition to the prying load, which induces nonlinear tension in the bolt and nonlinear compression in the joint. The main problems encountered in the design analysis of bolted joints with parameter uncertainties include random eigenvalues, response statistics, and probability of failure.

The combined effect of uncertainty in the boundary conditions and spatially variable material properties on the nonlinear panel aeroelastic response was studied by Lindsley, et al. (2002a, b). It was shown that the flutter problem of aeroelastic structures could be handled when random uncertainties are introduced in the structural model. Pinned and fixed boundary conditions were modeled as limiting cases of rotational springs on the boundary, which possessed zero and infinite stiffness, respectively. Accordingly, rotational spring stiffness was used to parameterize the boundary conditions. Parametric uncertainty was examined by modeling variability in Young's modulus and the boundary condition parameter. The variability in the boundary conditions was restricted to a single value along the plate boundary edges for each realization. For values of the dynamic pressure in the deterministic limit cycle oscillation (LCO) range, the variability in the boundary conditions affected the plate deflection in an essentially linear manner. However, for values of dynamic pressure in the neighborhood of the bifurcation point, the relationship was nonlinear. Variation in boundary conditions resulted in a softening effect of the clamped panel, and thus induced an increase in the amplitude of plate oscillations.

Structural and material uncertainties were also considered in studying the flutter of panels and shells by Liaw and Yang (1991a,b), and Kuttenukeuler and Ringertz (1998). For example, Liaw and Yang (1991a,b) quantified the effect of parameter uncertainties on the reduction of the structural reliability and stability boundaries of initially compressed laminated plates and shells. For buckling analysis, the uncertainties include modulus of elasticity, thickness, and fiber orientation of individual lamina, as well as geometric imperfections. For flutter analysis, further uncertainties such as mass density, air density, and in-plane load were also considered. Kuttenukeuler and Ringertz (1998) performed an optimization study of the onset of flutter, with respect to material and structural uncertainties.

A ground vibration test was used by Potter and Lind (2001) to obtain uncertainty models, such as natural frequencies and their associated variations, which can update analytical models for the purpose of predicting robust flutter speeds. Different norm approaches were used to formulate uncertainty models that cover the entire range of observed variations. It was found that the ∞ -norm produces the smallest uncertainty and the least conservative robust flutter speed. Lind and Brenner (2000) introduced a tool referred to as the "flutterometer" for predicting the onset of flutter during a flight test. The flutterometer computes a flutter for an analytical model with

respect to an uncertainty description. Brenner (2002a) considered a technique that identifies model parameters and their associated variances from flight data. Later Prazenica, et al. (2003) introduced a technique for estimating uncertainty descriptions based on a wavelet approach, but relies on the Volterra kernels.

The studies of panel flutter were concentrated on parametric analysis of stability boundaries and the amplitude of LCO under different boundary conditions. At the same time, it was shown that a panel subjected to a combination of airflow and in-plane loading experiences a complex range of motions, including static buckling (divergence), quasi-periodic motion, and chaos in addition to LCO. Dowell (1982) showed that a panel under the combined effect of fluid flow and in-plane compression exhibits chaotic motion for certain values of some control parameters. Dowell (1984) observed chaos, via period doubling and intermittency while increasing the compressive in-plane loading. The existence of multiple attractors and the coexistence of both symmetric and asymmetric LCO were observed by Bolotin, et al. (1998) using a two degree-of-freedom approximation of an elastic panel. They studied the transition between different stability regions. The stability regions of a simply supported two-dimensional panel subjected to compressive loading were revisited recently by Epureanu, et al. (2004). They used bifurcation diagrams for two control parameters to determine stability boundaries and Lyapunov exponents. The effect of damping on stability boundaries as well as on LCO was considered by Kuo, et al. (1972), Bismark-Nasr and Bones (2000), Bolotin, et al. (2002), Pourtakdoust and Fazelzadeh (2003). Kuo, et al. (1972) showed that the edge compression and viscous structural damping would result in an increase of flutter amplitudes while the aerodynamic damping would cause a reduction in the flutter amplitude.

Relaxation effects in structural joints cause time-dependent boundary conditions and depend on the level of structural vibration. In other words, there are uncertainties in the boundary conditions in addition to a random field due to system parameter uncertainties. In this case, aeroelastic structures will experience non-stationary time-frequency flutter, which is analyzed using time-frequency transforms such as spectrographs and wavelet transform. The time-frequency analysis techniques have recently been used to analyze flight flutter data by Brenner, et al. (1997), Johnson, et al. (2002), Staszewski and Cooper (2002), and Yu, et al. (2004). Brenner (1997) used time-frequency signal representations to analyze aeroelastic flight data. Mastroddi and Bettoli (1999) conducted wavelet analysis in the neighborhood of a Hopf bifurcation to capture the features of transient responses. In the neighborhood of aeroelastic flutter during flight tests, the time scale decompositions of continuous wavelet transform was used to analyze pre- and post-critical transient behavior of nonlinear aeroelastic structures. Brenner (2002b) applied the singular-value decomposition to aeroelastic pitch-plunge wing section models to detect instability and nonlinear dynamics from the time-frequency map.

The present work deals with the nonlinear panel flutter with relaxation in boundary conditions. The conventional boundary value problem of the panel involves time-dependent boundary conditions, which are converted to an autonomous form using a special coordinate transformation inspired by the work of Qiao, et al. (2000). The present analysis extends the analysis of Ibrahim, et al. (2004) to include six-mode interaction in the presence of boundary condition relaxation. The dynamic characteristics of the panel and the influence of initial conditions are predicted using phase plots, FFT plots, bifurcation diagrams of the first return, short time Fourier transform, wavelet transform, and Lyapunov exponents.

II. ANALYTICAL MODELING

II.1 Panel Flutter with Non-ideal Boundary Conditions

Consider a two dimensional panel exposed to supersonic flow as shown in Figure 1. In order to estimate the work done by aerodynamic loading, the pressure on the panel is represented by the linear piston theory, (Ashley and Zartarian, 1956),

$$\Delta p = p - p_\infty = \frac{\rho_\infty U_\infty^2}{M} \left[\frac{\partial w}{\partial x} + \frac{1}{U_\infty} \frac{\partial w}{\partial t} \right] \quad (1)$$

where $w(x,t)$ is the panel deflection, which is a function of position, x , and time, t . $M = U_\infty / a_\infty$ is the Mach number, U_∞ is the undisturbed gas flow speed, $a_\infty = \sqrt{\gamma p_\infty / \rho_\infty}$ is the speed of sound, p_∞ and ρ_∞ are the undisturbed free gas stream pressure and density, respectively. p is the pressure of the gas flow at the panel surface, $\gamma = C_p / C_v$ is the ratio of specific heats at constant pressure, C_p , and volume, C_v .

The governing nonlinear equation of motion for the panel is developed using Hamilton's principle, which yields (Ibrahim, et al., 1990)

$$m_p \frac{\partial^2 w}{\partial t^2} + D \left(1 + c \frac{\partial}{\partial t} \right) \frac{\partial^4 w}{\partial x^4} - \left[N_{x0} + \frac{Eh}{2a} \int_0^a \left(\frac{\partial w}{\partial x} \right)^2 dx \right] \frac{\partial^2 w}{\partial x^2} + \frac{\rho_\infty U_\infty^2}{M} \left[\frac{\partial w}{\partial x} + \frac{1}{U_\infty} \frac{\partial w}{\partial t} \right] = \Delta p_0 \quad (2)$$

m_p is the panel mass per unit area, a is the panel length, E is Young's modulus, h is the plate thickness, $D = Eh^3 / (12(1-\nu^2))$ is the panel stiffness, ν is Poisson's ratio, Δp_0 is the gas pressure difference across the panel, N_{x0} is the external in-plane load per unit span-wise length, and c is a linear viscous damping coefficient. Equation (2) is subject to the boundary conditions

$$D \frac{\partial^2 w(0,t)}{\partial x^2} - \alpha_1(t) \frac{\partial w(0,t)}{\partial x} = 0, \quad w(0,t) = 0 \quad (3a,b)$$

$$D \frac{\partial^2 w(a,t)}{\partial x^2} + \alpha_2(t) \frac{\partial w(a,t)}{\partial x} = 0, \quad w(a,t) = 0 \quad (3c,d)$$

where $\alpha_1(t)$ and $\alpha_2(t)$ measure the end slopes and represent torsional stiffness parameters such that if $\alpha_1(t) = \alpha_2(t) = \infty$ the panel is purely clamped-clamped. On the other hand, the panel is simply supported if $\alpha_1(t) = \alpha_2(t) = 0$. In real situations, $\alpha_1(t)$ and $\alpha_2(t)$ do not assume these limiting cases; instead, they are very large for clamped supports or very small for simple supports. In the dynamic case the boundary conditions (3a,c) are non-autonomous. In order to convert these conditions into an autonomous form, we introduce the following transformation of the response coordinate,

$$w(x,t) = \left[\left(\frac{x}{a} \right)^2 + 2g_1(z_1, z_2) \frac{x}{a} + g_2(z_1, z_2) \right] u(x,t) = \varphi(x; z_1, z_2) u(x,t) \quad (4)$$

where the dimensionless parameter $z_i(t) = D / a\alpha_i(t)$, $i = 1, 2$, represents the ratio of the bending rigidity to the torsional stiffness of the joints. The functions $g_1(z_1, z_2)$ and $g_2(z_1, z_2)$ are chosen to render the boundary conditions autonomous for the new coordinate $u(x,t)$. Possible expressions of these functions are

$$g_1(z_1, z_2) = -\frac{1+4z_2}{2(1+2z_1+2z_2)} \quad g_2(z_1, z_2) = -\frac{2z_1(1+4z_2)}{1+2z_1+2z_2} \quad (5)$$

In this case, the boundary conditions (3) become

$$\frac{\partial^2 u(0,t)}{\partial x^2} = \frac{\partial^2 u(a,t)}{\partial x^2} = 0 \quad \text{and} \quad u(0,t) = u(a,t) = 0. \quad (6)$$

Introducing the following non-dimensional parameters

$$\tau = t \sqrt{\frac{D}{m_p a^4}}, \quad \bar{w} = \frac{w}{h}, \quad \bar{x} = \frac{x}{a}, \quad \lambda = \frac{\rho_\infty U_\infty^2 a^3}{MD}, \quad \mu = \frac{\rho_\infty a}{m_p}, \quad \zeta = \frac{c}{a^2} \sqrt{\frac{D}{m_p}}, \quad \bar{N}_0 = N_{x0} \frac{a^2}{D}, \quad \bar{u} = \frac{u}{h},$$

$$\bar{p}_0 = \Delta p_0 \frac{a^4}{Dh}, \quad B_1 = 6(1-\nu^2), \quad \bar{\varphi} = [\bar{x}^2 + 2g_1(z_1, z_2)\bar{x} + g_2(z_1, z_2)], \quad \hat{\zeta} = \sqrt{\frac{\mu}{M}}$$

equation (2) becomes

$$\frac{\partial^2(\bar{\varphi}\bar{u})}{\partial \tau^2} + \left(1 + \zeta \frac{\partial}{\partial \tau}\right) \frac{\partial^4(\bar{\varphi}\bar{u})}{\partial \bar{x}^4} - \left[\bar{N}_0 + B_1 \int_0^1 \left(\frac{\partial(\bar{\varphi}\bar{u})}{\partial \bar{x}} \right)^2 d\bar{x} \right] \frac{\partial^2(\bar{\varphi}\bar{u})}{\partial \bar{x}^2} + \lambda \frac{\partial(\bar{\varphi}\bar{u})}{\partial \bar{x}} + \hat{\zeta} \sqrt{\lambda} \frac{\partial(\bar{\varphi}\bar{u})}{\partial \tau} = \bar{p}_0 \quad (7)$$

II.2 Relaxation of Boundary Stiffness

The relaxation process is phenomenologically modeled based on experimental results (Bickford, 1990). In this case, The torsional stiffness parameters are assumed functions of the number of vibration cycles, $n = n(\tau)$,

$$\bar{\alpha}_i(n) = \frac{a\alpha_i(n)}{D} = \frac{1}{z_i(n)} \quad (8)$$

where the overbar denotes a dimensionless parameter. An explicit analytical expression for the parameters $\bar{\alpha}_i(n)$ can be obtained from experimental records (Bickford, 1990), which reveal a slow drop between an original and an asymptotic value of the joint stiffness. An appropriate elementary function that emulates this behavior may be selected in the form

$$\bar{\alpha}(n) = \bar{\alpha}(\infty) + [\bar{\alpha}(0) - \bar{\alpha}(\infty)] \left[\frac{1 + \tanh[-k(n - n_c)]}{1 + \tanh[kn_c]} \right] \quad (9)$$

where the subscript i has been dropped, and n_c is a critical number of cycles, indicating the location of the inflection point with respect to the origin, $n = 0$. The parameter k is associated with the slope of the curve at the point, $n = n_c$. The parameters $\bar{\alpha}(0)$ and $\bar{\alpha}(\infty)$ are obtained from the experimental curve. The slope parameter k can be found by taking the derivative of equation (9) with respect to n , i.e.,

$$k = \frac{\partial \bar{\alpha}(n) / \partial n|_{n_c}}{[\bar{\alpha}(\infty) - \bar{\alpha}(0)]} [1 + \tanh[kn_c]] \quad (10)$$

One can write an expression for $z(\tau)$ by using relations (8) and (10) in the form

$$z(\tau) = Z_0 Z_\infty \left[Z_0 - (Z_0 - Z_\infty) \frac{1 + \tanh(-\chi(\tau - \tau_c))}{1 + \tanh(\chi\tau_c)} \right]^{-1} \quad (11)$$

where $Z_0 = z(0)$, $Z_\infty = z(\infty)$, $\chi = \frac{\langle \varpi \rangle}{2\pi k}$, and $\langle \varpi \rangle$ is the mean value of the response frequency, which can be taken as the center frequency. The phenomenological representation given by equation (11) can be used for any initial preload and will cause the panel to experience non-stationary behavior. Notice that the relaxation time interval documented by Bickford (1990) is very short for aerospace structural components. However, the present analysis serves to reveal the dynamic characteristics of panels under boundary conditions relaxation.

II.3 Galerkin Formulation

Galerkin's method is applied to discretize equation (7) by assuming the general solution in the form $\bar{u}(\bar{x}, \tau) = \sum_{n=1}^N \Psi_n(\bar{x}) q_n(\tau)$ and the corresponding weighting functions $\tilde{u}(\bar{x}, \tau) = \sum_{n=1}^N \Psi_n(\bar{x}) \tilde{q}_n(\tau)$ where N is the total number of the basis functions for $\bar{u}(\bar{x}, \tau)$; $q_n(\tau)$ are unknown functions to be determined (generalized coordinates); $\tilde{q}_n(\tau)$ are arbitrary functions of time and $\Psi_n(\bar{x})$ are the assumed orthonormal mode shapes. The resulting general differential equation is

$$\begin{aligned} \sum_{n=1}^N \ddot{q}_n(\tau) \delta_{nm} + \sum_{n=1}^N q_n(\tau) C_1(n, m) + \zeta \sum_{n=1}^N \dot{q}_n(\tau) C_1(n, m) - \sum_{n=1}^N q_n(\tau) \bar{N}_{x0} C_2(n, m) - \\ - B_1 \sum_{n=1}^N q_n(\tau) C_2(n, m) \left(\int_0^1 \left(\sum_{k=1}^N q_k(\tau) (\varphi'(\bar{x}) \Psi_k(\bar{x}) + \varphi(\bar{x}) \Psi'_k(\bar{x})) \right)^2 d\bar{x} \right) + \end{aligned}$$

$$+\sum_{n=1}^N q_n(\tau) D_1(n, m) + \lambda \sum_{n=1}^N q_n(\tau) D_2(n, m) + \hat{\zeta} \sqrt{\lambda} \sum_{n=1}^N \dot{q}_n(\tau) D_3(n, m) = \bar{p}_0 D_4(m) \quad (12)$$

where

$$\delta_{nm} = \int_0^1 \varphi(\bar{x}) \Psi_n(\bar{x}) \Psi_m(\bar{x}) d\bar{x},$$

$$C_1(n, m) = 6 \int_0^1 \varphi''(\bar{x}) \Psi_n''(\bar{x}) \Psi_m(\bar{x}) d\bar{x} + 4 \int_0^1 \varphi^{(3)}(\bar{x}) \Psi_n'(\bar{x}) \Psi_m(\bar{x}) d\bar{x} + \\ + 4 \int_0^1 \varphi'(\bar{x}) \Psi_n^{(3)}(\bar{x}) \Psi_m(\bar{x}) d\bar{x} + \int_0^1 \varphi^{(4)}(\bar{x}) \Psi_n(\bar{x}) \Psi_m(\bar{x}) d\bar{x} + \int_0^1 \varphi(\bar{x}) \Psi_n^{(4)}(\bar{x}) \Psi_m(\bar{x}) d\bar{x},$$

$$C_2(n, m) = 6 \int_0^1 \varphi''(\bar{x}) \Psi_n(\bar{x}) \Psi_m''(\bar{x}) d\bar{x} + 2 \int_0^1 \varphi'(\bar{x}) \Psi_n'(\bar{x}) \Psi_m''(\bar{x}) d\bar{x} + 6 \int_0^1 \varphi(\bar{x}) \Psi_n''(\bar{x}) \Psi_m(\bar{x}) d\bar{x},$$

$$D_1(n, m) = \int_0^1 \varphi'(\bar{x}) \Psi_n(\bar{x}) \Psi_m(\bar{x}) d\bar{x}; \quad D_2(n, m) = \int_0^1 \varphi(\bar{x}) \Psi_n'(\bar{x}) \Psi_m(\bar{x}) d\bar{x}; \quad D_3(n, m) = \delta_{nm},$$

$$D_4(m) = \int_0^1 \Psi_m(\bar{x}) d\bar{x}.$$

The general solution is assumed to be periodic in space,

$$\bar{u}(\bar{x}, \tau) = \sum_{n=1}^N q_n(\tau) \sin n\pi \bar{x} \quad (13)$$

where N is the total number of modes, $q_n(\tau)$ are the generalized coordinates. It has been established that accurate solution of the panel flutter can be achieved by using at least six modes (see, e.g., Dowell, 1966). The inclusion of six modes results in a complicated analysis where relaxation is considered. For this reason we introduce the simplification, $z_1 = z_2 = z/2$, which makes the boundary stiffness values to be equal. The resulting set of six equations may be written in matrix form,

$$[M(\tau)]\{\ddot{q}\} + [C(\zeta, \hat{\zeta}, \lambda, \tau)]\{\dot{q}\} + [K(\tau, \bar{N}_0, \lambda)]\{q\} = [D(\tau)]\{q^3\} + \sum_{i=1,3,5}^6 \sum_{j=1, j \neq i}^6 \{eq_i q_j^2\} \\ + \sum_i \sum_{j \neq k}^6 \sum_k \{fq_i q_j q_k\} + \{P\} \quad (14)$$

where $[M(\tau)]$ is the time dependent mass matrix and $[C(\zeta, \hat{\zeta}, \lambda, \tau)]$ is the damping matrix, which depends on the viscous damping ratio ζ , mass parameter, $\hat{\zeta}$, and relaxation parameter, $z(\tau)$. $[K(\tau, \bar{N}_0, \lambda)]$ is the stiffness matrix, $[D(\tau)]$ is the coefficient matrix of cubic terms, and $\{P\}$ is the pressure vector, whose elements are non-zero only for odd modes because it is the integral of a constant, \bar{p}_0 , and the sinusoidal basis functions. The structure of these matrices is given in the Appendix. The complete set of expressions for all coefficients of the matrices and vectors of equation (4) is documented in Beloiu (2005).

Equations (14) are solved numerically in the time domain for a typical relaxation curve. The resulting solution is given in terms of the transformed response, \bar{u} , or rather in terms of its modal coordinates, q_i , $i = 1..6$. One should estimate the modal response in terms of its physical generalized coordinate,

$$\bar{w}(\bar{x}, \tau) = \varphi(\bar{x})\bar{u}(\bar{x}, \tau) \quad \text{and} \quad \bar{w}(\bar{x}, \tau) = \sum_{n=1}^N \hat{q}_n(\tau) \sin n\pi\bar{x} \quad (15)$$

where $\bar{\varphi} = [\bar{x}^2 + 2g_1(z_1, z_2)\bar{x} + g_2(z_1, z_2)]$ and g_i are given by equation (5). The relationship between the physical coordinates $\hat{q}_n(\tau)$ and the generalized transformed coordinates $q_n(\tau)$ is

$$\sum_{n=1}^N \hat{q}_n(\tau) \sin n\pi\bar{x} = [\bar{x}^2 + 2g_1(z)\bar{x} + g_2(z)] \sum_{n=1}^N q_n(\tau) \sin n\pi\bar{x} \quad (16)$$

Integrating the above equation

$$\int_0^1 \left[\sum_{n=1}^N \hat{q}_n(\tau) \sin n\pi\bar{x} \right] d\bar{x} = \int_0^1 \left[(\bar{x}^2 + 2g_1(z)\bar{x} + g_2(z)) \sum_{n=1}^N q_n(\tau) \sin n\pi\bar{x} \right] d\bar{x}$$

gives the desired relation between the coordinates.

$$\hat{q}_n(\tau) = T_n(z)q_n(\tau) \quad (17)$$

where

$$T_n(z) = -\frac{(2n-1)^2 \pi^2}{2 + (2n-1)^2 \pi^2 z}, \quad n = 1, 3, 5, \dots, \quad T_n(z) = -\frac{(n-1)^2 \pi^2}{2 + (n-1)^2 \pi^2 z}, \quad n = 2, 4, 6, \dots \quad (18)$$

Therefore, the solution of equations (14) must be divided by $T_n(z)$ in order to recover the actual modal displacements. The next section presents the stability analysis and response characteristics under different values of the dynamic pressure and relaxation parameters.

III. LINEAR ANALYSIS

The stability analysis is carried out by estimating the natural frequencies of the six modes in the absence of system nonlinearities and by setting the non-homogeneous term in equations (14) to zero. The dependence of the real and imaginary components of the eigenvalues on the dynamic pressure is shown in Figures 2(a) and (b) for three different values of relaxation parameter ($z = 0.001, 0.1, \text{ and } 1$), damping parameter, $\zeta = 0.0$, mass parameter $\hat{\zeta} = 0.1$, and static axial load parameter $\bar{N}_0 = 0$. It is seen that the real parts are zero up to a critical value of the dynamic pressure, depending on the value of the relaxation parameter, z , above which one becomes negative and the other positive indicating the occurrence of panel instability (flutter). Note that the value $z = 0.0$ corresponds to a clamped-clamped panel, while $z = \infty$ corresponds to simple supports. As expected, the linear flutter point decreases for lower boundary stiffness. The dependence of the components of the first and second eigenvalues on the relaxation parameter, z , is shown in Figure 3 for three different values of dynamic pressure, $\lambda = 400, 450, \text{ and } 500$. It is seen that the eigenvalues possess negative real parts up to a critical value of relaxation parameter, above which one eigenvalue has a positive real part indicating the occurrence of flutter.

Figures 4 and 5 show the boundaries of panel flutter in terms of the critical value of aerodynamic pressure, λ_{cr} , and the relaxation parameter, z . These figures depict the influence of the in-plane load, \bar{N}_0 , and damping ratio, ζ , respectively. As expected, the compression in-plane loading results in a reduction of the critical flutter speed. The clamped panel ($z \ll 1$) requires more in-plane compression load to reach its flutter speed. With reference to Figure 5, for all values of relaxation parameter, the damping is non-beneficial as it increases from very small values up to a critical value, above which it becomes beneficial, depending on the value of the relaxation parameter. Figure 6 shows the dependence of flutter speed on the damping parameter, ζ . For a given relaxation parameter, there is a critical damping ratio, ζ_{cr} , above which the damping becomes beneficial and the critical speed increases with the damping. For $\zeta < \zeta_{cr}$ the damping is detrimental and results in a reduction the flutter speed. The value of ζ_{cr} is shown by a small circle on each curve and is determined by setting $d\lambda/d\zeta = 0$. The locus of these points is shown by the dotted curve in Figure 6.

IV. NONLINEAR ANALYSIS

IV.1 Bifurcation Analysis

The complete set of Equations (14) is solved numerically using the MATLAB© variable solver ode15 with relative error tolerance of 10^{-6} and absolute error tolerance of 10^{-9} . The numerical solution is carried out for a given damping parameter, ζ , and for different values of in-plane load, N_0 , dynamic pressure, λ , and relaxation parameter, z . In order to avoid the influence of transient motion, only the last portion of the steady state time history is taken to estimate the state of the panel. Depending on the system parameters and dynamic pressure the panel may exhibit different regimes such as (I) statically stable, (II) static buckling (divergence), (III) limit cycle oscillations, and (IV) multi-period oscillations and chaos. Figure 7 shows these four regimes on the plane of dynamic pressure, λ , versus in-plane pressure, $-N_0/\pi^2$, for three

different values of relaxation parameter $z = 0.001, 0.1$, and 1 , in addition to the case of simply supported panel. The two values of in-plane loads $-N_0/\pi^2 = 1$ and 4 represent the Euler buckling loads of simply-supported and clamped panels, respectively. It is seen that as the relaxation parameter increases (panel approaches simply supported case) the regions (III) of LCO and (IV) multi-period oscillations/chaos expand. The dynamics of the panels along lines A and B shown in Figure 7 will be examined later.

Figure 8 shows the dependence of LCO amplitude on dynamic pressure for zero in-plane loading and different discrete values of the relaxation parameter z . Note that, depending on the value of the relaxation parameter, there is a critical value of dynamic pressure at which LCO begins in the form of supercritical bifurcation. The relaxation results in moving the bifurcation point to lower values of dynamic pressure. Under compression in-plane loading, $\bar{N}_0 = -3\pi^2$ and under low values of dynamic pressure the panel experiences static buckling as shown in Figure 9. As the dynamic pressure increases the panel enters a stable state until the dynamic pressure reaches the critical value, λ_{cr} , above which the panel exhibits LCO. A three-dimensional diagram demonstrating the time evolution of LCO amplitude and its dependence on the dynamic pressure is shown in Figure 10 for zero in-plane loading and same parameters as in the previous figures.

Under the relaxation curve shown in Figure 11(a), the time history record of the total deflection at $x/a = 0.75$ is shown in Figure 11(b) for in-plane compression loading, $\bar{N}_0 = -6\pi^2$, and dynamic pressure, $\lambda = 200$. Over the whole time domain, the panel experiences two different regimes of oscillations, namely the growing amplitude LCO, and chaotic oscillations.

Chaotic flutter is usually detected by estimating the largest value of the Lypunov exponent. Lyapunov exponent measures the rate at which nearby trajectories converge or diverge, and are numerically calculated using the algorithm of Wolf, et al. (1985). Equations (14) may be rewritten in terms of a set of first-order differential equations in the form

$$\dot{\mathbf{x}} = \mathbf{f}(\mathbf{x}; t) \quad (19)$$

where $\mathbf{x} = \{\mathbf{q}, \dot{\mathbf{q}}\}^T$ is the state-space vector, where T denotes transpose and \mathbf{f} describes the nonlinear behavior of the system. Let $\mathbf{x}^*(t; \mathbf{x}_0)$ be the reference solution of the system (19) where \mathbf{x}_0 is the vector of initial conditions. In order to find the variation of trajectories in the neighborhood of the reference trajectory $\mathbf{x}^*(t)$, at each time step t_k we introduce the corresponding linearized equation

$$\dot{\mathbf{y}} = \mathbf{F}(\mathbf{x}^*(t_k))\mathbf{y} \quad (20)$$

where $\mathbf{F}(\mathbf{x}^*(t_k))$ is the $n \times n$ Jacobian matrix of the function \mathbf{f} evaluated at the reference solution $\mathbf{x}^*(t_k)$. First, we integrate the differential equation (19) with initial conditions \mathbf{x}_0 to determine the reference trajectory. Simultaneously, the linearized system (20), with initial condition $\mathbf{y}(0)$, is integrated for a small period of time Δt to obtain a set of vectors $\mathbf{y}_j(\Delta t)$,

($j=1, \dots, n$). The vectors $y_j(\Delta t)$ are orthonormalized using the Gram-Schmidt procedure. The next steps consist of integrating equations (19) and (20) for another successive time intervals Δt using $x^*(t_k)$ and the orthonormalized vector $y_j(\Delta t)$ as new initial conditions. Repeating the above procedure p times, the j th Lyapunov exponent can be obtained as an average increment of variation vector $y_j(t)$ during the test time Δt :

$$\lambda_j = \frac{1}{p\Delta t} \sum_{k=1}^p \ln \frac{\|y_j(t; t_k)\|}{\|y_j(0; t_k)\|} \quad (21)$$

where $\|\cdot\|$ denotes vector norm. To obtain reliable values of the λ_j , long time integration is necessary. In the present study, Lyapunov exponents are estimated using a non-dimensional time increment $\Delta \tau = 0.0001$. The computation starts after $\tau = 100$ and continues up to $\tau = 1,000$. Figure 12 shows some regions of relaxation parameter over which the Lyapunov exponent is positive, implying the existence of chaotic flutter. Note that extreme positive values of Lyapunov exponent are found for multi-period flutter regimes.

The bifurcation diagram shown in Figure 12 is obtained by plotting the first return points of the panel amplitude for in-plane load parameter $\bar{N}_0 = -5.8\pi^2$, damping factor $\zeta = 0.0001$, static pressure $\bar{p}_0 = 0$, mass ratio parameter $\hat{\zeta} = 0.1$, and dynamic pressure $\lambda = 200$. The relaxation parameter vary between $z = 0.0025$ and $z = 1$ with an increment of $\Delta z = 0.0025$. It is seen that for relatively small values of relaxation parameter, $z < 0.105$, the panel experiences symmetric LCO with increasing amplitude as the relaxation parameter increases from the absolute clamped case, $z = 0$. The figure may be classified into the regimes listed in Table I.

Table I: Panel flutter regimes

$0.001 \leq z \leq 0.0925$	Period-one, symmetric (about z -axis)
$0.0925 < z \leq 0.1025$	Period-one, asymmetric (about z -axis)
$0.1025 < z \leq 0.1700$	Chaos
$0.1700 < z \leq 0.1850$	Period-two, mixture of symmetric and asymmetric
$0.1850 < z \leq 0.2625$	Period-one, symmetric
$z = 0.2650$	Period-five, symmetric
$0.2650 < z \leq 0.2850$	Period-one, symmetric
$0.2850 < z \leq 0.3775$	Period-one, two, and three, symmetric and asymmetric
$z = 0.3800$	Period-eight, symmetric
$0.3800 < z \leq 0.3925$	Period-one and two, symmetric
$z = 0.3950$	Period-seven, symmetric
$0.3950 < z \leq 0.4025$	Period-one, symmetric
$z = 0.4050$	Period-four, symmetric
$0.4050 < z \leq 0.4825$	Period-one, asymmetric and asymmetric
$0.4825 < z \leq 0.4950$	Chaos
$0.4950 < z \leq 0.5075$	Period-doubling, asymmetric
$0.5075 < z \leq 0.6700$	Chaos
$0.6700 < z \leq 0.7275$	Period-four and seven, symmetric and asymmetric

$0.7275 < z \leq 0.7325$	Chaos
$0.7325 < z \leq 0.7375$	Period-six, asymmetric
$0.7375 < z \leq 0.8925$	Chaos
$0.8925 < z \leq 1$	Period-three, symmetric

For selected values of relaxation parameter, the phase plots are shown in Figure 13. The corresponding FFT plots are shown in Figure 14 and reveal n spikes for the multi-period regimes and continuous spectra for chaotic motion.

Figure 15 shows the bifurcation diagram and the corresponding Lyapunov exponent for $\lambda = 250$ and $N_0 = -6\pi^2$. The switching from symmetric to asymmetric LCO is more visible over the region $0.15 < z < 0.37$. After a window of symmetric LCO, the motion becomes chaotic ($z > 0.6325$) with the increasing of the Lyapunov exponent as the relaxation parameter increases. Switching between symmetric and asymmetric LCO, together with cascades of quasi-periodic motion, and chaotic flutter with windows of periodicity make the panel behavior very complex.

Figures 12 and 15 reveal only a partial view of the route to chaotic flutter during relaxation. To have a global picture over the parametric space of dynamic pressure and relaxation parameter for given values of in-plane load and relaxation parameter, the boundaries of chaotic flutter are shown in Figure 16 for two values of N_0 and two values of ζ . The dynamic pressure varies from $\lambda = 100$ to $\lambda = 300$ with a step size $\Delta\lambda = 5$, and relaxation parameter varies from $z = 0$ to $z = 1$ with step size $\Delta z = 0.05$ so that each map is represented by $41 \times 22 = 902$ points. The Lyapunov exponent is computed for each set of parameters. A positive Lyapunov exponent indicates chaotic flutter, which is labeled by a black dot. If all exponents are negative, the panel equilibrium position is stable. If the largest Lyapunov exponent is zero the panel experiences stable limit cycle. Both negative and zero Lyapunov exponents are labeled by a blank space. Figure 16(a) shows chaos boundaries for $N_0 = -6\pi^2$ and small damping ratio, $\zeta = 0.0001$. The motion is regular for $z < 0.1$. The relaxation process increases the chaos occurrence but not monotonically; instead, a complex pattern is observed. Higher in-plane loads enlarges the chaos boundaries as shown in Figure 16(c), however, the switching of windows with regular and chaotic motions is still visible. By maintaining the same in-plane load and increasing damping ratio to $\zeta = 0.001$, the chaos boundaries are reduced considerably, especially for lower z as shown in Figures 16(b,d).

With reference to the path line A at $N_0 = -6\pi^2$ shown in Figure 7, we consider the panel dynamic behavior in terms of the bifurcation diagram and Lyapunov exponent, shown in Figure 17 for relaxation parameter, $z = 1$. The aerodynamic pressure, λ , is taken as the control parameter. A similar analysis is found in Epureanu, et al. (2004) for a simply supported panel without structural damping. The dynamic pressure varies between $\lambda = 100$ and $\lambda = 300$ with a step increment of $\Delta\lambda = 0.25$. The bifurcation diagram begins with the buckled state of the panel up to $\lambda = 109$. The chaotic motion over the region $109.5 \leq \lambda \leq 152.5$ is followed by a region of multi-period oscillations up to $\lambda = 173$. Another window with chaotic motion is found over the range $173 < \lambda \leq 192$ followed by a wide window with period three motion. Increasing the aerodynamic pressure, the motion is chaotic but the chaos intensity decreases as suggested by the decreasing value of Lyapunov exponent. For $\lambda > 288$, the panel experiences LCO with

increasing amplitude. Figure 18 depicts the bifurcation diagram and corresponding Lyapunov exponent for the same path A but with relaxation parameter $z = 0.1$, which is much closer to the clamped state. The motion is much more sensitive to the change of control parameter over the dynamic pressure range $120.5 \leq \lambda \leq 156$. With the reference to the corresponding Lyapunov exponent, the panel motion exhibits a cascade of alternating chaotic and periodic oscillations. The character of the motion is changed abruptly over a small increment of λ .

With reference to the path line B at $\lambda = 140$ of Figure 7, we consider the panel dynamics behavior by varying the in-plane load N_0 . The bifurcation diagram illustrated in Figure 19 is determined for relaxation parameter, $z = 1$. It is seen that the panel is stable for small in-plane load up to $N_0 = 3.3$ above which it experiences LCO over the range, $3.3 < N_0 < 3.45$. At $N_0 = 3.45$ the panel experiences secondary bifurcation with symmetric period-3 oscillations. Increasing the in-plane load, the motion switches between asymmetric and symmetric multi-harmonic oscillations. Further increase of the in-plane loading results in a chaotic motion with three windows of periodicity: $4.22 < N_0 < 4.39$, $4.77 < N_0 < 4.96$, and $5.58 < N_0 < 5.87$.

For the same set of parameters, the response may be different depending on initial conditions. This is true not only for the chaotic motion but also for the periodic oscillations. Figure 20 shows phase portraits for four different sets of parameters. Each phase portrait is drawn for two different initial conditions (1) $q_1(\tau = 0) = 0.1$, $q_i(\tau = 0) = 0, i = 2, \dots, 6$, and (2) $q_1(\tau = 0) = 1$, $q_i(\tau = 0) = 0, i = 2, \dots, 6$, respectively. One can observe from Figures 20(a) and (b) that multi-periodic oscillations corresponding to initial condition set (1) becomes a period-3 oscillation in the case of initial condition set (2). In both cases, the response is symmetric. For other sets of parameters two asymmetric solutions co-exist as shown in Figures 20(c) and (d). The panel response follows one of these solutions, depending on the initial condition. The co-existence of symmetric and asymmetric LCO is better observed in the bifurcation diagram shown in Figure 21 for $N_0 = -6\pi^2$, and $z = 0.1$. The response is asymmetric over the range $233 < \lambda \leq 237.5$ depending on the initial conditions; after that, the response becomes symmetric independent of the initial conditions.

IV.2 Time-Frequency Analysis

The ultimate decision on whether the motion is chaotic or not is given by the presence of a positive Lyapunov exponent. However, the Lyapunov exponent is characterized by a slow convergence, which requires long time simulations and large computation resources. Time limitation may be critical, especially when experimental data is available for a limited time history record. Therefore, at least for preliminary investigations, the information from the bifurcation diagram, phase plot and power spectrum is generally sufficient. The relaxation of the boundary conditions results in time variation of the panel natural frequencies, and thus the flutter becomes non-stationary. The Fourier transform does not reveal the time dependency of the frequency of panel oscillations. The present work will adopt two techniques usually used for non-stationary signal analysis. These are the windowed Fourier transform, known as the spectrogram, originally developed by Gabor (1946), and the Morlet wavelet transform. Note that both transforms have time-frequency resolution limitations for the determination of the instantaneous frequencies. The windowed Fourier transform relies on the selected length of the window. Any special features occur during short time-scales smaller than the length of the

window, or with frequencies smaller than those contained in the window are lost and cannot be captured by the windowed Fourier transform. On the other hand, the wavelet transform has the advantage in that it follows the rapid variations of the instantaneous frequencies since it adjusts the length of the window according to the frequency content of the signal.

For the case of the short time Fourier transform, a real and symmetric window $g(t) = g(-t)$ is translated by τ and modulated by the frequency ϖ ,

$$g_{\tau, \varpi}(t) = e^{i\varpi t} g(t - \tau), \quad \|g\| = 1, \text{ and } \|g_{\tau, \varpi}\| = 1 \quad (22)$$

The short Fourier transform, known also as the short time Fourier transform, of the panel deflection $q_i(t)$ is

$$S\bar{w}(\tau, \varpi) = \int_{-\infty}^{\infty} \bar{w}(t) g(t - \tau) e^{-i\varpi t} dt \quad (23)$$

In the present work, the Kaiser (1974) window function is used. It has the following form

$$g(t) = \begin{cases} \frac{I_0\left(\beta\sqrt{1-(t/T)^2}\right)}{I_0(\beta)} & |t| < T \\ 0 & \text{otherwise} \end{cases} \quad (24)$$

where I_0 is the modified Bessel function of order zero and of first kind, β is a parameter that governs the shape of the window, and T is the signal total time. The spectrogram measures the energy density of the flutter deflection \bar{w} in the time-frequency neighborhood of (τ, ϖ) given by

$$P_s \bar{w}(\tau, \varpi) = |S\bar{w}(\tau, \varpi)|^2 = \left| \int_{-\infty}^{\infty} \bar{w}(t) g(t - \tau) e^{-i\varpi t} dt \right|^2 \quad (25)$$

Figures 22(a) and (b) show two cases of the FFT plots and spectrograms of the panel total deflection time history records for (a) $\lambda = 700$, and $\zeta = 0.0001$, and (b) $\lambda = 700$, and $\zeta = 0.02$, respectively. For low damping, Figure 22(a) shows the panel frequency decreases with time as the panel boundary conditions approach the case of simple supports. On the other hand, as the damping increases, the panel frequency increases with time. There are two factors competing with each other, namely, the structure geometric nonlinearity and the relaxation in the boundary conditions. For increased damping, the structure geometric nonlinearity overcomes the influence of relaxation and the frequency increases as shown in Figure 22(b).

Alternatively, we will use the continuous wavelet transform technique to present the time history records in two-dimensional function of time and frequency to reveal the wavelet modulus and phase. A wavelet is a function with some special properties. It should have a small concentrated burst of finite energy in the time domain and exhibit some oscillation in time. The wavelet transform can be regarded as a cross correlation between the wavelet and the panel time history record. To analyze signal structures of very different sizes, the wavelet transform decomposes

signals over dilated and translated wavelets. A wavelet is a function $\psi(t) \in L^2(\mathbb{R})$ with zero average. It is normalized $\|\psi\|=1$ and centered in the neighborhood of $t=0$. A family of wavelets is obtained by scaling ψ by s and translating it by τ (see, e.g., Mallat, 1999):

$$\psi_{\tau,s}(t) = \frac{1}{\sqrt{s}} \psi\left(\frac{t-\tau}{s}\right), \quad \|\psi_{\tau,s}\|=1 \quad (26)$$

The wavelet transform (WT) of the signal $\bar{w} \in L^2(\mathbb{R})$ at time τ and scale s is

$$W^{\bar{w}}(\tau, s) = \langle \bar{w}, \psi_{\tau,s} \rangle = \int_{-\infty}^{\infty} \bar{w}(t) \frac{1}{\sqrt{s}} \psi^*\left(\frac{t-\tau}{s}\right) dt \quad (27)$$

The Morlet wavelet is suitable for analyzing smooth signals. It is complex, but not admissible because it does not possess zero mean. Nevertheless, the mean value is very small, so they generally work well in computations even though they slightly violate some theoretical conditions. The mother wavelet for the Morlet wavelet is given by the following function

$$\psi(t) = \pi^{-1/4} e^{i\omega_0 t} e^{-|t|^2/2} \quad (28)$$

The modulus of the wavelet transform is defined as

$$|W_{\psi}^{\bar{w}}(\tau, s)| = \sqrt{\left(\text{Re}[W_{\psi}^{\bar{w}}(\tau, s)]\right)^2 + \left(\text{Im}[W_{\psi}^{\bar{w}}(\tau, s)]\right)^2} \quad (29)$$

and the phase is

$$\phi(\tau, s) = \tan^{-1} \left(\frac{\text{Im}[W_{\psi}^{\bar{w}}(\tau, s)]}{\text{Re}[W_{\psi}^{\bar{w}}(\tau, s)]} \right) \quad (30)$$

The square of the modulus $|W_{\psi}^{\bar{w}}(\tau, s)|^2$ represents the energy density distribution of the signal over the time-scale plane, (τ, s) . On the other hand, the phase measures the relative position of the signal and its analyzing wavelet. The graphical representation of the WT modulus in time-scale plane is called *scalogram*. The modulus and phase provide the time evolution of the frequency components of the analyzed signal. Figure 23 shows the time history, scalogram, and wavelet phase for fixed parameters $\lambda=132$, $N_0=-6\pi^2$, and $z=1$. The scalogram shown in Figure 23b illustrates a large spectrum of frequencies randomly distributed in time. According to Newland (1999a,b), the absolute phase is not a useful indicator because it depends on wavelet location. However, the rate of change of phase with time in the same frequency band is an interesting parameter because it is constant when the signal is harmonic of fixed frequency and phase. Figure 23(c) shows the projection of phase on the frequency-time plane and one can see the evolution of phase with time does not maintain a constant value. A better visualization of time-frequency evolution of the wavelet modulus is illustrated in the three-dimensional plot (Figure 23d). Similarly, Figure 24 shows the time history, wavelet modulus and wavelet phase

for fixed parameters $\lambda = 203.5$, $N_0 = -6\pi^2$, and $z = 0.1$. The wavelet scalogram shows a band of frequencies varying about a dominant component of $\omega^* = 20$ dimensionless frequency. In addition, intermittent higher frequency components randomly distributed in time are observed. Although the time history shows a certain degree of repeatability, the motion is still chaotic. Compared to the Lyapunov exponent, the wavelet transform is well suited to the analysis of short duration or intermittent signal components. However, the wavelet transform cannot provide a quantitative tool to measure chaos.

V. CONCLUSIONS

The nonlinear flutter of a two-dimensional panel exposed to supersonic gas flow involving six-mode interaction is studied in the presence of non-ideal boundary conditions. The deterministic study includes stability analysis in terms of dynamic pressure, relaxation parameter, damping ratio, and in-plane loading. For in-plane loading below the critical buckling value, the panel experiences LCO above a critical aerodynamic pressure governed by the relaxation parameter. For compressive in-plane loads, the panel experiences periodic, quasi-periodic and chaotic oscillations depending on the values of dynamic pressure, relaxation parameter and damping ratios. Bifurcation diagrams of the first return and the associated largest Lyapunov exponent are estimated by taking the dynamic pressure or the relaxation parameter or the in-plane loading as control parameters. The chaos regions represented by the positive largest Lyapunov exponent were found to be reduced for small relaxation parameter. The initial conditions were found to affect the behavior of the panel flutter in the periodicity and symmetry of oscillations. The time-frequency analyses of the panel flutter was estimated using the techniques of spectrogram and Morlet wavelet transform. The importance of these transforms is to reveal the degree of non-stationarity of panel flutter in terms of frequency variations and nonlinear behavior. The results presented herein show that variations in boundary fixity clearly affect aeroelastic flutter characteristics. It is recommended that phenomenological models of relaxation be integrated into aeroelastic models of more complex structures to ascertain whether relaxation could be an important factor in the observed variability of aeroelastic behavior between nominally identical aircraft.

References

- Ashly, H., and Zartarian, G., 1956, "Piston theory – a new aerodynamic tool for aeroelastician," *Journal of the Aeronautical Science* **23**(10), 1109-1118.
- Beloiu, D. M., 2005, *Non-Smooth Dynamics in Automotive and Aerospace Structures*, Ph.D. Dissertation, Wayne State University, Department of Mechanical Engineering, Detroit, Michigan.
- Bickford, J. H., 1990, *An Introduction to the Design and Behavior of Bolted Joints*, 2nd edition, Marcel Dekker, Inc., New York.
- Bismarck-Nasr, M.N., and Bones, C.A., 2000, "Damping effect in nonlinear panel flutter," *AIAA Journal* **38**(4), 711-713.
- Bolotin, V.V., Grishko, A.A., Kounadis, A.N., and Gantes, C.J., 1998, "Non-linear panel flutter in remote postcritical domains," *International Journal of Non-Linear Mechanics* **33**(5), 753-764.
- Bolotin, V.V., Grishko, A.A., and Panov, M.Yu., 2002, "Effect of damping on the postcritical behavior of autonomous non-conservative system," *International Journal of Non-Linear Mechanics* **37**, 1163-1179.
- Brenner, M. J., 1997, "Wavelet analysis of F/A-18 aeroelastic and aeroservoelastic flight test data,," NASA TM 4793.

- Brenner, M. J., 2002a, "Aeroelastodynamic uncertainty model identification from flight data," *Journal of Guidance, Control, and Dynamics* **25**(4), 748-754.
- Brenner, M. J., 2002b, "Non-stationary dynamics data analysis with wavelet-SVD filtering," *Mechanical Systems and Signal Processing* **17**(4), 765-786.
- Brenner, M. J., Lind, R. C., and Voracek, D. F., 1997, "Overview of recent flight flutter testing research at NASA Dryden," NASA TM-4792.
- Dowell, E. H., 1982, "Flutter of a buckled plate as an example of chaotic motion of a deterministic autonomous system," *Journal of Sound and Vibration* **85**(3), 333-344.
- Dowell, E. H., 1984, "Observation and evolution of chaos for an autonomous system," *ASME Journal of Applied Mechanics* **51**(1), 664-673.
- Epureanu, B.I., Liaosha, S.T., Paidoussis, M.P., 2004, "Coherent structures and their influence on the dynamics of aeroelastic panels," *International Journal of Non-Linear Mechanics* **39**, 977-991.
- Gabor, D., 1946, "Theory of communication," *J IEE* **93**, 429-457.
- Ibrahim, R. A., 1987, "Structural dynamics with parameter uncertainties," *ASME Appl Mech Rev* **40**(3), 309-328.
- Ibrahim, R. A., Orton, P. O. and Madaboosi, S. R., 1990, "Stochastic flutter of a panel subjected to random in-plane forces, part i: two-mode interaction," *AIAA Journal*, **28**(4), pp. 694-702.
- Ibrahim, R. A., and Pettit, C. L. (2004), "Uncertainties and dynamic problems of bolted joints and other fasteners," *Journal of Sound and Vibration*, in press.
- Ibrahim, R. A., Beloiu, D. M. and Pettit, C. L., 2004, "Influence of joint relaxation on deterministic and stochastic panel flutter," *AIAA Journal*, in press.
- Johnson, J. D., Lu, J., Dhawan, A. P., and Lind, R., 2002, "Real-time identification of flutter boundaries using the discrete wavelet transform," *Journal of Guidance, Control, and Dynamics* **25**(2), 334-339.
- Kuo, C.C., Morino, L., and Dugundji, J., 1972, "Perturbation and harmonic balance methods for nonlinear panel flutter," *AIAA Journal* **10**, 1479-1484.
- Kuttenkeuler, J., and Ringertz, U., 1998, "Aeroelastic tailoring considering uncertainties in material properties," *Structural Optimization* **15**, Springer-Verlag, 157-162.
- Liaw, D.G., and Yang, T.Y., 1991a, "Reliability of initially compressed uncertain laminated plates in supersonic flow," *AIAA Journal*, **29**(6), 952-960.
- Liaw, D.G., and Yang, T.Y., 1991a, "Reliability of uncertain laminated shells due to buckling and supersonic flutter," *AIAA Journal*, **29**(10), 1698-1708.
- Lind, R. and Brenner, M., 2000, "Flutterometer: An on-line tool to predict robust flutter margins," *Journal of Aircraft* **37**(6), 1105-1112.
- Lindsley, N. J., Beran, P. S., and Pettit, C. L., 2002a, "Effects of uncertainty on nonlinear plate response in supersonic flow," 9th AIAA Symp Multidisciplinary Analysis and Optimization, Atlanta, GA, Paper 2002-5600.
- Lindsley, N. J., Beran, P. S., and Pettit, C. L., 2002b, "Effects of uncertainty on nonlinear plate aeroelastic response," 43rd AIAA/ASME/ASCE/AHS/ASCE Struct Struct Dyn Mater Conf. Paper No. AIAA 2002-1271.
- Mallat, S., 1999, *A Wavelet Tour of Signal Processing*, 2nd Edition, Academic Press, New York.
- Manohar, C. S. and Ibrahim, R. A., 1999, "Progress in structural dynamics with stochastic parameter variations: 1987-1998," *ASME Appl. Mech Rev* **52**(5), 177-197.
- Mastroddi, F. and Bettoli, A., 1999, "Wavelet analysis for Hopf bifurcations with aeroelastic applications," *Journal of Sound and Vibration* **225**(5), 887-913.
- Newland, D. E., 1999a, "Ridge and phase identification in the frequency analysis of transient signals by harmonic wavelets," *ASME Journal of Vibration and Acoustics* **121**, 149-155.
- Newland, D. E., 1999b, "Harmonic wavelets in vibrations and acoustics," Royal Society meeting, *Wavelets: The Key to Intermittent information*, February 24-25, 1999.

- Potter, S. and Lind, R., 2001, "Developing uncertainty models for robust flutter analysis using ground vibration test data," AIAA 2001-1585, also as NASA/TM-2001-210392.
- Pourtakdoust, S.H., and Fazelzadeh, S.A., 2003, "Chaotic analysis of nonlinear viscoelastic panel flutter in supersonic flow," *Nonlinear Dynamics* **32**, 387-404.
- Prazenica, R. J., Lind, R., and Kurdila, A. J., 2003, "Uncertainty estimation from Volterra kernels for robust flutter analysis," *Journal of Guidance, Control, and Dynamics* **26**(2), 331-339.
- Qiao, S., Pilipchuk, V. N. and Ibrahim, R. A., 2000, "Modeling and simulation of elastic structures with parameter uncertainties and relaxation of joints," *ASME J Vib Acoust* **123**(1), 45-52.
- Staszewski, W. J., and Cooper, J. E., 2002, "Wavelet approach to flutter data analysis," *Journal of Aircraft* **39**(1), 125-132.
- Wolf, A., Swift, J.B., Swinney, H., and Vastano, J. A., 1985, "Determining Lyapunov exponents from time series," *Physica* **16D**, 285-317.
- Yu, K., Ye, J., Zou, J., Yang, B., and Yang, H., 2004, "Missile flutter experiment and data analysis using wavelet transform," *Journal of Sound and Vibration* **269**, 899-912.

APPENDIX

$$M(\tau) = \begin{bmatrix} 1 & 0 & m_{13} & 0 & m_{15} & 0 \\ 0 & 1 & 0 & m_{24} & 0 & m_{26} \\ m_{31} & 0 & 1 & 0 & m_{35} & 0 \\ 0 & m_{42} & 0 & 1 & 0 & m_{46} \\ m_{51} & 0 & m_{53} & 0 & 1 & 0 \\ 0 & m_{52} & 0 & m_{64} & 0 & 1 \end{bmatrix}, \quad m_{13}(\tau) = -\frac{9}{4[3 + \pi^2(1 + 6z(\tau))]}$$

$$C = \begin{bmatrix} \zeta b_{11} + \hat{\zeta}\sqrt{\lambda} & 0 & \zeta b_{12} + \hat{\zeta}b_{13}\sqrt{\lambda} & 0 & \zeta b_{14} + \hat{\zeta}b_{15}\sqrt{\lambda} & 0 \\ 0 & \zeta b_{21} + \hat{\zeta}\sqrt{\lambda} & 0 & \zeta b_{22} + \hat{\zeta}b_{23}\sqrt{\lambda} & 0 & \zeta b_{24} + \hat{\zeta}b_{25}\sqrt{\lambda} \\ \zeta b_{31} + \hat{\zeta}b_{32}\sqrt{\lambda} & 0 & \zeta b_{33} + \hat{\zeta}\sqrt{\lambda} & 0 & \zeta b_{34} + \hat{\zeta}b_{35}\sqrt{\lambda} & 0 \\ 0 & \zeta b_{41} + \hat{\zeta}b_{42}\sqrt{\lambda} & 0 & \zeta b_{43} + \hat{\zeta}\sqrt{\lambda} & 0 & \zeta b_{44} + \hat{\zeta}b_{45}\sqrt{\lambda} \\ \zeta b_{51} + \hat{\zeta}b_{52}\sqrt{\lambda} & 0 & \zeta b_{53} + \hat{\zeta}b_{54}\sqrt{\lambda} & 0 & \zeta b_{55} + \hat{\zeta}\sqrt{\lambda} & 0 \\ 0 & \zeta b_{61} + \hat{\zeta}b_{62}\sqrt{\lambda} & 0 & \zeta b_{63} + \hat{\zeta}b_{64}\sqrt{\lambda} & 0 & \zeta b_{65} + \hat{\zeta}\sqrt{\lambda} \end{bmatrix}$$

$$b_{11}(\tau) = \frac{\pi^4[51 + \pi^2(1 + 6z(\tau))]}{3 + \pi^2(1 + 6z(\tau))}.$$

$$K = \begin{bmatrix} c_{11}\bar{N}_0 + c_{12} & c_{13}\lambda + c_{14} & c_{15}\bar{N}_0 + c_{16} & c_{17}\lambda + c_{18} & c_{19}\bar{N}_0 + c_{110} & c_{111}\lambda + c_{112} \\ c_{21}\lambda + c_{22} & c_{23}\bar{N}_0 + c_{24} & c_{25}\lambda + c_{26} & c_{27}\bar{N}_0 + c_{28} & c_{29}\lambda + c_{210} & c_{211}\bar{N}_0 + c_{212} \\ c_{31}\bar{N}_0 + c_{32} & c_{33}\lambda + c_{34} & c_{35}\bar{N}_0 + c_{36} & c_{37}\lambda + c_{38} & c_{39}\bar{N}_0 + c_{310} & c_{311}\lambda + c_{312} \\ c_{41}\lambda + c_{42} & c_{43}\bar{N}_0 + c_{44} & c_{45}\lambda + c_{46} & c_{47}\bar{N}_0 + c_{48} & c_{49}\lambda + c_{410} & c_{411}\bar{N}_0 + c_{412} \\ c_{51}\bar{N}_0 + c_{52} & c_{53}\lambda + c_{54} & c_{55}\bar{N}_0 + c_{56} & c_{57}\lambda + c_{58} & c_{59}\bar{N}_0 + c_{510} & c_{511}\lambda + c_{512} \\ c_{61}\lambda + c_{62} & c_{63}\bar{N}_0 + c_{64} & c_{65}\lambda + c_{66} & c_{67}\bar{N}_0 + c_{68} & c_{69}\lambda + c_{610} & c_{611}\bar{N}_0 + c_{612} \end{bmatrix}$$

$$D = \begin{bmatrix} d_{11} & 0 & d_{13} & 0 & d_{15} & 0 \\ 0 & d_{22} & 0 & d_{24} & 0 & d_{26} \\ d_{31} & 0 & d_{33} & 0 & d_{35} & 0 \\ 0 & d_{42} & 0 & d_{44} & 0 & d_{46} \\ d_{51} & 0 & d_{53} & 0 & d_{55} & 0 \\ 0 & d_{62} & 0 & d_{64} & 0 & d_{66} \end{bmatrix}, \quad d_{11}(\tau) = \frac{1}{60}[-15 + 10\pi^2(1 + 3z(\tau)) + \pi^4(1 + 10z(\tau) + 30z^2(\tau))]B_1$$

$$\{eq_i q_j^2\} = \left\{ \begin{aligned} & e_{11}q_1q_2^2 + e_{12}q_1q_3^2 + e_{13}q_1q_4^2 + e_{14}q_1q_5^2 + e_{15}q_1q_6^2 + e_{16}q_3q_1^2 + e_{17}q_3q_2^2 + e_{18}q_3q_4^2 + \\ & e_{21}q_2q_1^2 + e_{22}q_2q_3^2 + e_{23}q_2q_4^2 + e_{24}q_2q_5^2 + e_{25}q_2q_6^2 + e_{26}q_4q_1^2 + e_{27}q_4q_2^2 + e_{28}q_4q_3^2 + \\ & e_{31}q_1q_2^2 + e_{32}q_1q_3^2 + e_{33}q_1q_4^2 + e_{34}q_1q_5^2 + e_{35}q_1q_6^2 + e_{36}q_3q_1^2 + e_{37}q_3q_2^2 + e_{38}q_3q_4^2 + \\ & e_{41}q_2q_1^2 + e_{42}q_2q_3^2 + e_{43}q_2q_4^2 + e_{44}q_2q_5^2 + e_{45}q_2q_6^2 + e_{46}q_4q_1^2 + e_{47}q_4q_2^2 + e_{48}q_4q_3^2 + \\ & e_{51}q_1q_2^2 + e_{52}q_1q_3^2 + e_{53}q_1q_4^2 + e_{54}q_1q_5^2 + e_{55}q_1q_6^2 + e_{56}q_3q_1^2 + e_{57}q_3q_2^2 + e_{58}q_3q_4^2 + \\ & e_{61}q_2q_1^2 + e_{62}q_2q_3^2 + e_{63}q_2q_4^2 + e_{64}q_2q_5^2 + e_{65}q_2q_6^2 + e_{66}q_4q_1^2 + e_{67}q_4q_2^2 + e_{68}q_4q_3^2 + \\ & + e_{19}q_3q_5^2 + e_{110}q_3q_6^2 + e_{111}q_5q_1^2 + e_{112}q_5q_2^2 + e_{113}q_5q_3^2 + e_{114}q_5q_4^2 + e_{115}q_5q_6^2 \\ & + e_{29}q_4q_5^2 + e_{210}q_4q_6^2 + e_{211}q_6q_1^2 + e_{212}q_6q_2^2 + e_{213}q_6q_3^2 + e_{214}q_6q_4^2 + e_{215}q_6q_5^2 \\ & + e_{39}q_3q_5^2 + e_{310}q_3q_6^2 + e_{311}q_5q_1^2 + e_{312}q_5q_2^2 + e_{313}q_5q_3^2 + e_{314}q_5q_4^2 + e_{315}q_5q_6^2 \\ & + e_{49}q_4q_5^2 + e_{410}q_4q_6^2 + e_{411}q_6q_1^2 + e_{412}q_6q_2^2 + e_{413}q_6q_3^2 + e_{414}q_6q_4^2 + e_{415}q_6q_5^2 \\ & + e_{59}q_3q_5^2 + e_{510}q_3q_6^2 + e_{511}q_5q_1^2 + e_{512}q_5q_2^2 + e_{513}q_5q_3^2 + e_{514}q_5q_4^2 + e_{515}q_5q_6^2 \\ & + e_{69}q_4q_5^2 + e_{610}q_4q_6^2 + e_{611}q_6q_1^2 + e_{612}q_6q_2^2 + e_{613}q_6q_3^2 + e_{614}q_6q_4^2 + e_{615}q_6q_5^2 \end{aligned} \right\},$$

$$e_{11}(\tau) = \frac{1}{240}[-15 + 40\pi^2(1 + 3z(\tau)) + 16\pi^4(1 + 10z(\tau) + 30z^2(\tau))]B_1$$

$$\{f_{q_i q_j q_k}\} = \left\{ \begin{aligned} & f_{11}q_1q_2q_4 + f_{12}q_1q_2q_6 + f_{13}q_1q_3q_5 + f_{14}q_1q_4q_6 + f_{15}q_2q_3q_4 + \\ & f_{21}q_1q_2q_3 + f_{22}q_1q_3q_4 + f_{23}q_1q_2q_5 + f_{24}q_2q_3q_5 + f_{25}q_1q_4q_5 + \\ & f_{31}q_1q_2q_4 + f_{32}q_1q_2q_6 + f_{33}q_1q_3q_5 + f_{34}q_1q_4q_6 + f_{35}q_2q_3q_4 + \\ & f_{41}q_1q_2q_3 + f_{42}q_1q_3q_4 + f_{43}q_1q_2q_5 + f_{44}q_2q_3q_5 + f_{45}q_1q_4q_5 + \\ & f_{51}q_1q_2q_4 + f_{52}q_1q_2q_6 + f_{53}q_1q_3q_5 + f_{54}q_1q_4q_6 + f_{55}q_2q_3q_4 + \\ & f_{61}q_1q_2q_3 + f_{62}q_1q_3q_4 + f_{63}q_1q_2q_5 + f_{64}q_2q_3q_5 + f_{65}q_1q_4q_5 + \\ & + f_{16}q_2q_3q_6 + f_{17}q_2q_4q_5 + f_{18}q_2q_5q_6 + f_{19}q_3q_4q_6 + f_{110}q_4q_5q_6 \\ & + f_{26}q_2q_4q_6 + f_{27}q_3q_4q_5 + f_{28}q_1q_3q_6 + f_{29}q_3q_5q_6 + f_{210}q_1q_5q_6 \\ & + f_{36}q_2q_3q_6 + f_{37}q_2q_4q_5 + f_{38}q_2q_5q_6 + f_{39}q_3q_4q_6 + f_{310}q_4q_5q_6 \\ & + f_{46}q_2q_4q_6 + f_{47}q_3q_4q_5 + f_{48}q_1q_3q_6 + f_{49}q_3q_5q_6 + f_{410}q_1q_5q_6 \\ & + f_{56}q_2q_3q_6 + f_{57}q_2q_4q_5 + f_{58}q_2q_5q_6 + f_{59}q_3q_4q_6 + f_{510}q_4q_5q_6 \\ & + f_{66}q_2q_4q_6 + f_{67}q_3q_4q_5 + f_{68}q_1q_3q_6 + f_{69}q_3q_5q_6 + f_{610}q_1q_5q_6 \end{aligned} \right\},$$

$$f_{11}(\tau) = -\frac{16}{27}(22 + 15\pi^2 z(\tau))B_1,$$

$$\{P(\tau)\} = \begin{Bmatrix} 2\bar{p}_0/\pi \\ 0 \\ 3\bar{p}_0/2\pi \\ 0 \\ 5\bar{p}_0/3\pi \\ 0 \end{Bmatrix}$$

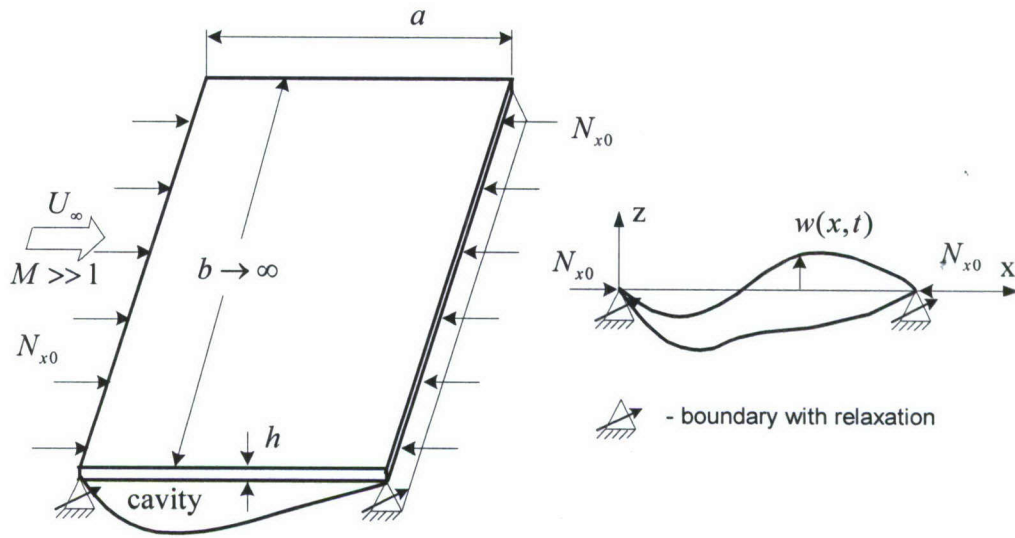
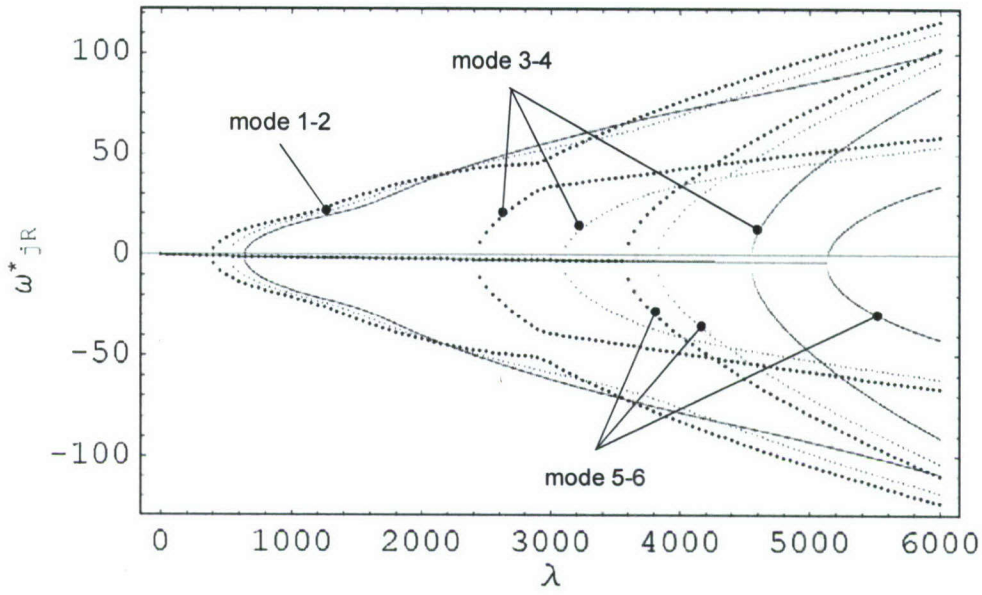
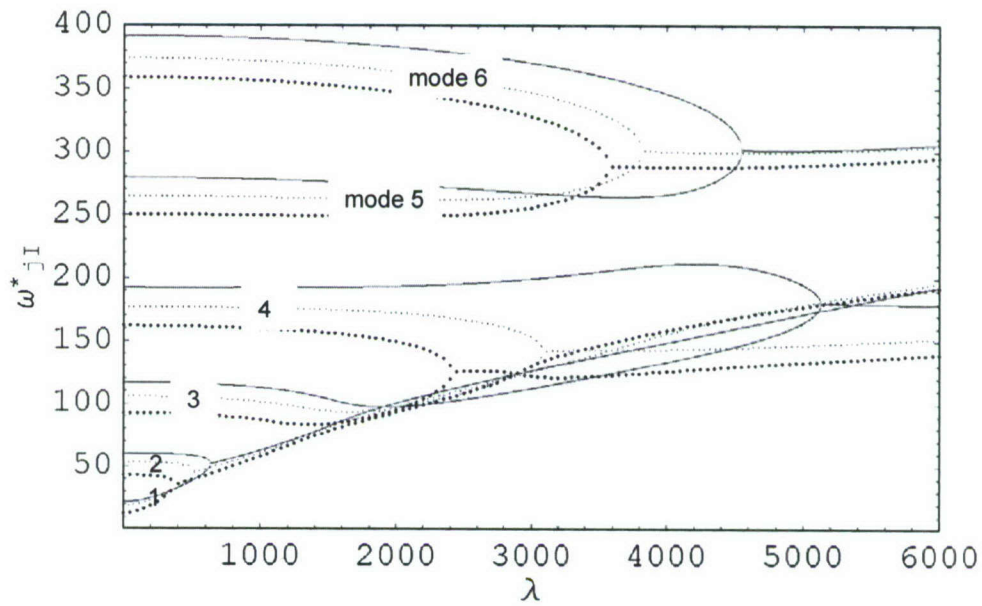


Figure 1. Schematic diagram of a two-dimensional panel with boundary conditions relaxation



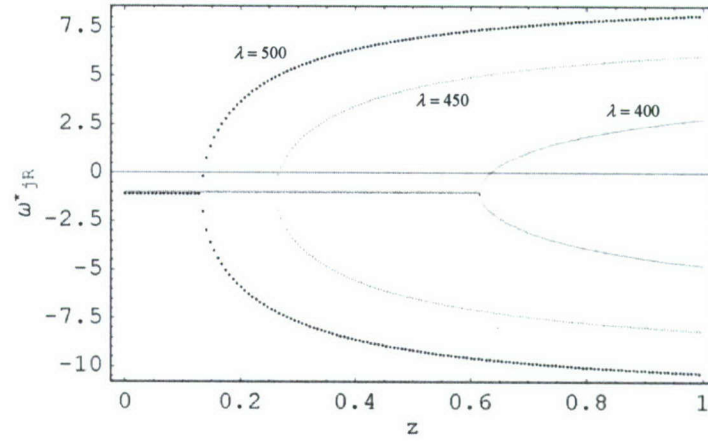
(a)



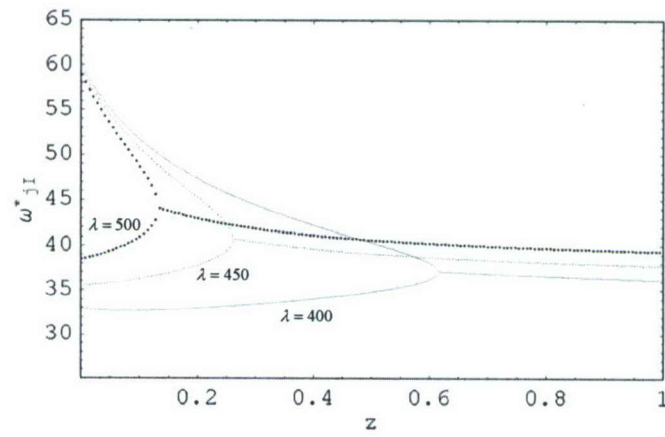
(b)

Figure 2. Dependence of real and imaginary parts of the panel natural frequency on dynamic pressure for $\zeta = 0$; $\hat{\zeta} = 0.1$; $\bar{N}_0 = 0$ (a) real parts, (b) imaginary parts.

— $z=0.001$; $z=0.1$; $z=1$;



(a)



(b)

Figure 3. Dependence of real and imaginary parts of the first and second natural frequencies on relaxation parameter z for $\zeta = 0; \hat{\zeta} = 0.1; \bar{N}_0 = 0$ (a) real parts, (b) imaginary parts.

— $\lambda = 400$, ... $\lambda = 450$, ... $\lambda = 500$

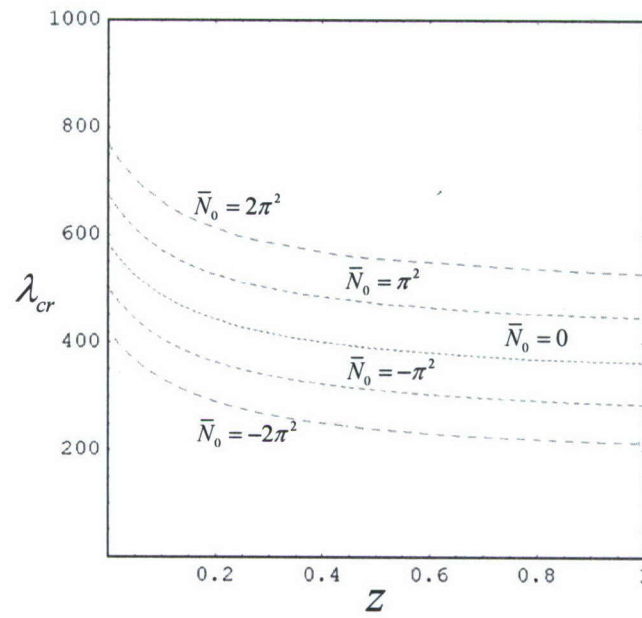


Figure 4. Boundaries of panel flutter on the plane for different values of in-plane load and for $\hat{\zeta} = 0.1$, $\zeta = 0.0001$.

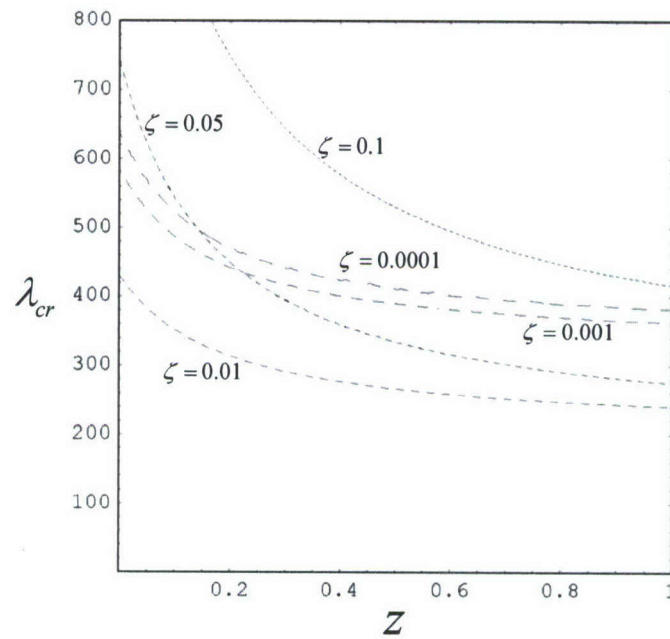


Figure 5. Boundaries of panel flutter for different values of damping factor showing the reversal effect of damping for $\hat{\zeta} = 0.1$, $\bar{N}_0 = 0$.

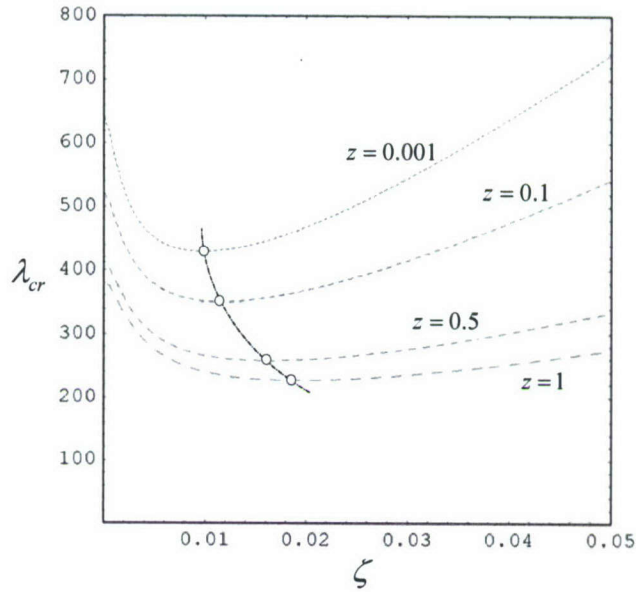


Figure 6. Boundaries of panel flutter on the $\lambda - \zeta$ plane for different values of relaxation parameter, z , and for $\bar{N}_0 = 0.0$; $\hat{\zeta} = 0.1$. Dashed curve indicates the critical damping ratio that separate between stabilizing and destabilizing damping effects.

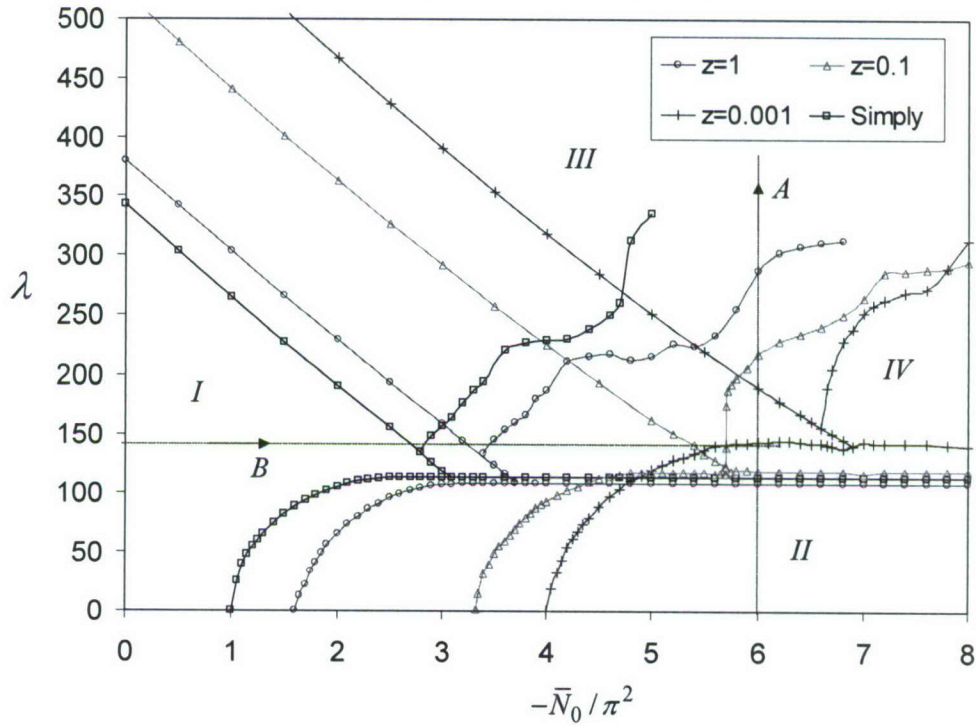


Figure 7. Bifurcation diagram showing the regions of different panel regimes for damping parameter $\zeta = 0.0001$ and different values of relaxation parameter.

(I) statically stable, (II) static buckling (divergence), (III) LCO, and (IV) multi-period oscillations and chaos.

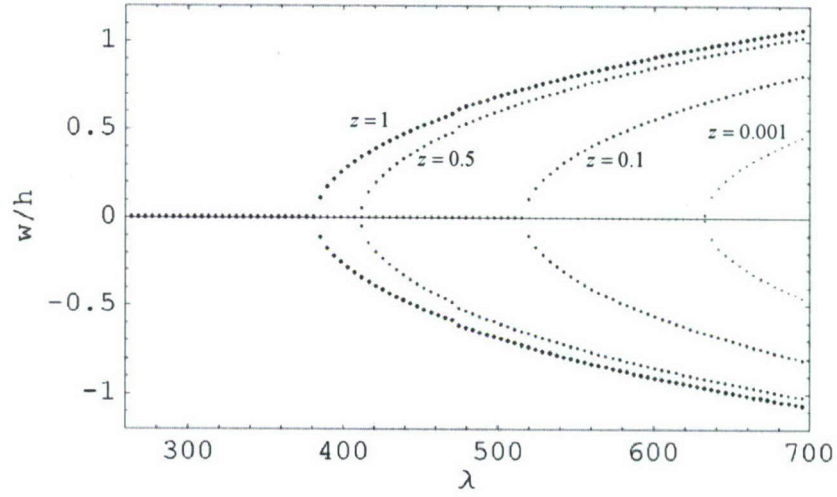


Figure 8. Bifurcation diagram for different values of relaxation parameter for $\zeta = 0.0001$, $\hat{\zeta} = 0.1$, $\bar{p}_0 = 0$, and $\bar{N}_0 = 0$.

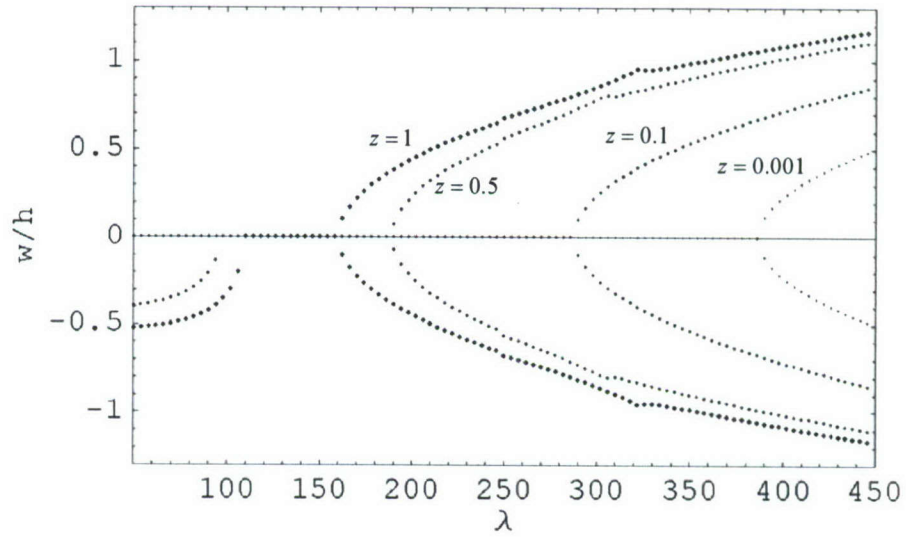


Figure 9. Bifurcation diagram for different values of relaxation parameter for $\zeta = 0.0001$, $\hat{\zeta} = 0.1$, $\bar{p}_0 = 0$, and $\bar{N}_0 = -3\pi^2$.

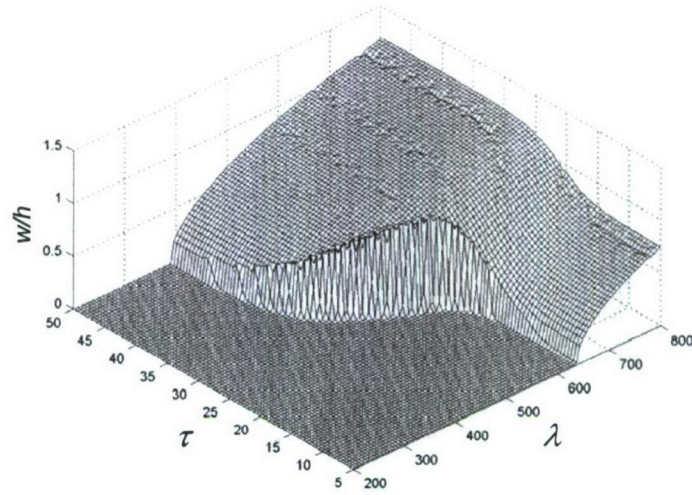
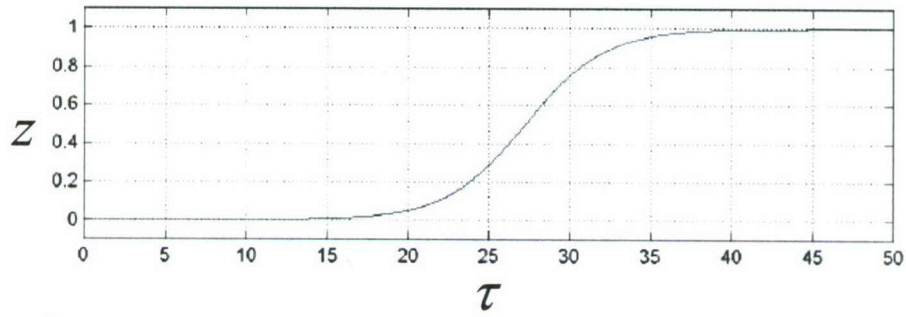
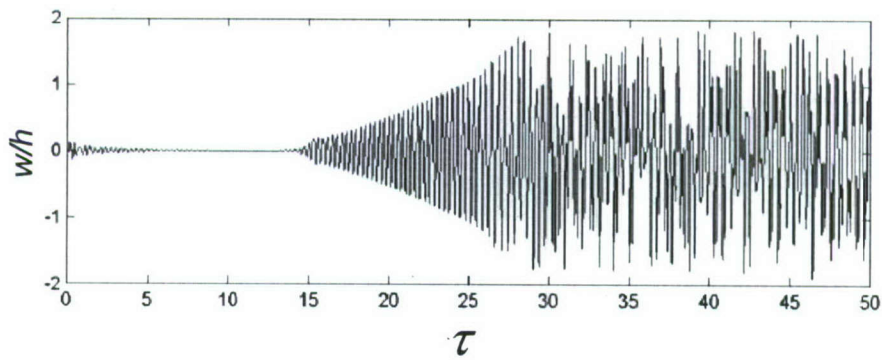


Figure 10. Three-dimensional plots of amplitudes time evolutions and their dependence on dynamic pressure for $\zeta = 0.0001$, $\hat{\zeta} = 0.1$, $\bar{p}_0 = 0.0$, and $\bar{N}_0 = 0$.



(a)



(b)

Figure 11. (a) Relaxation of boundary conditions and (b) time history record of panel deflection at $x/a = 0.75$, for $\zeta = 0.0001$, $\bar{p}_0 = 0$, $\hat{\zeta} = 0.1$, $\bar{N}_0 = -6\pi^2$, and $\lambda = 200$

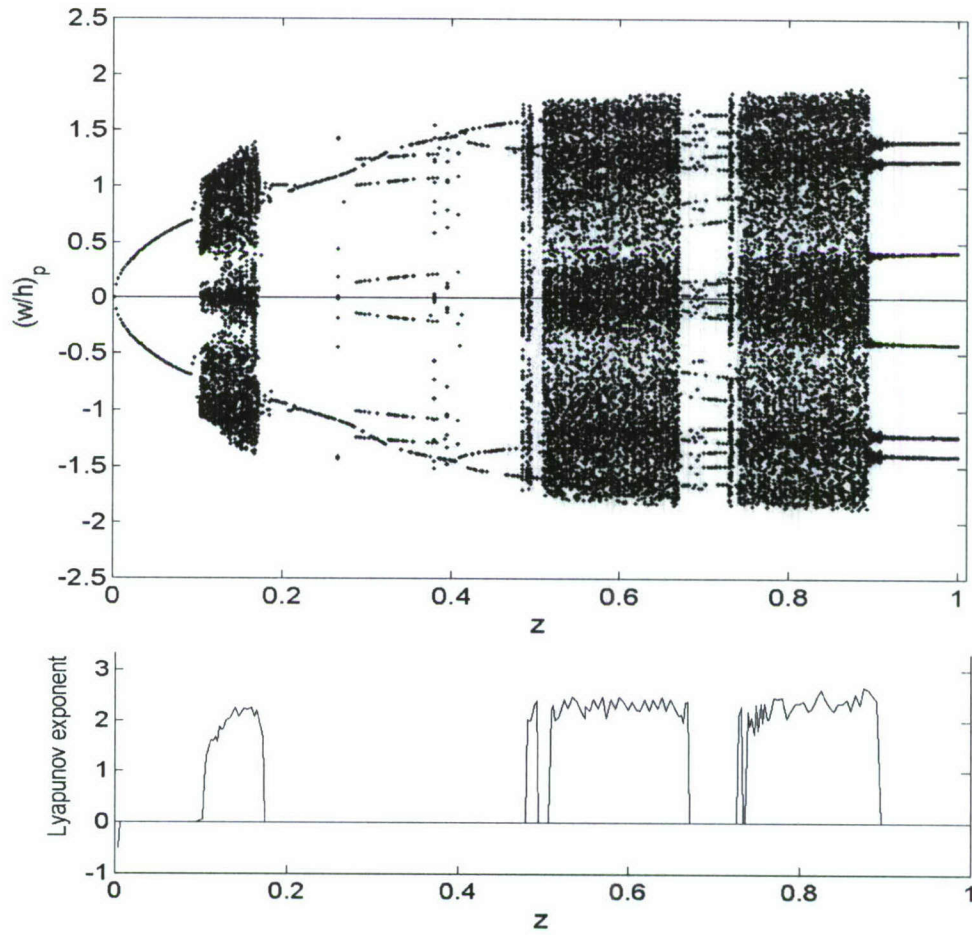


Figure 12. Bifurcation diagram and the corresponding largest Lyapunov exponent

for $\bar{N}_0 = -5.8\pi^2$, $\zeta = 0.0001$, $\bar{p}_0 = 0$, $\hat{\zeta} = 0.1$, and $\lambda = 200$

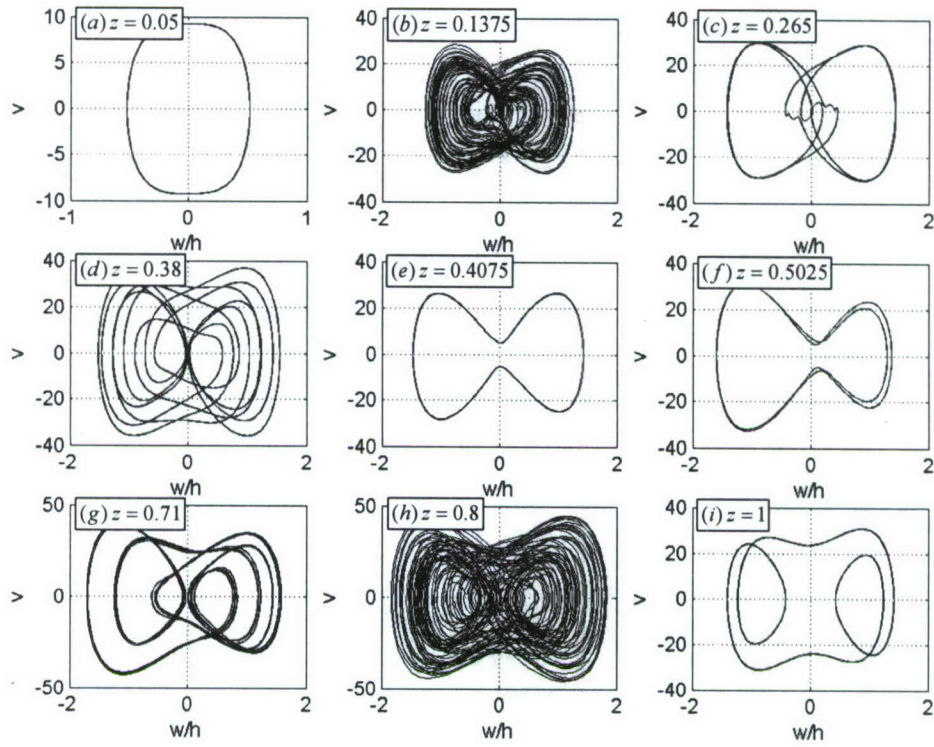


Figure 13. Phase plots for $\zeta = 0.0001$, $\bar{p}_0 = 0$, $\hat{\zeta} = 0.1$, $\bar{N}_0 = -5.8\pi^2$, and $\lambda = 200$ corresponding to Figure 12 for (a) $z = 0.05$; (b) $z = 0.1375$; (c) $z = 0.265$; (d) $z = 0.38$; (e) $z = 0.4075$; (f) $z = 0.5025$; (g) $z = 0.71$; (h) $z = 0.8$; (e) $z = 1$.

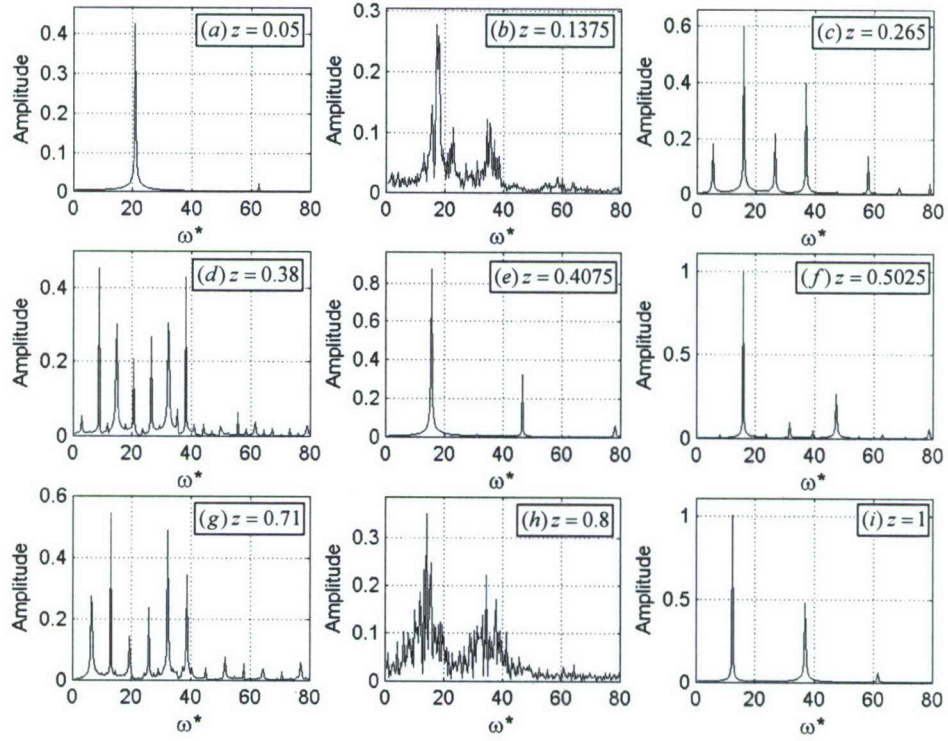


Figure 14. FFT plots for $\zeta = 0.0001$, $\bar{p}_0 = 0$, $\hat{\zeta} = 0.1$, $\bar{N}_0 = -5.8\pi^2$, and $\lambda = 200$ corresponding to Figure 12 for (a) $z = 0.05$; (b) $z = 0.1375$; (c) $z = 0.265$; (d) $z = 0.38$; (e) $z = 0.4075$; (f) $z = 0.5025$; (g) $z = 0.71$; (h) $z = 0.8$; (e) $z = 1$.

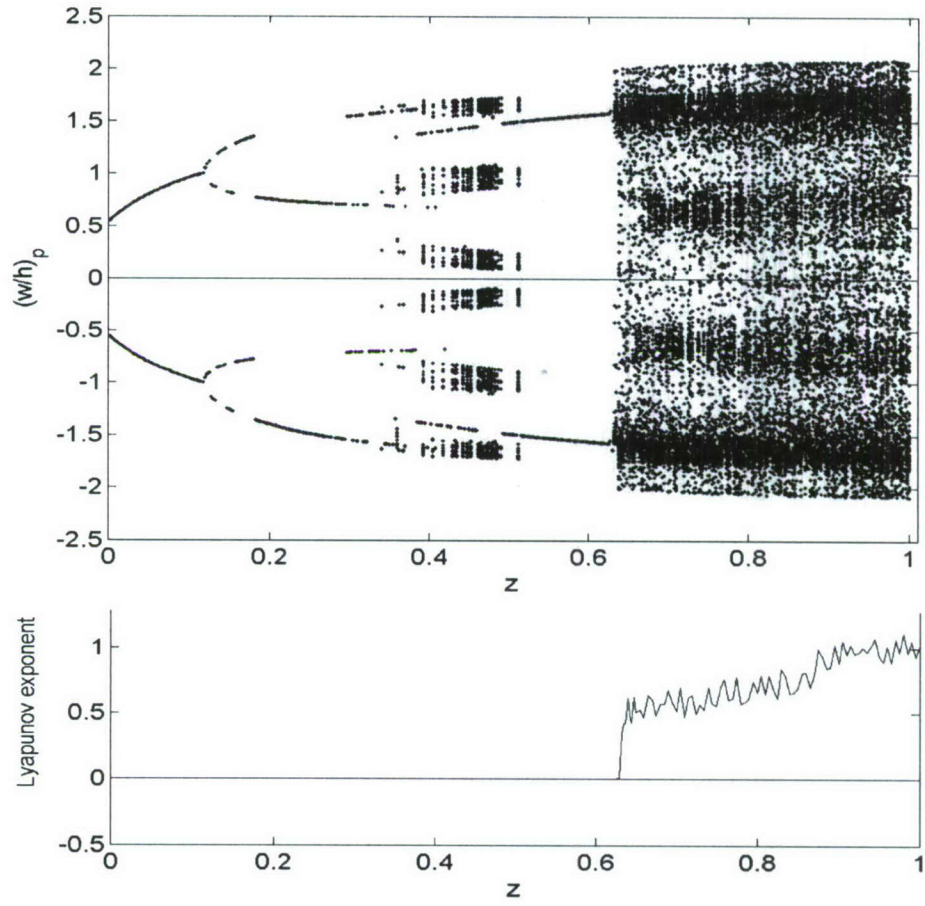


Figure 15. Bifurcation diagram of the first return and largest Lyapunov exponent for $\zeta = 0.0001$,

$$\bar{p}_0 = 0, \hat{\zeta} = 0.1, \bar{N}_0 = -6\pi^2, \text{ and } \lambda = 250.$$

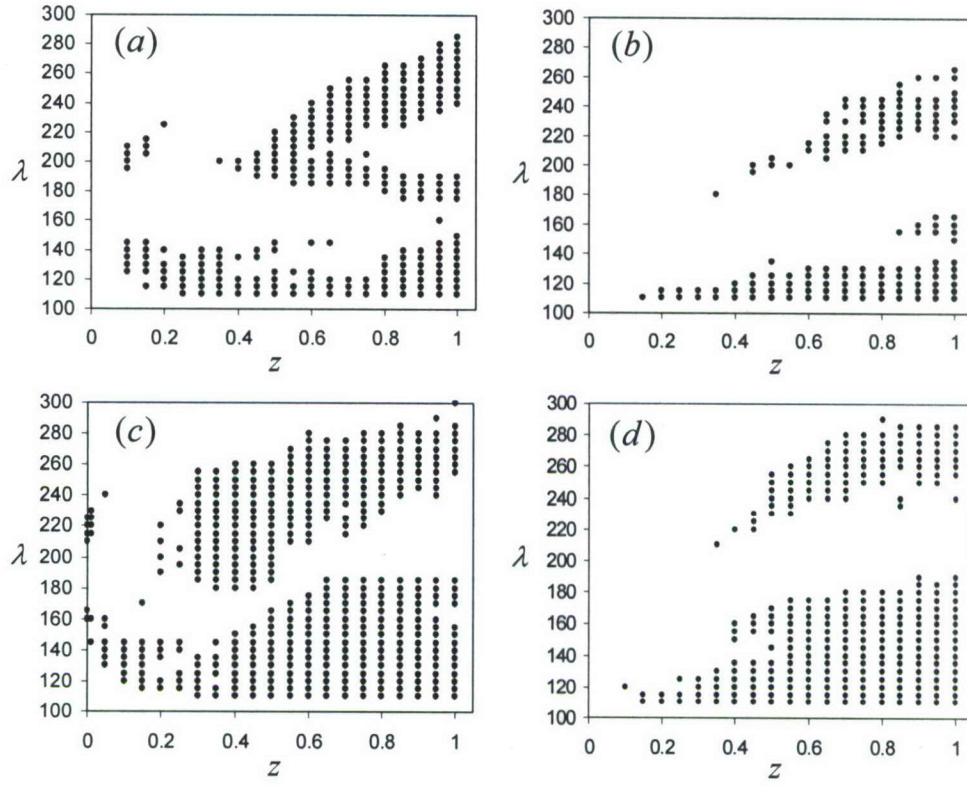


Figure 16. Chaos boundaries for $z=1$, $\hat{\zeta}=0.1$, $\bar{p}_0=0$

(a) $\bar{N}_0 = -6\pi^2$, $\zeta = 0.0001$

(b) $\bar{N}_0 = -6\pi^2$, $\zeta = 0.001$

(c) $\bar{N}_0 = -6.8\pi^2$, $\zeta = 0.0001$

(d) $\bar{N}_0 = -6.8\pi^2$, $\zeta = 0.001$

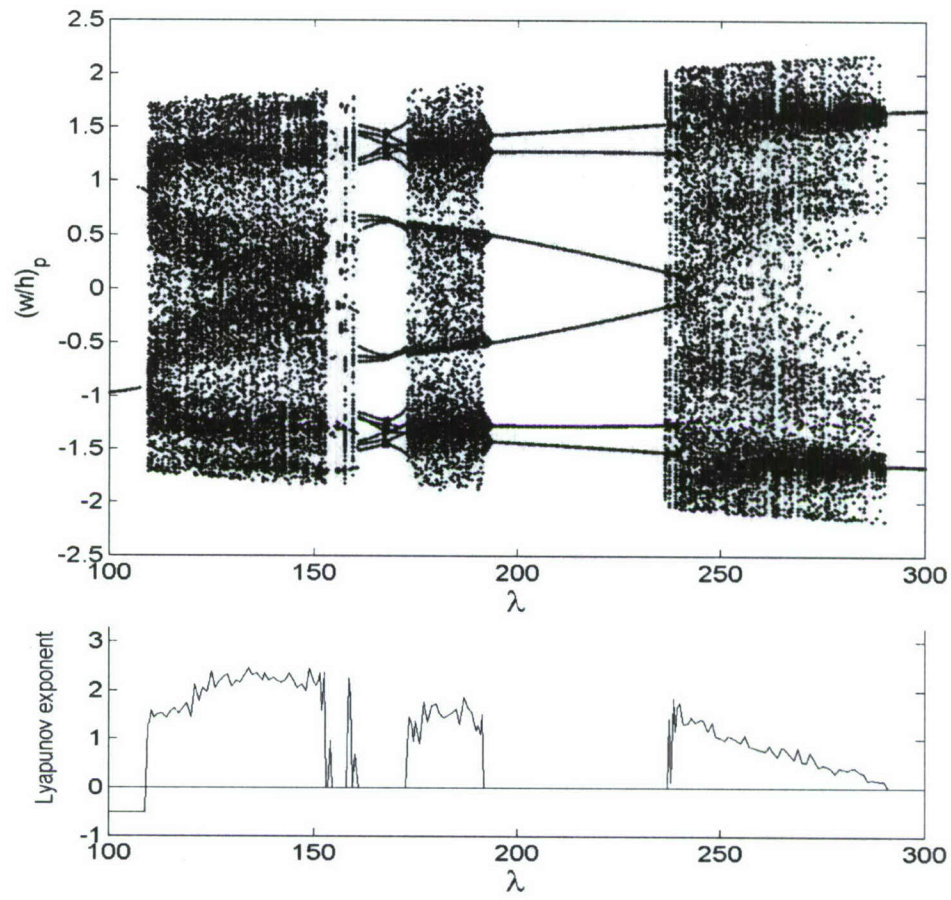


Figure 17. Bifurcation diagram of the first return and largest Lyapunov exponent along the path line A of Figure 7, for $\zeta = 0.0001$, $\bar{p}_0 = 0$, $\hat{\zeta} = 0.1$, $\bar{N}_0 = -6\pi^2$, and $z = 1$

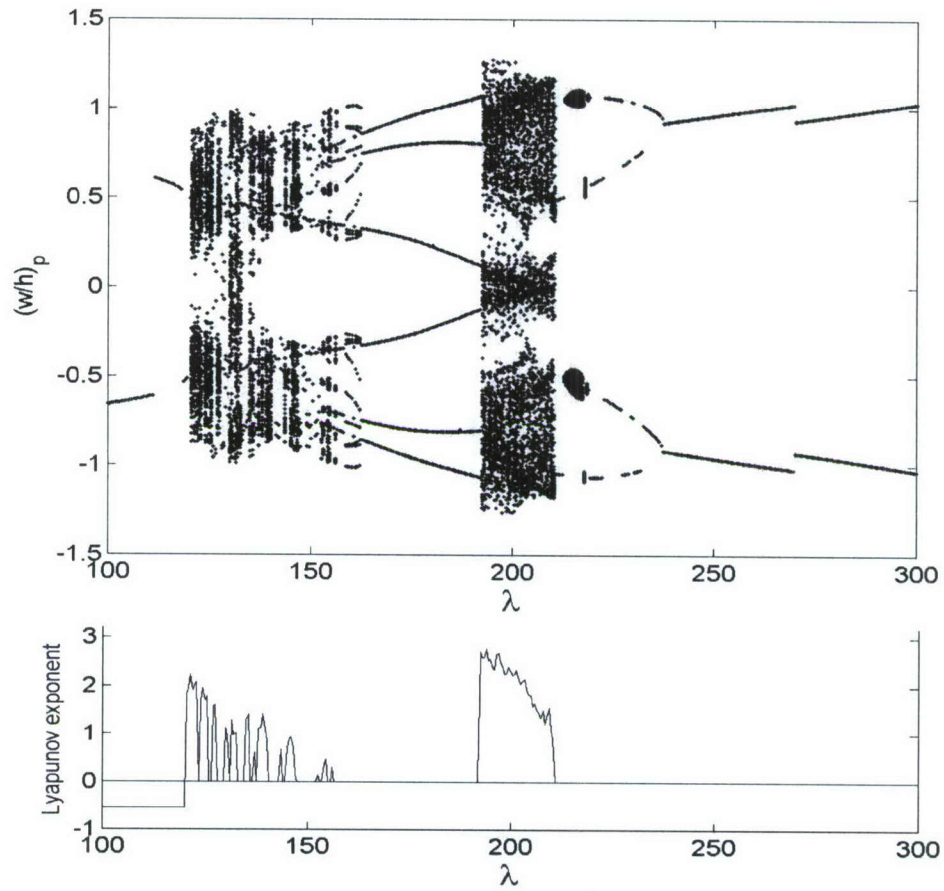


Figure 18. Bifurcation diagram of the first return and largest Lyapunov exponent along the path line A of Figure 7 for $\zeta = 0.0001$, $\bar{p}_0 = 0$, $\hat{\zeta} = 0.1$, $\bar{N}_0 = -6\pi^2$, and $z = 0.1$

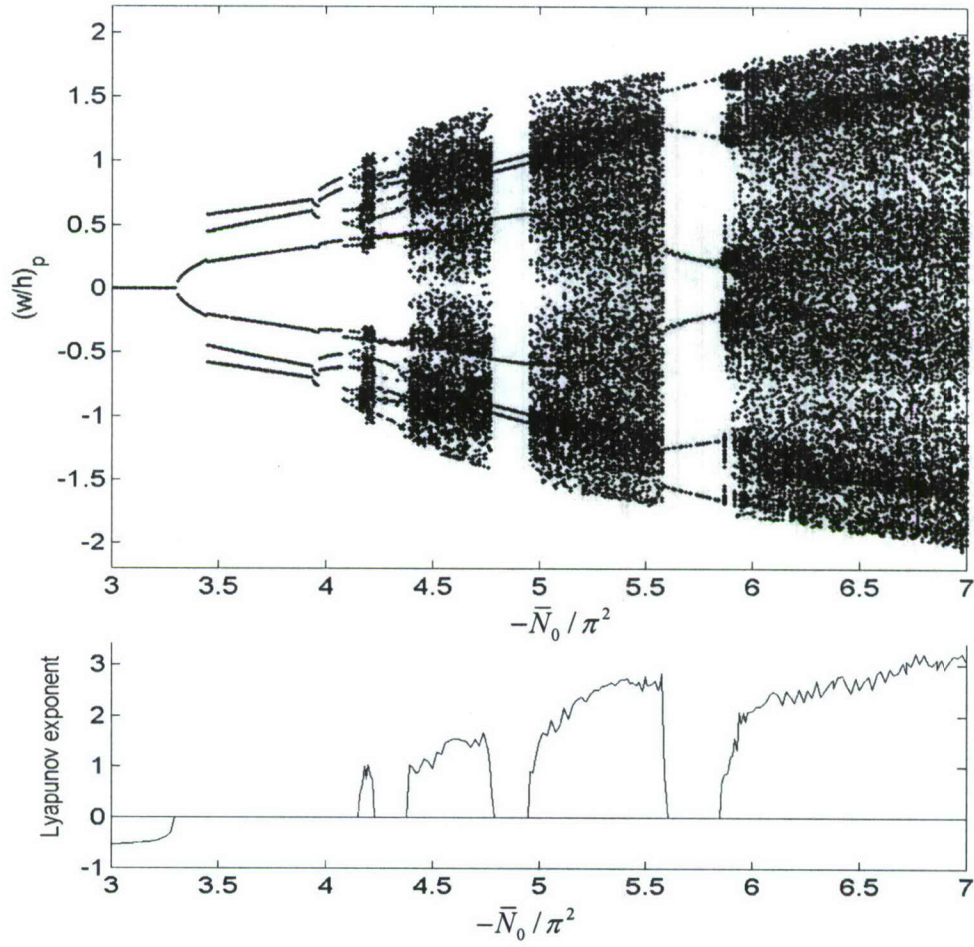


Figure 19. Bifurcation diagram of the first return and Lyapunov exponent along the path line B of Figure 7 for $\zeta = 0.0001$, $\bar{p}_0 = 0$, $\hat{\zeta} = 0.1$, $\lambda = 140$, and $z = 1$

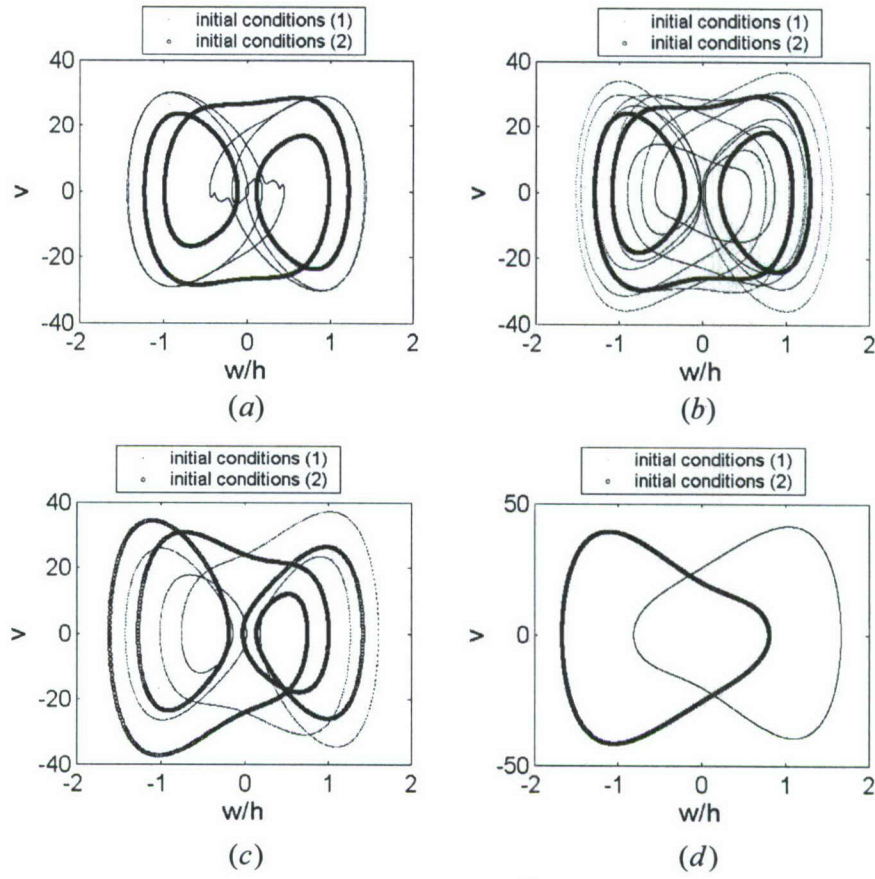


Figure 20. Phase diagrams for $\zeta = 0.0001$, $\bar{p}_0 = 0$, $\hat{\zeta} = 0.1$, for two sets of initial conditions:

(1) $q_1(\tau = 0) = 0.1$, $q_i(\tau = 0) = 0, i = 2, \dots, 6$. (2) $q_1(\tau = 0) = 1$, $q_i(\tau = 0) = 0, i = 2, \dots, 6$.

(a) $\lambda = 200$, $\bar{N}_0 = -5.8\pi^2$, $z = 0.265$; (b) $\lambda = 200$, $\bar{N}_0 = -5.8\pi^2$, $z = 0.38$; (c) $\lambda = 179$, $\bar{N}_0 = -6\pi^2$, $z = 0.5$; (d) $\lambda = 270$, $\bar{N}_0 = -6\pi^2$, $z = 0.5$.

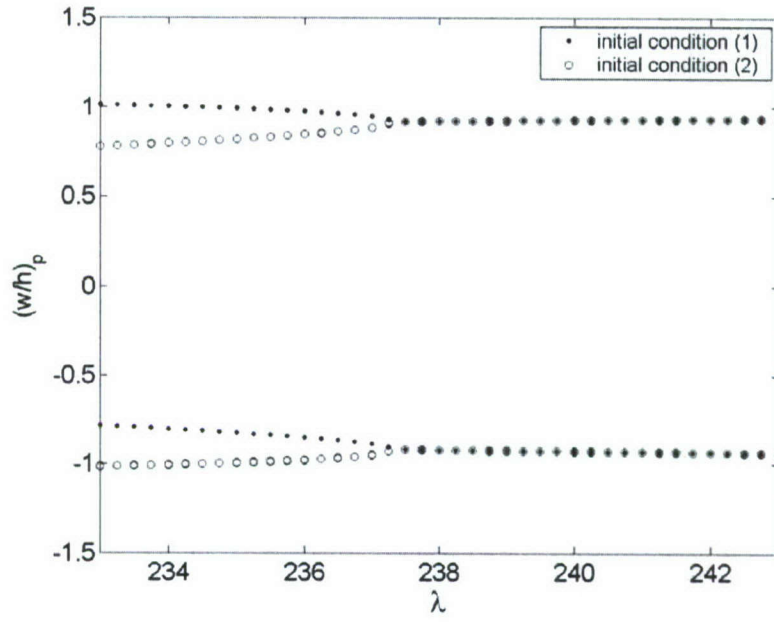
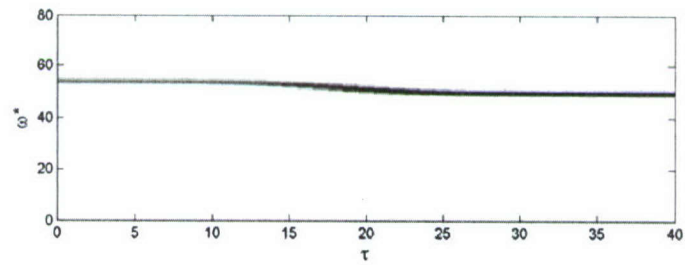
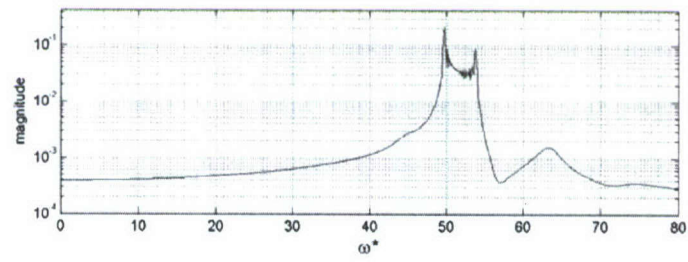
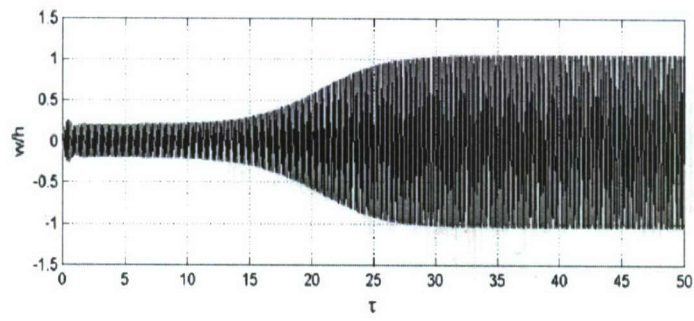
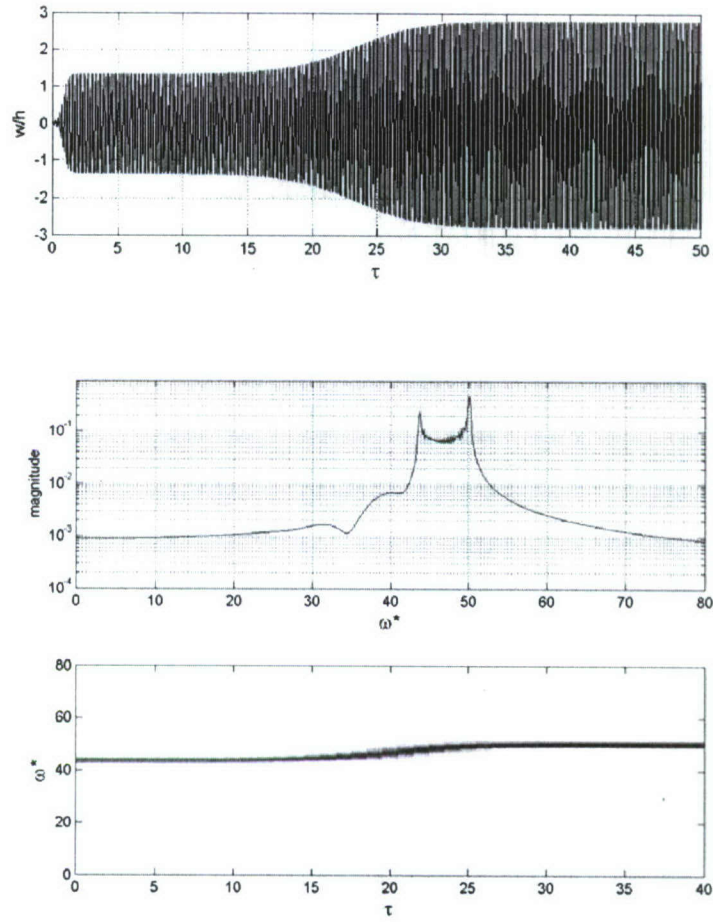


Figure 21. Section of bifurcation diagram of the first return for $\zeta = 0.0001$, $\bar{p}_0 = 0$, $\hat{\zeta} = 0.1$, $\bar{N}_0 = -6\pi^2$, and $z = 0.1$ for initial conditions (1) $q_1(\tau = 0) = 0.1$, $q_i(\tau = 0) = 0, i = 2, \dots, 6$, and initial conditions (2) $q_1(\tau = 0) = 1$, $q_i(\tau = 0) = 0, i = 2, \dots, 6$



(a) $\lambda = 700, \zeta = 0.0001$



(b) $\lambda = 700, \zeta = 0.02$.

Figure 22. FFT plots and spectrograms for $\bar{p}_0 = 0, \bar{N}_0 = 0, \hat{\zeta} = 0.1$

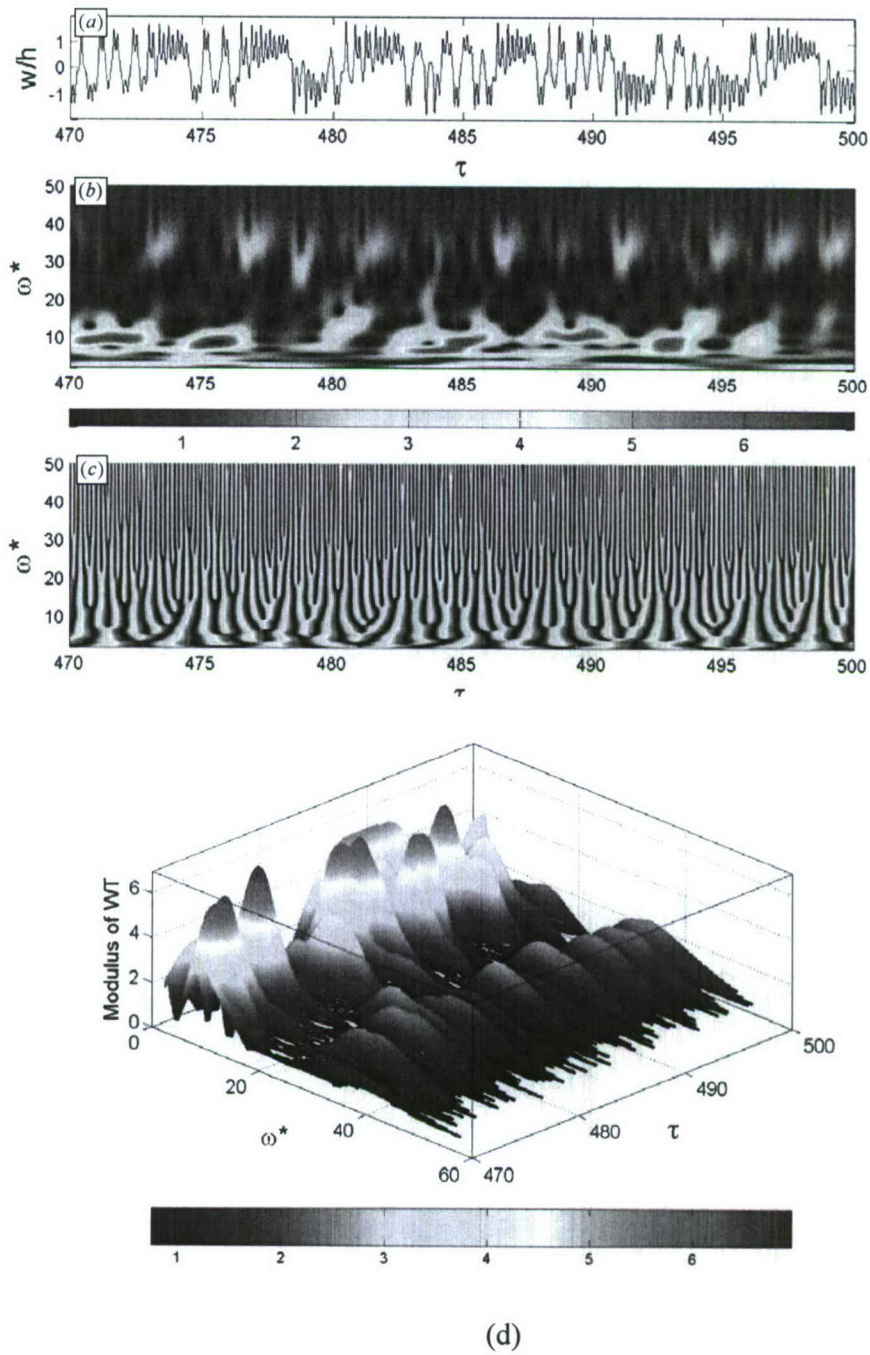
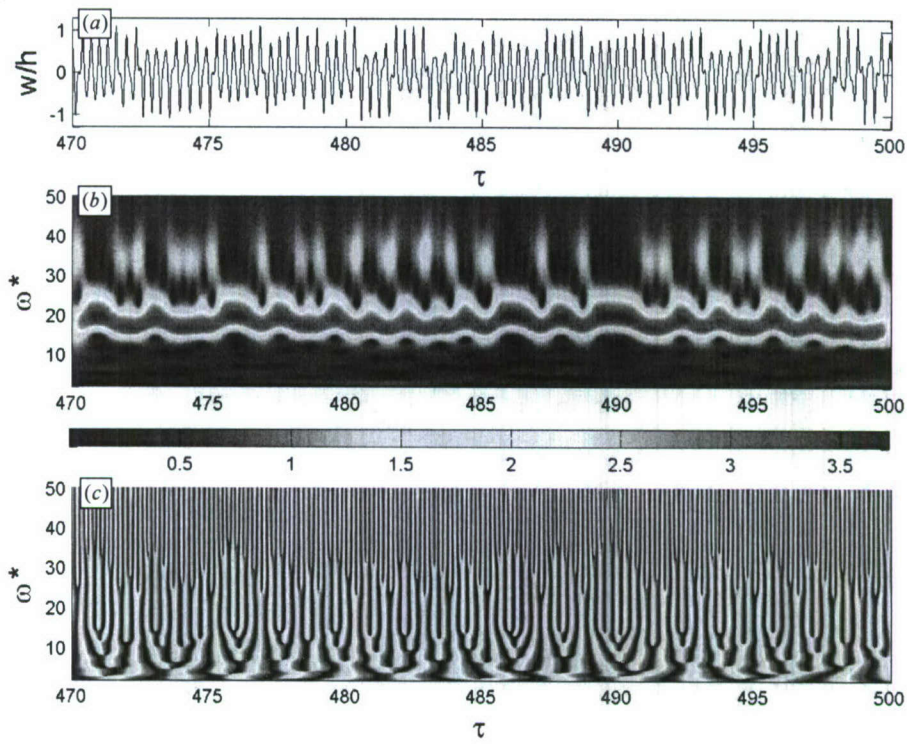
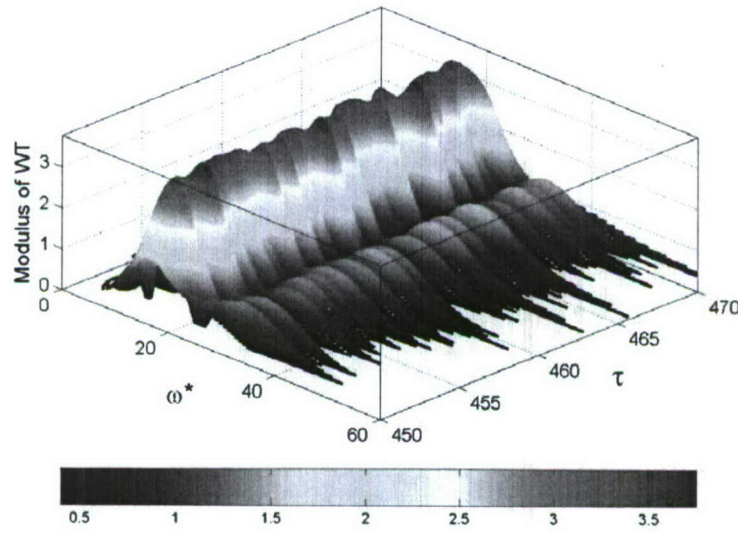


Figure 23. (a) Time history, (b) modulus of WT, (c) phase of WT, (d) three dimensional plot of modulus of WT for $\zeta = 0.0001$, $\bar{p}_0 = 0$, $\hat{\zeta} = 0.1$, $\lambda = 132$, $\bar{N}_0 = -6\pi^2$, and $z = 1$



(a)



(b)

Figure 24. (a) Time history, (b) modulus of WT, (c) phase of WT, (d) three dimensional plot of modulus of WT for $\zeta = 0.0001$, $\bar{p}_0 = 0$, $\hat{\zeta} = 0.1$, $\lambda = 203.5$, $\bar{N}_0 = -6\pi^2$, and $z = 0.1$

CHAPTER 3

FLUTTER SUPPRESSION OF A PLATE-LIKE WING VIA PARAMETRIC EXCITATION

Summary of Results

The possibility of suppressing wing flutter via parametric excitation along the plane of highest rigidity in the neighborhood of combination resonance is explored. The nonlinear equations of motion in the presence of incompressible fluid flow are derived using Hamilton's principle and Theodorsen's theory for modeling aerodynamic forces. In the presence of air flow, the bending and torsion modes possess nearly the same frequency. Under parametric excitation and in the absence of air flow, each mode oscillates at its own natural frequency. In the neighborhood of combination resonance, the nonlinear response is determined using the multiple scales method at the critical flutter speed and at slightly higher airflow speed. The domains of attraction and bifurcation diagrams are obtained to reveal the conditions under which the parametric excitation can provide stabilizing effect. The basins of attraction for different values of excitation amplitude reveal:

- Stabilizing effect that takes place above a critical excitation level. Below that level, the response experiences limit cycle oscillations, cascade of period doubling, and chaos.
- For flow speed slightly higher than the critical flutter speed, the response experiences a train of spikes, known as "*firing*," a term that is borrowed from neuroscience, followed by "*refractory*" or *recovery* effect, up to an excitation level above which the wing is stabilized.
- The results of the multiple scales method are verified using numerical simulation of the original nonlinear differential equations.

State-of-the Art

Aeroelastic structures flutter as a result of interaction between structural and aerodynamic forces at a critical airflow speed, which is referred to as the flutter speed. The critical speed can be determined based on the linear theory of small oscillations [1-4]. However, as the amplitude of oscillation increases the structural forces exhibit nonlinear characteristics that bring the response into a bounded limit cycle oscillation (LCO) in addition to other nonlinear phenomena. Structural nonlinearities can be geometric that can affect the whole structure [5, 6] or concentrated [7]. Generally, flutter of aeroelastic structures is undesirable and the main goal of aeroelasticians to suppress and alleviate its effect. The next two subsections review the influence of concentrated and geometric nonlinearities on the flutter of lifting structures exposed to subsonic airflow. The modeling of aerodynamic loading has been an important factor in developing the equations of motion and will be outlined in the third subsection. Related to the control and suppression of flutter is the stabilizing effect imparted via parametric excitation. This interesting phenomenon is assessed in Section 2.

1.1 EFFECT OF CONCENTRATED NONLINEARITY

Concentrated nonlinearity acts locally in control mechanisms or connecting parts between wing and external stores. This nonlinearity results from backlash in linkage elements of the control

system, dry friction in control cable and push rod ducts, kinematic limitation of the control surface deflection, and application of spring tab systems provided for relieving pilot operation. Breitbach [8] determined the flutter boundaries for three different configurations distinguished by different types of nonlinearities in the rudder and aileron control system of a sailplane. The hysteretic damping was found to result in a considerable stabilizing effect and increase of flutter speed. Similar effects of nonlinearities due to friction and backlash on the dynamic behavior of aircraft were reported by De Ferrari, et al., [9]. The effects of control system nonlinearities, such as actuator force or deflection limits, on the performance of an active flutter suppression system were examined by Peloubet, et al., [10] and others [11, 12]. Reed, et al., [11] showed that a nonlinear system which is stable with respect to small disturbances may be unstable with respect to large ones. Another important feature was that a store mounted on a pylon with low pitch stiffness can provide a substantial increase in flutter speed and reduce the dependency of flutter on the mass and inertia of stores relative to that of stiff-mounted stores. A detailed review of structural and aerodynamic nonlinearities with more emphasis on concentrated structural nonlinearities is given by Lee, et al., [13].

Free-play nonlinearity effects have been the subject several studies [14-18]. For example, Laurenson and Trn [14] investigated the flutter of a missile with control surfaces having free-play nonlinearity. At a particular flight speed, the amplitude of oscillation, caused by external excitation, starts to build up. Due to the presence of free-play nonlinearity in combination with increasing amplitude of oscillation, the effective stiffness of the system increases and the motion becomes stable at some limited amplitude. Kim and Lee [16] found that responses involving LCO and chaotic motion are highly influenced by the pitch-to-plunge frequency ratio in an airfoil with free-play nonlinearity. Experimental studies [17] of a wing model with free-play nonlinearity in pitch showed the appearance of double LCO. Alighanbary [18] studied three-degree-of-freedom airfoil-aileron dynamics with free-play nonlinearity in the aileron hinge moment. Bifurcation analysis indicated various LCO solutions for velocities well below the linear flutter boundary. Depending on the initial conditions and air speed, quasi-periodic and chaotic oscillations were reported for the aileron motion. In a series of papers, Bae and Lee [19] and Bae, et al., [20-22] considered the influence of structural nonlinearities, represented by free-play and bilinear, on various types of LCO and periodic motions. The subsonic unsteady aerodynamic forces were modeled using the doublet-hybrid method originally proposed by Ueda and Dowell [23]. Zhao and Hu [24] considered similar structural nonlinearities and used unsteady vortex lattice model to predict the LCO of an airfoil section.

1.2 EFFECT OF GEOMETRIC NONLINEARITY

The analysis of two-dimensional airfoil with cubic stiffness nonlinearities was conducted in references [25-29]. Lee, et al., [25] found that the flutter boundary was dependent on the initial conditions for a soft spring, while for a hard spring flutter was independent of initial conditions, and both linear and nonlinear flutter speeds were identical. Further, LCO was observed for velocities greater than the flutter speed. A jump phenomenon in the pitch amplitude was numerically detected by Lee, et al., [26], and its location was found to depend on the given initial conditions. A frequency relation was derived by Liu, et al., [27] who observed that the frequency and amplitude of limit cycle oscillations do not depend on the choice of initial conditions. A secondary bifurcation after the primary Hopf bifurcation was detected by Liu and Dowell [28]. Furthermore, starting from different initial conditions, the motion may jump from one limit cycle to another for different values of fluid flow speeds. A chaotic region was found by Zhao and

Young [29] for certain elastic axis positions, and the chaotic motion appeared only at air flow speed higher than the linear divergent speed.

Price, et al., [30] studied the response of a two-dimensional airfoil with bilinear and cubic stiffness nonlinearities. LCO with period one was obtained at velocities well below the flutter boundary. In some cases, where the airfoil was subjected to small pre-loads, the motion is chaotic for both bilinear and cubic nonlinearities. This was confirmed for cubic nonlinearity using Lyapunov exponents. Sing and Brenner [31] observed asymmetric LCO for certain values of flow speed and elastic axis location.

A singular perturbation technique based on normal-form method was used to analyze the stability of limit cycles of wing-flap flutter [32-34]. For example, Dessi and Mastroddi [32] analyzed limit-cycle stability reversal via singular perturbation and wing-flap flutter. A three-degree-of-freedom aeroelastic typical section with a trailing-edge control surface was modeled by including nonlinear springs in torsional stiffness and hinge elastic moment. The numerical analysis revealed the presence of stable and unstable LCOs, along with stability reversal in the neighborhood of Hopf bifurcation. Collier and Chamara [33] investigated the sub-critical and supercritical nature of the flutter Hopf bifurcation of a two-degree-of-freedom system with nonlinear restoring forces. Under certain conditions, the instability gave rise to stable LCOs while for other conditions unstable periodic orbits emerged.

Nonlinear modal interaction of aeroelastic structures can result in the occurrence of internal resonance [35]. As the free stream speed increases the nonlinear solution reveals a LCO close to the initial conditions. For the flow speed at which the aeroelastic frequencies are in 3:1 internal resonance, the root-mean-square amplitude of plunge degree-of-freedom was found to increase. Near 1:1 internal resonance, the response grows without limit. It was also found that for an aeroelastic system with cubic nonlinearity, large response amplitudes were predicted as the system frequencies pass through a 3:1 internal resonance.

Marzocca, et al., [36] considered the determination of the sub-critical aeroelastic response and flutter instability of a two-dimensional wing section. The analytical model includes the stiffness and damping nonlinearities in plunging and pitching degrees of freedom. In addition to the aerodynamic loads, an arbitrary time-dependent external pressure pulse was considered. At zero flow speed the plunging amplitudes were found slightly larger than those at the small flow speeds. However, this trend is reversed when the flow speed is further increased and in such case larger amplitudes are experienced near the flutter speed. For the flow speed greater than the flutter speed the response becomes unbounded. Recently, Tang and Dowell [37] examined the influence of geometric structural nonlinear coupling among the bending deflection, chord-wise bending deflection, and twist about the deformed axis on flutter speed and LCO of high-aspect-ratio wings. They found that LCO above and below the perturbation flutter boundary generally occurs over a limited range of flow speed, depending on initial conditions.

1.3. AERODYNAMIC MODELING

The analysis of aeroelastic flutter usually depends on the methods of modeling and the nature of the unsteady external disturbances to the structure. Linear modeling is based on linear representation of aerodynamic, elastic, and inertia forces. Nonlinear modeling, on the other hand, considers the inherent nonlinearity of any of these forces or combination of them. Ashley [38] presented the state-of-the-art up to 1978 of solved and unsolved problems of aeroelastic stability.

Resolved problems include the torsional and flexural-torsional divergence of conventional lifting surfaces, and subsonic and supersonic flutter of isolated lifting surfaces. It is believed that the unresolved problems include deterministic and stochastic flutter of nonlinear aeroelastic structures in the presence of time-varying in-plane excitations. This in addition to the stochastic flutter of linear and nonlinear aeroelastic structures in transonic and supersonic flow regimes. Recently, some attempts have been made to study the random response of typical wing section by Poirel and Price [39, 40]. The present work considers the deterministic flutter of nonlinear aeroelastic lifting structures in the presence of time-varying in-plane excitations as a means to suppress flutter.

One of the critical issues of flutter analysis is the determination of aerodynamic forces acting on an oscillating airfoil. Unlike other vibration problems, these forces depend on the airfoil motion itself, thus resulting in an interaction between elastic, inertia, and aerodynamic forces. The magnitude of aerodynamic forces is influenced by the free stream Mach number. Several theories have been developed to account for the Mach number effect. These include (a) the modified strip analysis [41], (b) the modified two-dimensional loading [42], (c) the rectangular wing theory [43] and (d) the subsonic kernel function [44]. The modified strip analysis is based on Theodorsen's work [45], and is restricted to non-stationary, incompressible, potential flow at subsonic speeds.

It is believed that the early analysis of wing flutter in an incompressible subsonic flow was based on a quasi-stationary formulation. Theodorsen [45] developed a non-stationary formulation that accounts for the lag effects of the unsteady aerodynamics for different frequencies. The analysis was based on the assumption of harmonic oscillations of the wing. Later, Theodorsen and Garrick [46] conducted an experimental investigation to examine the validity of the predicted flutter speed and frequency. Theodorsen's solution was divided into two parts: a non-circulatory flow component that contributes to the lift and moment with a virtual mass, and a circulatory component that takes into account the vortex caused by the wake. The circulation function is a complex function whose real part modifies the load component in-phase with the angle of attack, while its imaginary part accounts for the out-of-phase load component. Wagner and Jones (see, e.g., Fung [3]) introduced an approximation to Theodorsen's function in order to predict the wing dynamic behavior in unsteady aerodynamic field.

Although it would seem straightforward to use the real and imaginary parts directly in flutter analysis, this procedure was found to give poor results in comparison with experimental results as reported by Yates [41]. The large phase angles of complex circulation functions associated with two-dimensional flow were found to be inappropriate for three-dimensional wings. Yates found that if phase angles remained moderately small the calculated flutter speed would be relatively insensitive to changes in the magnitude of the imaginary part. The real part of the circulation function is usually given in terms of the first eigenvalue of the coupled modes and Mach number for different values of a frequency parameter (non-dimensional flow speed). The modified strip theory includes alterations in the expressions of lift, moment, and circulation function in order to approximate the effects of the span finite length. Small disturbances to the flow are assumed, which imply that the resultant fluid speed differs only slightly from the free stream speed.

1.4 SCOPE OF THE PRESENT WORK

The purpose of the present study is to explore the possibility of suppressing flutter of a cantilever wing via parametric excitation in the neighborhood of combination parametric resonance of summed-type. The excitation of the clamped end is applied in the plane of largest rigidity such that the bending and torsion modes are cross-coupled through the excitation. This type of excitation owes its origin to a possible longitudinal vibration of aircraft engines. The sources of nonlinearities are due to the small in-plane displacement and nonlinear curvature. The paper is organized as follows. Section 2 deals with the analytical modeling of the nonlinear wing under aerodynamic loading. The aerodynamic lift and moment are modeled based on Theodorsen's theory and the equations of motion are developed using Hamilton's principle. Since the reference axis passes through the elastic axis of the wing, there will be a linear coupling in the equations of motion in addition to the nonlinear. Thus, the equations of motion differ from those derived by Ibrahim and Hijawi [47] due to the presence of linear coupling and aerodynamic loading. Section 3 presents a linear analysis of the system normal modes and parametric stability boundaries in the absence and presence of airflow at flutter speed. In the absence of aerodynamic forces, the response dynamic behavior is determined using multiple scales method in the neighborhood of combination resonance. The parametric excitation at the critical flutter speed and at slightly higher value than the flutter speed is considered in Section 4. Section 5 presents numerical simulation of the original coupled bending and torsion equations of motion of wing. It is interesting to find out that the parametric excitation results in stabilization of the flutter wing when the excitation amplitude exceeds a critical value. Parametric excitation of aeroelastic structures has been considered for a limited number of studies [48, 49]. For example, Lumbantobing and Haaker [48] studied the parametric excitation of a plunge oscillator and a seesaw oscillator. Both oscillators are described by a nonlinear Mathieu equation where the origin of nonlinearity is the dependence on the flow angle of attack. It was found that by increasing the air flow speed above the critical value the equilibrium position is re-stabilized. However, if the parametric excitation is due to longitudinal turbulence, the frequency of coalescence occurs at a lower air flow speed [39, 40]. Chin, et al., [49] obtained the modulated equations of a simply supported panel in a supersonic flow to calculate the equilibrium solutions and their stability. In the neighborhood of combination parametric resonance, they identified the excitation parameters that suppress flutter and those that lead to complex motions.

2. Analytical Modeling of a Plate-Like Wing

Consider a cantilever wing having a straight elastic axis, z , perpendicular to the fuselage as shown in Figure 1(a). The wing deformation can be measured by the bending deflection, $u(z,t)$, and torsional angle, $\alpha(z,t)$, about the elastic axis. The displacements of the elastic axis along y , and z axes are $v(z,t)$ and $w(z,t)$, respectively. The deflection, $u(z,t)$, is considered positive downward and $\alpha(z,t)$ is positive when the leading edge is up (clockwise). The chord-wise distortion will be neglected. The airfoil is exposed to an incompressible fluid flow of speed U_∞ . Figure 1(b) shows the projections of the model where b is half of the chord, δ_1 is the distance between the elastic axis and mid-chord, δ_2 is the distance between the aerodynamic center and mid-chord, and δ_3 is the distance between the elastic axis and inertia axis.

The cantilever wing is modeled as a plate-like beam subjected to periodic base excitation, $Y(t)$, in the plane of largest rigidity and involves nonlinear coupling between bending and torsion

modes. This coupling arises mainly from the fact that the centers of mass of cross-sections undergo a small but important displacement, v , in the plane of excitation. This displacement is measured in terms of the second-order of the fundamental bending, u , and torsion, α , displacements. Under an initial bending displacement, Δu , with a slight twist, α , of the beam cross-section, there will be an inevitable very small displacement $\Delta v \ll \Delta u$ associated with these displacements. When the beam is released from this state, the inertia force acting through the bending displacement, $u(z,t)$, will give a torque to the beam cross-section. Similarly, because of the small rotation of the principal planes of the cross-section, the inertia force contributes a bending moment about the local plane of minimum bending stiffness proportional to the twist angle, α . The bending-torsion coupling of the wing can be realized by considering the curvatures, κ_x , κ_y , and κ_z about x , y , and z -axes, [50],

$$\kappa_x = -\frac{\partial^2 v}{\partial z^2} + \frac{\partial^2 u}{\partial z^2} \alpha, \quad \kappa_y = \frac{\partial^2 v}{\partial z^2} \alpha + \frac{\partial^2 u}{\partial z^2}, \quad \kappa_z = -\frac{\partial \alpha}{\partial z} + \frac{\partial v}{\partial z} \frac{\partial^2 u}{\partial z^2} \quad (1)$$

Note that the curvature κ_x is very small and can be set to zero and thus one can write

$$\frac{\partial^2 v}{\partial z^2} = \frac{\partial^2 u}{\partial z^2} \alpha \quad (2)$$

This relationship represents the projection of the curvature of the beam in the plane Oxz on the Oy -axis, which gives the curvature in the plane Oyz , see Figure 1. It is clear that the displacement v can be expressed in terms of u and α through double integration of relation (2). Furthermore, one can approximate the curvature about z -axis by the linear relationship $\kappa_z = -\partial \alpha / \partial z$. Neglecting the extension of the beam elastic axis, the lateral displacement, $v(z,t)$, and axial drop, $w(z,t)$, may be expressed in terms of the bending deflection and the twist angle in the form:

$$v(z,t) = \int_0^z (l - \xi) \frac{\partial^2 u(\xi,t)}{\partial \xi^2} \alpha d\xi \quad (3)$$

$$w(z,t) = \int_0^z \frac{1}{2} \left(\frac{\partial u(\xi,t)}{\partial \xi} \right)^2 d\xi \quad (4)$$

The kinetic energy is:

$$T = \frac{1}{2} \iiint \rho \left[\left(\frac{\partial u}{\partial t} + \delta_3 \frac{\partial \alpha}{\partial t} \right)^2 + \left(\frac{\partial w}{\partial t} \right)^2 + \left(\frac{\partial v}{\partial t} + \frac{\partial Y}{\partial t} \right)^2 \right] dx dy dz + \frac{1}{2} \int_0^l I_0 \left(\frac{\partial \alpha}{\partial t} \right)^2 dz \quad (5)$$

where, ρ is the wing density, I_0 is the mass moment of the inertia (about the inertia axis) per unit length and l is the wing length. The strain potential energy due to bending and torsion is

$$V = \frac{1}{2} EI \int_0^l \left\{ \frac{\partial^2 u}{\partial z^2} \left[1 + \left(\frac{\partial u}{\partial z} \right)^2 \right] \right\}^2 dz + \frac{1}{2} cGJ \int_0^l \left(\frac{\partial \alpha}{\partial z} \right)^2 dz \quad (6)$$

where E is Young's modulus, I is the area moment of inertia of the wing cross-section about y axis, J is the polar moment of inertia of the wing cross-section about z axis, G is the modulus of rigidity, and c is a correction constant due to the noncircular cross-section of the wing. The curvature is expressed up to cubic order.

For incompressible flow, the aerodynamic lift per unit span is obtained based on Theodorsen's theory [45] in the form

$$L = 2\pi\rho_\infty U_\infty b B(k) \left[U_\infty \alpha + \frac{\partial u}{\partial t} + b \left(\frac{1}{2} - a \right) \frac{\partial \alpha}{\partial t} \right] + \pi\rho_\infty b^2 \left(\frac{\partial^2 u}{\partial t^2} - ba \frac{\partial^2 \alpha}{\partial t^2} \right) + \pi\rho_\infty b^2 U_\infty \frac{\partial \alpha}{\partial t} \quad (7)$$

The aerodynamic moment about the elastic axis, z , per unit span is

$$M = 2\pi\rho_\infty U_\infty b^2 \left(\frac{1}{2} + a \right) B(k) \left(U_\infty \alpha + \frac{\partial u}{\partial t} + b \left(\frac{1}{2} - a \right) \frac{\partial \alpha}{\partial t} \right) + \pi\rho_\infty ab^3 \left(\frac{\partial^2 u}{\partial t^2} - ba \frac{\partial^2 \alpha}{\partial t^2} \right) - \left(\frac{1}{2} - a \right) \pi\rho_\infty b^3 U_\infty \frac{\partial \alpha}{\partial t} - \frac{\pi\rho_\infty b^4}{8} \frac{\partial^2 \alpha}{\partial t^2} \quad (8)$$

where ρ_∞ is the air density, $a = \delta_1 / b$, $B(k)$ is the circulation function, which depends on the reduced frequency parameter, $k = b\omega / U_\infty$, where ω is the natural frequency of the wing coupled modes and will be determined later. The circulation function is a complex quantity represented by [3, 51]:

$$B(k) = F(k) + iG(k) \quad (9)$$

where $F(k) = 1 - \frac{0.165k^2}{k^2 + 0.00207} - \frac{0.335k^2}{k^2 + 0.09}$, and $G(k) = -\frac{0.000883735k + 0.108008k^3}{0.000186323 + 0.0920702k^2 + k^4}$ are given by Jones [51].

Applying Hamilton's principle

$$\int_{t_0}^{t_1} \delta(T - V) dt + \int_{t_0}^{t_1} \left[- \int_0^l L \delta u dz + \int_0^l M \delta \alpha dz \right] dt = 0 \quad (10)$$

and carrying out the variational process, gives the equations of motion and associated boundary conditions. The boundary conditions are

$$\alpha|_{z=0} = \frac{\partial \alpha}{\partial z}|_{z=0} = \frac{\partial \alpha}{\partial z}|_{z=l} = 0, \quad u|_{z=0} = \frac{\partial u}{\partial z}|_{z=0} = 0, \quad \frac{\partial^2 u}{\partial z^2}|_{z=l} = \frac{\partial^3 u}{\partial z^3}|_{z=l} = 0 \quad (11)$$

Considering only the first mode in bending and torsion, expanding the solutions in terms of the generalized coordinates and mode shapes

$$u(z, t) = u_0(t)f(z); \quad \alpha(z, t) = \alpha_0(t)\phi(z) \quad (12a, b)$$

where $f(z) = \cosh(1.875z/l) - \cos(1.875z/l) - 0.734[\sinh(1.875z/l) - \sin(1.875z/l)]$, and $\phi(z) = \sin(\pi z/2l)$.

Applying Galerkin's method gives the following two coupled nonlinear ordinary differential equations

$$\begin{aligned} m \left[1 + \frac{\pi b^2 \rho_\infty}{m} + \frac{c_1}{l^2} u_0^2(t) - c_2 \alpha_0^2(t) \right] \ddot{u}_0(t) + 2\pi b \rho_\infty B(k) U_\infty \dot{u}_0(t) + \left[K_u + m \frac{c_1}{l^2} \dot{u}_0^2(t) \right] u_0(t) + \\ K_{u3} u_0^3(t) + \left[c_6 (S_\alpha - a\pi b^3 \rho_\infty) - c_2 m u_0(t) \alpha_0(t) \right] \ddot{\alpha}_0(t) + \\ \left[2\pi b \rho_\infty c_6 B(k) U_\infty^2 - 2c_2 m \dot{u}_0(t) \dot{\alpha}_0(t) \right] \alpha_0(t) + c_6 \pi b^2 \rho_\infty [1 + (1-2a)B(k)] U_\infty \dot{\alpha}_0(t) + \\ c_3 m \alpha_0(t) \ddot{Y}(t) = 0 \end{aligned} \quad (13)$$

$$\begin{aligned} \left[I_\alpha + \left(\frac{1}{8} + a^2 \right) \pi b^4 \rho_\infty + c_4 m u_0^2(t) \right] \ddot{\alpha}_0(t) + \left(\frac{1}{2} - a \right) [1 - (1+2a)B(k)] \pi b^3 \rho_\infty U_\infty \dot{\alpha}_0(t) + \\ \left[K_\alpha - (1+2a)B(k) \pi b^2 \rho_\infty U_\infty^2 \right] \alpha_0(t) + \left[c_7 (S_\alpha - a\pi b^3 \rho_\infty) + c_4 m u_0(t) \alpha_0(t) \right] \ddot{u}_0(t) - \\ c_7 (1+2a) \pi b^2 \rho_\infty B(k) U_\infty \dot{u}_0(t) + 2c_4 m \dot{u}_0(t) \dot{\alpha}_0(t) u_0(t) + c_5 m u_0(t) \ddot{Y}(t) = 0 \end{aligned} \quad (14)$$

where m is the wing mass per unit length, $I_\alpha = I_0 + m\delta_3^2$, I_α is the wing mass moment of the inertia (about the elastic axis) per unit length, and $S_\alpha = m\delta_3$, $K_u = 12.3596EI_y/l^4$, $K_\alpha = \pi^2 cGJ/4l^2$, $K_{u3} = 80.8579EI_y/l^6$, $c_1 = 4.597$, $c_2 = 0.222567$, $c_3 = 0.42$, $c_4 = 0.4552$, $c_5 = 0.84129$, $c_6 = 0.677861$, and $c_7 = 1.3557$.

Rearranging the equations of motion, introducing the non-dimensional parameters $\bar{u} = u_0/b$, $\bar{Y} = Y/b$, $\tau = \omega_\alpha t$, and linear viscous damping with damping factors ζ_u and ζ_α , equations (13) and (14) take the non-dimensional form

$$(1 + \mu + c_1 d^2 \bar{u}^2 - c_2 \bar{\alpha}^2) \bar{u}'' + (c_6 (x_\alpha - a\mu) - c_2 \bar{u} \alpha) \alpha'' + 2 \left(r\zeta_u + \frac{\mu}{k_\alpha} B(k) \right) \bar{u}' +$$

$$c_6 \frac{\mu}{k_\alpha} [1 + B(k)(1 - 2a)] \alpha' + [r^2 + c_1 d^2 \bar{u}'^2] \bar{u} + 2 \left(c_6 \frac{\mu B(k)}{k_\alpha^2} - c_2 \bar{u}' \alpha' \right) \alpha + c_8 d^2 r^2 \bar{u}^3 + c_3 \alpha \bar{Y}''(\tau) = 0 \quad (15)$$

$$\begin{aligned} (c_7 (x_\alpha - a\mu) + c_4 \bar{u} \alpha) \frac{1}{r_\alpha^2} \bar{u}'' + \left(1 + \frac{\mu}{r_\alpha^2} \left(\frac{1}{8} + a^2 \right) + \frac{c_4}{r_\alpha^2} \bar{u}^2 \right) \alpha'' - c_7 (1 + 2a) \frac{\mu}{k_\alpha r_\alpha^2} B(k) \bar{u}' + \\ + \left[2\zeta_\alpha - \left(\frac{1}{2} - 2a^2 \right) \frac{\mu}{k_\alpha r_\alpha^2} B(k) + \left(\frac{1}{2} - a \right) \frac{\mu}{k_\alpha r_\alpha^2} \right] \alpha' + \frac{2c_4}{r_\alpha^2} \bar{u}' \alpha' \bar{u} + \\ \left[1 - (1 + 2a) \frac{\mu}{k_\alpha^2 r_\alpha^2} B(k) \right] \alpha + \frac{c_5}{r_\alpha^2} \bar{u} \bar{Y}''(\tau) = 0 \end{aligned} \quad (16)$$

where a prime denotes differentiation with respect to the non-dimensional time τ , the subscript 0 is dropped, $k_\alpha = \frac{b\omega_\alpha}{U_\infty}$, $\mu = \frac{\pi b^2 \rho_\infty}{m}$, $d = \frac{b}{l}$, $x_\alpha = \frac{S_\alpha}{mb}$, $r_\alpha = \sqrt{\frac{I_\alpha}{mb^2}}$, $a = \frac{\delta_1}{b}$, $r = \frac{\omega_u}{\omega_\alpha}$,

$\omega_u = \sqrt{K_u/m}$, $\omega_\alpha = \sqrt{K_\alpha/I_\alpha}$, and $c_8 = 6.5421$

Equations (15) and (16) will be solved for linear modal analysis, parametric stability boundaries, and response LCO in the absence and presence of air flow.

3. MODAL ANALYSIS AND PARAMETRIC STABILITY

The purpose of the linear analysis is to determine the critical flutter speed and the corresponding coupled frequencies on the system parameters and airflow speed. Under parametric excitation it is important to determine stability boundaries in the neighborhood of combination parametric resonance at the flutter speed. The linear equations of motion are:

$$\begin{aligned} (1 + \mu) \bar{u}'' + c_6 (x_\alpha - a\mu) \alpha'' + 2 \left(r\zeta_u + \frac{\mu}{k_\alpha} B(k) \right) \bar{u}' + c_6 \frac{\mu}{k_\alpha} [1 + B(k)(1 - 2a)] \alpha' + r^2 \bar{u} \\ + 2c_6 \frac{\mu B(k)}{k_\alpha^2} \alpha + c_3 \alpha \bar{Y}''(\tau) = 0 \end{aligned} \quad (17)$$

$$\begin{aligned} c_7 (x_\alpha - a\mu) \frac{1}{r_\alpha^2} \bar{u}'' + \left[1 + \frac{\mu}{r_\alpha^2} \left(\frac{1}{8} + a^2 \right) \right] \alpha'' - c_7 (1 + 2a) \frac{\mu}{k_\alpha r_\alpha^2} B(k) \bar{u}' + \left[2\zeta_\alpha - \left(\frac{1}{2} - 2a^2 \right) \frac{\mu}{k_\alpha r_\alpha^2} B(k) \right. \\ \left. + \left(\frac{1}{2} - a \right) \frac{\mu}{k_\alpha r_\alpha^2} \right] \alpha' + \left[1 - (1 + 2a) \frac{\mu}{k_\alpha^2 r_\alpha^2} B(k) \right] \alpha + \frac{c_5}{r_\alpha^2} \bar{u} \bar{Y}''(\tau) = 0 \end{aligned} \quad (18)$$

In the absence of parametric excitation, equations (17) and (18) are linearly coupled and may be solved for the eigenvalues for the following parameters: air mass parameter $\mu = 1/38$, elastic axis location $a = -0.36$, inertia axis location $x_\alpha = 0.024$, inertia ratio $r_\alpha = 0.62$, bending-to-torsion frequency ratio $r = 0.5$, and damping factors $\zeta_\alpha = 0.001$, $\zeta_u = 0.001$. To estimate the critical flutter speed, the solution of equations (17) and (18) is expressed in the form:

$$\bar{u} = u_a e^{i\bar{\omega}\tau} \quad \text{and} \quad \alpha = \alpha_a e^{i\bar{\omega}\tau} \quad (19)$$

where $\bar{\omega} = \omega / \omega_\alpha$ is the nondimensional natural frequency of the wing coupled modes.

Substituting equations (19) into equations (17) and (18), and setting the parametric excitation to zero, gives

$$\left[-(1+\mu)\bar{\omega}^2 + 2i\left(\zeta_u r + \frac{\mu}{k_\alpha} B(k)\right)\bar{\omega} + r^2 \right] u_a + \left\{ -c_6(x_\alpha - a\mu)\bar{\omega}^2 + ic_6 \frac{\mu}{k_\alpha} [1 + B(k)(1-2a)]\bar{\omega} + 2c_6 \frac{\mu B(k)}{k_\alpha^2} \right\} \alpha_a = 0 \quad (20)$$

$$\left[-c_7(x_\alpha - a\mu)\bar{\omega}^2 - ic_7(1+2a)\frac{\mu}{k_\alpha} B(k)\bar{\omega} \right] u_a + \left\{ -1 - \frac{\mu}{r_\alpha^2} \left(\frac{1}{8} + a^2 \right) \bar{\omega}^2 + i \left[2\zeta_\alpha - \left(\frac{1}{2} - 2a^2 \right) \frac{\mu B(k)}{k_\alpha r_\alpha^2} + \left(\frac{1}{2} - a \right) \frac{\mu}{k_\alpha r_\alpha^2} \right] \bar{\omega} + \left[1 - (1+2a) \frac{\mu B(k)}{k_\alpha^2 r_\alpha^2} \right] \right\} \alpha_a = 0 \quad (21)$$

Substituting for $B(k)$ from the equation (9), replacing $k = \frac{b\omega_\alpha}{U_\infty} \frac{\omega}{\omega_\alpha} = k_\alpha \bar{\omega}$, and rearranging, gives the characteristic equation:

$$\begin{vmatrix} AA(k_\alpha, \bar{\omega}) & BB(k_\alpha, \bar{\omega}) \\ DD(k_\alpha, \bar{\omega}) & EE(k_\alpha, \bar{\omega}) \end{vmatrix} = 0 \quad (22)$$

where the elements of the determinant are given in Appendix A. Traditionally, (see e.g., Fung [3]), the flutter speed and flutter frequencies are determined by setting the real and imaginary parts of the determinant (22) to zero. By giving a series of values of k the corresponding values of $\bar{\omega}$ were determined from the real and imaginary parts of the determinant. The intersection of the curves corresponding to the two parts establishes the flutter frequency and flutter speed. Instead, we will numerically solve the determinant (22) as a function of the flow speed. In view of the presence of $\bar{\omega}$ up to fourth order in the denominators of circulation functions F and G , the resulting frequency equation is found to be of order 12. Careful inspection of this equation reveals that the free terms (coefficient of $\bar{\omega}^0$) and coefficients of lower order terms $\bar{\omega}$, $\bar{\omega}^2$ up to fourth or fifth-order are extremely small, resulting in almost zero roots. The numerical solution gives two different complex roots and their conjugates. The values of the remaining roots were found to be almost near zero. The real components $(\omega_{re}/\omega_\alpha)_1$ and $(\omega_{re}/\omega_\alpha)_2$ represent dimensionless natural frequencies of the coupled modes, and the imaginary components $(\zeta_{im})_1/\omega_\alpha$ and $(\zeta_{im})_2/\omega_\alpha$ stand for the corresponding damping factors. The dependence of the eigenvalue components on the flow speed parameter $U_\infty/b\omega_\alpha$ is shown in Figure 2(a) when both circulation functions F and G are considered. It is seen that $-(\zeta_{im})_1/\omega_\alpha$ is always negative

while $-(\zeta_{im})_2/\omega_\alpha$ switches to a positive value at the critical airflow speed $U_\infty/b\omega_\alpha = 5.04$ indicating the occurrence of flutter.

If one ignores the imaginary component of the circulation function, i.e., $G=0$, the resulting natural frequencies shown in Figure 2(b) are found very close to those shown in Figure 2(a). For the case of Figure 2(a) the critical flutter speed ratio is $(U_\infty/b\omega_\alpha)_{G \neq 0} = 5.04$, while for the case of Figure 2(b) $(U_\infty/b\omega_\alpha)_{G=0} = 4.965$. The error between the two flutter speeds obtained in both cases is 1.5%. Since this error is less than 2% we will ignore the contribution of G .

It is interesting to note that at zero flow speed, the two natural frequencies possess the ratio 0.5.

Under parametric excitation, $\bar{Y} = Y_0 \cos(\bar{\Omega}\tau)$, where $\bar{\Omega} = \Omega/\omega_\alpha$, equations (17) and (18) are considered for stability analysis. Consider the solution of equations (17) and (18) in the form

$$\bar{u} = a_1 \sin\left(\frac{\bar{\Omega}\tau}{2}\right) + b_1 \cos\left(\frac{\bar{\Omega}\tau}{2}\right); \quad \alpha = A_1 \sin\left(\frac{\bar{\Omega}\tau}{2}\right) + B_1 \cos\left(\frac{\bar{\Omega}\tau}{2}\right) \quad (23a,b)$$

Substituting equations (23) into equations (17) and (18) and equating the coefficients of $\sin(\bar{\Omega}\tau/2)$ and $\cos(\bar{\Omega}\tau/2)$ gives a set of four linear homogeneous algebraic equations. The determinant of the coefficients of these equations establishes the frequency equation:

$$\begin{vmatrix} \frac{\bar{\Omega}^2}{4}(1+\mu) - r^2 & \frac{c_6 \bar{\Omega}^2}{4}(x_\alpha - a\mu) - \frac{1}{2}c_3 Y_0 \bar{\Omega}^2 - c_6 \frac{2B(k)\mu}{k_\alpha^2} \\ \bar{\Omega} \left(\frac{B(k)\mu}{k_\alpha} + r\zeta_u \right) & \frac{c_6 \bar{\Omega} \mu}{2k_\alpha} (1 + B(k)(1-2a)) \\ -\frac{c_7 \bar{\Omega}^2}{4}(x_\alpha - a\mu) + \frac{1}{2}c_5 Y_0 \bar{\Omega}^2 & r_\alpha^2 - \frac{r_\alpha^2 \bar{\Omega}^2}{4} - \frac{B(k)\mu}{k_\alpha^2} (1+2a) - \frac{\bar{\Omega}^2 \mu}{32} - \frac{1}{4}a^2 \bar{\Omega}^2 \mu \\ -\frac{c_7 B(k) \bar{\Omega} \mu}{2k_\alpha} (1+2a) & \frac{\bar{\Omega} \mu}{4k_\alpha} (1-2a - B(k)(1-4a^2)) + r_\alpha^2 \bar{\Omega} \zeta_\alpha \\ \bar{\Omega} \left(\frac{B(k)\mu}{k_\alpha} + r\zeta_u \right) & \frac{c_6 \bar{\Omega} \mu}{2k_\alpha} (1 + B(k)(1-2a)) \\ r^2 - \frac{\bar{\Omega}^2}{4}(1+\mu) & -\frac{c_6 \bar{\Omega}^2}{4}(x_\alpha - a\mu) - \frac{1}{2}c_3 Y_0 \bar{\Omega}^2 + \frac{2c_6 B(k)\mu}{k_\alpha^2} \\ \frac{c_6 B(k) \bar{\Omega} \mu}{2k_\alpha} (1+2a) & -\left(\frac{\bar{\Omega} \mu}{4k_\alpha} (1-2a - B(k)(1-4a^2)) + r_\alpha^2 \bar{\Omega} \zeta_\alpha \right) \\ -\frac{c_6 \bar{\Omega}^2}{4}(x_\alpha - a\mu) - \frac{1}{2}c_5 Y_0 \bar{\Omega}^2 & r_\alpha^2 - \frac{r_\alpha^2 \bar{\Omega}^2}{4} - \frac{B(k)\mu}{k_\alpha^2} (1+2a) - \frac{\bar{\Omega}^2 \mu}{32} - \frac{1}{4}a^2 \bar{\Omega}^2 \mu \end{vmatrix} = 0 \quad (24)$$

The roots of this equation depend on the excitation amplitude and flow speed. These roots are known to be the boundary frequencies of the instability regions. The instability regions are bounded by periodic solutions of period $2T$, where T is the period of parametric excitation. The stability boundaries belonging to zero flow speed, $U_\infty / b\omega_\alpha = 0$, are given by the solid curves in Figure 3, while those belonging to the critical flow speed, $U_\infty / b\omega_\alpha = 4.965$, are shown by the dashed curves. At the critical airflow speed, the stability boundary touches the frequency axis at excitation frequency ratio $\Omega / (\omega_\alpha + \omega_u) = 1.04$ regardless of the damping of the structure. In the absence of airflow, there are two instability regions, a narrow region at excitation frequency ratio less than 1 and a wider one at excitation frequency greater than one. At and above the critical speed there is only one instability region and it is wider than those below the critical speed. The bottom of each instability regions at zero air speed moves away from the frequency axis. Inside instability regions, one should consider the system inherent nonlinearities that are responsible to bring the response amplitude into a bounded LCO.

4. NONLINEAR ANALYSIS

4.1 RESONANCE CONDITIONS

The nonlinear modal interaction is examined by considering the coupled nonlinear equations of motion (15) and (16) using multiple scales method [52]. The equations of motion are first written in terms of the linearized principal coordinates. Consider the equations of motion in non-dimensional form:

$$\mathbf{M}(\mathbf{u}(\tau))\mathbf{u}''(\tau) + \mathbf{K}(k)\mathbf{u}(\tau) = \mathbf{F}_{nl}(\mathbf{u}(\tau), \mathbf{u}'(\tau), \bar{Y}''(\tau), k) \quad (25)$$

$$\text{where } \mathbf{u}(\tau) = \begin{Bmatrix} \bar{u}(\tau) \\ \alpha(\tau) \end{Bmatrix}, \mathbf{F}_{nl} = \begin{Bmatrix} f_{n1} \\ f_{n2} \end{Bmatrix}, \bar{Y}(\tau) = Y_0 \sin(\bar{\Omega}\tau), \bar{\Omega} = \frac{\Omega}{\omega_\alpha},$$

$$\mathbf{M} = \begin{pmatrix} 1 + \mu + c_1 d^2 \bar{u}^2 - c_2 \alpha^2 & c_6 (x_\alpha - a\mu) - c_2 \bar{u}\alpha \\ \frac{c_7 (x_\alpha - a\mu) + c_4 \bar{u}\alpha}{r_\alpha^2} & 1 + \frac{\mu}{r_\alpha^2} \left(\frac{1}{8} + a^2 \right) + \frac{c_4}{r_\alpha^2} \bar{u}^2 \end{pmatrix}, \mathbf{K} = \begin{pmatrix} r^2 & 2c_6 \frac{\mu B(k)}{k_\alpha^2} \\ 0 & 1 - (1+2a) \frac{\mu}{k_\alpha^2 r_\alpha^2} B(k) \end{pmatrix}$$

$$f_{n1} = -2 \left(r\zeta_u + \frac{\mu}{k_\alpha} B(k) \right) \bar{u}' - \frac{c_6 \mu}{k_\alpha} [1 + B(k)(1-2a)] \alpha' - c_1 d^2 \bar{u}'^2 \bar{u} + 2c_2 \bar{u}' \alpha' \alpha - c_8 d^2 r^2 \bar{u}^3 - c_3 \alpha \bar{Y}''$$

$$f_{n2} = (1+2a) \frac{c_7 \mu}{k_\alpha r_\alpha^2} B(k) \bar{u}' - \left[2\zeta_\alpha - \left(\frac{1}{2} - 2a^2 \right) \frac{\mu}{k_\alpha r_\alpha^2} B(k) + \left(\frac{1}{2} - a \right) \frac{\mu}{k_\alpha r_\alpha^2} \right] \alpha' - 2 \frac{c_4}{r_\alpha^2} \bar{u}' \alpha' \bar{u} - \frac{c_5}{r_\alpha^2} \bar{u} \bar{Y}''$$

Multiplying equation (25) by the inverse of mass matrix, gives

$$\mathbf{I}\mathbf{u}'' + \mathbf{M}^{-1}\mathbf{K}\mathbf{u} = \mathbf{M}^{-1}\mathbf{F}_{nl} \quad (26)$$

where \mathbf{I} is the identity matrix. The inverse of the mass matrix is then expanded into a Taylor series up to cubic order. The normal mode natural frequencies are determined from the conservative system, $\mathbf{I}\mathbf{u}'' + \tilde{\mathbf{K}}\mathbf{u} = 0$, and are given by:

$$\bar{\omega}_1^2(k) = \frac{p_3(k) - \sqrt{p_4(k)}}{2 \left[8r_\alpha^2 (1+\mu) + (1+8a^2)(1+\mu)\mu - 8c_6 c_7 (x_\alpha - a\mu)^2 \right]} \quad (27a)$$

$$\bar{\omega}_2^2(k) = \frac{p_3(k) + \sqrt{p_4(k)}}{2 \left[8r_\alpha^2 (1+\mu) + (1+8a^2)(1+\mu)\mu - 8c_6 c_7 (x_\alpha - a\mu)^2 \right]} \quad (27b)$$

where $p_3(k)$ and $p_4(k)$ are given in Appendix B. $\bar{\omega}_1 = \omega_1 / \omega_\alpha$, and $\bar{\omega}_2 = \omega_2 / \omega_\alpha$. The corresponding modal matrix is:

$$\mathbf{P}(k) = \begin{pmatrix} 1 & 1 \\ p_1(k) & p_2(k) \end{pmatrix} \quad (28)$$

where $p_1(k)$ and $p_2(k)$ are the modal ratios given in Appendix B. The following coordinate transformation is introduced:

$$\mathbf{u}(\tau) = \mathbf{P}(k)\mathbf{v}(\tau) \quad (29)$$

where $\mathbf{v}(\tau) = \begin{Bmatrix} v_1(\tau) \\ v_2(\tau) \end{Bmatrix}$ are the principal coordinates. The equations of motion become:

$$\mathbf{I}\mathbf{v}''(\tau) + \Lambda(k)\mathbf{v}(\tau) = \hat{\mathbf{F}}_{nl} (v_1(\tau), v_2(\tau), v_1'(\tau), v_2'(\tau), k) \quad (30)$$

$$\text{where } \Lambda(k) = \begin{pmatrix} \bar{\omega}_1^2(k) & 0 \\ 0 & \bar{\omega}_2^2(k) \end{pmatrix}, \quad \hat{\mathbf{F}}_{nl} (v_1, v_2, v_1', v_2', k) = \begin{Bmatrix} \hat{F}_{nl1} \\ \hat{F}_{nl2} \end{Bmatrix}, \quad Y_{0u} = Y_0 \bar{\Omega}^2,$$

$$\begin{aligned} \hat{F}_{nl1} = \varepsilon \{ & (q_3 v_2^2 + q_4 v_1'^2 + q_5 v_2'^2 + q_6 v_1' v_2' + q_7 v_1' v_2 + q_8 v_2' v_2) v_1 + (q_9 v_1'^2 + q_{10} v_1' v_2' + q_{11} v_2'^2) v_2 + q_{12} v_1' \\ & + q_{13} v_2' + q_{14} v_1^3 + q_{15} v_2^3 + (q_{16} v_2 + q_{17} v_1' + q_{18} v_2') v_1^2 + (q_{19} v_1' + q_{20} v_2') v_2^2 - (q_1 v_2 + q_2 v_1) Y_{0u} \sin(\bar{\Omega} \tau) \} \end{aligned}$$

$$\begin{aligned} \hat{F}_{nl2} = \varepsilon \{ & (s_3 v_2^2 + s_4 v_1'^2 + s_5 v_2'^2 + s_6 v_1' v_2' + s_7 v_1' v_2 + s_8 v_2' v_2) v_1 + (s_9 v_1'^2 + s_{10} v_1' v_2' + s_{11} v_2'^2) v_2 + s_{12} v_1' \\ & + s_{13} v_2' + s_{14} v_1^3 + s_{15} v_2^3 + (s_{16} v_2 + s_{17} v_1' + s_{18} v_2') v_1^2 + (s_{19} v_1' + s_{20} v_2') v_2^2 - (s_1 v_2 + s_2 v_1) Y_{0u} \sin(\bar{\Omega} \tau) \} \end{aligned}$$

and a prime denotes differentiation with respect to the non-dimensional time τ . $q_1 \dots q_{20}$, and $s_1 \dots s_{20}$ are coefficients that depend on the flow speed. The solution of these equations is expressed in terms of two time scales $T_0 = \tau$ and $T_1 = \varepsilon \tau$

$$v_1(\tau, \varepsilon) = v_{10}(T_0, T_1) + \varepsilon v_{11}(T_0, T_1) + \dots, \quad v_2(\tau, \varepsilon) = v_{20}(T_0, T_1) + \varepsilon v_{21}(T_0, T_1) + \dots \quad (31a, b)$$

Substituting equations (31) into equations (30) and collecting terms of the same order of ε , the following equations are obtained:

Equations of order ε^0 are:

$$D_0^2 v_{10} + \bar{\omega}_1^2 v_{10} = 0 \quad (32a)$$

$$D_0^2 v_{20} + \bar{\omega}_2^2 v_{20} = 0 \quad (32b)$$

Equations of order ε are:

$$\begin{aligned} D_0^2 v_{11} + \bar{\omega}_1^2 v_{11} = & (q_3 v_{20}^2 + q_4 D_0 v_{10}^2 + q_5 D_0 v_{20}^2 + q_6 D_0 v_{10} D_0 v_{20} + q_7 D_0 v_{10} v_{20} + q_8 D_0 v_{20} v_{20}) v_{10} \\ & + (q_9 D_0 v_{10}^2 + q_{10} D_0 v_{10} D_0 v_{20} + q_{11} D_0 v_{20}^2) v_{20} + q_{12} D_0 v_{10} + q_{14} v_{10}^3 + q_{13} D_0 v_{20} + q_{15} v_{20}^3 \\ & + (q_{16} v_{20} + q_{17} D_0 v_{10} + q_{18} D_0 v_{20}) v_{10}^2 + (q_{19} D_0 v_{10} + q_{20} D_0 v_{20}) v_{20}^2 \\ & - \frac{1}{2} i (q_1 v_{20} + q_2 v_{10}) Y_{0u} (e^{-i\bar{\Omega}T_0} - e^{i\bar{\Omega}T_0}) - 2D_0 D_1 v_{10} \} \end{aligned} \quad (33a)$$

$$\begin{aligned} D_0^2 v_{21} + \bar{\omega}_2^2 v_{21} = & (s_3 v_{20}^2 + s_4 D_0 v_{10}^2 + s_5 D_0 v_{20}^2 + s_6 D_0 v_{10} D_0 v_{20} + s_7 D_0 v_{10} v_{20} + s_8 D_0 v_{20} v_{20}) v_{10} \\ & + (s_9 D_0 v_{10}^2 + s_{10} D_0 v_{10} D_0 v_{20} + s_{11} D_0 v_{20}^2) v_{20} + s_{12} D_0 v_{10} + s_{14} v_{10}^3 + s_{13} D_0 v_{20} + s_{15} v_{20}^3 \\ & + (s_{16} v_{20} + s_{17} D_0 v_{10} + s_{18} D_0 v_{20}) v_{10}^2 + (s_{19} D_0 v_{10} + s_{20} D_0 v_{20}) v_{20}^2 \\ & - \frac{1}{2} i (s_1 v_{20} + s_2 v_{10}) Y_{0u} (e^{-i\bar{\Omega}T_0} - e^{i\bar{\Omega}T_0}) - 2D_0 D_1 v_{10} \} \end{aligned} \quad (33b)$$

The zeroth-order solution is:

$$v_{10}(T_0, T_1) = A[T_1] e^{i\bar{\omega}_1 T_0} + \bar{A}[T_1] e^{-i\bar{\omega}_1 T_0}; \quad v_{20}(T_0, T_1) = Q[T_1] e^{i\bar{\omega}_2 T_0} + \bar{Q}[T_1] e^{-i\bar{\omega}_2 T_0} \quad (34a,b)$$

Equations (33) contain secular terms, which give rise to following resonance conditions:

- (a) Combination parametric resonance $\bar{\Omega} = \bar{\omega}_1 + \bar{\omega}_2$, i.e., $\Omega = \omega_1 + \omega_2$
- (b) One-to-one internal resonance $\omega_1 = \omega_2$
- (c) One-to-three internal resonance $\omega_1 = 3\omega_2$
- (d) Three-to-one internal resonance $3\omega_1 = \omega_2$

The third and fourth resonance conditions are excluded because Theodorsen's theory is only applicable near flutter speed, i.e., when $\omega_1 \approx \omega_2$. The first two cases will be considered.

4.2 RESPONSE AT ZERO FLOW SPEED

The results of the previous section revealed that the normal mode frequencies in the absence of air flow are not equal and possess the ratio $\omega_1 / \omega_2 = 0.5$. Setting secular terms corresponding to the combination parametric resonance, $\bar{\Omega} = \bar{\omega}_1 + \bar{\omega}_2$, to zero and introducing the detuning parameter σ_ε , defined by $\bar{\Omega} = \bar{\omega}_1 + \bar{\omega}_2 + \varepsilon \sigma_\varepsilon$, gives the solvability conditions

$$\frac{1}{2}iq_1\bar{Q}Y_{0u}e^{i\sigma_e T_1} + iq_{12}\bar{\omega}_1 A + (3q_{14} + iq_{17}\omega_1 + q_4\bar{\omega}_1^2)A^2\bar{A} + 2(q_3 + iq_{19}\omega_1 + q_5\bar{\omega}_2^2)AQ\bar{Q} - 2i\bar{\omega}_1 A' = 0 \quad (35a)$$

$$\frac{1}{2}is_2\bar{A}Y_{0u}e^{i\sigma_e T_1} + is_{13}\bar{\omega}_2 Q + (3s_{15} + is_{20}\omega_2 + s_{11}\bar{\omega}_2^2)Q^2\bar{Q} + 2(s_{16} + is_{18}\omega_2 + s_9\bar{\omega}_1^2)QA\bar{A} - 2i\bar{\omega}_2 Q' = 0 \quad (35b)$$

Introducing the following polar transformations

$$A = b_1 e^{i\beta_1}; \quad Q = b_2 e^{i\beta_2} \quad (36a,b)$$

and separating imaginary and real parts gives the following first-order differential equations:

$$2b_1' = q_{12}b_1 + q_{17}b_1^3 + 2q_{19}b_2^2b_1 + \frac{q_1}{2\bar{\omega}_1}b_2Y_{0u}\cos(\sigma_e T_1 - \beta_1 - \beta_2) \quad (37a)$$

$$2\bar{\omega}_1 b_1 \beta_1' = -(3q_{14} + q_4\bar{\omega}_1^2)b_1^3 - 2[q_3 + q_5\bar{\omega}_2^2]b_1b_2^2 + \frac{q_1}{2}b_2Y_{0u}\sin(\sigma_e T_1 - \beta_1 - \beta_2) \quad (37b)$$

$$2b_2' = s_{13}b_2 + s_{20}b_2^3 + 2s_{18}b_1^2b_2 + \frac{s_2}{2\bar{\omega}_2}b_1Y_{0u}\cos(\sigma_e T_1 - \beta_1 - \beta_2) \quad (37c)$$

$$2\bar{\omega}_2 b_2 \beta_2' = -2(s_{16} + s_9\bar{\omega}_1^2)b_2b_1^2 - (3s_{15} + s_{11}\bar{\omega}_2^2)b_2^3 + \frac{s_2}{2}b_1Y_{0u}\sin(\sigma_e T_1 - \beta_1 - \beta_2) \quad (37d)$$

The above four algebraic equations contain three unknowns and the dependence on the detuning parameter will not appear explicitly. In this case, it is possible to combine two of these equations into one through the following transformation:

$$\gamma_e = \sigma_e T_1 - \beta_1 - \beta_2 \quad \text{and} \quad \beta_1' + \beta_2' = \sigma_e - \gamma_e' \quad (38)$$

where a prime denotes differentiation with respect to T_1 . The resulting equations are:

$$2b_1' = q_{12}b_1 + q_{17}b_1^3 + 2q_{19}b_2^2b_1 + \frac{q_1}{2\bar{\omega}_1}b_2Y_{0u}\cos(\gamma_e) \quad (39a)$$

$$2b_2' = s_{13}b_2 + s_{20}b_2^3 + 2s_{18}b_1^2b_2 + \frac{s_2}{2\bar{\omega}_2}b_1Y_{0u}\cos(\gamma_e) \quad (39b)$$

$$\begin{aligned} \gamma_e' = \sigma_e - & \left[\frac{q_1}{4\bar{\omega}_1} \frac{b_2}{b_1} + \frac{s_2}{4\bar{\omega}_2} \frac{b_1}{b_2} \right] Y_{0u} \sin \gamma_e + \left[\frac{3q_{14} + q_4\bar{\omega}_1^2}{2\bar{\omega}_1} + \frac{s_{16} + s_9\bar{\omega}_1^2}{\bar{\omega}_2} \right] b_1^2 \\ & + \left[\frac{3s_{15} + s_{11}\bar{\omega}_2^2}{2\bar{\omega}_2} + \frac{q_3 + q_5\bar{\omega}_2^2}{\bar{\omega}_1} \right] b_2^2 \end{aligned} \quad (39c)$$

Equations (39) are numerically integrated for different values of excitation amplitude in the neighborhood of combination parametric resonance, i.e., $\Omega \approx \omega_1 + \omega_2$, internal frequency ratio $\omega_1 / \omega_2 = 0.5$, and the external excitation detuning parameter $\sigma_e = 0$. Over a very small range of excitation amplitude, $0 < Y_0 < 0.0008$, the zero equilibrium is dynamically stable and the damping energy overcomes input energy. At a threshold value of excitation amplitude the equilibrium position loses its stability and both bending and torsion amplitudes achieve steady state values over the excitation amplitude range $0.0008 < Y_0 < 0.0018$. Above that range and over the region $0.0018 < Y_0 < 0.003$, the response amplitudes experience Hopf bifurcation. The response then experiences another bifurcation in the form of period doubling over the region, $0.003 < Y_0 < 0.0055$. Above that region, the response exhibits regular periodic (but not harmonic) oscillations. Figure 4 shows the bifurcation diagram using the initial conditions $\bar{u}(0) = 0.1$, $\alpha(0) = 0.1$, $\bar{u}'(0) = 0$, $\alpha'(0) = 0$, and system parameters $\mu = 1/38$, $a = -0.36$, $x_\alpha = 0.024$, $r_\alpha = 0.62$, $r = 0.5$, $\zeta_\alpha = 0.001$, $\zeta_u = 0.001$, and $d = 0.1$. The bifurcation diagram reveals the upper and lower pairs of local maxima and minima by taking the excitation amplitude as the control parameter.

4.3 RESPONSE AT CRITICAL AND POST-CRITICAL FLUTTER SPEEDS

Introducing the external, σ_e , and internal, σ_i , detuning parameters, defined such that $\bar{\Omega} = \bar{\omega}_1 + \bar{\omega}_2 + \varepsilon\sigma_e$ and $\bar{\omega}_2 = \bar{\omega}_1 + \varepsilon\sigma_i$, gives the solvability conditions

$$\begin{aligned} \frac{1}{2}i(q_{11}\bar{Q}e^{i\sigma_e T_1} + q_{12}\bar{A}e^{i(\sigma_e + \sigma_i)T_1})Y_{0u} + iq_{13}\bar{\omega}_2 e^{i\sigma_i T_1}Q + iq_{12}\bar{\omega}_1 A + (3q_{14} + iq_{17}\bar{\omega}_1 + q_{18}\bar{\omega}_1^2)A^2\bar{A} \\ + (q_{16} + iq_{17}\bar{\omega}_1 - q_{18}\bar{\omega}_1^2 - iq_{18}\bar{\omega}_2 + q_{19}\bar{\omega}_1\bar{\omega}_2)e^{-i\sigma_i T_1}A^2\bar{Q} + (q_{13} - iq_{19}\bar{\omega}_1 + iq_{18}\bar{\omega}_2 + q_{10}\bar{\omega}_1\bar{\omega}_2 - q_{15}\bar{\omega}_2^2)e^{2i\sigma_i T_1}Q^2\bar{A} \\ + (3q_{15} + iq_{20}\bar{\omega}_2 + q_{11}\bar{\omega}_2^2)e^{i\sigma_i T_1}Q^2\bar{Q} + 2(q_{16} + q_{19}\bar{\omega}_1^2 + iq_{18}\bar{\omega}_2)e^{i\sigma_i T_1}QA\bar{A} \\ + 2(q_{13} + iq_{19}\bar{\omega}_1 + q_{15}\bar{\omega}_2^2)AQ\bar{Q} - 2i\bar{\omega}_1 A' = 0 \end{aligned} \quad (40a)$$

$$\begin{aligned} \frac{1}{2}i(s_{12}\bar{A}e^{i\sigma_e T_1} + s_{13}\bar{Q}e^{i(\sigma_e + \sigma_i)T_1})Y_{0u} + is_{12}\bar{\omega}_1 e^{-i\sigma_i T_1}A + is_{13}\bar{\omega}_2 Q + (3s_{15} + is_{20}\bar{\omega}_2 + s_{11}\bar{\omega}_2^2)Q^2\bar{Q} \\ + (s_{13} + is_{18}\bar{\omega}_2 - s_{15}\bar{\omega}_2^2 - is_{19}\bar{\omega}_1 + s_{10}\bar{\omega}_1\bar{\omega}_2)e^{i\sigma_i T_1}Q^2\bar{A} + (s_{16} - is_{18}\bar{\omega}_2 + is_{17}\bar{\omega}_1 + s_{19}\bar{\omega}_1\bar{\omega}_2 - s_{14}\bar{\omega}_1^2)e^{-2i\sigma_i T_1}A^2\bar{Q} \\ + (3s_{14} + is_{17}\bar{\omega}_1 + s_{14}\bar{\omega}_1^2)e^{-i\sigma_i T_1}A^2\bar{A} + 2(s_{13} + s_{15}\bar{\omega}_2^2 + is_{19}\bar{\omega}_1)e^{-i\sigma_i T_1}AQ\bar{Q} \\ + 2(s_{16} + is_{18}\bar{\omega}_2 + s_{19}\bar{\omega}_1^2)QA\bar{A} - 2i\bar{\omega}_2 Q' = 0 \end{aligned} \quad (40b)$$

Introducing the following polar transformations

$$A = b_1 e^{i\beta_1}; \quad Q = b_2 e^{i\beta_2} \quad (41a,b)$$

and separating imaginary and real parts gives four first-order differential equations. By setting the left-hand sides of these equations to zero, one obtains four algebraic equations containing three unknowns, since the two phase angles are combined as one unknown. In addition, the

dependency on the detuning parameter does not explicitly appear. In this case, one may introduce the following transformation:

$$\gamma_e = \sigma_e T_1 - \beta_1 - \beta_2, \quad \gamma_i = \sigma_i T_1 - \beta_1 + \beta_2, \quad \beta'_1 + \beta'_2 = \sigma_e - \gamma'_e, \quad \beta'_1 - \beta'_2 = \sigma_i - \gamma'_i \quad (42)$$

where a prime denotes differentiation with respect to T_1 . The resulting equations are:

$$2b'_1 = q_{12}b_1 + q_{17}b_1^3 + 2q_{19}b_2^2b_1 + \frac{q_1}{2\bar{\omega}_1}b_2Y_{0u}\cos\gamma_e + \frac{q_{13}\bar{\omega}_2}{\bar{\omega}_1}b_2\cos\gamma_i + \frac{b_2^3}{\bar{\omega}_1}[q_{20}\bar{\omega}_2\cos\gamma_i + C_1\sin\gamma_i] \\ + \frac{b_1^2b_2}{\bar{\omega}_1}[C_2\cos\gamma_i + C_3\sin\gamma_i] + \frac{b_1}{2\bar{\omega}_1}q_2Y_{0u}\cos(\gamma_e + \gamma_i) + C_4b_1b_2^2\cos 2\gamma_i + C_5b_1b_2^2\sin 2\gamma_i \quad (43a)$$

$$2b'_2 = s_{13}b_2 + s_{20}b_2^3 + 2s_{18}b_1^2b_2 + \frac{s_2}{2\bar{\omega}_2}b_1Y_{0u}\cos(\gamma_e) + \frac{s_{12}\bar{\omega}_1}{\bar{\omega}_2}b_1\cos\gamma_i + \frac{b_1^3}{\bar{\omega}_2}[s_{17}\bar{\omega}_1\cos\gamma_i - C_6\sin\gamma_i] \\ + \frac{b_2^2b_1}{\bar{\omega}_2}[C_7\cos\gamma_i - C_8\sin\gamma_i] + \frac{b_2}{2\bar{\omega}_2}s_1Y_{0u}\cos(\gamma_e - \gamma_i) - b_2b_1^2(C_9\cos 2\gamma_i + C_{10}\sin 2\gamma_i) \quad (43b)$$

$$\gamma'_e = \sigma_e + \frac{1}{4\bar{\omega}_1\bar{\omega}_2b_1b_2}\{-2q_{13}\bar{\omega}_2^2b_2^2\sin\gamma_i + b_1^4[C_{11}\bar{\omega}_1\cos\gamma_i + 2s_{17}\bar{\omega}_1^2\sin\gamma_i] + 2s_{12}\bar{\omega}_1^2b_1^2\sin\gamma_i \\ + b_2^4(C_{12}\bar{\omega}_2\cos\gamma_i - 2q_{20}\bar{\omega}_2^2\sin\gamma_i) + C_{13}b_1^2b_2^2\cos\gamma_i + C_{14}b_1^2b_2^2\sin\gamma_i + 2C_{15}b_1^3b_2 + 2C_{16}b_1^3b_2\cos 2\gamma_i \\ + 2C_{17}b_1^3b_2\sin 2\gamma_i + 2C_{18}b_2^3b_1 + 2C_{19}b_2^3b_1\cos 2\gamma_i - 2C_{20}b_2^3b_1\sin 2\gamma_i - C_{21}Y_{0u}\sin\gamma_e \\ - Y_{0u}b_1b_2[s_1\bar{\omega}_1\sin(\gamma_e - \gamma_i) + q_2\bar{\omega}_2\sin(\gamma_e + \gamma_i)]\} \quad (43c)$$

$$\gamma'_i = \sigma_i + \frac{1}{4\bar{\omega}_1\bar{\omega}_2b_1b_2}\{-2q_{13}\bar{\omega}_2^2b_2^2\sin\gamma_i - b_1^4[C_{22}\bar{\omega}_1\cos\gamma_i + 2s_{17}\bar{\omega}_1^2\sin\gamma_i] - 2s_{12}\bar{\omega}_1^2b_1^2\sin\gamma_i \\ + b_2^4(C_{23}\bar{\omega}_2\cos\gamma_i - 2q_{20}\bar{\omega}_2^2\sin\gamma_i) + C_{24}b_1^2b_2^2\cos\gamma_i + C_{25}b_1^2b_2^2\sin\gamma_i + 2C_{26}b_1^3b_2 \\ + 2b_1^3b_2(C_{27}\cos 2\gamma_i + C_{28}\sin 2\gamma_i) + 2C_{29}b_2^3b_1 + 2b_2^3b_1(C_{30}\cos 2\gamma_i - C_{31}\sin 2\gamma_i) \\ + C_{32}Y_{0u}\sin\gamma_e + Y_{0u}b_1b_2[s_1\bar{\omega}_1\sin(\gamma_e - \gamma_i) - q_2\bar{\omega}_2\sin(\gamma_e + \gamma_i)]\} \quad (43d)$$

where the coefficients C_i are defined in Appendix C. Note that equations (43) contain four unknowns namely the response amplitudes, b_1 , and b_2 , and the two phase angles, γ_e and γ_i . Furthermore, the dependency on the external and internal detuning parameters explicitly appears in equations (43c) and (43d). The solution of these equations is obtained numerically for different values of excitation amplitude, at the critical and post-critical flutter speeds. In both cases, the response is estimated in the neighborhood of combination parametric resonance, i.e., $\Omega \approx \omega_1 + \omega_2$, internal frequency ratio, $\omega_1/\omega_2 \approx 1$, external excitation detuning parameter, $\sigma_e = 0$, internal resonance detuning parameter $\sigma_i = 0.061$, and system parameters $\mu = 1/38$, $a = -0.36$, $x_\alpha = 0.024$, $r_\alpha = 0.62$, $r = 0.5$, $\zeta_\alpha = 0.001$, $\zeta_u = 0.001$, $d = 0.1$.

4.3.1 Response at Critical Flutter Speed

In the absence of parametric excitation, the solution of these equations reveals the coexistence of different fixed points implying limit cycle oscillations (LCO). Each fixed point is created from a certain domain of initial conditions. There are three possible values of the fixed point and each is achieved for certain values of initial conditions. The three fixed points are

$$\{u, \alpha\} = \{0, 0\}, \{0.15, -0.11\}, \text{ and } \{1.4, 0.325\}$$

The domains of attraction of each of the above fixed points are shown in Figure 5(a), where the empty space is belonging to the zero fixed point.

Under parametric excitation, the same scenario is preserved up to an excitation level $Y_0 = 0.00875$ at which the response experiences Hopf bifurcation around each fixed point in addition to a new fixed point that also experiences Hopf bifurcation. At $Y_0 = 0.00875$, there are four different values of initial conditions, which lead to four different attractors. These initial conditions are:

$$\{u_0, \alpha_0, u'_0, \alpha'_0\} = \{0.5, 0.04, 0, 0\}, \{0.5, 0.05, 0, 0\}, \{0.5, 0.7, 0, 0\}, \text{ and } \{0.45, 0.07, 0, 0\}.$$

The domains of attraction corresponding to this case are shown in Figure 5(b).

Over another range of excitation amplitude, $0.00875 < Y_0 < 0.0125$, the response experiences Hopf bifurcation for relatively high range of initial conditions below which the response settles at the static equilibrium position. For example, under excitation amplitude, $Y_0 = 0.01$, the basin of attraction of this response is shown in Figure 5(c) and it reveals that the basin of initial conditions that leads to non-zero response is shifted away to either higher positive values or negative values. At excitation amplitude $Y_0 = 0.0125$ an additional bifurcation around a new point takes place depending on the initial conditions. For example, the two sets of initial conditions $\{0.3, -0.1, 0, 0\}$ and $\{0.5, 0.1, 0, 0\}$, yield two different periodic attractors under $Y_0 = 0.014$. Figure 5(d) shows the basins of attraction. In the first and third quadrants the basins of attraction are diminished to one positive or negative point, i.e., $\{0.5, 0.1, 0, 0\}$ or $\{-0.5, -0.1, 0, 0\}$. These two sets of initial conditions lead to large amplitude oscillations. Another two basins of attraction located in the second and fourth quadrants lead to another attractor of very small amplitude.

As the excitation amplitude increases, additional bifurcations take place in the form of cascade of period doubling depending on initial conditions. Figure 6(a) shows samples of time history records, phase diagrams, and FFT plots under excitation amplitude $Y_0 = 0.015$, and initial conditions $\{0.5, -0.1, 0, 0\}$. It is seen that the bifurcation takes place in the form of period doubling. The domain of attraction of this attractor is slightly enlarged than the corresponding case of Figure 5(d). There is another periodic attractor of period two, shown in Figure 6(b) that

oscillates with larger amplitude than the first attractor and emanates from one point of initial conditions in the first and third quadrants shown in Figure 5(e).

Under excitation amplitude $Y_0 = 0.016$, the response experiences another bifurcation of period four. There are two different attractors similar to those displayed in Figure 5(e). Any further increase of excitation amplitude results in chaotic motion as shown in Figure 7, which is generated under excitation amplitude $Y_0 = 0.017$ and different domains of attraction. The spectrum of the time history records is continuous. The Poincaré maps displayed in Figures 7(a) and (b) do not cover a smooth closed curve but constitute a set of randomly scattered points implying that the motion turned out to be chaotic. The Poincaré maps are obtained based on the period of the first return. The domains of attraction corresponding to the small amplitude oscillation attractor are expanded as shown in Figure 5(f).

Figure 8 presents the bifurcation diagram by taking the excitation amplitude as the control parameter. It is seen that for a region of initial conditions, the parametric excitation acts as a stabilizer source of the wing flutter where under these regions the response achieves its static equilibrium position. Outside this domain of initial conditions, the equilibrium position loses its stability and the response may possess fixed points, Hopf bifurcation, cascade of period doubling, and eventually chaotic motion. It is seen that at each bifurcation point, branches of symmetric and asymmetric periodic solutions meet in the form of supercritical symmetry-breaking bifurcation.

It is obvious that the response exhibits multiple attractors, each with its own domain of attraction. One or two of these attractors, namely the zero response or small amplitude LCO about a small mean, are superior and desirable in the post flutter region. In order to achieve that desirable performance one may use one of the current techniques used to control chaos (see, e.g., [53]). For the present case, the domains of attractions of undesirable performance can be shifted away only by increasing the parametric excitation amplitude. Figure 9 shows the dependence of the percentage of domains of attraction that lead to non-zero flutter oscillation on the excitation amplitude. It is seen that as the excitation amplitude increases both the domains of attraction for low and large response amplitude decrease until critical excitation amplitude, $Y_{cr} \approx 0.01375$, above which the parametric excitation suppresses the wing flutter.

4.3.2 Response at Post-Critical Flutter Speed

At a flow speed that is slightly higher than the critical flutter speed, $U_\infty / b\omega_\alpha = 5.02$, the wing enters in the post flutter region. In the absence of parametric excitation the wing experiences Hopf bifurcation of different amplitude oscillations depending on initial conditions. For all values of initial conditions occupied in Figure 10(a), there are two domains of response amplitudes. Low oscillation amplitudes shown by the region of small solid triangles, \blacktriangle , and large amplitudes shown by solid squares, \blacksquare . Under very small excitation amplitude, the response experiences multi-periods. Over the excitation amplitude range, $0.001 \leq Y_0 < 0.003$, the response experiences multi-periods with growing amplitudes. For example, under excitation amplitude, $Y_0 = 0.0025$, Figures 11(a) and (b) show time history records, phase portraits, Poincaré mapping and FFT plots for two different sets of boundary conditions.

Over another excitation amplitude range, $0.003 < Y_0 < 0.005$, there are two domains of attraction one of them leads to small amplitude oscillations with multi-period as in the previous range, while the other leads to periodic then cascade of period doubling with high amplitude oscillations. Figures 12(a) and (b) show samples of time history records, phase diagram, and FFT for the two cases under excitation amplitude $Y_0 = 0.004$. Figure 12(a) includes also Poincaré maps.

The next region of excitation amplitude, $0.005 < Y_0 < 0.01$, is characterized by chaotic motion for all possible initial conditions. However, one set of initial conditions leads to a chaotic attractor with small amplitude oscillations, while the other set leads to large amplitude oscillations as shown in Figures 13(a) and (b), respectively for $Y_0 = 0.0075$. There is a small window around $Y_0 = 0.01$ characterized by period doubling for all possible initial conditions.

A new regime of response behavior emerges at excitation level range, $0.01 < Y_0 < 0.014$ characterized by a train of spikes known as the “firing” state [54] for certain regions of initial conditions. The remaining initial conditions lead to periodic attractor. For example, under excitation amplitude, $Y_0 = 0.013$, Figures 14(a) and (b) show typical time history records of the firing state. Figures 14(c) and (d) show the periodic regime. Figure 10(b) show the domains of attraction of these four attractors. Note the period between the spikes in the firing state varies substantially. As the excitation amplitude increases the period between the spikes (called the “refractory” or “recovery” period) increases and for the some initial condition the recovery period becomes infinitely large declaring a stabilization effect. Figures 15(a)-(c) show samples of time history records belonging to these regimes. Figure 10(c) shows the domains of attraction that lead to these different attractors. At excitation levels, $Y_0 \geq 0.015$, the response achieves the zero equilibrium position.

Figures 16(a) and (b) show the bifurcation diagram which summarizes all the above stated regimes. In order to appreciate the stabilization effect of parametric excitation, Figure 17 gives the dependence of the percentage of the area of domain of attraction on the excitation amplitude.

5. NUMERICAL SIMULATIONS

The purpose of the numerical simulation of the original equations of motion is to validate the multiple scales predictions. Equations of motion (15) and (16) are numerically integrated for different values of excitation amplitude. The numerical integration is carried out in the absence of air flow and in the presence of air flow at the critical flutter speed for $\mu = 1/38$, $a = -0.36$, $x_\alpha = 0.024$, $r_\alpha = 0.62$, $r = 0.5$, $\zeta_\alpha = 0.001$, $\zeta_u = 0.001$, $d = 0.1$. The following subsections present just representative samples of the numerical simulation and are not considered exhaustive.

5.1 ZERO FLOW SPEED

Under parametric excitation with frequency close to the sum of the first two mode frequencies, $\Omega \approx \omega_1 + \omega_2$, and normal modal frequencies ratio $\omega_1 / \omega_2 \approx 0.5$, the wing response is obtained for different excitation amplitudes. Under all values of excitation amplitude, the response of both bending and torsion exhibits periodic modulated signals as shown in Figures 18(a)-(d). At

relatively low excitation amplitude, the modulation effect is very weak as demonstrated in Figure 18(a) and becomes significant as the excitation amplitude increases. The simulations are carried out for initial conditions $\bar{u}(0) = 0.5$, $\alpha(0) = 0.1$, $\bar{u}'(0) = 0$, $\alpha'(0) = 0$. The bifurcation diagram is shown in Figure 19 which is obtained for initial conditions $\bar{u}(0) = 0.5$, $\alpha(0) = 0.1$, $\bar{u}'(0) = 0$, $\alpha'(0) = 0$.

5.2 CRITICAL FLUTTER SPEED

Under flutter flow speed $U_\infty / b\omega_\alpha = 4.965$ and parametric excitation with frequency close to the sum of the first two mode frequencies, $\Omega = \omega_1 + \omega_2$, and internal frequencies having the relationship $\omega_2 = \omega_1 + 0.061$, the wing response is obtained for different values of excitation amplitudes and initial conditions. Under zero excitation amplitude, and depending on initial conditions, there exist two different LCOs. At excitation amplitude $Y_0 = 0.00875$, and depending on initial conditions the response either preserves the zero equilibrium, or possesses multi-period oscillations as shown in Figure 20(a). These two attractors are maintained up to excitation amplitude 0.013 above which the response is attracted to either the zero response or to a chaotic motion as shown in Figure 20(b) for $Y_0 = 0.014$. Note that the shown Poincaré maps are obtained based on the excitation period. As the excitation amplitude increases, say to $Y_0 = 0.016$, the chaotic regime is characterized by occasional spikes followed by relaxation period as shown in Figure 20(c). The zero response is not shown for this case. At excitation amplitude $Y_0 = 0.017$ the non-zero response becomes more ordered after experiencing spiky transition period as shown in Figure 20(d).

5.3 POST-CRITICAL SPEED

At slightly higher value of flow speed than the critical flutter speed, say, $U_\infty / b\omega_\alpha = 5.02$, the numerical simulation is presented for selected values of excitation amplitude. At zero excitation amplitude the wing wings experiences LCOs in bending and torsion. The zero attractor disappears for all excitation levels up to excitation amplitude of 0.013. As the excitation level increases from a low value up to 0.013, the response time history records experience multi-periods and Figures 21(a)-(d) show the sequence of development of the response time history records for different values of excitation amplitude. For excitation levels of 0.014, and above, the zero attractor emerges for certain domain of attraction in addition to a multi-period attractor depending on the initial conditions. For example, Figures 22(a) and (b) show time history records at excitation level 0.015 for two different sets of initial conditions. The domains of attraction that lead to zero attractor are enlarged as the excitation amplitude increases and this confirms the results predicted by the multiple scales method.

5. CONCLUSIONS

The nonlinear flutter of a cantilever wing is studied analytically and numerically in the absence and presence of parametric excitation. In the absence of nonlinearities, the regions of parametric instability are obtained for different values of flow speed.

- At the critical flutter speed the bottom of instability region touches the frequency axis.

- Below and above the critical speed the instability regions move away from the frequency axis.
- As the excitation amplitude increases the responses experiences a cascade of period doubling and eventually chaotic motion.
- At critical excitation amplitude the response exhibits stabilization state to the zero equilibrium attractor over a wide range of initial conditions. This new and unexpected feature motivated the authors to add a review assessment of parametric excitation-induced stability.
- The stabilization effect was also manifested at a flow speed that is slightly higher than the critical flutter speed. However, the stabilization effect was preceded by new phenomena such as firing and recovery states.
- The numerical simulation of the original equations of motion has confirmed the multiple scales findings.

Appendix A: Elements of equation (22)

$$AA(k_\alpha, \bar{\omega}) = \bar{\omega}^2 (A_R + iA_I) + 2ir\zeta_u \bar{\omega} + r^2,$$

$$BB(k_\alpha, \bar{\omega}) = \bar{\omega}^2 (B_R + iB_I),$$

$$DD(k_\alpha, \bar{\omega}) = \bar{\omega}^2 (D_R + iD_I),$$

$$EE(k_\alpha, \bar{\omega}) = \bar{\omega}^2 (E_R + iE_I) + 2ir_\alpha \zeta_\alpha \bar{\omega} + r_\alpha^2$$

where

$$A_R = -\left(1 + \mu + \frac{2\mu G(k)}{k_\alpha \bar{\omega}}\right), \quad A_I = \frac{2\mu F(k)}{k_\alpha \bar{\omega}}, \quad B_R = c_6 \left[-x_\alpha + \left(a + \frac{2F(k)}{(k_\alpha \bar{\omega})^2} - (1-2a) \frac{G(k)}{k_\alpha \bar{\omega}} \right) \mu \right],$$

$$B_I = \frac{c_6 \mu}{k_\alpha \bar{\omega}} \left[1 + \frac{2G(k)}{(k_\alpha \bar{\omega})} - (1-2a) F(k) \right], \quad D_R = c_7 \left[-x_\alpha + \left(a + (1+2a) \frac{G(k)}{k_\alpha \bar{\omega}} \right) \mu \right],$$

$$D_I = -c_7 (1+2a) \frac{\mu F(k)}{k_\alpha \bar{\omega}}, \quad E_R = -r_\alpha^2 + \mu \left[-\left(\frac{1}{8} + a^2 \right) + \left(\frac{1}{2} - 2a^2 \right) \frac{G(k)}{k_\alpha \bar{\omega}} - (1+2a) \frac{F(k)}{(k_\alpha \bar{\omega})^2} \right],$$

$$E_I = \frac{\mu}{k_\alpha \bar{\omega}} \left[\frac{1}{2} - a - \left(\frac{1}{2} - 2a^2 \right) F(k) - (1+2a) \frac{G(k)}{k_\alpha \bar{\omega}} \right],$$

$$F(k_\alpha \bar{\omega}) = 1 - \frac{0.165(k_\alpha \bar{\omega})^2}{(k_\alpha \bar{\omega})^2 + 0.00207} - \frac{0.335(k_\alpha \bar{\omega})^2}{(k_\alpha \bar{\omega})^2 + 0.09}, \text{ and}$$

$$G(k_\alpha \bar{\omega}) = -\frac{0.000883735k_\alpha \bar{\omega} + 0.108008(k_\alpha \bar{\omega})^3}{0.000186323 + 0.0920702(k_\alpha \bar{\omega})^2 + (k_\alpha \bar{\omega})^4}.$$

Appendix B: The parameters $p_i, i=1,2,3,4$ in equations (27) and (28)

$$p_1(k) = \frac{16c_7 r^2 (x_\alpha - a\mu)}{8r_\alpha^2 (1 + \mu - r^2) - \mu \left[r^2 (1 + 8a^2) + \frac{8B(k)}{k_\alpha^2} (1 + \mu + 2c_6 c_7 x_\alpha + 2a(1 + \mu - c_6 c_7) \mu) \right] + \sqrt{p_4(k)}},$$

$$p_2(k) = \frac{16c_7 r^2 (x_\alpha - a\mu)}{8r_\alpha^2 (1 + \mu - r^2) - \mu \left[r^2 (1 + 8a^2) + \frac{8B(k)}{k_\alpha^2} (1 + \mu + 2c_6 c_7 x_\alpha + 2a(1 + \mu - c_6 c_7) \mu) \right] - \sqrt{p_4(k)}},$$

$$p_3(k) = 8r_\alpha^2 (1 + r^2 + \mu) + \mu \left[r^2 (1 + 8a^2) - \frac{8B(k)}{k_\alpha^2} (1 + \mu (1 + 2a(1 - c_6 c_7)) + 2(a + c_6 c_7 x_\alpha)) \right],$$

$$p_4(k) = p_3^2 - 32r^2 \left[r_\alpha^2 - \frac{B(k)\mu}{k_\alpha^2} (1 + 2a) \right] \left[8r_\alpha^2 (1 + \mu) + \mu (1 + \mu) (1 + 8a^2) - 8c_6 c_7 (x_\alpha - a\mu)^2 \right].$$

Appendix C: Coefficients C_i in equations (43)

$$C_1 = 3q_{15} + q_{11} \bar{\omega}_2^2, \quad C_2 = q_7 \bar{\omega}_1 + q_{18} \bar{\omega}_2, \quad C_3 = q_{16} + 3q_9 \bar{\omega}_1^2 - q_6 \bar{\omega}_2 \bar{\omega}_1$$

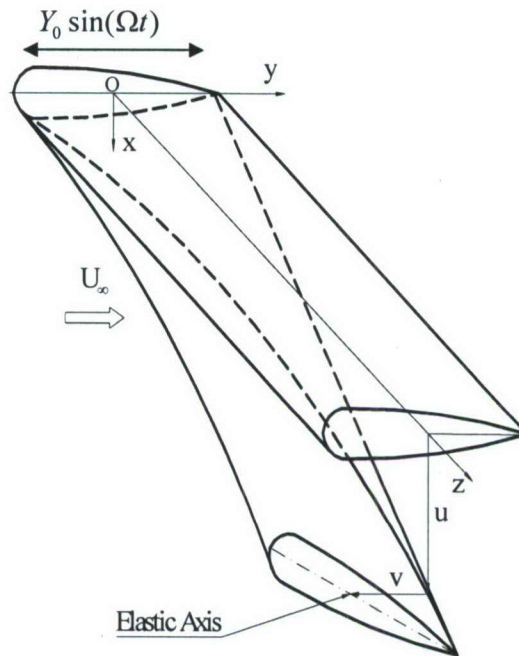
$$\begin{aligned}
C_4 &= -q_{19} + q_8 \frac{\bar{\omega}_2}{\bar{\omega}_1}, & C_5 &= \frac{q_3}{\bar{\omega}_1} + q_{10} \bar{\omega}_2 - q_5 \frac{\bar{\omega}_2^2}{\bar{\omega}_1}, & C_6 &= 3s_{14} + s_4 \bar{\omega}_1^2, & C_7 &= s_{19} \bar{\omega}_1 + s_8 \bar{\omega}_2 \\
C_8 &= s_3 + 3s_5 \bar{\omega}_2^2 - s_{10} \bar{\omega}_1 \bar{\omega}_2, & C_9 &= -s_7 + s_{18} \frac{\bar{\omega}_2}{\bar{\omega}_1}, & C_{10} &= \frac{s_{16}}{\bar{\omega}_2} + s_6 \bar{\omega}_1 - s_9 \frac{\bar{\omega}_1^2}{\bar{\omega}_2} \\
C_{11} &= 6s_{14} + 2s_4 \bar{\omega}_1^2, & C_{12} &= 6q_{15} + 2q_{11} \bar{\omega}_2^2, \\
C_{13} &= 2(3s_3 \bar{\omega}_1 + 3q_{16} \bar{\omega}_2 + (q_9 + s_{10}) \bar{\omega}_1^2 \bar{\omega}_2 + (q_6 + s_5) \bar{\omega}_1 \bar{\omega}_2^2) \\
C_{14} &= 2[3s_{19} \bar{\omega}_1^2 + (q_7 - s_8) \bar{\omega}_1 \bar{\omega}_2 - 3q_{18} \bar{\omega}_2^2], & C_{15} &= (2s_{16} \bar{\omega}_1 + 2s_9 \bar{\omega}_1^3 + 3q_{14} \bar{\omega}_2 + q_4 \bar{\omega}_1^2 \bar{\omega}_2) \\
C_{16} &= s_{16} \bar{\omega}_1 - s_9 \bar{\omega}_1^3 + s_6 \bar{\omega}_1^2 \bar{\omega}_2, & C_{17} &= s_7 \bar{\omega}_1^2 - s_{18} \bar{\omega}_1 \bar{\omega}_2, & C_{18} &= 2q_3 \bar{\omega}_2 + 2q_5 \bar{\omega}_2^3 + 3s_{15} \bar{\omega}_1 + s_{11} \bar{\omega}_2^2 \bar{\omega}_1 \\
C_{19} &= q_3 \bar{\omega}_2 - q_5 \bar{\omega}_2^3 + q_{10} \bar{\omega}_2^2 \bar{\omega}_1, & C_{20} &= q_8 \bar{\omega}_2^2 - q_{19} \bar{\omega}_1 \bar{\omega}_2, & C_{21} &= s_2 \bar{\omega}_1 b_1^2 + q_1 \bar{\omega}_2 b_2^2, & C_{22} &= 6s_{14} + 2s_4 \bar{\omega}_1^2, \\
C_{23} &= 6q_{15} + 2q_{11} \bar{\omega}_2^2, & C_{24} &= 2[-3s_3 \bar{\omega}_1 + 3q_{16} \bar{\omega}_2 + (q_9 - s_{10}) \bar{\omega}_1^2 \bar{\omega}_2 + (q_6 - s_5) \bar{\omega}_1 \bar{\omega}_2^2] \\
C_{25} &= 2[-3s_{19} \bar{\omega}_1^2 + (q_7 + s_8) \bar{\omega}_1 \bar{\omega}_2 - 3q_{18} \bar{\omega}_2^2], & C_{26} &= [-2s_{16} \bar{\omega}_1 - 2s_9 \bar{\omega}_1^3 + 3q_{14} \bar{\omega}_2 + q_4 \bar{\omega}_1^2 \bar{\omega}_2] \\
C_{27} &= -s_{16} \bar{\omega}_1 + s_9 \bar{\omega}_1^3 - s_6 \bar{\omega}_1^2 \bar{\omega}_2, & C_{28} &= -s_7 \bar{\omega}_1^2 + s_{18} \bar{\omega}_1 \bar{\omega}_2, & C_{29} &= 2q_3 \bar{\omega}_2 + 2q_5 \bar{\omega}_2^3 - 3s_{15} \bar{\omega}_1 - s_{11} \bar{\omega}_2^2 \bar{\omega}_1, \\
C_{30} &= q_3 \bar{\omega}_2 - q_5 \bar{\omega}_2^3 + q_{10} \bar{\omega}_2^2 \bar{\omega}_1, & C_{31} &= q_8 \bar{\omega}_2^2 - q_{19} \bar{\omega}_1 \bar{\omega}_2, & C_{32} &= s_2 \bar{\omega}_1 b_1^2 - q_1 \bar{\omega}_2 b_2^2.
\end{aligned}$$

References

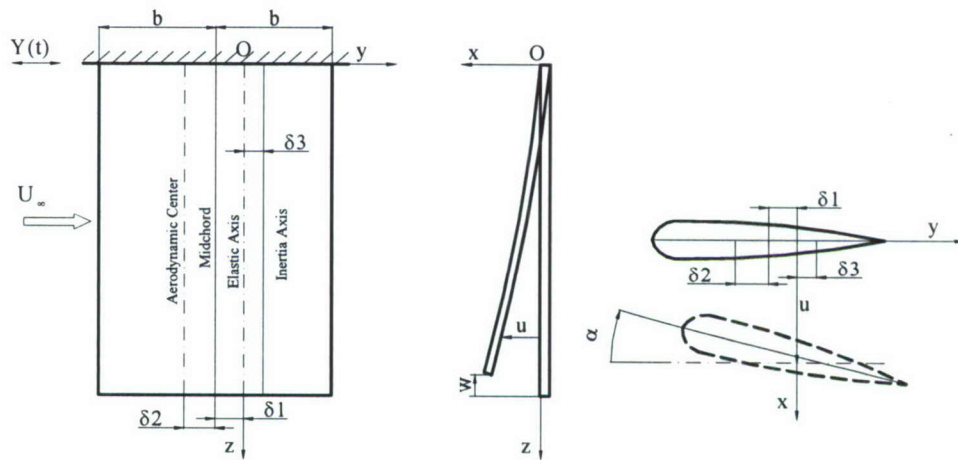
1. Bisplinghoff, R. L., Ashley, H., and Halfman, R. L., *Aeroelasticity*, Addison-Wesley Publishing Co., Reading, Massachusetts, 1955.
2. Bisplinghoff, R. L. and Ashley, H., *Principles of Aeroelasticity*, Dover Publications, New York, 1962.
3. Fung, Y. C., *Introduction to the Theory of Aeroelasticity*, Dover Publications, New York, 1968.
4. Dowell, E. H., Curtis, H. C., Scanlan, R. H., and Sisto, F., *A modern Course in Aeroelasticity*, Sijthoff & Noordhoff, Alphen and den Rijn, The Netherlands, 1976.
5. Bolotin, V. V., *The Dynamic Stability of Elastic Systems*, Holden-Day, San Francisco, 1964.
6. Barr, A. D., 'Some developments in parametric stability and nonlinear vibration,' *Proceedings of the International Conference on Recent Advances in Structural Dynamics*, Southampton, England, 1980, 545-568.
7. Breitbach, E. J., *Effect of structural nonlinearities on aircraft vibration*, Advisory Group for Aerospace Research and Development of NATO, AGARD Report No. 665, 1977.
8. Breitbach, E. J., *Flutter analysis of an airplane with multiple structural nonlinearities in the control system*, NASA Technical Report 1620, 1980.
9. De Ferrari, G., Chesta, L., Sensburg, O., and Lotze, A., *Effects of nonlinearity of wing-store flutter*, Advisory Group for Aerospace Research and Development of NATO, AGARD Report No. 687, 1980.
10. Peloubet, R. P., Jr., Haller, R. L., and Bolding R. M., 'F-16 flutter suppression system investigation,' *Proc of the AIAA/ASME/ASCE/AHS 21st Structures, Structural Dynamics & Materials Conference*, Seattle, Washington, 1980, 620-634.
11. Reed, W. H. III, Foughner, J. T., Jr., and Runyan, H. L., 'Decoupler pylon: A simple effective wing/store suppressor,' *Journal of Aircraft* 17(3), 1980, 206-211.
12. Desmarais, R. N. and Reed, W. H. III, 'Wing/store flutter with nonlinear pylon stiffness,' *Journal of Aircraft* 19(11), 1981, 984-987.
13. Lee, B. H. K., Price, S. J., and Wong, Y. S., 'Nonlinear aeroelastic analysis of airfoils: bifurcation and chaos,' *Progress in Aerospace Sciences* 35, 1999, 205-334.

14. Laurenson, R. M. and Trn, R. M., 'Flutter analysis of missile control surfaces containing structural nonlinearities,' *AIAA Journal* **18**(10), 1980, 1245-1251.
15. Woolston, D. S., Runyan, H. W. and Andrews, R. E., 'An investigation of effects of certain type of structural nonlinearities on wing and control surface flutter,' *Journal of Aeronautical Sciences* **24**, 1957, 57-63.
16. Kim, S. H. and Lee, I., 'Aeroelastic analysis of a flexible airfoil with a free-play non-linearity,' *Journal of Sound and Vibration* **193**(4), 1996, 823-846.
17. Yang, Z. C. and Zhao, L. C., 'Analysis of limit cycle flutter of an airfoil in incompressible flow,' *Journal of Sound and Vibration* **123**(1), 1988, 1-13.
18. Alighanbari, H., 'Aeroelastic response of an airfoil-aileron combination with free-play in aileron hinge,' *Journal of Aircraft* **39**(4), 2002, 711-713.
19. Bae, J. S. and Lee, I., 'Limit cycle oscillation of missile control fin with structural nonlinearity,' *Journal of Sound and Vibration* **269**(3-5), 2004, 669-687.
20. Bae, J. S., Yang, S. M., and Lee, I., 'Linear and nonlinear aeroelastic analysis of fighter-type wing with control surface,' *Journal of Aircraft* **39**, 2002, 697-708.
21. Bae, J. S., Kim, D. K., Shin, W. H., Lee, I., and Kim, S. H., 'Nonlinear aeroelastic analysis of deployable missile control fin,' *Journal of Spacecraft and Rockets* **41**(2), 2004, 264-271.
22. Bae, J. S., Inman, D. J., and Lee, I., 'Effects of structural nonlinearity on subsonic aeroelastic characteristics of an aircraft wing with control surface,' *Journal of fluids and structures* **19**, 2004, 747-763.
23. Ueda, T. and Dowell, E. H., 'A new solution method for lifting surfaces in subsonic flow,' *AIAA Journal* **20**, 1982, 348-355.
24. Zhao, Y. H. and Hu, H. Y., 'Aeroelastic analysis of a nonlinear airfoil based on unsteady vortex lattice model,' *Journal of Sound and Vibration* **276**, 2004, 491-510.
25. Lee, B. H. K., Jiang, L. Y., and Wong, Y. S., 'Flutter of an airfoil with a cubic restoring force,' *Journal of Fluids and Structures* **13**, 1999, 75-101.
26. Lee, B. H. K., Liu, L., and Chung, K. W., 'Airfoil motion in subsonic flow with strong cubic nonlinear restoring forces,' *Journal of Sound and Vibration* **281**, 2005, 699-717.
27. Liu, L., Wong, Y. S., and Lee, B. H. K., 'Application of the centre manifold theory in non-linear aeroelasticity,' *Journal of Sound and Vibration* **234**(4), 2000, 641-659.
28. Liu, L. and Dowell, E. H., 'The secondary bifurcation of an aeroelastic airfoil motion: effects of high harmonics,' *Nonlinear Dynamics* **37**, 2004, 31-49.
29. Zhao, L. C. and Yang, Z. C., 'Chaotic motions of an airfoil with non-linear stiffness in incompressible flow,' *Journal of Sound and Vibration* **138**(2), 1990, 245-254.
30. Price, S. J., Alighanbari, H., and Lee, B. H. K., 'The aeroelastic response of a two-dimensional airfoil with bilinear and cubic structural nonlinearities,' *Journal of Fluids and Structures* **9**, 1995, 175-193.
31. Singh, S. N. and Brenner, M., 'Limit cycle oscillation and orbital stability in aeroelastic systems with torsional nonlinearity,' *Nonlinear Dynamics* **31**, 2003, 435-450.
32. Dessi, D. and Mastroddi, F., 'Limit-cycle stability reversal via singular perturbation and wing-flap flutter,' *Journal of Fluids and Structures* **19**, 2004, 765-783.
33. Collier, B. D. and Chamara, P. A., 'Structural non-linearities and the nature of the classic flutter instability,' *Journal of Sound and Vibration* **227**, 2004, 711-739.
34. Shahrzad, P. and Mahzoon, M., 'Limit cycle flutter of airfoils in steady and unsteady flows,' *Journal of Sound and Vibration* **256**(2), 2002, 213-225.
35. Gilliatt, H. C., Strganac, T. W., and Kurdila, A. J., 'An investigation of internal resonance in aeroelastic systems,' *Nonlinear Dynamics* **31**, 2003, 1-22.
36. Marzocca, P., Librescu, L., and Silva, W., 'Aeroelastic response of nonlinear wing sections using a functional series technique,' *AIAA Journal* **40**(5), 2002, 813-824.

37. Tang, D. M. and Dowell, E. H., 'Effects of geometric structural nonlinearity on flutter and limit cycle oscillations of high-aspect-ratio wings,' *Journal of Fluids and Structures* **19**, 2004, 291-306.
38. Ashley, H., 'Some observations on four current subjects related to aeroelastic stability,' *Israel Journal of Technology* **16**, 1978, 3-22.
39. Poirel, D. and Price, S. J., 'Random binary (coalescence) flutter of a two-dimensional linear airfoil,' *Journal of Fluids and Structures* **18**, 2003, 23-42.
40. Poirel, D. and Price, S. J., 'Response probability structure of a structurally nonlinear fluttering airfoil in turbulent flow,' *Probabilistic Engineering Mechanics* **18**, 2003, 185-202.
41. Yates, E. C., Jr., *Calculation of flutter characteristics for finite span swept or unswept wings at subsonic and supersonic speeds by a modified strip analysis*, NACA RM L47L10, 1958.
42. Garrick, I. E. and Rabinow, S. I., *Flutter and oscillating air force calculations for an airfoil in a two-dimensional supersonic flow*, NACA Rept No. 846, 1946.
43. Lesing, H. C., Troutman, J. L., and Menees, G. P., *Experimental determination of the pressure distribution on a rectangular wing oscillating in the first bending mode for mach numbers from 0.24 to 1.3*, NASA TN D-344, 1960.
44. Watkins, C. E., Woolston, D. S., and Cunningham, H. J., *A systematic kernel function procedure for determining aerodynamic forces on oscillating or steady finite wings at subsonic speeds*, NASA TR R-48, 1959.
45. Theodorsen, T., *General theory of aerodynamic instability and mechanism of flutter*, NACA Rept No. 496, 1935.
46. Theodorsen, T. and Garrick, I. E., *Mechanics of flutter: A theoretical and experimental investigation of flutter problem*, NACA Rept. 685, 1940.
47. Ibrahim, R. A. and Hijawi, M., 'Deterministic and stochastic response of nonlinear coupled bending-torsion modes in a cantilever beam,' *Nonlinear Dynamics* **16**(3), 1998, 259-292.
48. Lumbantobing, H. and Haaker, T. I., 'On the parametric excitation of some nonlinear aeroelastic oscillators,' *Journal of Fluids and Structures* **19**, 2004, 221-237.
49. Chin, C., Nayfeh, A. H., and Mook, D. T., 'The response of a nonlinear system with a non-semisimple one-to-one resonance to a combination resonance,' *International Journal of Bifurcation and Chaos* **5**(1), 1995, 971-982.
50. Love, A. E. H., *A Treatise on the Mathematical Theory of Elasticity*, Dover, New York, 1944.
51. Jones, R. T., *The unsteady lift of a wing of finite aspect ratio*, NACA Rept 681, 1940.
52. Nayfeh, A. H., and Mook, D., *Nonlinear Oscillations*, Wiley Interscience, New York, 1979.
53. Boccaletti, S., Grebogi, C., Lai, Y. -C., Mancini, H., and Maza, D., 'The control of chaos: Theory and applications,' *Physics Reports* **329**, 2000, 103-197.
54. Lindner, B., Garcia-Ojalvo, J., Neiman, A., Schimansky-Geier, L., 'Effects of noise in excitable systems,' *Physics Reports* **392**, 2004, 321-424.



(a)



(b)

Figure 1. Schematic diagram of the analytical model, coordinates axes, and deformations.

- Plate-like cantilever wing showing the coordinate frame
- Locations of different axes and deformations in bending, torsion, and longitudinal.

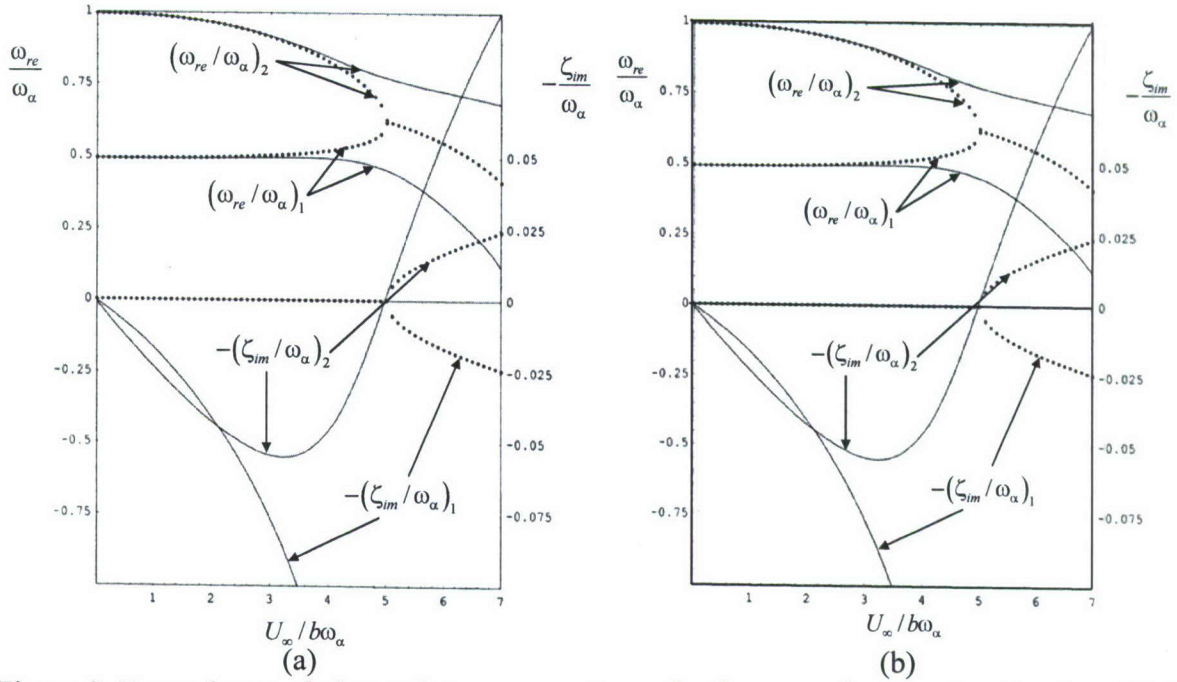


Figure 2. Dependence of eigenvalue components on the flow speed parameter showing: (a) the influence of the imaginary component of circulation function, $G \neq 0$ and (b) its absence, $G = 0$.

— Eigenvalue components in the presence of aerodynamic and structure damping
 Eigenvalue components in the absence of aerodynamic and structure damping.

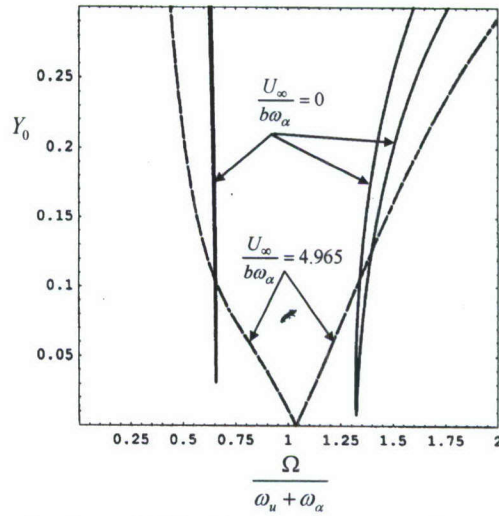


Figure 3. Stability boundaries in the neighborhood of parametric combination resonance at zero flow speed and at critical flow speed.

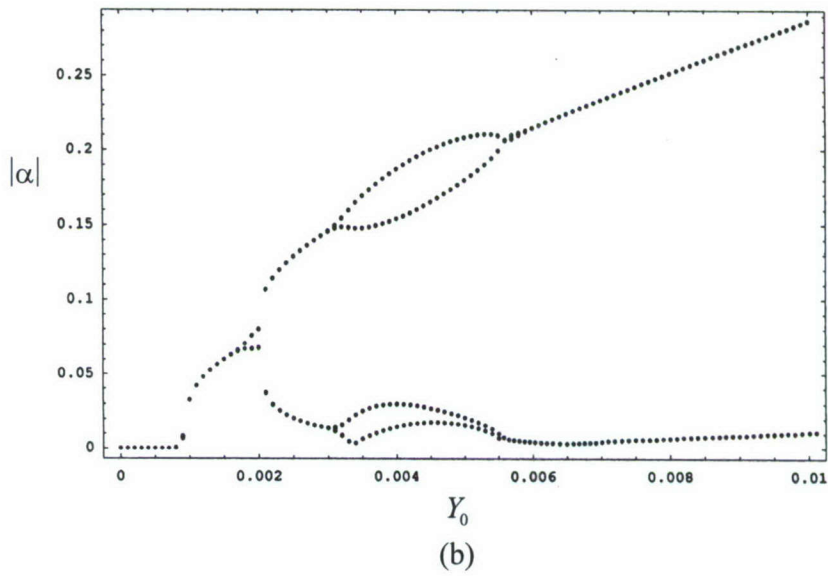
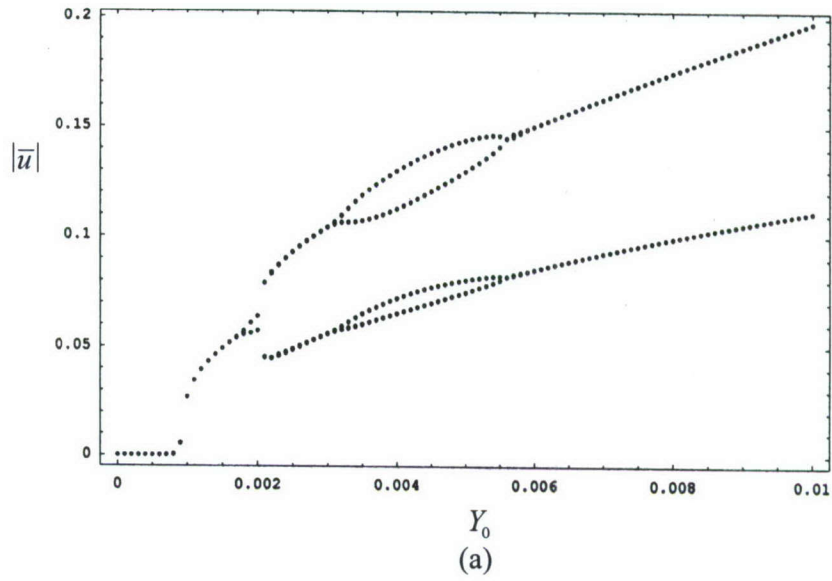


Figure 4. Bifurcation diagram at zero critical flow speed estimated at $\Omega = \omega_1 + \omega_2$, $\omega_1 = 0.5\omega_2$, for $\sigma_e = 0$, $\bar{u}(0) = 0.1$, $\alpha(0) = 0.1$, $\bar{u}'(0) = 0$, $\alpha'(0) = 0$.

- (a) Dependence of bending response on excitation amplitude.
- (b) Dependence of torsion response on excitation amplitude.

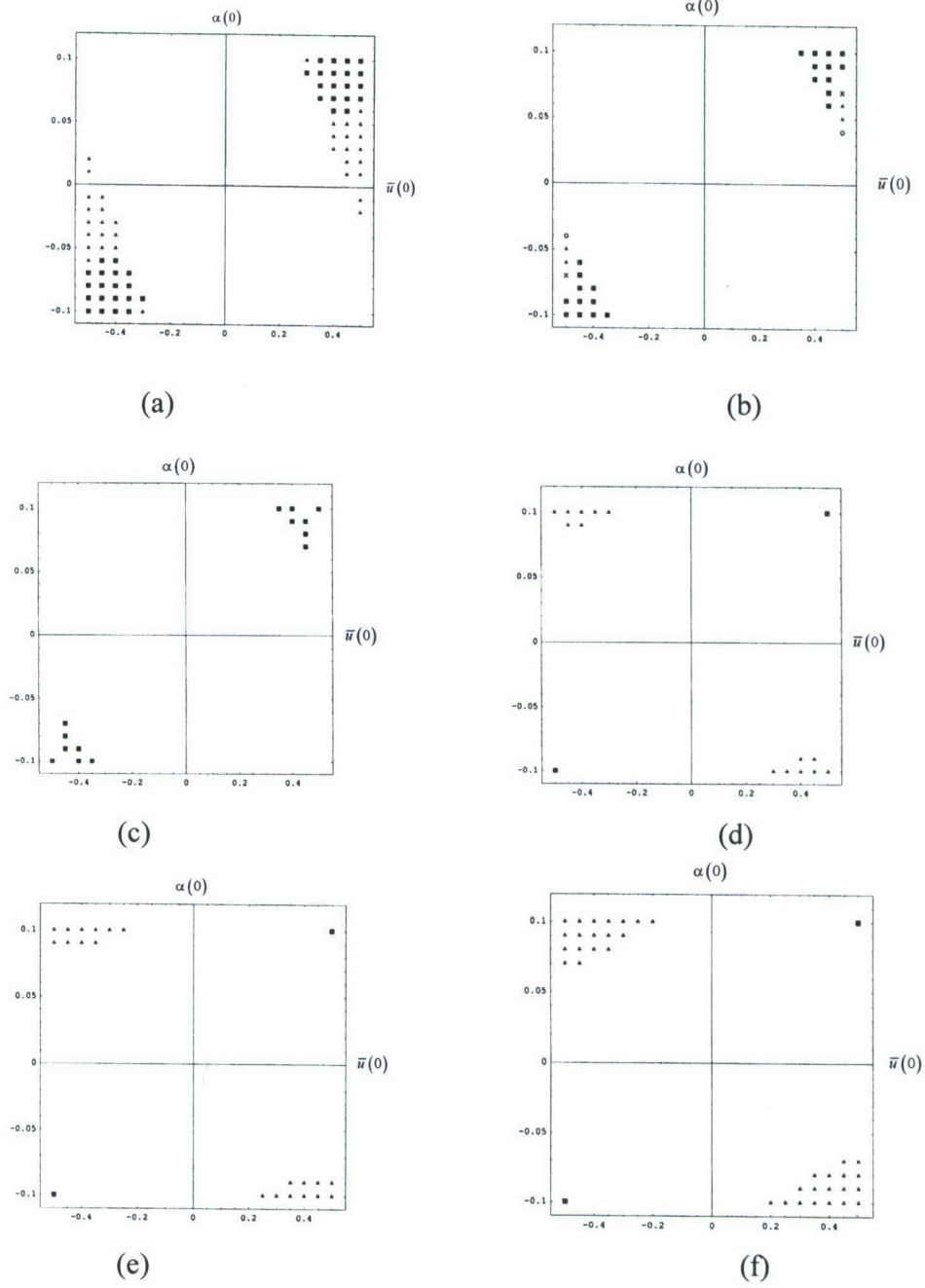


Figure 5. Domains of attractions for different values of excitation amplitude.

(a) $Y_0 = 0$; (b) $Y_0 = 0.00875$; (c) $Y_0 = 0.01$; (d) $Y_0 = 0.014$; (e) $Y_0 = 0.015$; (f) $Y_0 = 0.017$

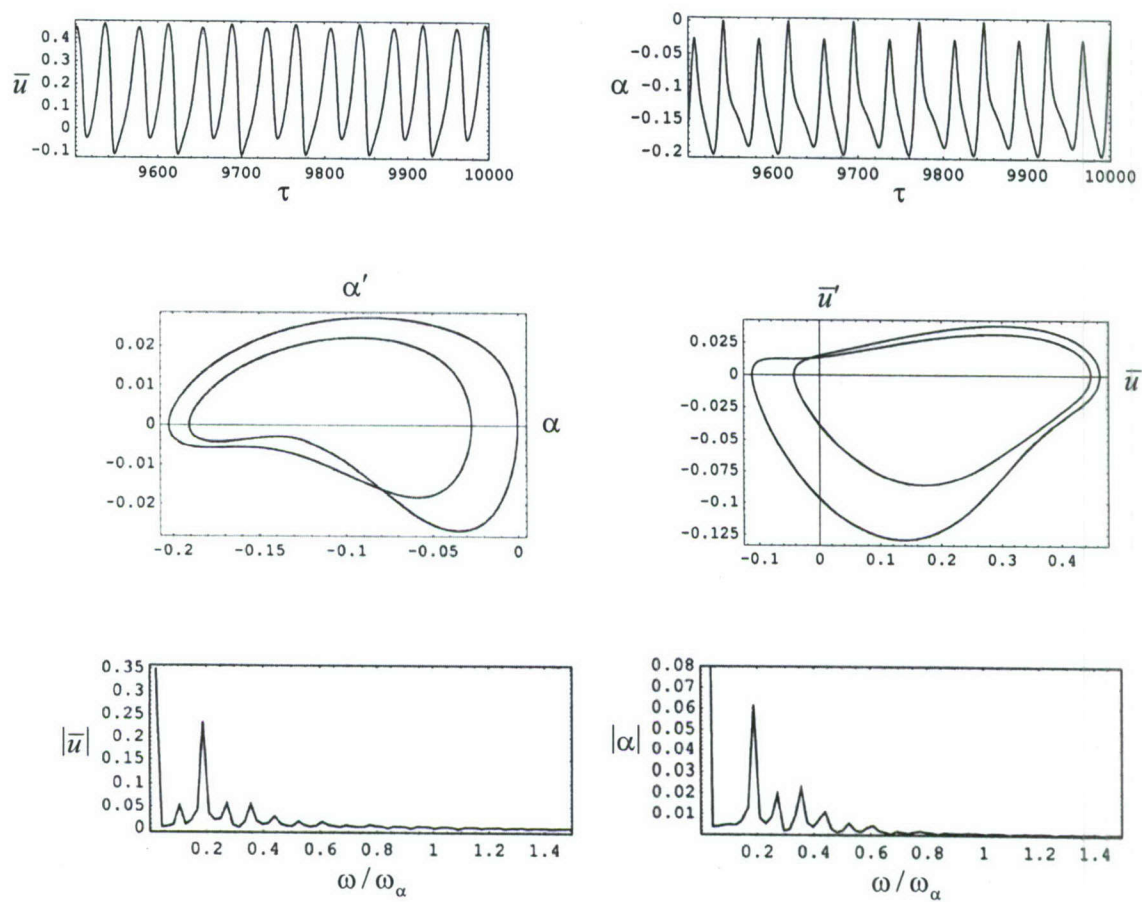


Figure 6(a).

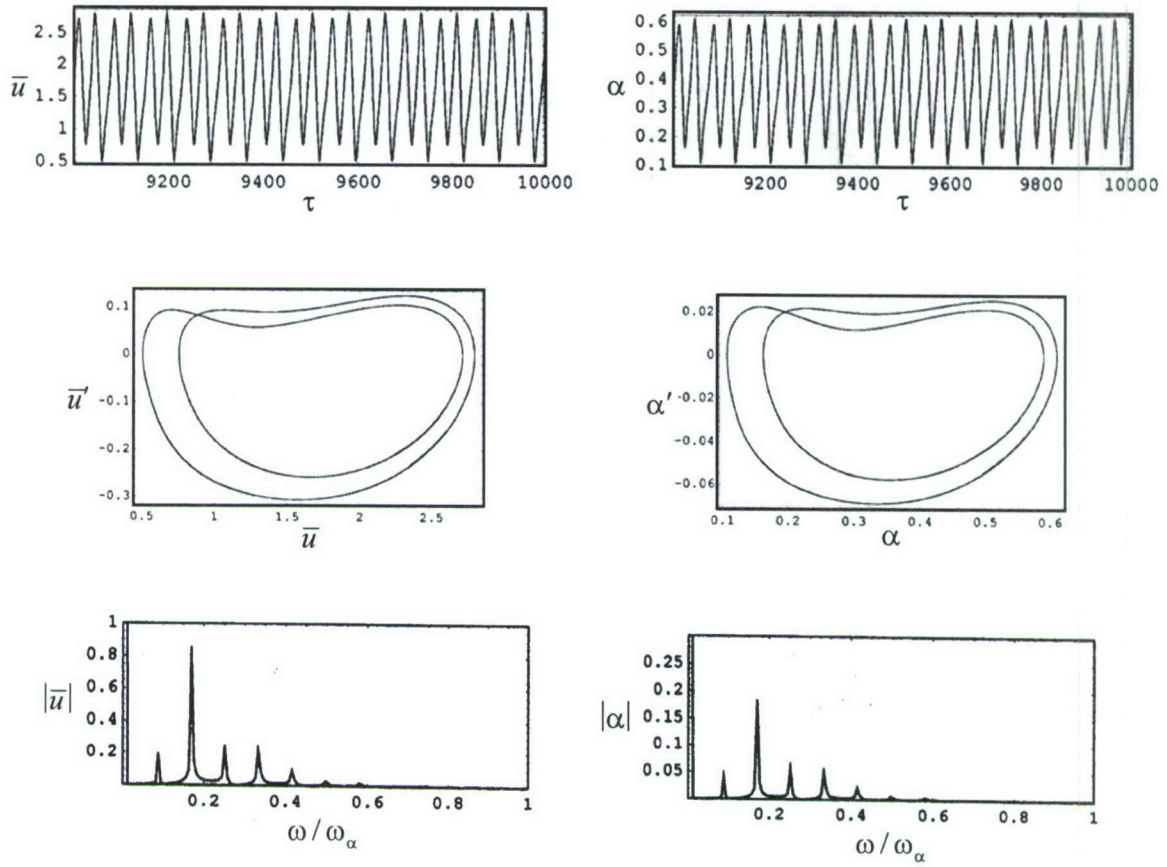


Figure 6(b).

Figure 6. Time history records, phase portraits, FFT plots at critical flow speed $U_\infty / b\omega_\alpha = 4.965$, for $Y_0 = 0.015$; $\Omega = \omega_1 + \omega_2$, $\omega_1 = \omega_2$, $\sigma_e = 0$, $\sigma_i = 0.061$, and for two sets of initial conditions.

(a) $\bar{u}(0) = 0.5$, $\alpha(0) = -0.1$, $\bar{u}'(0) = 0$, $\alpha'(0) = 0$;

(b) $\bar{u}(0) = 0.5$, $\alpha(0) = 0.1$, $\bar{u}'(0) = 0$, $\alpha'(0) = 0$

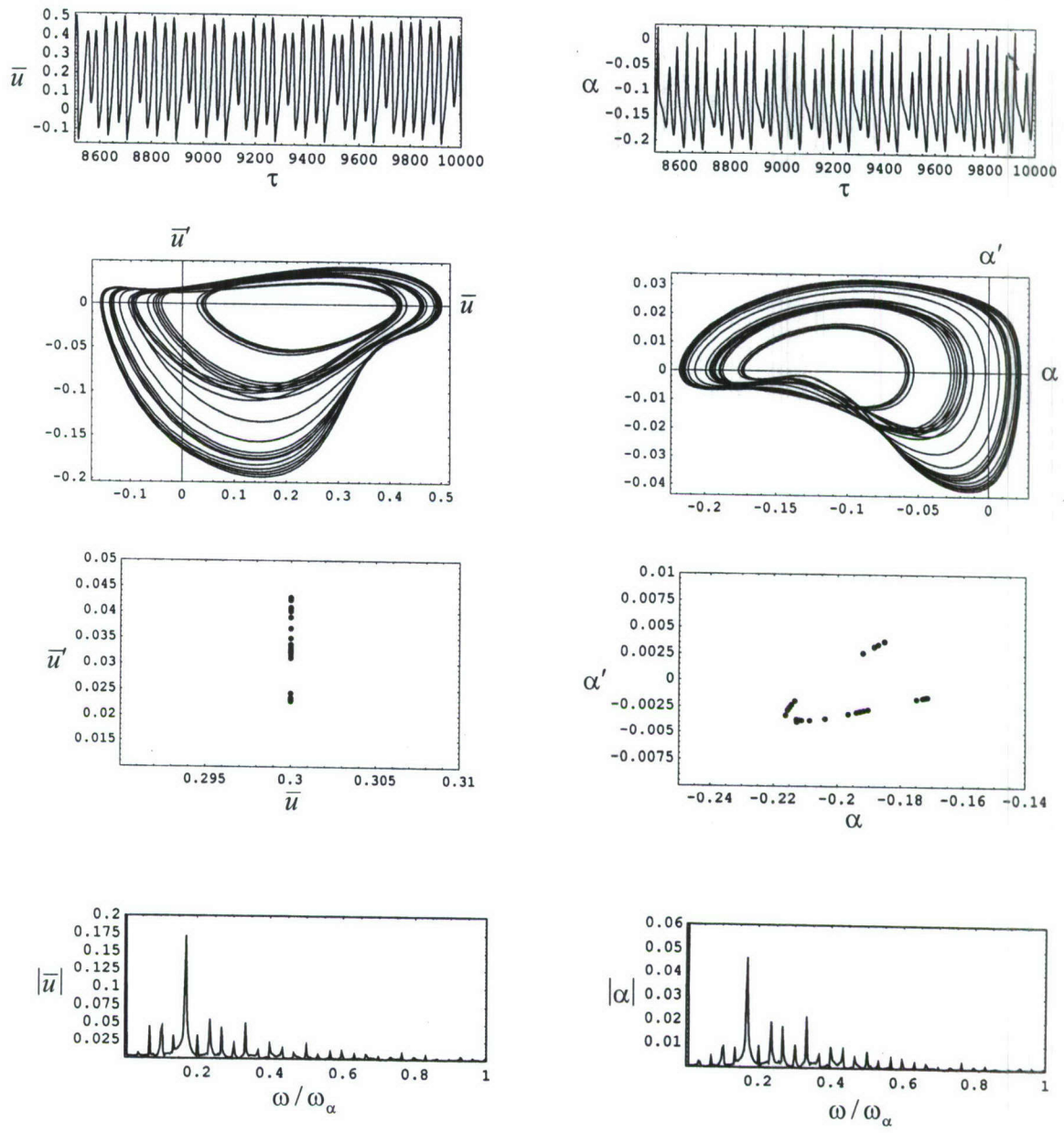


Figure 7(a).

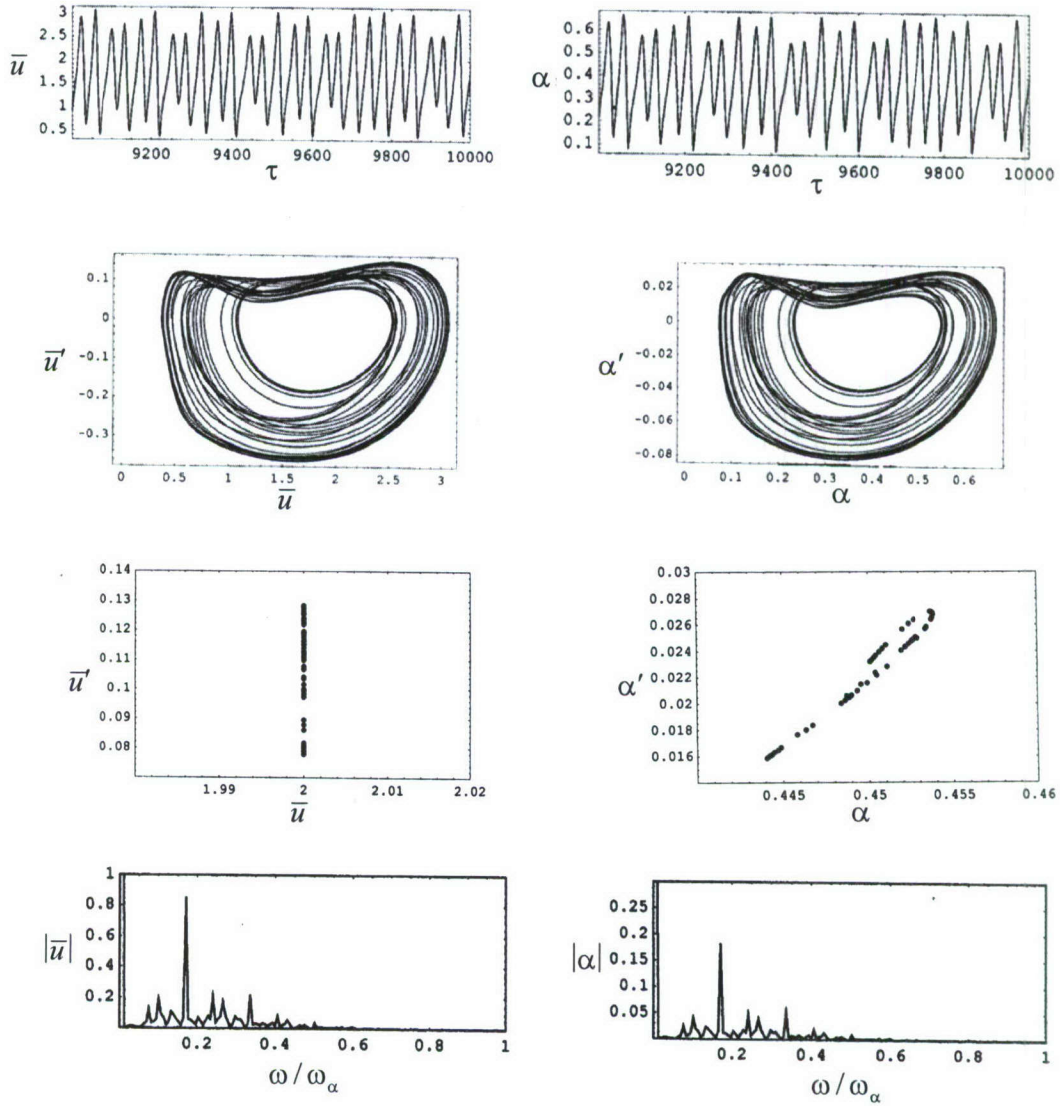
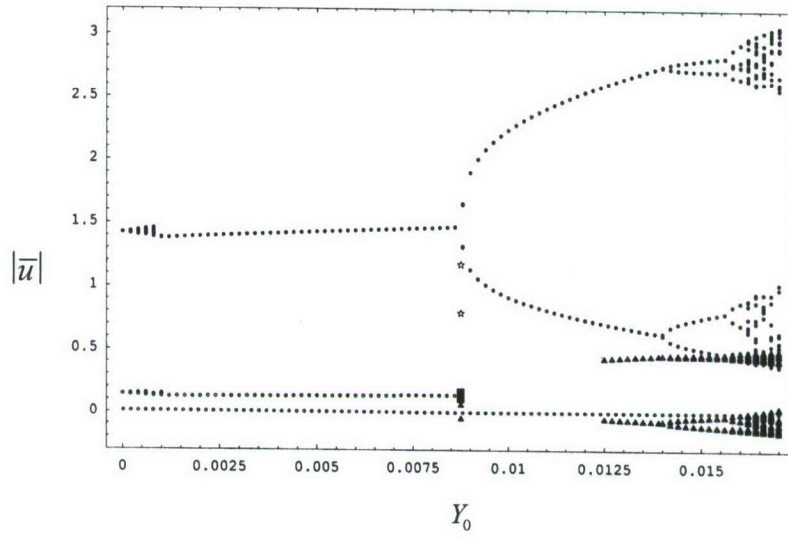


Figure 7(b).

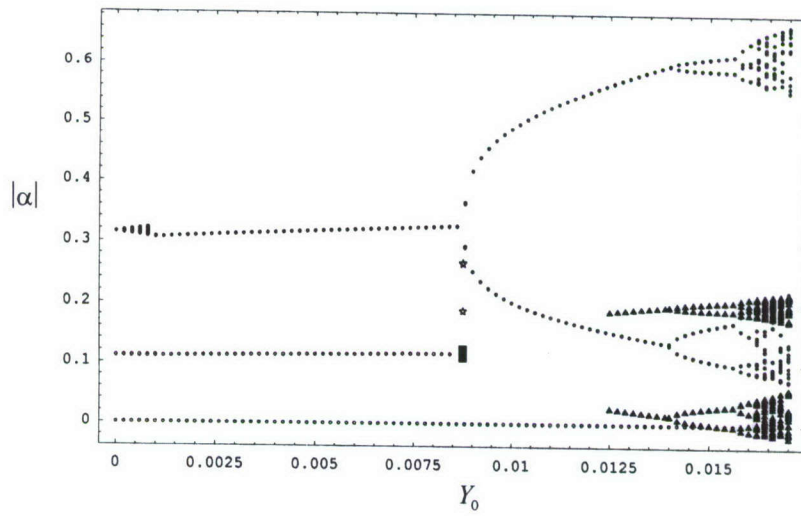
Figure 7. Time history records, phase portraits, Poincaré maps, and FFT plots at critical flow speed $U_\infty / b\omega_\alpha = 4.965$, excitation amplitude $Y_0 = 0.017$; $\Omega = \omega_1 + \omega_2$, $\omega_1 = \omega_2$, $\sigma_e = 0$, $\sigma_i = 0.061$, for two different sets of initial conditions

(a) $\bar{u}(0) = 0.5$, $\alpha(0) = -0.1$, $\bar{u}'(0) = 0$, $\alpha'(0) = 0$

(b) $\bar{u}(0) = 0.5$, $\alpha(0) = 0.1$, $\bar{u}'(0) = 0$, $\alpha'(0) = 0$



(a)



(b)

Figure 8. Bifurcation diagrams at critical flow speed $U_\infty / b\omega_\alpha = 4.965$, $\Omega = \omega_1 + \omega_2$, $\omega_1 = \omega_2$, $\sigma_e = 0$, $\sigma_i = 0.061$.

- (a) Dependence of bending amplitude on excitation amplitude.
- (b) Dependence of torsion amplitude on excitation amplitude.

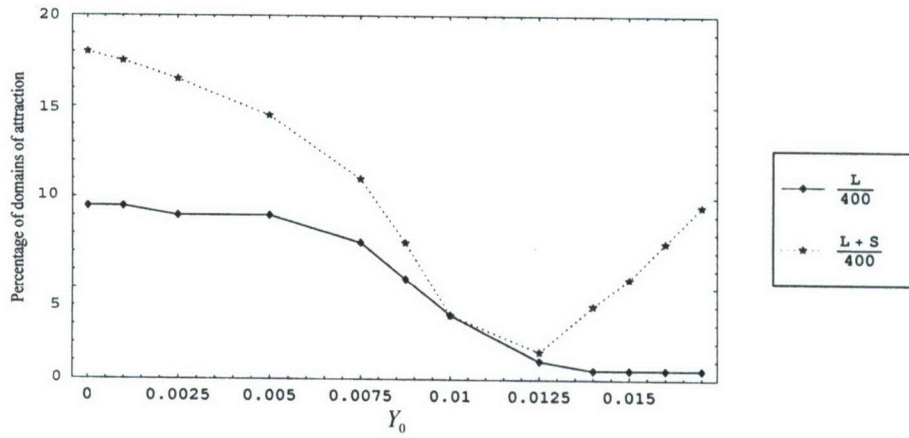


Figure 9. Stabilization effect of parametric excitation at critical flow speed $U_\infty / b\omega_\alpha = 4.965$ showing the percentage of domains of attraction for large amplitude response (solid diamond curve) and large plus small amplitude responses (dotted solid circle curve).

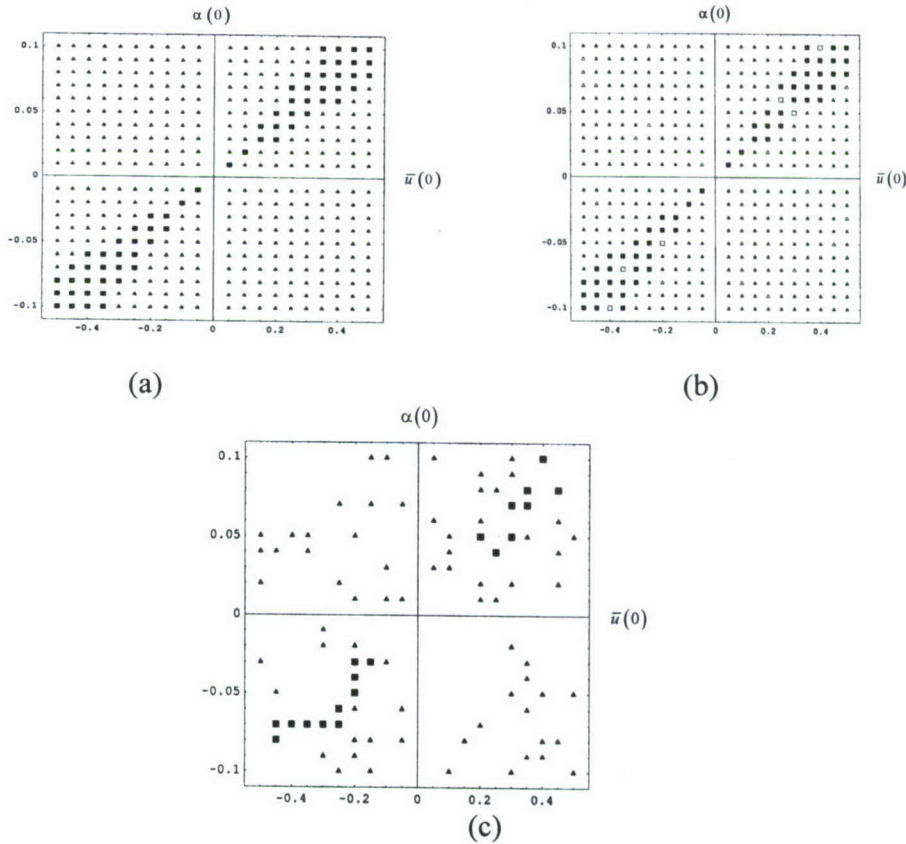


Figure 10. Domains of attraction at post-critical flow speed $U_\infty / b\omega_\alpha = 5.02$ for $\Omega = \omega_1 + \omega_2$, $\omega_1 = \omega_2$, $\sigma_e = 0$, $\sigma_i = 0.061$, and different values of excitation amplitude. (a) $Y_0 = 0$; (b) $Y_0 = 0.013$; (c) $Y_0 = 0.014$.

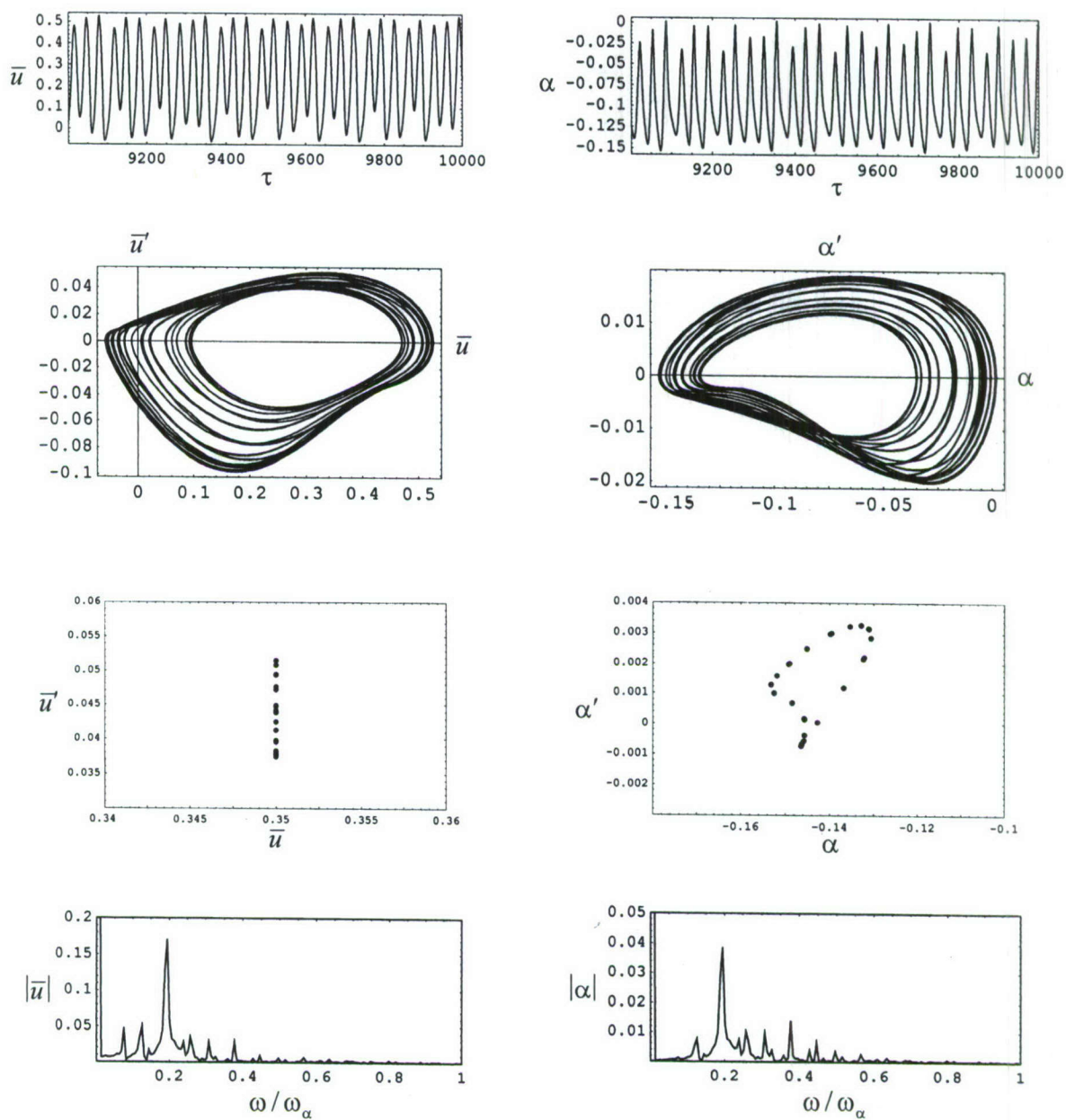


Figure 11(a).

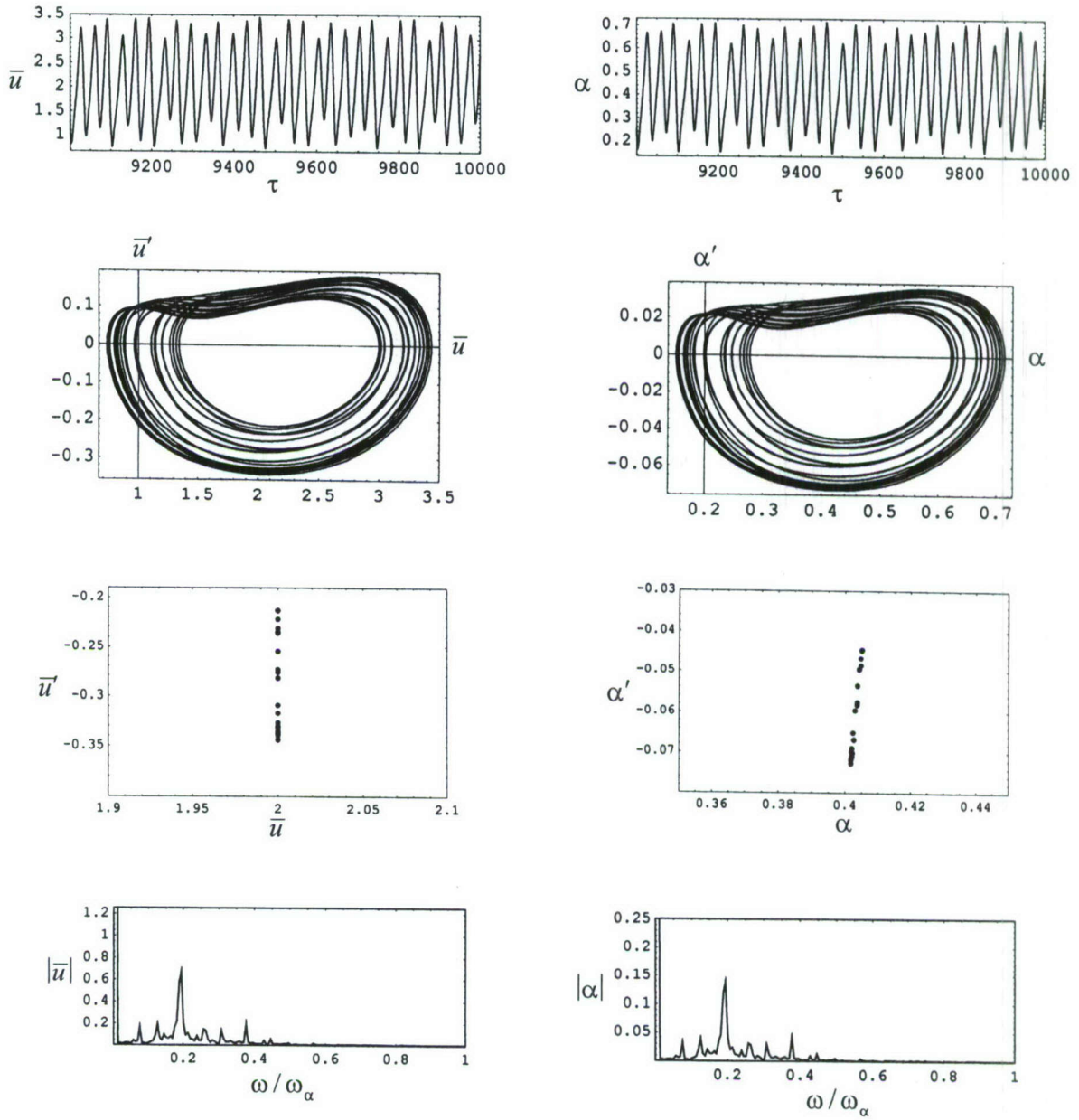


Figure 11(b).

Figure 11. Time history records, phase portraits, Poincaré maps and FFT plots at post-critical speed $U_\infty / b\omega_\alpha = 5.02$, $Y_0 = 0.0025$; $\Omega = \omega_1 + \omega_2$, $\omega_1 = \omega_2$, $\sigma_e = 0$, $\sigma_i = 0.061$, and for two different sets of initial conditions.

(a) $\bar{u}(0) = 0.2$, $\alpha(0) = 0.01$, $\bar{u}'(0) = 0$, $\alpha'(0) = 0$

(b) $\bar{u}(0) = 0.5$, $\alpha(0) = 0.1$, $\bar{u}'(0) = 0$, $\alpha'(0) = 0$

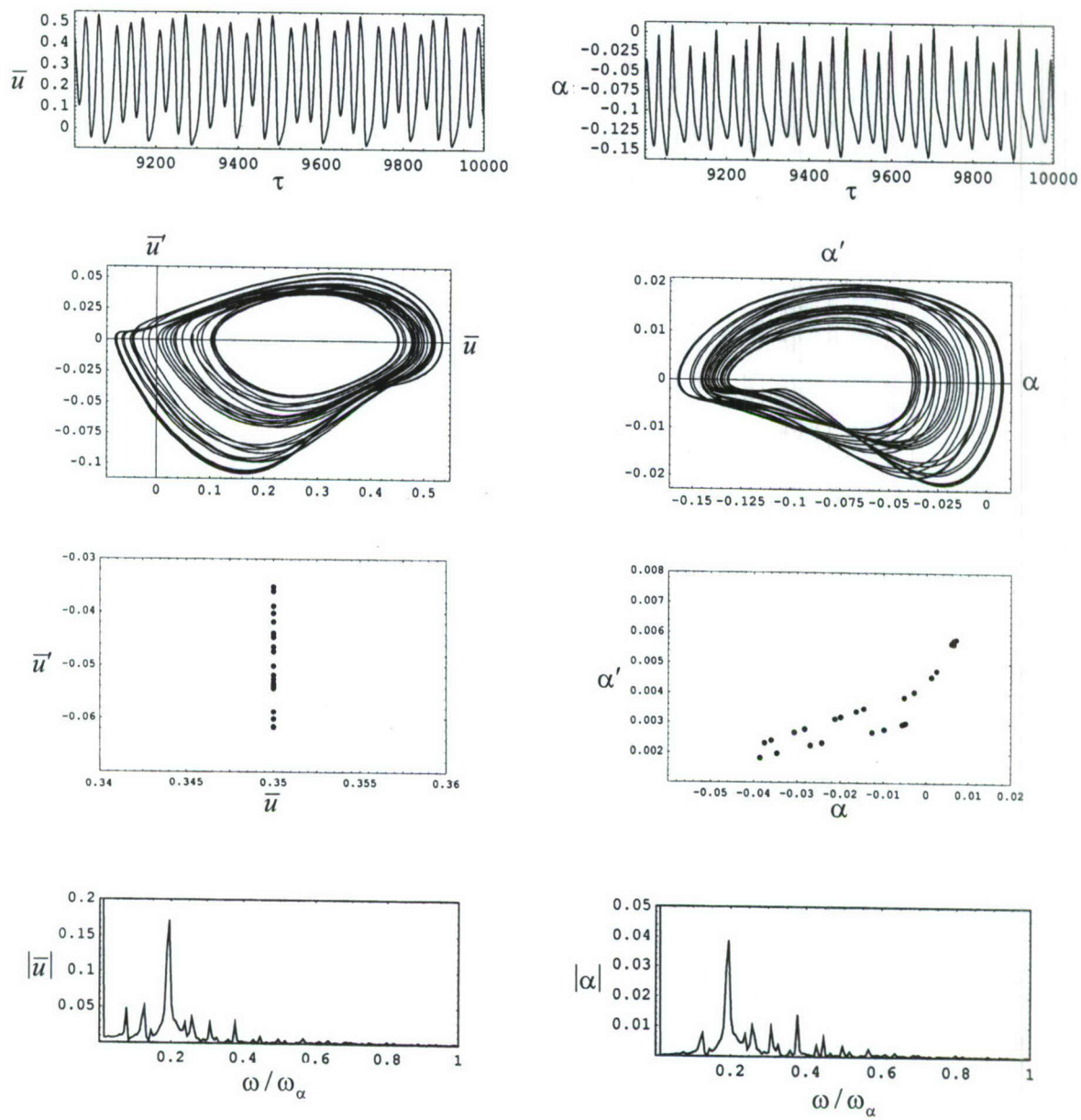


Figure 12(a).

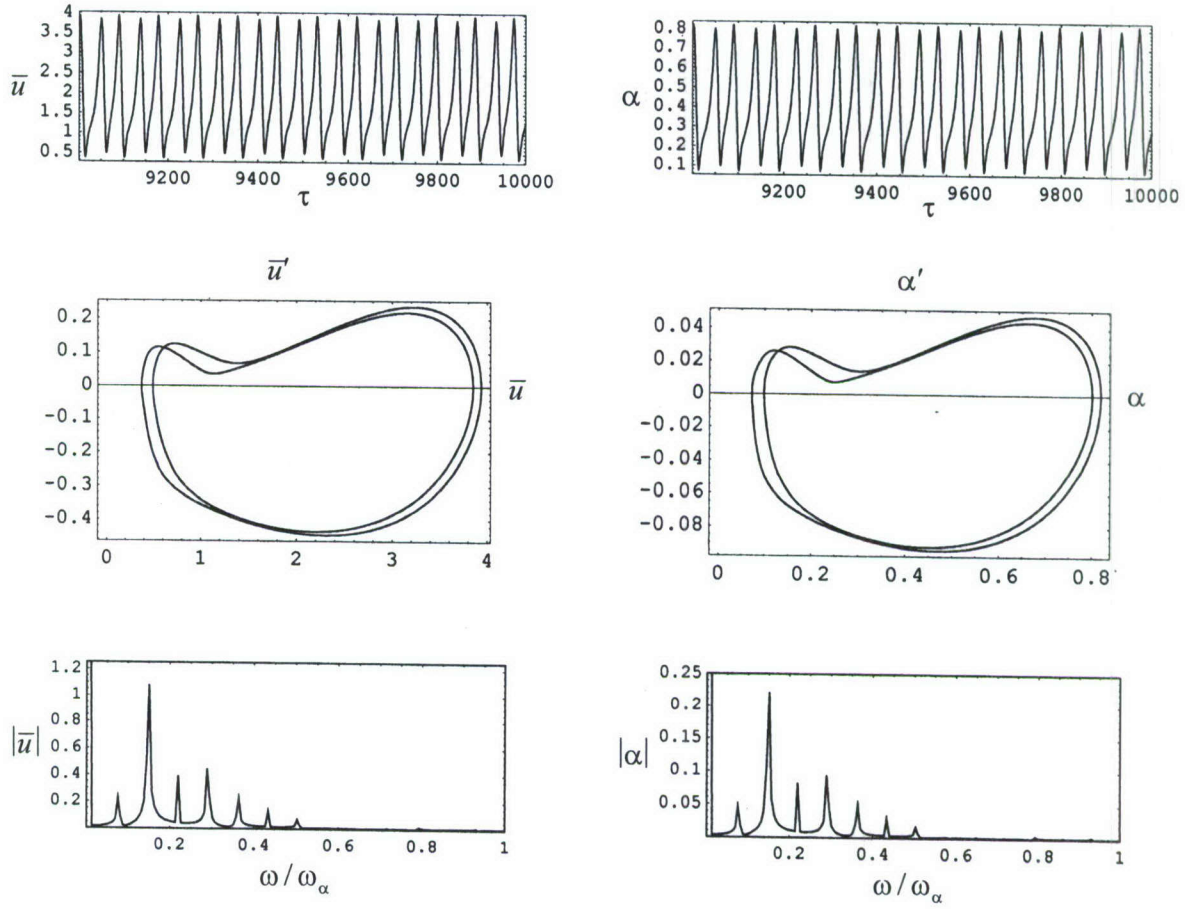


Figure 12(b).

Figure 12. Time history records, phase portraits, Poincaré maps and FFT plots at post-critical speed $U_\infty / b\omega_\alpha = 5.02$, $Y_0 = 0.004$; $\Omega = \omega_1 + \omega_2$, $\omega_1 = \omega_2$, $\sigma_e = 0$, $\sigma_i = 0.061$, and for two different sets of initial conditions.

(a) $\bar{u}(0) = 0.2$, $\alpha(0) = 0.01$, $\bar{u}'(0) = 0$, $\alpha'(0) = 0$

(b) $\bar{u}(0) = 0.5$, $\alpha(0) = 0.1$, $\bar{u}'(0) = 0$, $\alpha'(0) = 0$

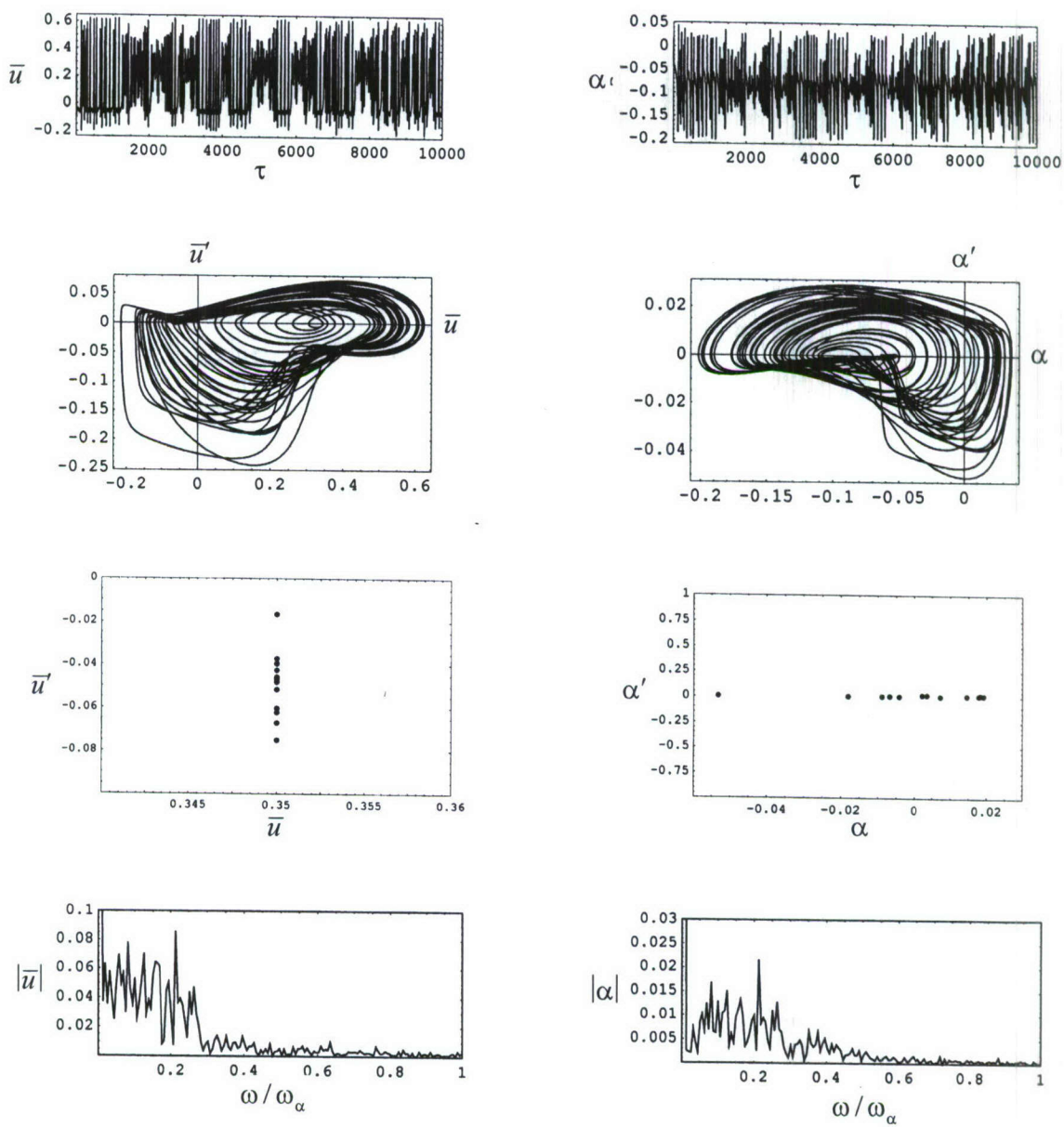


Figure 13(a).

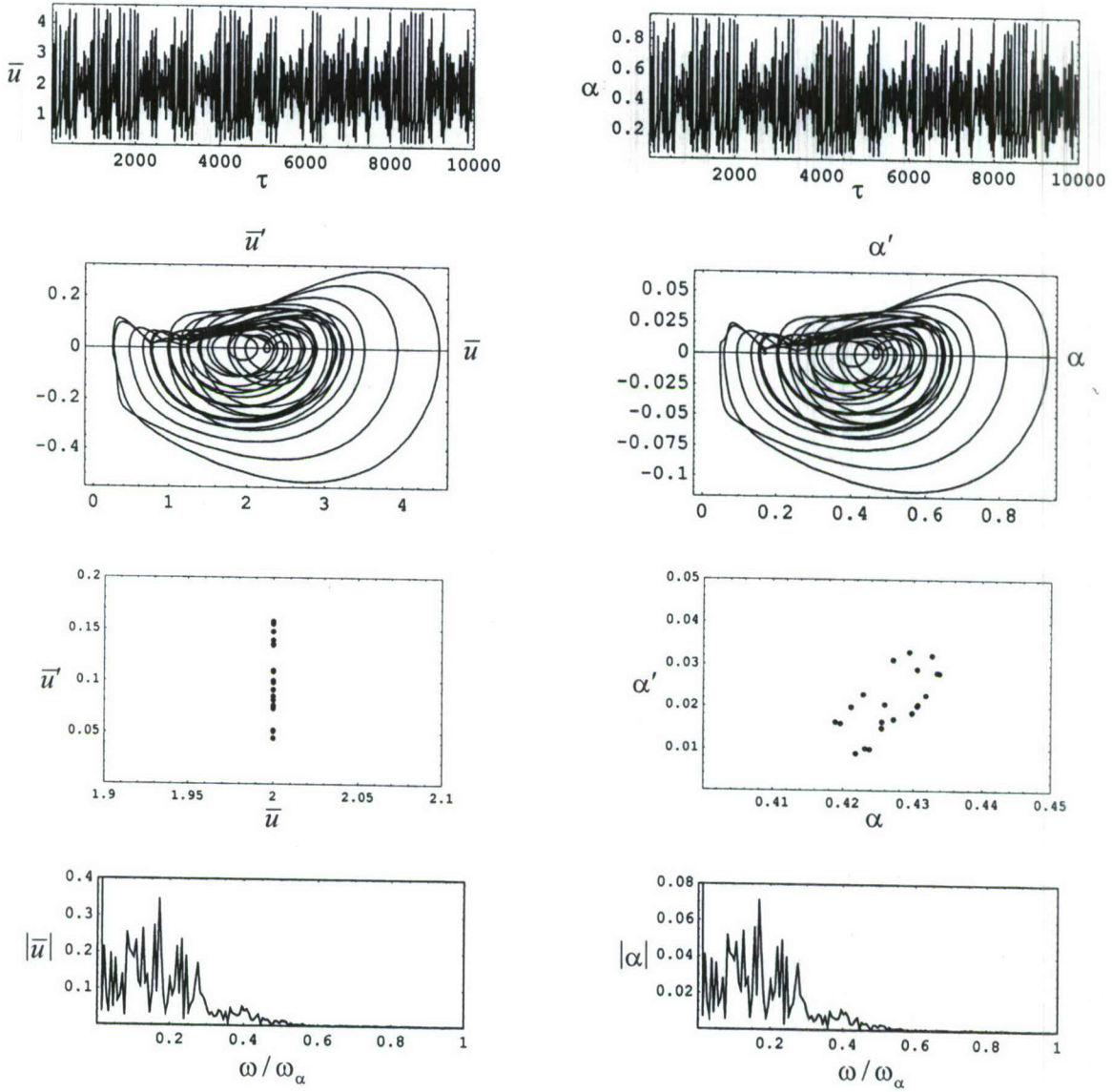


Figure 13(b).

Figure 13. Time history records, phase portraits, Poincaré maps and FFT plots at post-critical speed $U_\infty / b\omega_\alpha = 5.02$, $Y_0 = 0.0075$; $\Omega = \omega_1 + \omega_2$, $\omega_1 = \omega_2$, $\sigma_e = 0$, $\sigma_i = 0.061$, and for two different sets of initial conditions.

(a) $\bar{u}(0) = 0.2$, $\alpha(0) = 0.01$, $\bar{u}'(0) = 0$, $\alpha'(0) = 0$

(b) $\bar{u}(0) = 0.5$, $\alpha(0) = 0.1$, $\bar{u}'(0) = 0$, $\alpha'(0) = 0$

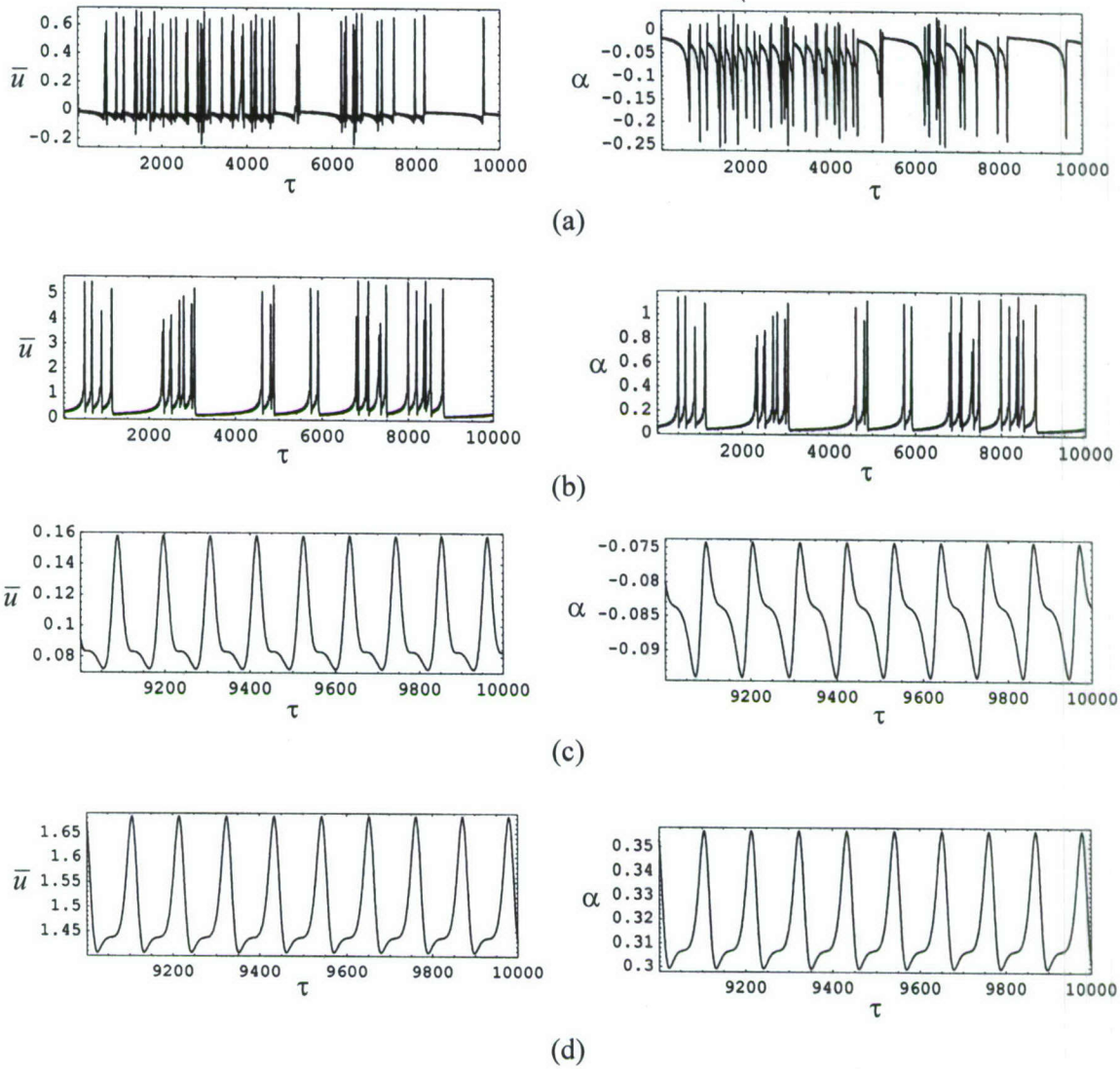


Figure 14. Time history records showing the influence of initial conditions on generating firing (a, b) and periodic (c, d) states at post-critical speed $U_{\infty}/b\omega_{\alpha} = 5.02$, $Y_0 = 0.013$;

$\Omega = \omega_1 + \omega_2$, $\omega_1 = \omega_2$, $\sigma_e = 0$, $\sigma_i = 0.061$.

(a) $\bar{u}(0) = 0.1$, $\alpha(0) = 0.02$, $\bar{u}'(0) = 0$, $\alpha'(0) = 0$

(b) $\bar{u}(0) = 0.1$, $\alpha(0) = 0.02$, $\bar{u}'(0) = 0$, $\alpha'(0) = 0$

(c) $\bar{u}(0) = 0.2$, $\alpha(0) = 0.02$, $\bar{u}'(0) = 0$, $\alpha'(0) = 0$

(d) $\bar{u}(0) = 0.4$, $\alpha(0) = 0.1$, $\bar{u}'(0) = 0$, $\alpha'(0) = 0$

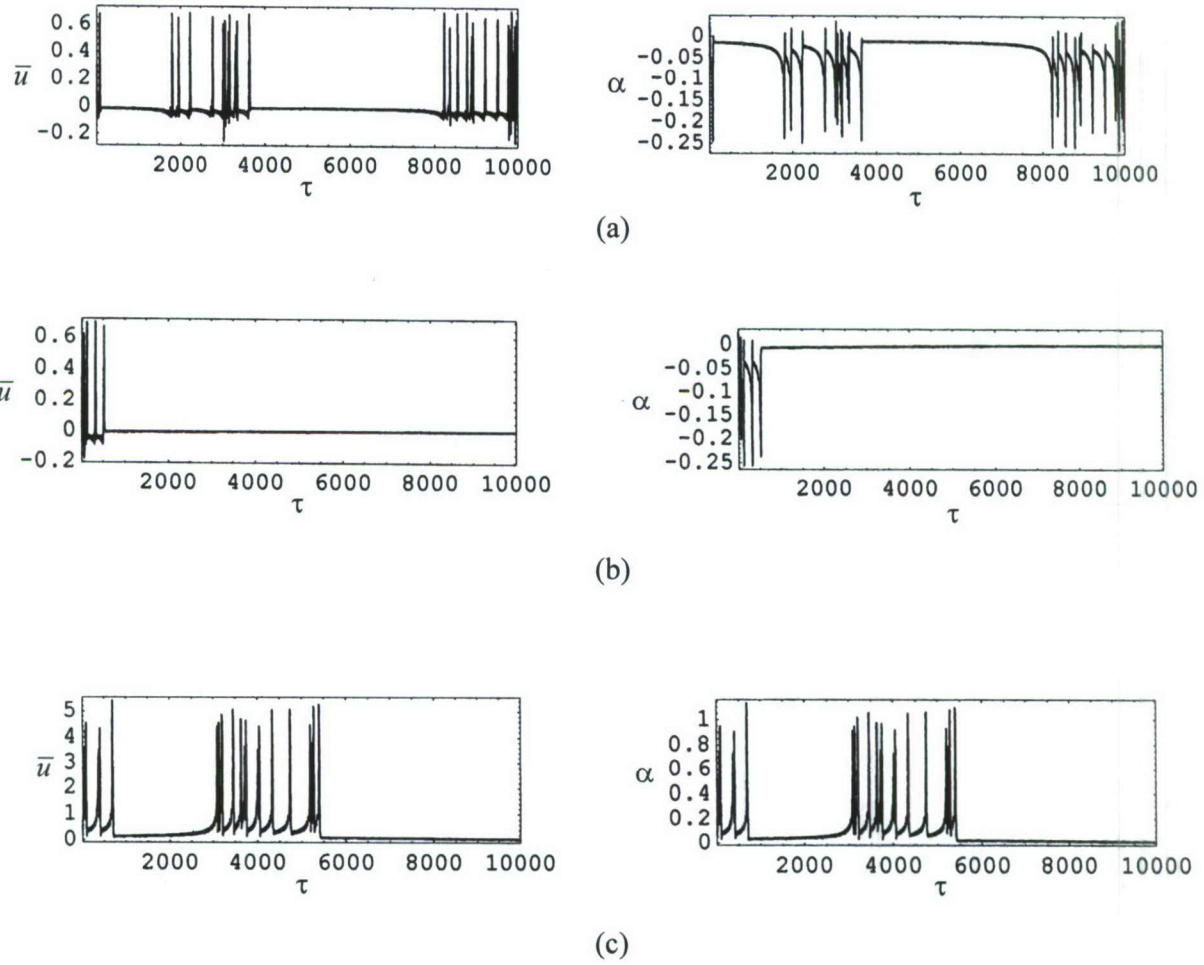


Figure 15. Time history records showing the influence of initial conditions on generating firing (a, b) and periodic (c, d) states at post-critical speed $U_\infty/b\omega_\alpha = 5.02$, $Y_0 = 0.014$; $\Omega = \omega_1 + \omega_2$, $\omega_1 = \omega_2$, $\sigma_e = 0$, $\sigma_i = 0.061$.

(a) $\bar{u}(0) = 0.3$, $\alpha(0) = 0.02$, $\bar{u}'(0) = 0$, $\alpha'(0) = 0$

(b) $\bar{u}(0) = 0.35$, $\alpha(0) = 0.02$, $\bar{u}'(0) = 0$, $\alpha'(0) = 0$

(c) $\bar{u}(0) = 0.25$, $\alpha(0) = 0.07$, $\bar{u}'(0) = 0$, $\alpha'(0) = 0$

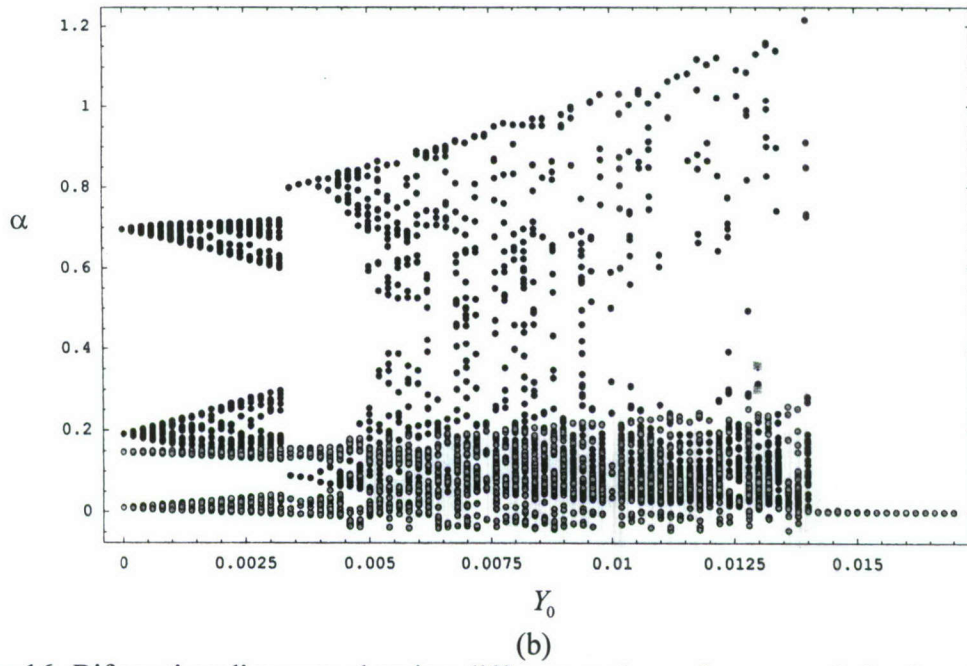
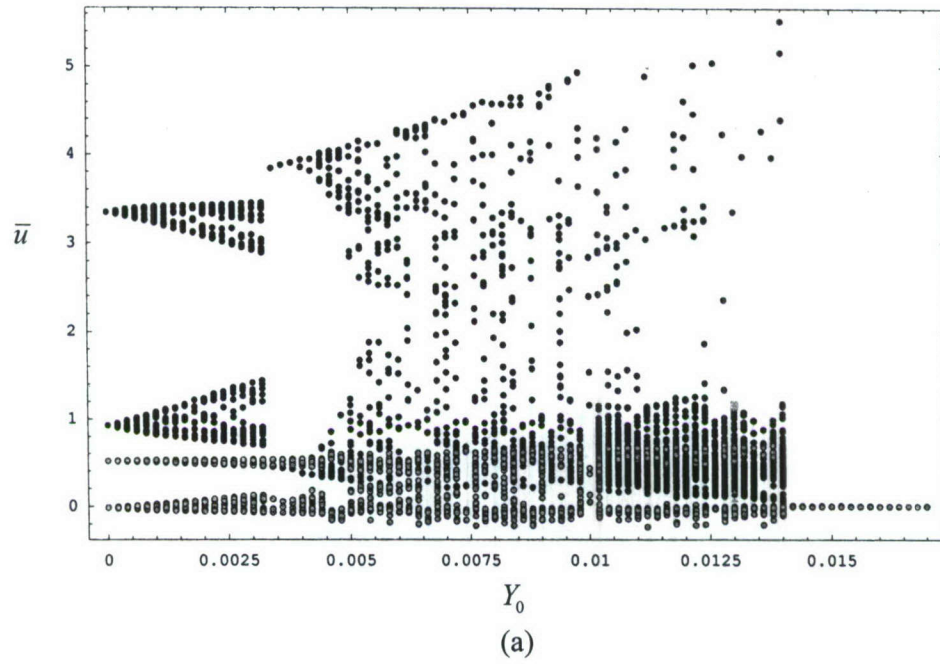


Figure 16. Bifurcation diagrams showing different regions of response behavior at post-critical flow speed $U_\infty / b\omega_\alpha = 5.02$, $\Omega = \omega_1 + \omega_2$, $\omega_1 = \omega_2$, $\sigma_e = 0$, $\sigma_i = 0.061$
 (a) Dependence of bending amplitude on excitation amplitude
 (b) Dependence of torsion amplitude on excitation amplitude

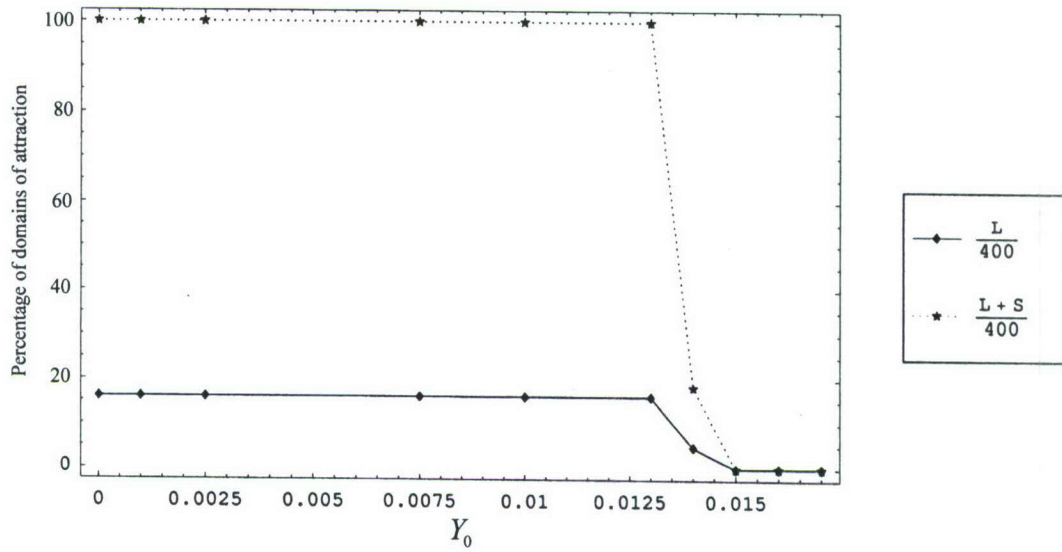


Figure 17. Stabilization effect of parametric excitation at post-critical flow speed $U_\infty / b\omega_\alpha = 5.02$ showing the percentage of domains of attraction for large amplitude response (diamond-solid curve) and large plus small amplitude responses (star-dotted curve).

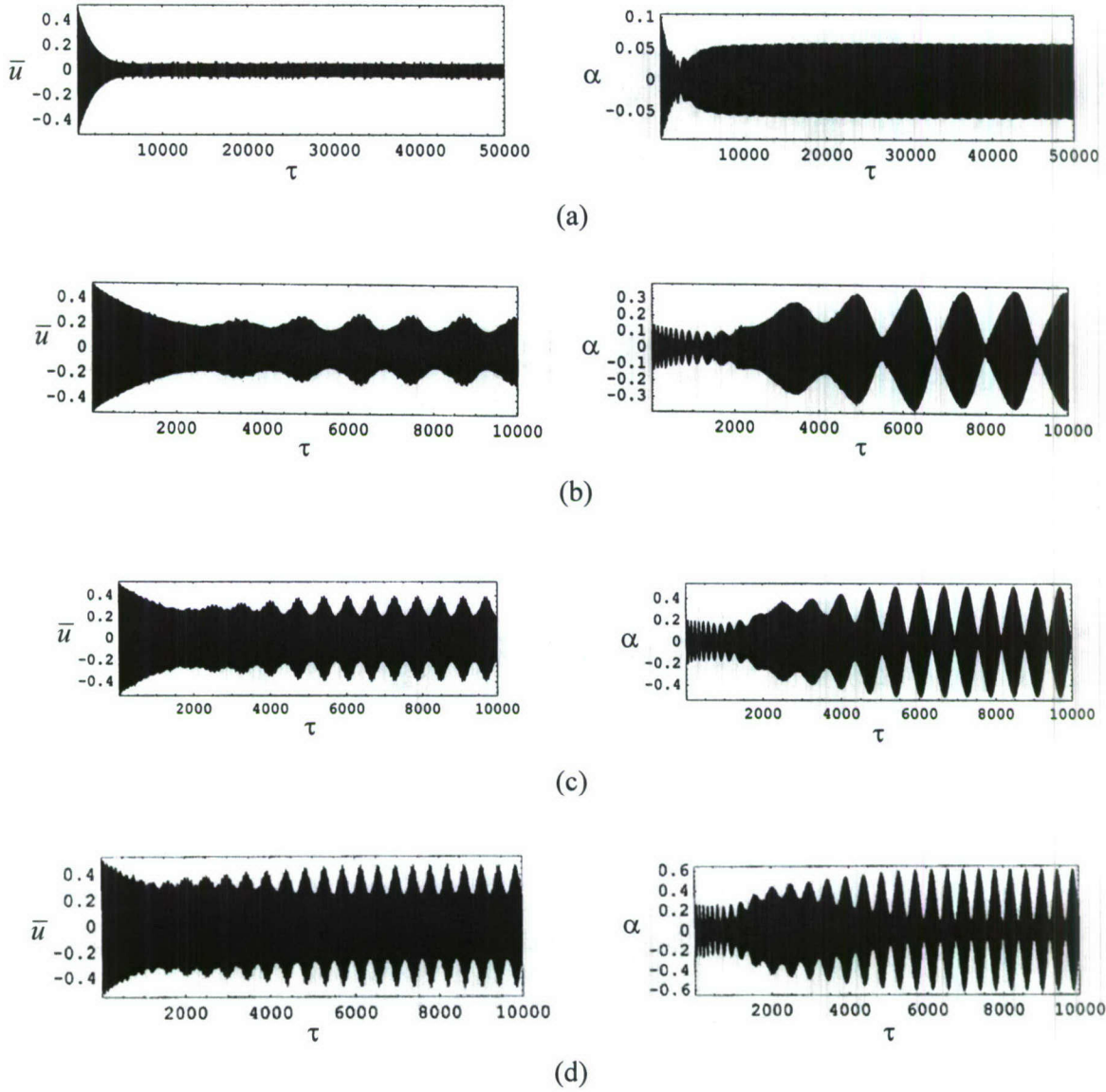
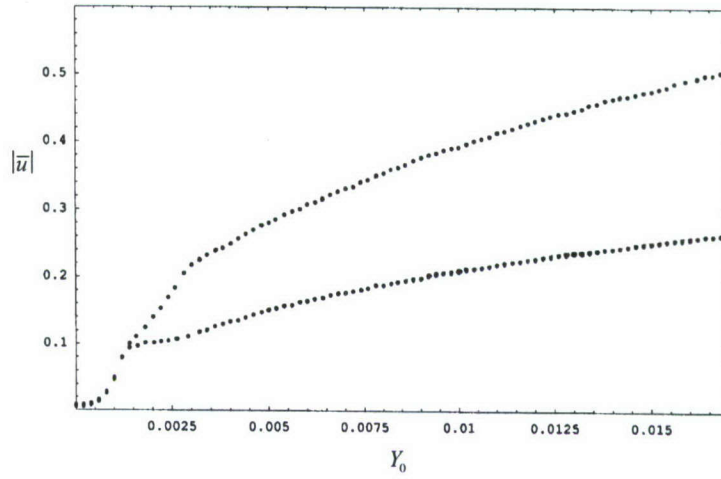
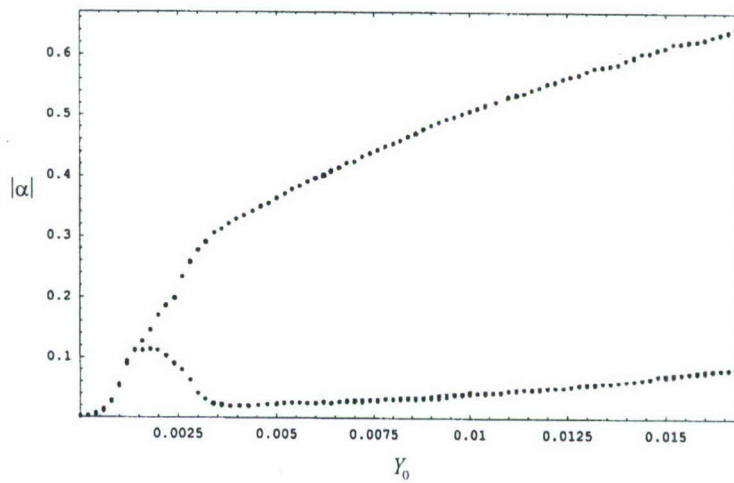


Figure 18. Response time history records according to numerical simulation at zero critical flow speed for different values of excitation amplitude and for the same initial conditions $\bar{u}(0) = 0.5$, $\alpha(0) = 0.1$, $\bar{u}'(0) = 0$, $\alpha'(0) = 0$.
 (a) $Y_0 = 0.001$; (b) $Y_0 = 0.005$; (c) $Y_0 = 0.01$; (d) $Y_0 = 0.015$.



(a)



(b)

Figure 19. Bifurcation diagram according to the numerical simulation of equations of motion at zero flow speed and $\Omega = \omega_1 + \omega_2$, $\omega_1 = 0.5\omega_2$, $\bar{u}(0) = 0.5$, $\alpha(0) = 0.1$, $\bar{u}'(0) = 0$, $\alpha'(0) = 0$.

- (a) Dependence of bending response amplitude on excitation amplitude
 (b) Dependence of torsion response amplitude on excitation amplitude

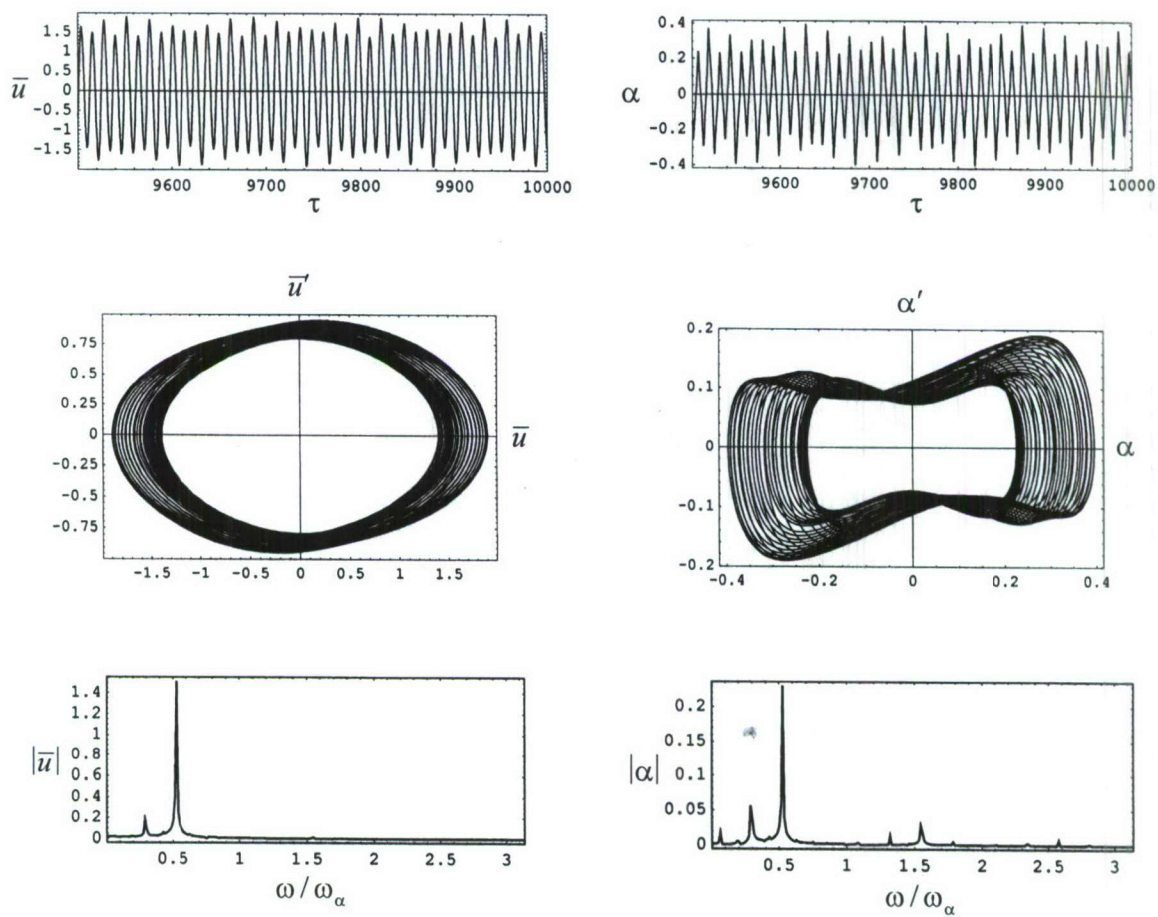


Figure 20(a)

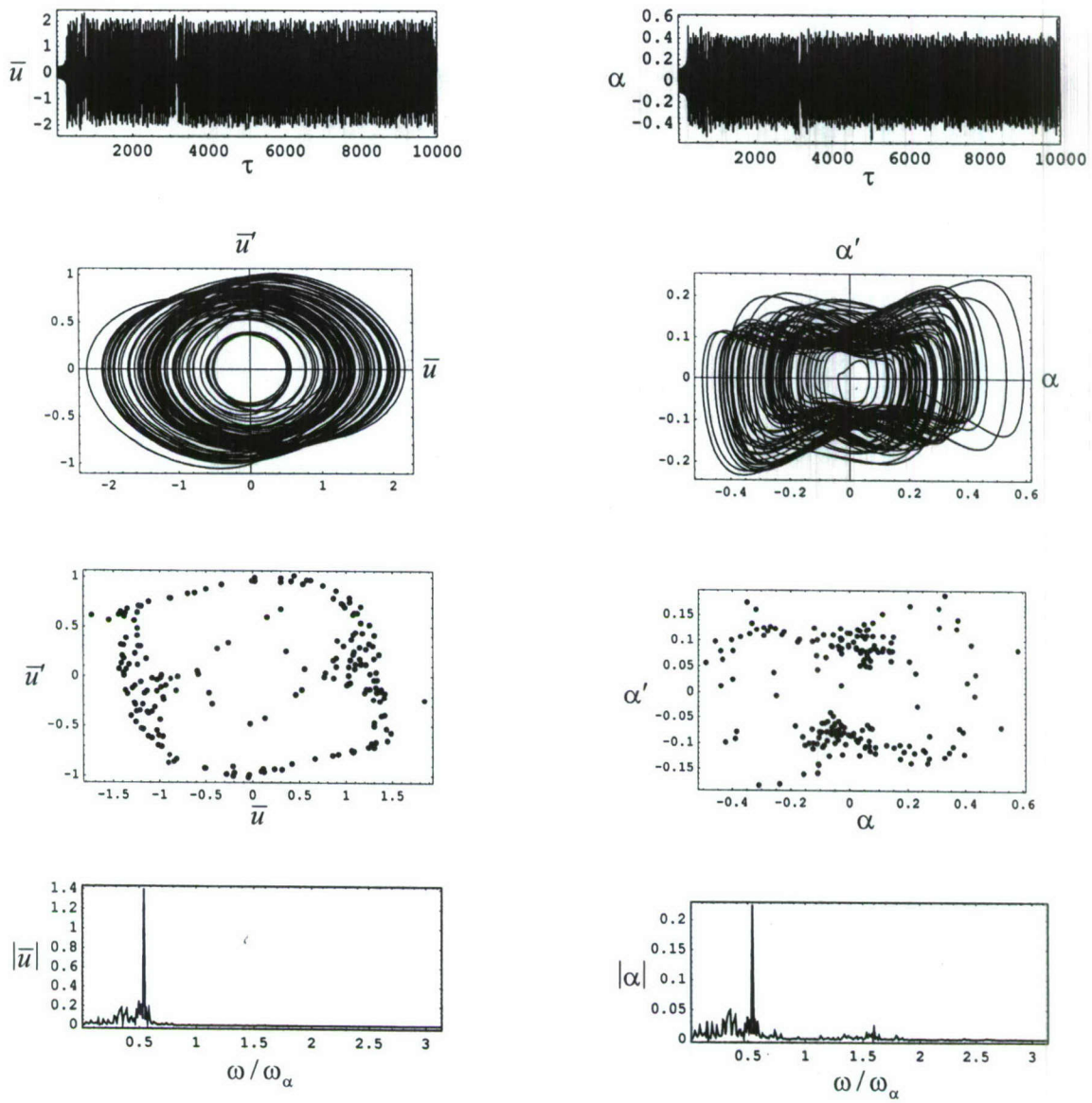


Figure 20(b).

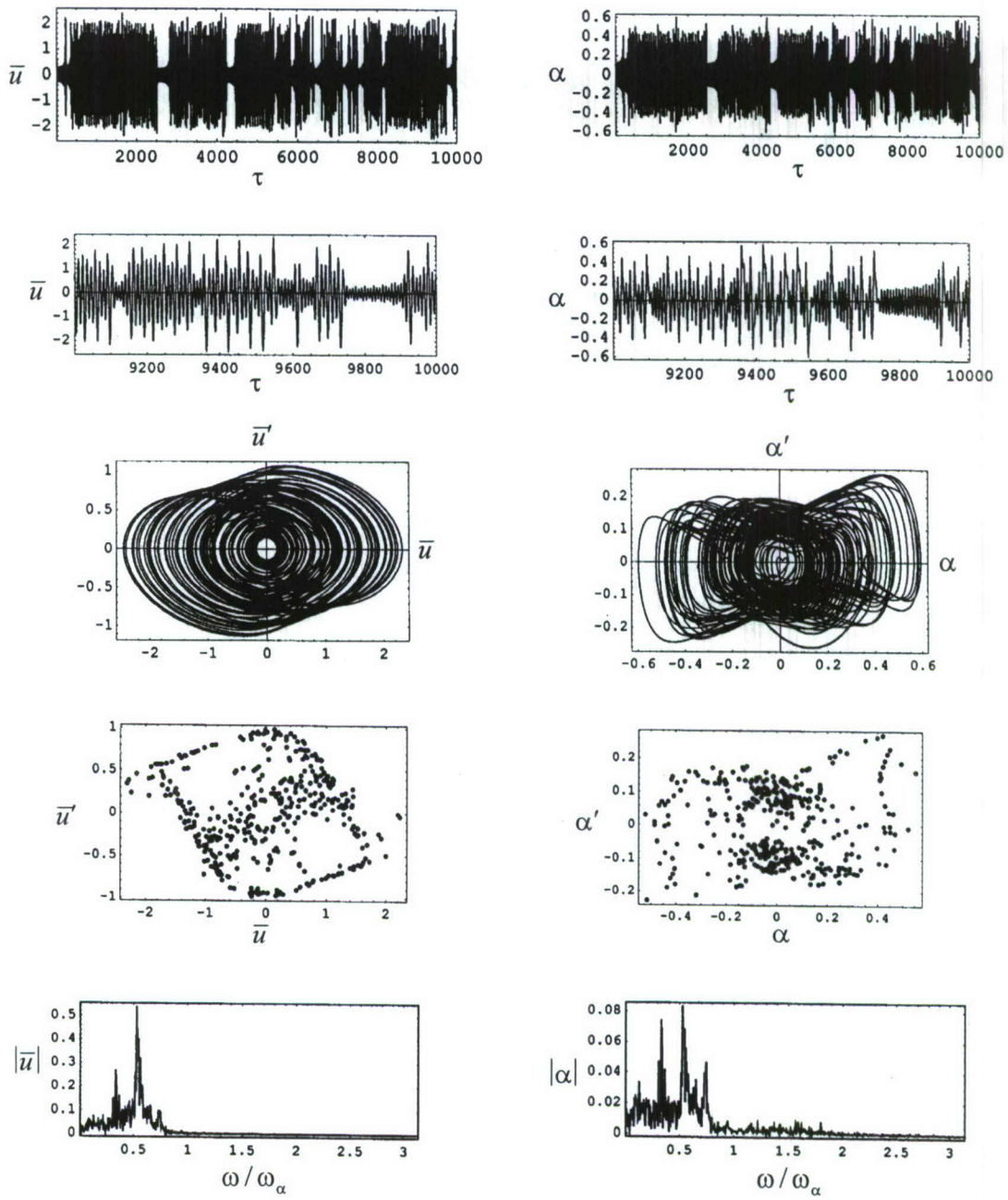


Figure 20(c).

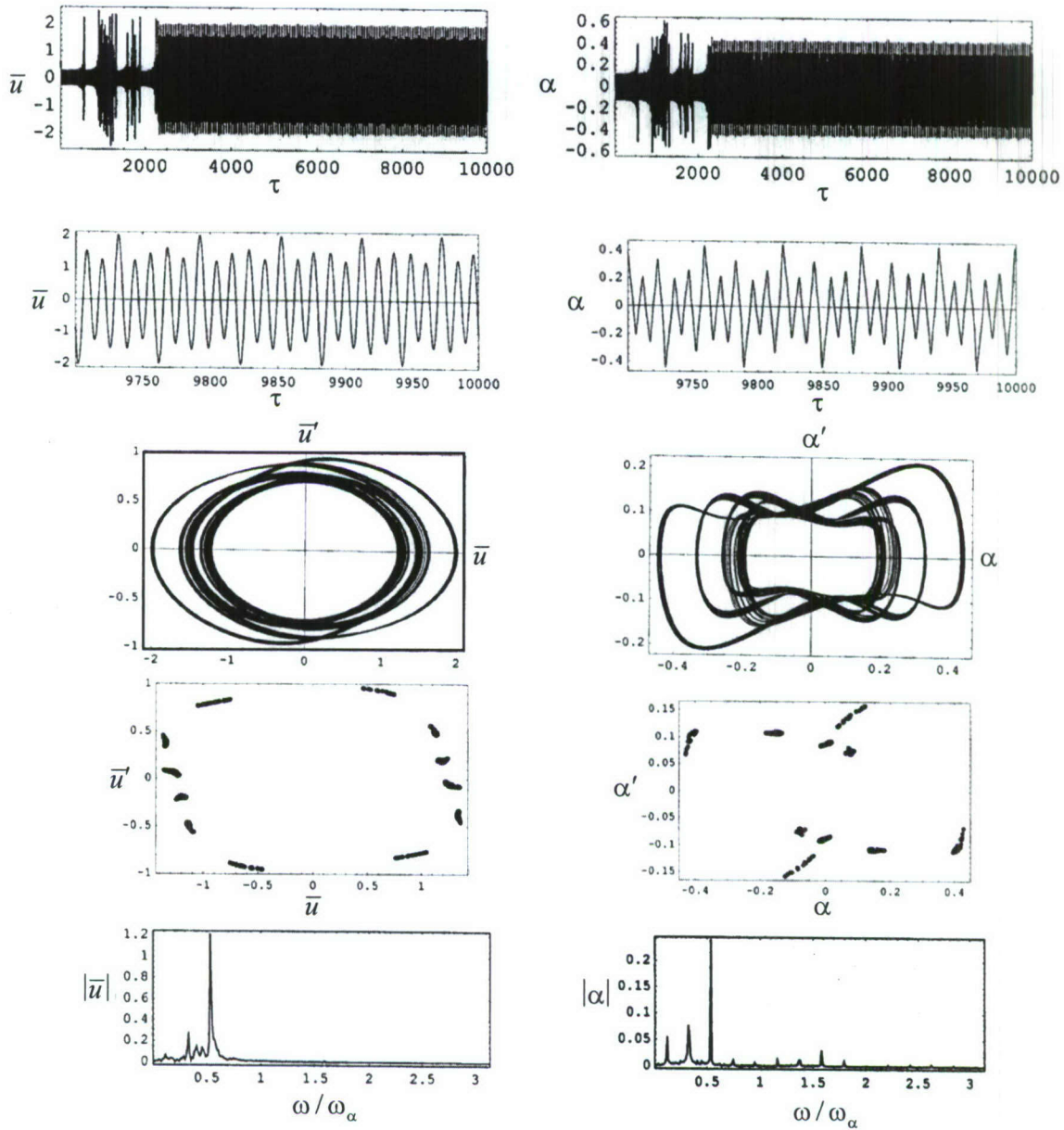
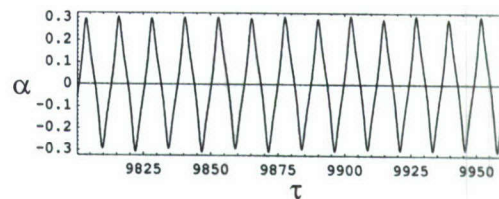
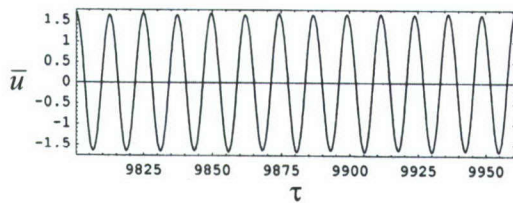


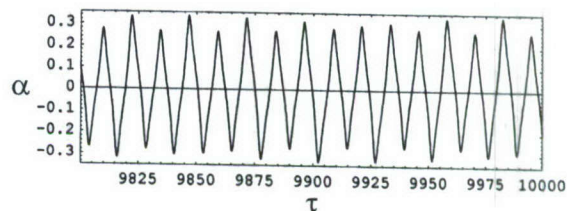
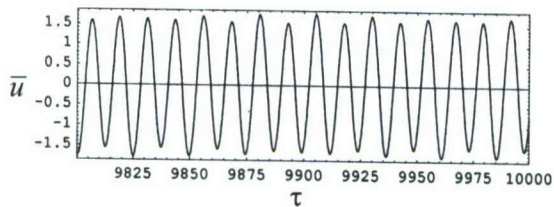
Figure 20(d).

Figure 20. Selected samples of numerical simulation time history records, phase portraits, Poincaré maps (for b,c) and FFT plots for different values of excitation amplitude and different sets of initial conditions, at critical flow speed.

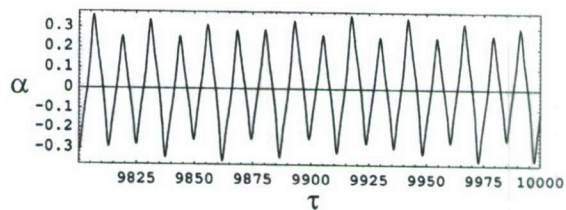
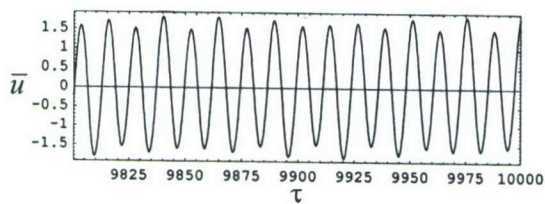
- (a) $Y_0 = 0.00875$, $\bar{u}(0) = 0.5$, $\alpha(0) = 0.04$, $\bar{u}'(0) = 0$, $\alpha'(0) = 0$
- (b) $Y_0 = 0.014$, $\bar{u}(0) = 0.5$, $\alpha(0) = 0.1$, $\bar{u}'(0) = 0$, $\alpha'(0) = 0$
- (c) $Y_0 = 0.016$, $\bar{u}(0) = 0.6$, $\alpha(0) = 0.1$, $\bar{u}'(0) = 0$, $\alpha'(0) = 0$
- (d) $Y_0 = 0.017$, $\bar{u}(0) = 0.6$, $\alpha(0) = 0.1$, $\bar{u}'(0) = 0$, $\alpha'(0) = 0$



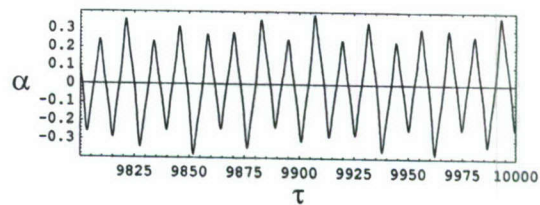
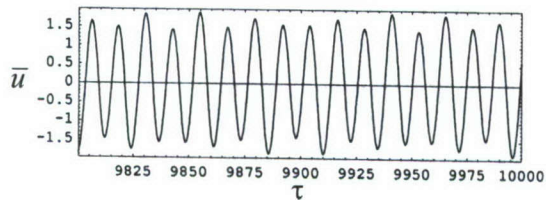
(a)



(b)



(c)



(d)

Figure 21. Sample of numerical simulation time history records at pos-critical speed $U_{\infty}/b\omega_{\alpha} = 5.02$, $\Omega = \omega_1 + \omega_2$, $\omega_2 = \omega_1 + 0.061$, $\bar{u}(0) = 0.1$, $\alpha(0) = 0.01$, $\bar{u}'(0) = 0$, $\alpha'(0) = 0$, and for different values of excitation amplitude.

(a) $Y_0 = 0.001$; (b) $Y_0 = 0.005$; (c) $Y_0 = 0.0075$; (d) $Y_0 = 0.01$

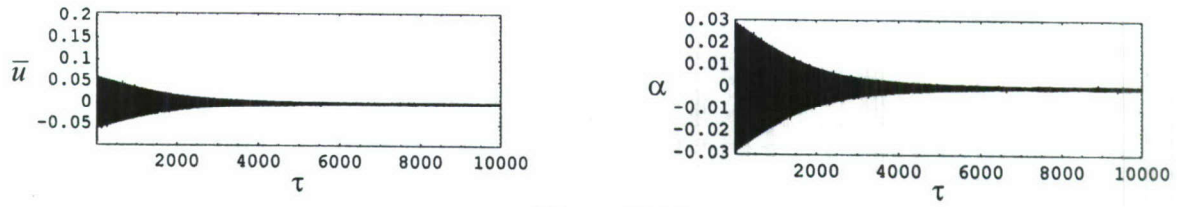


Figure 22(a).

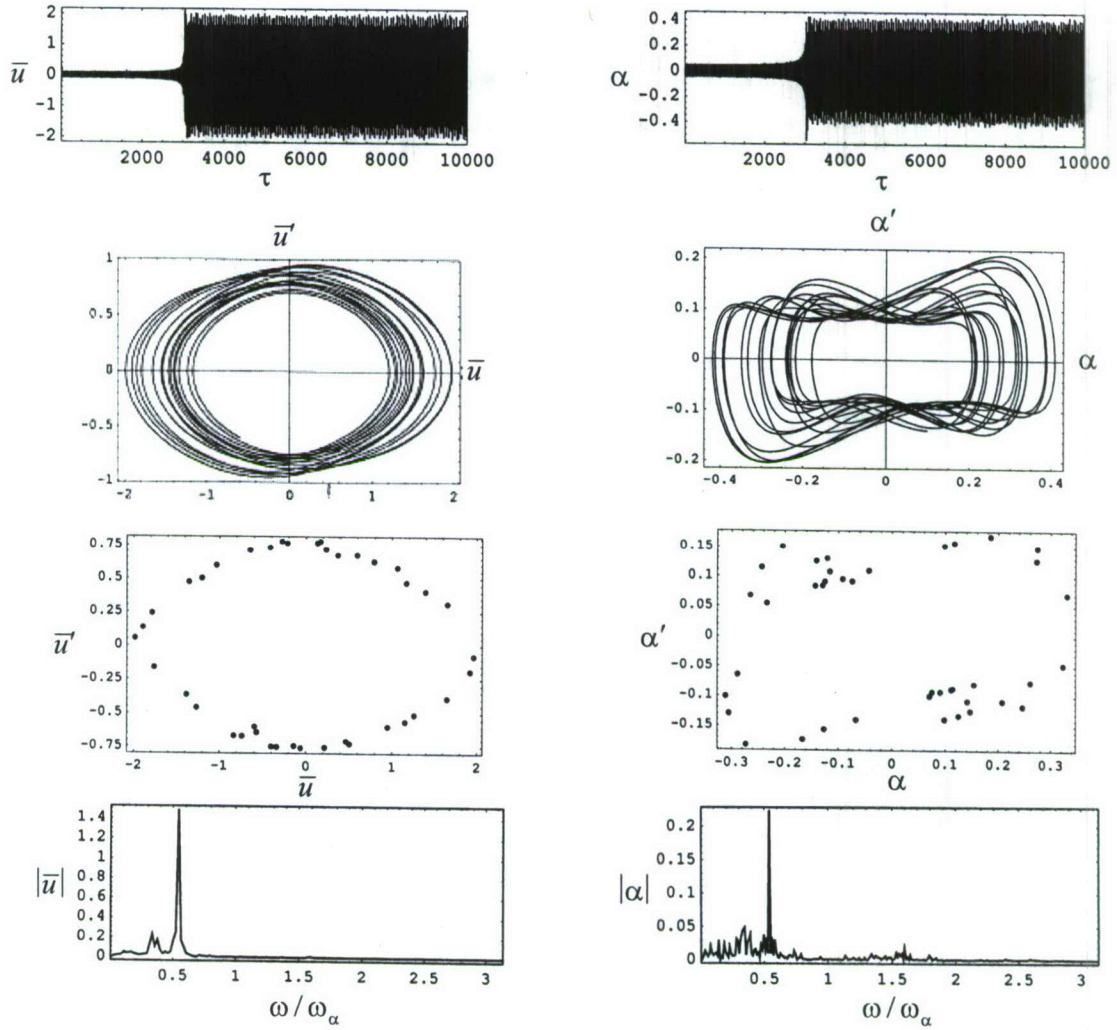


Figure 22(b).

Figure 22. Samples of numerical simulation time history records at post-critical flow speed $U_\infty / b\omega_\alpha = 5.02$, excitation amplitude $Y_0 = 0.015$ for

- (a) a set of initial conditions that lead to zero response: $\bar{u}(0) = 0.2$, $\alpha(0) = 0.01$, $\bar{u}'(0) = 0$, $\alpha'(0) = 0$
- (b) a set that lead to quasi-periodic response: $\bar{u}(0) = 0.3$, $\alpha(0) = 0.01$, $\bar{u}'(0) = 0$, $\alpha'(0) = 0$

APPENDIX

Publications Generated from the Grant:

1. Ibrahim, R. A. and Pettit, C. L., 2005, "Uncertainties and Dynamic Problems of Bolted Joints and other Fasteners," *Journal of Sound and Vibration* **279**(3-5), 857-936.
2. Ibrahim, R. A., Beloiu, D. M., and Pettit, C. L., 2005, "Influence of Joint Relaxation on Deterministic and Stochastic Panel Flutter," *AIAA Journal* **43**(7), 1444-1454.
3. Beloiu, D. M., Ibrahim, R. A., and Pettit, C. L., 2005, "Influence of Boundary Conditions Relaxation on Panel Flutter with Compressive In-Plane Loads," *Journal of Fluids and Structures* **21**, 743-767.
4. Ibrahim, R. A. and Castravete, S. C., 2006, "Flutter Suppression of a Plate-Like Wing Via Parametric Excitation," *Nonlinear Dynamics* **46**(4), 387-426.
5. Ibrahim, R. A., 2006, "Excitation-Induced Stability and Phase Transition: A Review," *Journal of Vibration and Control* **12**(10), 1093-1170.
6. Castravete, C. and Ibrahim, R. A., 2008, "Effect of Stiffness Uncertainties on the Flutter of a Cantilever Wing," *AIAA Journal*, in print.
7. Thoppul, S. D., Gibson, R. F., and Ibrahim, R. A., 2008, "Phenomenological Modeling and Numerical Simulation of Relaxation in Bolted Composite Joints," *Journal of Composite Materials*, in print.

Conference Proceedings:

1. Ibrahim, R. A., Beloiu, D. M., and Pettit, C. L., 2003, "Influence of Boundary Conditions Relaxation on Panel Flutter," IUTAM Symposium on *Chaotic Dynamics and Control of Systems and Processes in Mechanics*, Rome, Italy, 8-13 June 2003. Published by Springer, 2005, 223-232, Dordrecht, The Netherlands, G. Rega and F. Vestroni, (Editors).
2. Ibrahim, R. A. Beloiu, D.M and Pettit, C. L., 2003, "Influence on Boundary Conditions Relaxation on Panel Flutter: Deterministic and Stochastic," AFOSR Workshop Contractors Meeting, Santa Fe, New Mexico, September 8-11, 2003.
3. Ibrahim, R. A. Beloiu, D.M and Pettit, C. L., 2004, "Influence of Joint Relaxation on Deterministic and Stochastic Panel Flutter," Flow Induced Vibration, de Langre & Axisa ed., Ecole Polytechnique, Paris, July 6-9.
4. Ibrahim, R. A. Beloiu, D.M and Pettit, C. L., 2004, "Influence of Boundary Conditions Relaxation on Panel Flutter with in-Plane Loads," AFOSR Workshop Contractors Meeting, Winter Green, VA, August 18-20.
5. Ibrahim, R. A. Beloiu, D.M and Pettit, C. L., 2004, "Six-Mode Interaction of Panel Flutter with Joint Relaxation, Part I: Deterministic Analysis," Proc IMECE2004, November 13-19, 2004, Anaheim, California USA, IMECE2004-60184.
6. Ibrahim, R. A. and Castravete*, S. C., 2005, "Nonlinear Bending-Torsion Flutter of a Cantilever Wing Subjected to Parametric Excitation," Proceedings of the ASME Vibration Conference, Long Beach California, September 25-27, 2005.

7. Ikeda*, T. and Ibrahim, R. A. 2006, "Horizontal Ground Random Excitation of Structures Carrying a Rigid Container Filled with Liquid," Proceedings of the ASME Conference on Pressure Piping and Vessels, Paper No. PVP2006-ICPVT11-93750, Vancouver, Canada, July 23-27, 2006.
8. Thoppul*, S. D., Gibson, R. F., and Ibrahim, R. A., 2006, "Analytical and Experimental Characterization of the Effects of Vibration on Relaxation in Composite Bolted Joints," Proceedings of the 21st Technical Conference of the American Society of Composites, Dearborn, MI.
9. Ibrahim*, R. A. and Castravete, S., 2006, "Influence of Parameter Uncertainties on the Flutter of a Cantilever Wing," AFOSR Annual Meeting, Seattle, WA.
10. Castravete, S. C. And Ibrahim*, R. A., 2007, "Flutter Characteristics of a Cantilever Wing with Parameter Uncertainties Using Stochastic Finite Element," International Symposium on Recent Advances in Mechanics (structural/solid), Dynamical Systems (deterministic/stochastic) and Probability Theory (mathematical/applied), Palermo, Italy on June 3-6, 2007.
11. Ibrahim, R. A. and Castravete, S. C., 2008, "Stabilization of Dynamic Systems via Parametric Excitation," Proceedings of the 9th Cairo University International Conference on Mechanical Design and Production, Giza, EGYPT, January 8-10, 2008.

Ph.D. Theses Generated

1. D. Marian Dimitru Beloiu, Ph.D., "Non-smooth Dynamics of Disk Brake Systems and Aeroelastic Panels," July 2005, Wayne State University.
2. Stefan C. Castravete, Ph.D., "Nonlinear Flutter of a Cantilever Wing Including the Influence of Structural Uncertainties," May 2007.